Spectroscopy and Photochemistry of Europium atoms in low temperature solids - an experimental and theoretical study

A Thesis submitted by

Owen Byrne, B.Sc. (Hons.)

to the **National University of Ireland** in fulfilment of the
requirements for the Degree of Doctor of Philosophy

NUI MAYNOOTH
Ollscoil na hÉireann Má Nuad

Based on research carried out in the
Low Temperature Laboratory,
Department of Chemistry,
National University of Ireland, Maynooth.

Research Supervisor: Dr. John G. McCaffrey
Head of Department: Prof. John P. Lowry

Maynooth,
Co. Kildare,
Ireland.

November, 2010

TABLE OF CONTENTS

Abstract VII

Chapter I - Introduction

I.1 Matrix-Isolation - History, Development and Overview 1

I.2 Rare Gas (RG) host lattices 3

I.3 Matrix effects on electronic transitions 9
  I.3.I Matrix Shift 9
  I.3.II Stokes Shift 9
  I.3.III Enhancement of electronic transitions 11
  I.3.IV Jahn-Teller effect 13

I.4 LS and *jj* Coupling Schemes 15

I.5. Geometry optimisation, vibrational frequency calculations 18

I.6 Luminescence Spectroscopy of Eu/RG Systems 22

References 25

Chapter II - Experimental

II.1 Introduction 28

II.2 Matrix-isolation Apparatus 28

II.3 Gas handling system 32

II.4 M/RG Sample Preparation 33
  II.4.I Metal vaporisation 33
  II.4.II Sample Deposition 36

II.5 Luminescence measurements 37
  II.5.I UV/Vis Spectroscopy 37
  II.5.II Infrared Absorption Spectroscopy 44

References 46

Chapter III - Eu(y^8P)/RG Absorption and Excitation Spectroscopy

Sites of isolation in solid RG's and the observation of Eu dimers

III.1 Introduction 48

III.2 Eu/RG Absorption Spectroscopy 50
- III.2.I Eu/Ar 50
- III.2.II Eu/Kr 53
- III.2.III Eu/Xe 56
- III.2.IV Eu/RG Absorption Spectroscopy Summary 58

III.3 Eu Dimer and Concentration Study 60
- III.3.I Eu/Ar 61
- III.3.II Eu/Kr 64
- III.3.III Eu/Xe 66
- III.3.IV Eu/RG Dimer formation Summary 68

III.4 Eu(y^8P)/RG Excitation Spectroscopy 70
- III.4.I Eu/Ar 70
- III.4.II Eu/Kr 72
- III.4.III Eu/Xe 73
- III.4.IV Eu/RG Excitation Summary 75

III.5 Polarisability study – site assignments 77

III.6 UV Absorption Features 80

III.7 Conclusion 85

References 87

Chapter IV - Luminescence spectroscopy of the y^8P state of atomic europium isolated in the rare gas solids, (RG = Ar, Kr and Xe)

IV.1 Introduction 88

IV.2 Eu(y^8P)/Ar Luminescence 90
- IV.2.I. Eu/Ar - $\lambda_{Em.} \approx 455$ nm 91
- IV.2.II Eu/Ar - $\lambda_{Em.} \approx 560$ nm 99
- IV.2.III Eu/Ar - $\lambda_{Em.} \approx 679$ nm 105
- IV.2.IV Eu/Ar - $\lambda_{Em.} \approx 800$ nm 110
- IV.2.V Eu(y^8P)/Ar Luminescence Summary 114

IV.3 Eu(y^8P)/Kr Luminescence 115
- IV.3.I Eu/Kr - $\lambda_{Em.} \approx 467$ nm 116
- IV.3.II Eu/Kr - $\lambda_{Em.} \approx 573$ nm 121
- IV.3.III Eu/Kr - $\lambda_{Em.} \approx 683$ nm 127
- IV.3.IV Eu/Kr - $\lambda_{Em.} \approx 800$ nm 128
- IV.3.V Eu(y^8P)/Kr Luminescence Summary 133

IV.4 Eu(y^8P)/Xe Luminescence **134**
IV.4.I Eu/Xe - $\lambda_{Em.} \approx 483$ *nm* 135
IV.4.II Eu/Xe - $\lambda_{Em.} \approx 589$ *nm* 138
IV.4.III Eu/Xe - $\lambda_{Em.} \approx 823$ *nm* 140
IV.4.IV Eu(y^8P)/Xe Luminescence Summary 141

IV.5 Eu(y^8P)/RG Luminescence **143**
IV.5.I Red and Blue site Luminescence 144
IV.5.II Temperature Effects 153

IV.6 Eu(z^6P)/RG Resonance Fluorescence **157**
IV.6.I Eu(z^6P)/Ar 157
IV.6.II Eu(z^6P)/Kr 159
IV.6.III Eu(z^6P)/Xe 163
IV.6.IV Eu(z^6P)/RG 166
IV.6.V Eu(z^6P)/RG Summary 174

IV.7 Conclusion **175**

References **176**

Chapter V - Identification of matrix-isolated europium ions

V.1 Introduction **177**

V.2 Eu/Xe **178**

V.3 Eu/Kr **187**

V.4 Eu/Ar **194**

V.5 Eu/RG Discussion **200**
V.5.I Eu/RG Visible Absorption Spectroscopy 200
V.5.II Eu/RG UV Absorption Spectroscopy 207
V.5.III Eu^+/RG Luminescence 208
V.5.IV Matrix-isolated ion formation *in situ* 212
V.5.V Eu/RG - UV Site-Specific Features 215

V.6 Conclusion **216**

References **218**

Chapter VI - UV/Vis, Infrared and DFT study of the reactivity of matrix-isolated europium atoms with dinitrogen and carbon monoxide

VI.1 Eu/N_2 220
VI.1.I UV/Vis Absorption Spectroscopy 220
VI.1.II Infrared Absorption Spectroscopy 222
VI.1.III Eu/N_2 Absorption Summary 229

VI.2 Eu/CO 229
VI.2.I UV/Vis Absorption Spectroscopy 229
VI.2.II Infrared Absorption Spectroscopy 231
VI.2.III Eu/CO Absorption Summary 234

VI.3 Geometry Optimisation and Vibrational Analysis 235
VI.3.I Introduction 235
VI.3.II Eu:N_2 236
VI.3.III Eu:CO 242

VI.4 Molecular Bonding and MO Diagrams of Eu:X (X = N_2, CO) 248
VI.4.I Introduction 248
VI.4.II Europium dinitrogen complexes - MO diagrams 250
VI.4.III Europium carbonyl complexes - MO diagrams 253
VI.4.IV Molecular Bonding of Eu:X (X = N_2, CO) Summary 255

VI.5 Conclusion 256

References 259

Chapter VII - Conclusion 261

Declaration

This thesis has not been submitted before, in whole or in part, to this or any other University for any degree, and is, except where otherwise stated, the original work of the author.

Owen Byrne

Acknowledgements

Firstly, I would like to thank my supervisor, Dr. John Mc Caffrey, for allowing me the privilege to work in his research laboratory. I have gained an immense amount of knowledge and undergone much personal development since I began my PhD studies here under his excellent supervision and guidance.

I would like to thank my research group colleagues, past and present, Ciarán, Paddy, Nadia, Maryanne and Martin. In particular, a special thanks to Martin for all your support and many discussions on metal atom spectroscopy and life in general and to Ciarán for our often complex debates on DFT! I must also thank Noel Williams for his ability to restore any piece of equipment, old or new, to working order with minimum fuss.

To the Gents: Richard, John W., Denis - I will always have your back, Dec and Finno "phfuaft,!.". Thanks for the banter…

A word of thanks to all the Post Grads in the Chemistry Department; Fiachra, Foxy, Paul, Niamh, Carol, Louise, Alanna, Trish, Rob D (no better man to keep the Newbridge torch alight), Lorna, Eimear, Roisin, Lynn, Gama, Ken, Keeley, Laura and Niall to name but a few. And who could forget Chem Italia; Valeria, Adelaide, Enrico and the honorary Italian, Sinead. Thank you for the tastiest birthday cakes ever and for some memorable Tuesday night table quizzes with Steve Back, where the right answer isn't always correct - the smallest unit of time, anybody?!

A special word of gratitude to those who haven't been mentioned yet and were extra good to me when I needed it; Linda, Gillian, Shero, Conor and Rob. I wouldn't have made it through without yer support. An extra mention to Denis for joining me on the lunchtime Byrne-Diet and many foundation building afternoons.

To some of my longest friends; from the degree days, a special mention to Mick, the only man I know that can eat a Wagon Wheel in one sitting. And Paul, there's never a dull moment when you're around. To my oldest mates, my home-boys; Kenny, Archie, Mackie and Donnelly.

And lastly but certainly not least, My Family. I couldn't have asked for a better home. My parents, Eithne and Pat, I wouldn't be here without your love - you carried me through some tough times. Thank you. To the Byrne Brothers, Kevin, Noel and Joe, you are always there for me. Thanks for all your support, advice and kindness. Ye made me who I am today.

Abstract

This thesis presents an experimental and theoretical study of the luminescence, reactivity and ionisation of atomic europium isolated in cryogenic thin films of rare gases argon, krypton and xenon. Many studies are available concerning the spectroscopy of matrix-isolated main group metal atoms, however, the lanthanide series remains relatively undocumented. A thorough investigation of matrix-isolated europium is performed in this thesis in an effort to develop the spectroscopy of the f-block metal atom elements. Absorption spectroscopy identifies the visible s → p type y^8P ↔ a^8S and the UV f → d type ^{8}P ↔ a^8S electronic transitions of atomic Eu. The absorption spectra are complicated showing numerous features due to multiple guest site occupancy in the host lattices upon deposition. Annealing simplifies spectra, removing one thermally unstable site of isolation in each RG. Site-specific excitation spectra allow further deconvolution of complicated absorption spectra and the identification of two lattice vacancy types occupied by the metal guest. The spherical nature of the [Xe]$4f^7 6s^2$ ground state of europium coupled with predicted Eu-RG diatomic bond lengths, allows attribution of these occupied sites to hexa-vacancies and tetra-vacancies.

The complex visible y^8P state luminescence was probed using steady-state and time-resolved methods. Multiple emission features are identified with y^8P state excitation. Specific excitation in each particular site simplified the emission profiles yielding four emission bands. Based on their spectral location and temporal characteristics the observed emission features are assigned as y^8P resonance fluorescence, emission from the z^6P and a^8D excited states to the ground state and emission of the metastable a^{10}D electronic state. The solid state lifetimes of the a^8D and a^{10}D states are the first ever reported for these states. Excitation spectra in the region of the z^6P state identify the $z^6P_{5/2}$, and $z^6P_{7/2}$ levels. The $z^6P_{3/2}$ level is not identified in accordance with the ΔJ = 0, ±1 electric-dipole selection rule. The effect of each hosts increased capability for distortion is obvious in the excitation spectra recorded in this region. The $z^6P_{5/2}$ excitation band is observed to progress from a structureless feature in solid Ar to a resolved triplet in the Xe lattice. The greater capability for distortion of the Xe host causing Jahn-Teller threefold splitting of this state.

The effects of y^8P state laser irradiation on the Eu/RG samples are then investigated. The atomic absorption features are completely removed by this process and replaced with multiple new higher energy absorptions. Based on their spectral location, intensity distribution and lifetime characteristics, these new features are attributed to singly ionised europium formed in the lattice during irradiation. The ionisation shows a strong power dependence suggesting the ion is formed via a multi-photon process. Annealing reforms the neutral species implying the free ionised electron is stabilised in the host lattice. The visible luminescence of the states of $4f^7(^8S°_{7/2})6p_{1/2}$ and $4f^7(^8S°_{7/2})6p_{3/2}$ configuration of Eu^+/RG are investigated using time-resolved and steady-state techniques. Observed emission features are attributed to relaxation from particular electronic states of the ion. Absorption spectroscopy identifies two lattice trapping sites occupied in Ar and Kr and only one site in solid Xe. The site occupied in all three hosts is attributed to the interstitial octahedral site based on comparison to Eu^+-RG predicted diatomic bond lengths. The additional site present in Ar and Kr results from occupancy of a single vacancy.

Atomic Eu isolated in argon matrices doped with dinitrogen or carbon monoxide undergoes photochemistry during lamp irradiation. UV/Vis absorption spectra identify atomic isolation upon deposition. Following y^8P state irradiation all atomic features are completely removed. Infrared absorption spectra in the region of the N-N and C-O stretches show ligand complexation with the metal centre occurs. A vibrational frequency analysis of the Eu:N_2 and Eu:CO complexes is performed using the hybrid B3LYP, the DFT BP86 and the post-Hartree-Fock MP2 methods. The appropriateness of each functional at describing lanthanide metal chemistry is compared. BP86 is found to be the most accurate. A vibrational frequency analysis at the BP86 level allows identification of the binary europium dinitrogen complexes in both the side-on and end-on orientation in low ligand concentration samples in solid argon. The side-on species is calculated to be in the region of 900 cm^{-1} lower in energy. The mono-ligated carbon bound Eu(CO) species is observed in samples of 0.1 % CO in Ar. Analysis of the bonding molecular orbitals shows europium in a high-spin $[Xe]4f^7 5d^1 6s^1$ state is involved. Metal-ligand interactions occur via a classic synergistic σ donation/π back-bonding scheme. The high-spin state of europium is occupied as it reduces σ repulsion by removal of an s electron and increases the metal's ability for π back-bonding by promotion of an electron to a d-orbital allowing a greater degree of ligand co-ordination.

Chapter I

Matrix-Isolated metal atom spectroscopy

Introduction

I.1 Matrix-Isolation - History, Development and Overview

Matrix-isolation is a technique in which a guest atom, ion or reactive intermediate is trapped in a rare gas (RG) solid at low temperatures. The concentration of the guest must be small enough to avoid formation of dimer species $(guest)_2$ or aggregates $(guest)_n$ but high enough to allow recording of absorption and luminescence spectra[1]. Generally guest to host ratios of between 10^4 and 10^5 are employed in order to achieve complete isolation of the guest species and prevent any guest-guest interaction.

The two main advantages of matrix-isolation are, firstly the ability to stabilise and investigate reactive intermediates in the low temperature host which would be otherwise difficult to generate and maintain in appreciable abundance in the gas phase. Secondly, under matrix-isolated conditions, the guest species cannot interact with each other and interact only weakly with the surrounding inert matrix, thereby simulating the gas phase but in most cases being less complicated as at these low temperatures only the lower electronic and vibrational quantum states are populated and rotational motion is quenched.

The earliest known ‘matrix-isolation type’ studies were performed in the 1920’s in the research laboratory of Kamerlingh Onnes in Leiden. There Vegard studied the emission spectra of nitrogen and oxygen atoms in solid nitrogen and nitrogen/rare gas lattices using liquid helium or liquid hydrogen coolants. These refrigerants were not widely available at the time causing the experiments not to be repeated or developed until later years. In the 1950’s in the laboratory of George C. Pimental the first matrix studies of the current era were begun by Whittle and Pimentel. Prototype experiments were successful only after a sustained period of development of reliable low-temperature cells and systematic investigation of the effects of concentration, deposition conditions and temperature upon isolation efficiency and deposition rate[2]. Samples were kept in low pressure (10^{-8} mbar) chambers ensuring sample purity and preventing contaminates from freezing to the cold window. High vacuum also protects the sample chamber from conductive sources of heat and allows the low (< 10 K) temperatures to be achieved. Another advantage of the matrix-isolation technique is the wide optical transparency the RG hosts provide, allowing spectroscopic investigations from the vacuum UV to the far-infrared spectral regions to be performed.

Pimental's work was predominately carried out at 15 to 20 K. In 1958 the first infrared detection of the HNO molecule was achieved in a matrix and was soon followed by the detection of HCO in 1960[2]. Since then, cryogenic coolers have developed and improved, generally producing temperatures of 10 K or below allowing the use of lower melting point hosts such as Ne and Ar. Furthermore, the lower temperatures now available improve the rigidity and 'glassiness' of the matrix material thus reducing unwanted light scattering.

Matrix-isolated samples can be prepared by deposition of a pre-mixed gaseous combination of guest and RG or by co-deposition of the species to be studied with the host gas. In either case the guest species must be volatile or else vaporisation of the bulk guest must be performed. Several techniques are employed for bulk vaporisation, the most common being laser ablation, resistive heating and sputtering by electron bombardment. Resistive heating and sputtering techniques are the most appropriate when neutral guest species are desired. Laser ablation of the bulk is proficient at vaporising large amounts of guest however it can complicate experiments as it also produces a significant amount of ions. In some experiments, a reactive material such as methane or carbon monoxide is used as the host material to study the reaction of the host with the guest species.

Since Pimental's early work on free radicals, matrix-isolation has developed into the realm of matrix-isolated metal atom spectroscopy. UV/Vis luminescence spectra allow one to probe the metal atom electronic excited states accessible from its ground state and the relaxation pathways followed in returning to its fully relaxed state. Often multiple metal trapping sites occur within the lattice, resulting in the appearance of several absorption maxima which can be identified and deciphered with UV/Vis excitation spectroscopy. The magnitude of interaction between the guest metal and the host can also be probed leading to a measure of fundamental interactions occurring in the matrix[3].

Furthermore, photochemistry of metal atoms with molecules can be controlled and investigated in solid matrices such as the reactivity of transition metals isolated in nitrogen matrices[4]. Upon deposition, metal atoms are isolated in the lattice. During irradiation however, the guest metal complexes to a nitrogen molecule forming a completely new weakly bound product. The ability to probe and control such a fascinating reaction and the possibility to thoroughly analyse guest metal excited states and relaxation pathways inspired much research of matrix-isolated metal atom luminescence.

Interestingly there seems to be very little luminescence spectroscopy of matrix-isolated lanthanides available in the literature. To the best of our knowledge only the luminescence of the Tm/Ne[5] system has been thoroughly investigated. There also exists some work on the f → d type UV absorptions of Eu/RG from the 1970's [6,7,8]. Other than these, there exists two absorption studies of the Yb/RG[9] and Ho/RG[10] systems which briefly mention fluorescence features but in no great detail. Lanthanide metal atom matrix-isolated spectroscopy appears to be relatively un-chartered and is therefore a worthwhile area to be developed. This thesis will present a full systematic study of the visible luminescence of Eu/RG and photoreactivity of Eu isolated in molecular matrices but first, some introductory comments regarding the RG hosts are made.

I.2 Rare Gas (RG) host lattices

As mentioned earlier, one advantage of the matrix-isolation technique is the wide optical transparency the rare gas hosts provide. The high ionisation potentials of the RG's mean that they exhibit no electronic absorptions until the vacuum UV region. The lowest energy strong absorption corresponding to the first resonance transition $ns^2np^6 \rightarrow ns^2np^5(n+1)s^1$ for each host is listed in Table I.1. In the solid state the RG's will have weaker absorptions at somewhat lower energy, effectively making these matrix materials opaque at slightly longer wavelengths than those listed in Table I.1.

Table I.1 Wavelength positions of the first resonance $[ns^2np^6 \rightarrow ns^2np^5(n+1)s^1]$ transition of each of the rare gases.

First resonance transitions of rare gases[11]

Rare Gas	Wavelength (nm)
Ne	80
Ar	104
Kr	125
Xe	160

From the short wavelength vacuum UV limit RG matrices are free from interfering absorption bands throughout the UV, visible and IR regions. Only in the far-infrared region may there possibly be bands associated with the motions of the crystal lattice (lattice modes), but such modes have not been observed in mid-IR matrix-isolation studies and are not considered a concern. Furthermore, in the case of vibrational spectroscopy, the RG hosts are monatomic and have no molecular vibrations so can not give rise to any IR or Raman bands that might interfere with spectra. For all practical purposes the RG matrix may be considered fully optically transparent from the vacuum UV to the far-infrared with no interfering bands due to the host lattice. This allows a wide range of spectroscopic investigations to be performed on a matrix-isolated guest species.

The most commonly used matrix materials (Ne, Ar, Kr and Xe) are known from X-ray diffraction methods to crystallise in a face centred cubic (*fcc*) packing structure at low temperatures[11]. A unit cell of the *fcc* crystal lattice is presented in Figure I.1. Each atom is surrounded by 12 equidistant nearest neighbours in a cubo-octahedral symmetry with a nearest neighbour distance, R, which can be expressed as:

$$R = \frac{a}{\sqrt{2}} = 0.707a \qquad \text{Equation I.1}$$

where a is the lattice parameter as displayed in Figure I.1. There are 6 next nearest neighbours located at a distance of the lattice parameter, a, away[12]. The lattice parameters for each of the rare gas hosts used in matrix-isolation are listed in Table I.2.

The metal atom systems studied by the Maynooth Group to date all exist in spherically symmetric S ground states. This is also the case for atomic europium. The regularly packed *fcc* lattice allows consideration of possible sites of isolation for spherical ground state metal atoms within the host. There exists five types of spherical vacancies worthy of consideration in a *fcc* crystal, the size of each is displayed in Table I.2. Three of these sites are presented in a two layer space filled representation of a *fcc* unit in Figure I.2.

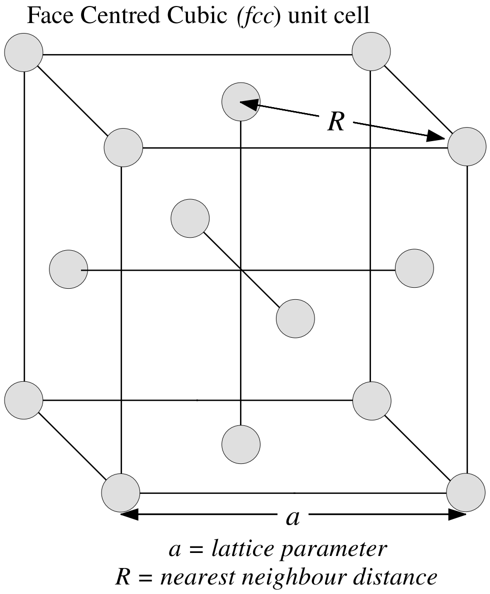

Figure I.1 One unit of a face centred cubic (*fcc*) packed crystal lattice structure that the rare gas solids exhibit. The lattice parameter, *a*, and the nearest neighbour distance, R, are displayed.

Interstitial Sites

The simplest sites are the interstitial sites where the guest metal atom is located between the host atoms in an intact and undistorted lattice. The *fcc* packed atoms occupy only 74 % of the volume[11], leaving 26 % unoccupied where a small guest species may reside. There are two possible interstitial sites, tetrahedral and octahedral.

The tetrahedral interstitial (T_d Int.) site is represented in Figure I.2 by the smallest circles. There are eight of these vacancies per unit cell. This site has four neighbouring atoms as the vacancy is located at the centre of four RG atoms forming a regular tetrahedron. These tetrahedral sites are extremely small, accommodating (without distortion) spheres of less than one quarter the diameter of the host atom[11]. Their diameter can be calculated using Equation I.2, where sv is the size of a single vacancy lattice site

$$T_d = \left(\frac{\sqrt{3}}{\sqrt{2}} - 1\right) sv \qquad \textit{Equation I.2}$$

The octahedral interstitial (I_{oh} Int.) site is a vacancy located at the centre of the *fcc* unit cell and is intrinsic to the close packed *fcc* lattice. It corresponds to the void between six atoms, three atoms arranged as a triangle on one layer and an oppositely oriented triangle from an adjacent layer[13]. Thus it has six nearest neighbours in octahedral symmetry. Its diameter is calculated using Equation I.3. Its size and position is displayed in the centre of Figure I.2. It can accommodate only spheres smaller than one half the diameter of the host atom[11].

$$I_{oh} = a - sv \qquad \textit{Equation I.3}$$

Single substitutional site

The next simplest possible site in the lattice is that of the single substitutional site (ss), also known as the single-vacancy site (sv), in which one host RG atom is replaced by a guest metal atom as shown in Figure I.2. Many s-block and transition metal atoms may be expected to adopt such a site as they are comparable in size to the host atoms. The necessary condition for a stable one atom substitution site is that the van der Waals radius of the guest is smaller than or equal to the host atom radius[1]. For a particular host, the substitutional site diameter can be calculated using the lattice parameter, *a*, to be:

$$sv = \frac{a}{\sqrt{2}} = 0.707a \qquad \textit{Equation I.4}$$

Multiple substitutional sites

From the discussion above it is obvious metal atoms will require site sizes approaching the sv site in the RG matrix. Larger, multiple substitutional sites, in which several contiguous matrix atoms are replaced such as tetra-vacancies (tv's) and hexa-vacancies (hv's) should also be considered for metal atoms.

A tetra-vacancy (tv) site is created with the removal of a tetrahedron of four adjacent host atoms surrounding a tetrahedral interstitial (T_d Int.) site in the *fcc* lattice. The centre of a tv therefore coincides with the centre of the T_d Int. site and the regular *fcc* packing allows one to calculate this site size using the lattice parameter, *a*

$$tv = \frac{\sqrt{11}}{4}a \qquad \textit{Equation I.5}$$

A corresponding hexa-vacancy (hv) is produced when the six atoms surrounding the I_{oh} Int site are removed. The centre of the hv coincides with the centre of the octahedral interstitial site and its radius can be calculated from

$$hv = \frac{\sqrt{3}}{2}a \qquad \text{Equation I.6}$$

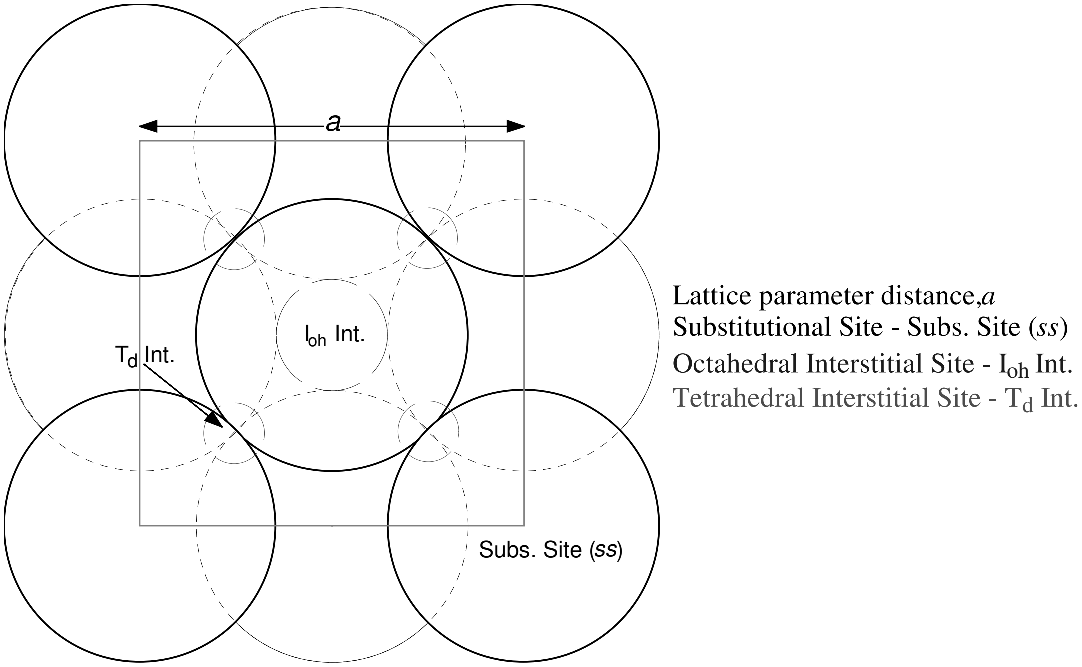

Figure I.2 A two layer space filled representation of a *fcc* unit highlighting both interstitial sites (I_{Oh} Int. and I_{Td} Int.) and the single substitutional site (ss).

Table I.2 Lattice Parameter (*a*), Site Sizes for the Solid Rare-Gas Hosts in a *fcc* unit cell. All distances are quoted in Angstroms (Å).

RG Solid	Lat.Param. (*a*, Å)[14]	T_d (Å)	I_{oh} (Å)	sv (Å)	tv (Å)	hv (Å)
Ne	4.462	0.709	1.307	3.155	3.699	3.864
Ar	5.312	0.844	1.556	3.756	4.404	4.598
Kr	5.644	0.897	1.653	3.991	4.679	4.884
Xe	6.131	0.974	1.796	4.335	5.083	5.308

The regular *fcc* packing structure of RG solids provides the opportunity to identify all possible sites of isolation for spherical guest species. The sizes, in Angstrom units, of these vacancy types are listed in Table I.2. For metal atom systems exhibiting spherical ground states, a comparison of the ground state M-RG diatomic bond length versus the available lattice vacancy sizes allows prediction of the site types occupied by the guest species.

For the interstitial sites, however, it is more appropriate to compare the M-RG diatomic bondlengths to the inter-nuclear separation of neighbouring atoms as opposed to comparison with the diameter of the interstitial sites listed in Table I.2. The distance from the centre of an interstitial lattice vacancy to the centre of the nearest neighbouring RG atom can be calculated using Equation I.7 and Equation I.8. The resulting inter-atomic distances are listed in Table I.3. These values are compared to M-RG diatomic bond lengths when investigating possible metal atom occupancy of interstitial sites.

$$T_d = \frac{sv}{2} \qquad \textit{Equation I.7}$$

$$\mathrm{I}_{\mathrm{oh}} = \frac{a}{2} \qquad \textit{Equation I.8}$$

Table I.3 Lattice Parameter (a), internuclear separation from the centre of the interstitial sites ($\mathrm{T_d}$, $\mathrm{I_{oh}}$) to the centre of its nearest neighbour for each RG *fcc* lattice. The site size of the single vacancy is also listed for comparison. All distances are quoted in Angstroms (Å).

RG Solid	Lat.Param. (a, Å)[14]	$\mathrm{T_d}$ (Å)	$\mathrm{I_{oh}}$ (Å)	sv (Å)
Ne	4.462	1.578	2.231	3.155
Ar	5.312	1.878	2.655	3.756
Kr	5.644	1.996	2.822	3.991
Xe	6.131	2.168	3.065	4.335

Generally, for metal atom systems, site sizes nearing the sv and tv will be necessary to accommodate the guest while for larger metal atoms such as sodium and the lanthanides the hv's must also be considered.

I.3 Matrix effects on electronic transitions

Although the interaction between the guest species and the inert host is negligible some weak interaction does occur causing several slight differences in electronic transitions compared to the gas phase. These effects are matrix shifts, Stokes shifts, enhancement of electronic transitions and Jahn-Teller distortion, all of which are discussed below.

I.3.I Matrix Shift

In a matrix, the metal-rare gas (M-RG) interaction is so weak that their electronic states may be considered as those of an isolated metal atom slightly perturbed by its RG partner(s)[1]. Thus the electronic structure of the system is determined by that of the guest metal atom. However, although the M-RG interactions are weak, they do effect the electronic spectra of the system. Electronic absorptions in the matrix usually do not occur at exactly the same energy as for the free metal in the gas phase, a frequency shift known as a matrix shift is observed. This is particularly evident for S → P type transitions. The matrix shift is a sum of two independent effects[1]:

1) short range repulsive interaction which decreases when the vacancy radius increases

2) long range attractive interaction which increases with increasing host polarisability

The addition of both effects implies a better stabilisation of the excited atom in larger, more polarisable hosts. Generally in Xe matrices absorptions are shifted to lower energy than the gas phase while in Ar and Kr matrix shifts to higher energy are observed.

I.3.II Stokes Shift

Another effect of the matrix compared to gas phase electronic transitions is the occurrence of a Stokes shift in the solid state. S → P type transitions of matrix-isolated M-RG systems such as Mn, Zn, Cd, Na and Hg exhibit a shift between the absorption and emission maxima. This shift is known as a Stokes shift and is an effect of the surrounding matrix.

For a metal atom in the gas phase, absorption and emission occur at exactly the same energy. This is presented schematically in left of Figure I.3. In the matrix, however, the metal atom remains isolated in a spherical site within the lattice while transitions between a configuration with a spherical (or quasispherical) symmetry and that involving an anisotropic p orbital occur. The excited atom is effectively larger than the ground-state atom but the lattice site remains the same size. The excited guest will experience greater short range repulsive forces from the host atoms thereby shifting its potential. This is seen in right of Figure I.3. In this situation, the vertical Frank-Condon transition in absorption does not now correspond to the excited state's energy minimum ($E_1(v_0)$) but is in fact to higher vibrational levels ($E_1(v_n)$). The vibrational levels in the solid state are caused by interaction with lattice phonons in both the ground E_0 and excited E_1 states.

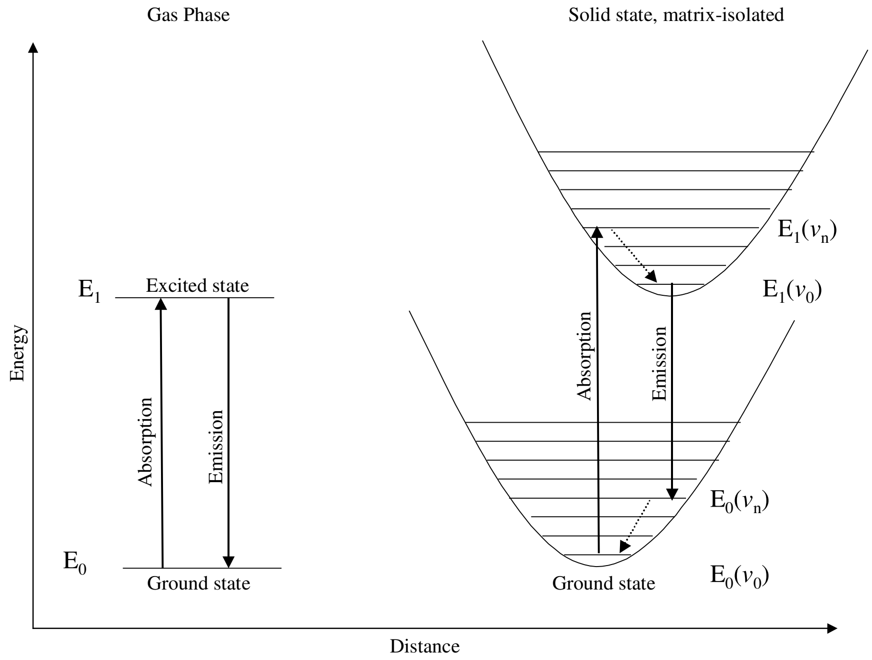

Figure I.3 Comparison of the effects of the surrounding matrix on the ground and excited state potentials versus the gas phase. Left of figure shows the gas phase situation where $E_{abs} = E_{em}$. Right of figure displays how short range repulsive interactions with the host shift the excited state potential causing a difference in energy between absorption and emission in the solid state known as the Stokes shift. The vibrational levels in the solid state are due to interaction with lattice phonons.

Following absorption to higher vibrational levels of the excited state ($E_1(v_n)$) non-radiative relaxation in the lattice occurs so that the radiatively emitted fluorescence originates from the lowest phonon level of the excited state ($E_1(v_0)$). Again due to Frank-Condon considerations, the transition is towards higher phonon levels of the ground state surface ($E_0(v_n)$). The difference in energy between absorption and emission is presented diagrammatically in Figure I.3 and can be expressed as:

$$Stokes\ shift = E_{abs} - E_{em} \qquad \textit{Equation I.9}$$

where $E_{abs} = E_1(v_n) - E_0(v_0)$

$E_{em} = E_1(v_0) - E_0(v_n)$

This energy difference between absorption and emission is known as the Stokes shift, the magnitude of which is a measure of the difference between equilibrium configurations of the ground and excited states in the matrix.

I.3.III Enhancement of electronic transitions

The RG matrix surrounding the guest metal atom also effects the observed lifetimes of the excited states. The effective field of the host generally enhances electronic transitions thus lifetime values are substantially shorter than the gas phase. Decay times for emission features in the matrix are investigated at different temperatures and when observed to be independent of temperature are taken to be the intrinsic radiative lifetimes of the excited state isolated in the solid rare gas host. Once the radiative lifetime is identified a correction for the effective field[15,16] can be made with Equation I.10 which considers the difference in the effective field strengths of the light acting on the guest in a surrounding dielectric medium (matrix, τ_{obs}) and of the light acting on the same guest in vacuum (τ_{cor}).

$$\tau_{cor} = \tau_{obs}\, n[s(n^2 - 1) + 1]^2 \qquad \textit{Equation I.10}$$

The formula is a function of the index of refraction of the given rare gas host, *n*, and a 'shape parameter' *s*. The *s* parameter is a depolarisation factor related to the symmetry of the site accommodating the guest atom. For spherical cavities such as a single substitutional site in the rare gas lattice, $s = 1/3$ and Equation I.10 becomes

$$\tau_{cor} = \tau_{obs}\, n[(n^2 + 2)/3]^2 \qquad \textit{Equation I.11}$$

Furthermore, a λ^3 extrapolation of the excited state lifetime plots the dependence between the matrix lifetimes and their emission wavelength. The extrapolation is based on the relationship between the Einstein A coefficient for the emission decay rate $A_{i,j}$ and the radiative lifetime of a level *i* (τ_i). It is given by Equation I.12

$$A_{i,j} = (64\,\pi^4/3h\lambda^3)\mu^2_{i,j} = {}^1/\tau_i \qquad \textit{Equation I.12}$$

Equation I.12 allows one to correlate the gas phase lifetime with the matrix shifted emission wavelength, an example of which is shown in Figure I.4 for the $y^8P \rightarrow a^8S$ transition of atomic Eu in the red site of Ar and Kr which is explained in more detail in Chapter IV. Briefly, the gas phase $y^8P \rightarrow a^8S$ transition is identified by an open diamond. The λ^3 extrapolation of this value is displayed by a solid line predicting the expected lifetime at different emission wavelengths. The uncorrected matrix lifetimes plotted versus their observed matrix emission wavelengths are displayed as filled triangles. When corrected for the effective field of the surrounding solid using Equation I.11 the resulting filled squares are found. Refractive index values of 1.32, 1.43 and 1.49 are used for Ar, Kr and Xe respectively[17] throughout this thesis. The corrected values are in very good agreement with the λ^3 extrapolation allowing assignment of the observed matrix emission to a particular electronic transition observed in the gas phase.

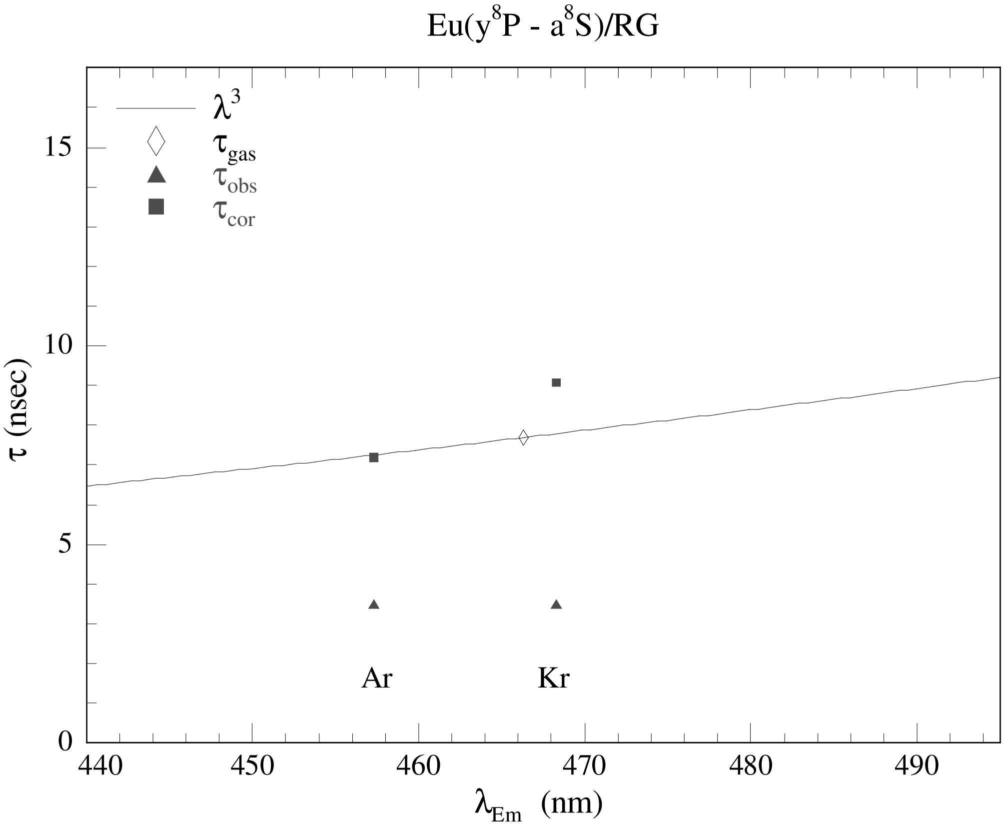

Figure I.4 A comparison of the lifetimes recorded at 10 K for the Eu($y^8P \rightarrow a^8S$) emission features in the red site of Ar and Kr and a λ^3 extrapolation of the gas phase lifetime of the y^8P state of atomic Eu. The uncorrected data and the data corrected for the effective field of the surrounding host are shown by filled triangles and closed squares respectively.

In summary, when comparing matrix recorded lifetimes to gas phase values one must consider the effects of the matrix spectral shift on emission wavelength values and the effective field of the surrounding RG solid both of which are accounted for using Equation I.10 and the λ^3 extrapolation.

I.3.IV Jahn-Teller effect

Unlike the gas phase, where electronic transitions are sharp and structureless, underlying structure is evident on many absorption bands of S → P type transitions of matrix-isolated metal atoms systems. For many years the origin of this structure was the source of much debate. Some proposed it related to guest atoms residing in different vacancies within the lattice, and while site-specific excitation spectra deconvoluted the absorption spectra to some degree and explained part of the structure there still appeared a triplet feature in the excitation spectra corresponding to atoms in a particular matrix site. Two main effects were argued to be the cause of this triplet structure, crystal field splitting (CFS) of the electronic state caused by interaction with the surrounding RG host atoms or a manifestation of the Jahn-Teller (JT) effect.

The crystal field effect was proposed to be caused by static distortion or a vacancy adjacent to the metal site of occupancy causing a lowering of the symmetry and thus the degeneracy of the guest atom in the *fcc* solid. Calculations considering covalent and dispersion forces proposed CFS as the source of the splitting in the Mg/Ar system[18]. However following this a magnetic circular dichroism (MCD) study of the Mg/RG systems showed experimentally that the source of the structure on the $^1S \rightarrow {}^1P$ absorption in the matrix was in fact due to JT distortion[19]. It was later proved beyond doubt using MCD that CFS was not the source of the triplet structure for Na and Li isolated in solid Xe either[20]. Moreover, recent work on crystal field splitting induced by the RG solids indicates that the spin-orbit levels derived from P terms are less prone to CFS[3]. It is well known that crystal fields of cubic symmetry do not induce splitting of P terms. On the basis of experimental observations, it appears that they will not be split by a cubic CF in the matrix thus ruling out CFS as the source of the structure on S → P type absorptions.

The other possibility proposed was that the splitting results from the Jahn-Teller effect. For an electronically degenerate state in a site of high symmetry, distortion occurs to lower the symmetry, remove the degeneracy, and lower the energy. This is known as the Jahn-Teller effect and it is outlined in Figure I.5. In this case we are dealing with a triply degenerate P (p_x,p_y,p_z) state isolated in a highly symmetric spherical site within the lattice. Vibrations of the host lattice could lower the symmetry and thereby remove the degeneracy resulting in the threefold absorption band.

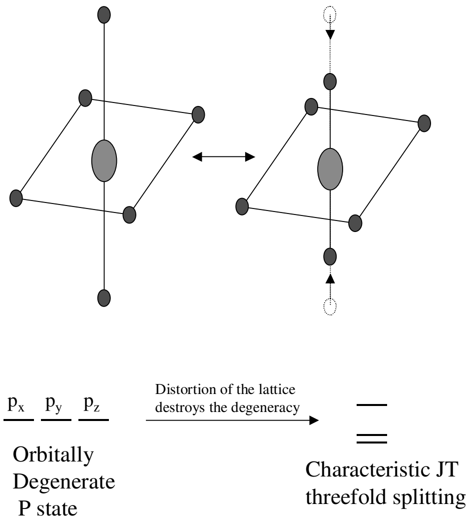

Jahn-Teller effect on P state absorptions in RG solids

Figure I.5 Representation of Jahn-Teller distortion of an electronically degenerate P state in the RG lattices.

Rose *et al*[20] showed conclusively that the characteristic triplet structure in Li/Xe and Na/Xe is a consequence of a strong Jahn-Teller effect and that simple crystal field models cannot account for the structure. Based on these considerations, it has become widely accepted in the matrix-isolation community that JT effects are the source of the threefold splitting on S → P absorptions of metal atom systems.

It should also be noted that JT splitting is not always observed for P state absorptions in the matrix. If there is sufficiently large spin-orbit splitting between the J-levels of a particular P state, spin-orbit coupling can completely reduce the Jahn-Teller distortions to zero[21] and individual spin-orbit states are observed.

I.4 LS and *jj* Coupling Schemes

The electronic states of lighter atoms are described using a LS or Russell-Saunders coupling scheme. However, when dealing with heavy atoms such as lanthanides another method known as the *jj* coupling scheme may be more appropriate. The following section discusses both schemes with particular focus on *jj* coupling which becomes important for heavy metals such as europium studied in this thesis.

The magnetic moments caused by orbital and spin angular momenta of each electron in an atom interact with each other. The strength of this interaction between the spin and orbital motions of the electrons is referred to as spin-orbit coupling, and depends strongly on the atom concerned.

The spin of one electron in a system can interact with[22]:

a) the spins of the other electrons

b) its own orbital motion

c) the orbital motion of the other electrons.

Coupling *c)* is called spin-other-orbital interaction and is normally so small it can be ignored. Interactions *a)* and *b)* are more important and the methods of treating them involve two types of approximation. They are known as LS (Russell-Saunders) and *jj* coupling and represent both extremes. Atomic structure is accurately described for light to moderately heavy atoms using the most commonly employed LS coupling scheme. However in ground configurations of heavy atoms and many excited configurations of light and heavy atoms the *jj* coupling scheme becomes more appropriate[23].

LS coupling assumes that the quantum numbers L and S can be dealt with separately. Individual orbital angular momenta, l, of the valence electrons couple to give the total angular momentum L. Similarly the individual electrons spins, s, couple to give total spin angular momentum S. The total electronic angular momentum of the atom, J, is the vector sum of the orbital (L) and spin (S) angular momenta and is calculated from these values by[23]

$$J = L + S, L + S - 1, \ldots\ldots, |L - S| \qquad \textit{Equation I.13}$$

This LS coupling approximation serves as a useful basis for describing states of most atoms. However, the magnitude of the spin-orbit coupling depends very strongly upon the nuclear charge and for very heavy atoms, spin-orbit coupling is large. In this case the total angular momentum quantum number J is determined by the *jj*-coupling scheme. Electrons are considered to move independently of one another and in these circumstances the individual values j, l, and s are the good quantum numbers. Each electron's l and s couple to give j the total angular momentum of a particular electron. The total electronic angular momentum J of the atom is then the vector sum of each electron's angular momentum, j_i, and is found by[23]

$$\mathrm{J} = \sum_{\mathrm{i}} j_{\mathrm{i}} = \sum_{\mathrm{i}} l_{\mathrm{i}} + s_{\mathrm{i}} \qquad \textit{Equation I.14}$$

Notation for the LS coupling scheme is well known and universally standardised however the *jj* coupling scheme is not. Notation used in this thesis is the same as that employed by the National Institute of Standards and Technology (NIST) some examples of which follow.

***jj* coupling notation**

In the examples below, lower-case j indicates the angular momentum of one electron or of each electron in a group (l_j^N) and is indicated by the subscripts. The total angular momentum, J, for a particular group and/or level is indicated by a further subscript yielding notation in the form $(l_j^N)_\mathrm{J}$ where N is the number of electrons in a particular group.

<u>Examples of *jj* coupling notation</u>[24]

1) $(6p^2_{1/2})_0$

2) $(6p^2_{1/2}\,6p_{3/2})^\circ_{3/2}$

3) $4d^3_{5/2}\,4d^2_{3/2}\ \ ({}^9/_2,\,2)_{11/2}$

4) $3d^{\,9}({}^2\mathrm{D}_{5/2})4p_{3/2}\ \ ({}^5/_2,\,{}^3/_2)^\circ_3$

5) $4f^{\,11}({}^2\mathrm{H}^\circ_{9/2}\ 2)6s6p({}^3\mathrm{P}^\circ_1)\ \ ({}^9/_2,\,1)_{7/2}$

6) $5f^{\,4}_{7/2}5f^{\,5}_{5/2}\ (8,{}^5/_2)^\circ_{21/2}7p_{3/2}\ \ ({}^{21}/_2,\,{}^3/_2)_{10}$

7) $5f^{\,3}_{7/2}\ 5f^{\,3}_{5/2}\ ({}^9/_2,\,{}^9/_2)_9 7s7p({}^3\mathrm{P}^\circ_2)\ \ (9,2)^\circ_7$

The $6p^2$ and $6p^3$ ground configurations of neutral Pb and Bi have relatively large spin-orbit interaction of the $6p$ electrons and produce *jj*-coupling. The ground levels of these atoms is given by the first two examples (*1* and *2*).

In example *1*, the notation for two $6p$ electrons each having $j = 1/2$ and a total angular momentum J = 0 is shown. The second example extends this notation to the case of a $6p^3$ configuration divided into two groups according to the two possible j values (1/2, 3/2) with total angular momentum of J = 3/2.

The third example is different. The $(J_1, J_2)_J$ term and level notation shown on the right is used because each of the two electron groups $4d\,^3{}_{5/2}$ and $4d\,^2{}_{3/2}$ has more than one allowed total J_i value. The convention is that J_1 applies to the total angular momentum of the group on the left ($J_1 = 9/2$ for the $4d\,^3{}_{5/2}$ group) and J_2 to that on the right ($J_2 = 2$ for the $4d^2{}_{3/2}$ group). While the total angular momentum of the whole system is J = 11/2.

Examples *4* and *5* both have core electrons in *LS* coupling. In *4*, the d^9 core electrons exhibit a LS coupled $^2D_{5/2}$ state while the 4p valence electron is *jj* coupled with $j = 3/2$ yielding total angular momentum J = 3.

In examples *6* and *7*, *jj* coupling is indicated for the $5f$ core electrons. Since the J_1 and J_2 values in the final (J_1, J_2) term have already been given as subscripts in the configuration, the (J_1, J_2) term notations are redundant in these examples.

The *jj* coupling notation is utilised for the electronic states of singly ionised europium discussed in Chapter V of this thesis. The europium ion has gas phase absorptions in the 270 to 420 nm spectral region which are listed in Table I.4. Considering the $4f^7(^8S°_{7/2})6p_{1/2}$ configuration excited state, the core f-electrons experience LS coupling yielding a $^8S_{7/2}$ term while the valence electrons are described by *jj* coupling notation. The possible total angular momenta of the system, J, is found by summing the individual j_i's vectorially

$$J = j_1+j_2,\ (j_1+j_2)-1, \ldots\ldots |j_1-j_2| \qquad \textit{Equation I.15}$$

In this case $j_1 = 7/2$ (from $^8S_{7/2}$) and $j_2 = 1/2$ (from $6p_{1/2}$) leading to two possible angular momenta values, J = 3 and J = 4 respectively. This results in two terms labelled $(7/2, 1/2)_3$ and $(7/2, 1/2)_4$.

Likewise for the $4f^7(^8S°_{7/2})6p_{3/2}$ configuration, j_1 = 7/2 and j_2 = 3/2, Equation I.15 finds three possible values of total angular momentum, J = 3, 4 and 5. This results in three terms labelled $(7/2, 3/2)_3$, $(7/2, 3/2)_4$ and $(7/2, 3/2)_5$. Conversely, terms of the $4f^6 5d^1 6s^1$ configuration excited state are described using *LS* coupling as y^9P_J.

Table I.4 Spectral locations and electronic configurations of the states involved in the allowed transitions from the $a^9S°_4$ ground state of the europium cation in the gas phase.

Persistent Lines of Singly Ionised Europium (Eu^+)[25]

Configuration	Terms	λ (nm)	cm^{-1}
$4f^7(^8S°_{7/2})6p_{1/2}$	$(7/2, 1/2)_3$	420.51	23774.28
	$(7/2, 1/2)_4$	412.97	24207.86
$4f^7(^8S°_{7/2})6p_{3/2}$	$(7/2, 3/2)_5$	381.97	26172.83
	$(7/2, 3/2)_4$	372.49	26838.5
	$(7/2, 3/2)_3$	368.84	27104.07
$4f^6(^7F)5d\ (^8P)6s$	y^9P_3	290.67	34393.57
	y^9P_4	281.39	35527.02
	y^9P_5	272.78	36648.95

I.5. Geometry optimisation, vibrational frequency calculations

Absorption features identified in the IR spectral region in Chapter VI are attributed by comparison to geometry optimisations and vibrational frequency analysis. These calculations were carried out using the Gaussian03 Software[26] (Gaussian03, revision E.01) on a quad core computer (Processor type AMD64, 2.8 GHz) with the Linux Red Hat operating system (EL, Server 5.3) using both density functional theory (DFT) and post-Hartree-Fock *ab initio* methods.

DFT methods are generally used for calculations of optimum geometries and vibrational frequencies of molecules. In these techniques the energy of a many electron system can formally be expressed as a functional of the electron density. All information about the electronic system is extracted from the electron density rather than from the wave function. Since, for any system, the electron density is a function of only three spatial coordinates, it is a much simpler function to approximate than the full electronic wave function, making DFT a highly attractive approach to the molecular many-body problem and thus its widespread and successful use.

The advantage of density functional theory is the reduction of the many-electron problem to a three dimensional field equation. The solution is less complicated and expensive than conventional correlated *ab initio* methods. Unfortunately, even though the electronic energy is a function of the electron density, in practice, this function is only known in an approximate manner and approximations are made in its solution, i.e. simplifying descriptions that incorporate the most important features of the electronic system which can lead to erroneous results particularly for weakly bound systems.

Another more advanced method, which accounts for the full range of intermolecular interactions (electrostatic, induction and dispersion effects) is Møller-Plesset (MP) perturbation theory. It is a post-Hartree-Fock *ab initio* method which performs a Hartree-Fock calculation yielding an approximate determination of the ground-state wave function and ground-state energy of a quantum many-body system. This is followed by a Møller-Plesset correlation energy correction which adds electron correlation effects. In the Hartree-Fock (HF) method electron repulsions are averaged but this is improved with MP by adding electron correlation which leads to a more accurate way of considering the electron repulsions. MP2 is the most economical way to correct for the lack of dynamic electron correlation in Hartree-Fock Theory.

The advantages of MP theory include the ability to describe van der Waals attractive forces and size-consistency. The MP2 level gives good structures and predicts well the IR spectra for many molecules. In particular, for many small and medium size molecules, optimisation at the MP2/cc-pVTZ level gives good geometries[27]. The main disadvantage is it is computationally much more expensive than DFT.

To allow comparison between each functional, calculations in this study were performed using the DFT BP86 method, the post-Hartree-Fock MP2 functional and the common B3LYP hybrid functional which includes a mixture of Hartree-Fock exchange with DFT exchange correlation. Correlation energies used in MP2 depend strongly on the chosen basis set. In general, large correlation consistent basis sets provide the best results while use of smaller basis may lead to erroneous outcomes. Therefore the large aug-cc-pVTZ basis set was used on the C, O and N atoms and the segmented basis set[28,29] augmented by 2pdfg diffuse functions[30] and a 28 electron core potential[29,31] (ECP28MWB) was used on the europium atom. This augmented basis set and ECP of Eu is the best available in the literature and was employed with success previously for calculations of weakly van der Waals bound Eu_2 dimer[29].

Although large basis sets improve the accuracy of results, the basis set superposition error (BSSE) is unavoidable when using finite basis sets. This error is widely recognised, and particularly prevalent for intermolecular van der Waals bonded systems[32]. It is due to the fact that for a chosen system, each fragment in the system uses to some extent the basis functions of the other fragments thus introducing a nonphysical attraction between fragments, causing an energy lowering of the system. BSSE is reduced by using sufficiently large basis sets and the inclusion of diffuse functions on these basis sets but there will always be some inherent BSSE in any calculation. The largest BSSE effect is observed in molecules with weaker interaction energies.

To correct for BSSE the most popular technique is the counterpoise (CP) correction defined in the Gaussian03 Software[26]. It is known CP corrections lead to larger optimised intermolecular distances compared to CP-uncorrected optimised systems but much more accurate results. Thus, CP must be used to correct both the optimised geometry and the interaction energy[33].

Vibrational analysis with the Gaussian03 Software[26] by default involves consideration of the vibrational levels of the molecular system operating within the simple harmonic oscillator model. At the lowest energy of the system, the atoms settle at an internuclear distance such that the attractive and repulsive forces are balanced and the total energy of the whole system is a minimum. This is considered the equilibrium distance or bond length and is found through a geometry optimisation calculation. Moving atoms closer together causes the repulsive forces (C_{12}) to rise rapidly while pulling them apart is resisted by attractive forces (C_6). The energy required to overcome these forces may be plotted against internuclear distance to yield a potential energy diagram of the system as in Figure I.6[34]. In the harmonic oscillator model, the compression and extension of a bond is assumed to behave like a spring obeying Hooke's law of elasticity[35]. This model forms a symmetric vibrational potential surface with equally spaced vibrational levels and is an excellent starting point for the analysis of vibrational spectra.

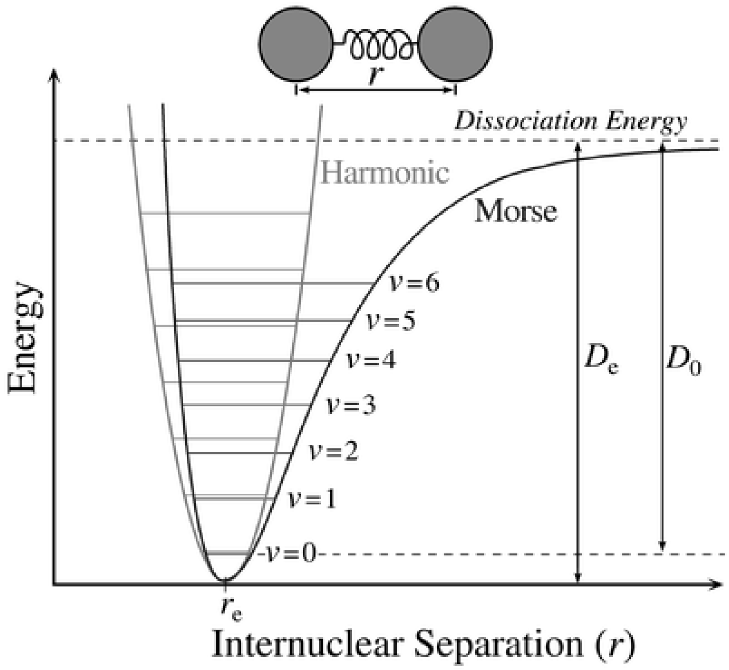

Figure I.6 The Morse/anharmonic potential and harmonic oscillator potential. Unlike the energy levels of the harmonic oscillator potential, which are evenly spaced, the Morse potential level spacing decreases as the energy approaches the dissociation energy. The dissociation energy, D_e, is larger than the true energy required for dissociation, D_0, due to the zero point energy (ZPE) of the lowest ($v = 0$) vibrational level[34].

However, this approach is not physically accurate. Real molecules do not obey exactly Hooke's elasticity law. For example, if the bond between atoms is stretched there comes a point at larger distances where the bond will break and the molecule dissociates. Actual bonds are described more accurately by the anharmonic oscillator model[35] which can be represented by a Morse Potential. Here the oscillation frequency decreases steadily with increasing vibrational energy level unlike the equally spaced vibrational levels in the harmonic oscillator approach.

Frequencies calculated with the Gaussian03 Software[26] using the simple harmonic oscillator model are generally acceptable for analysis of experimental spectra once they are corrected to account for the neglect of anharmonicity by use of a scaling factor. A comprehensive list of scaling factors for vibrational levels calculated with various functionals and basis sets have been investigated and supplied by Truhlar's group[36]. In addition to this, the Gaussian03 Software[26] allows one to calculate anharmonic frequencies and thus achieve more realistic theoretical results.

This process is not generally employed as it is much more time consuming and computationally expensive than the harmonic technique.

In this study geometry optimisations and vibrational frequencies are computed using both the MP2 method and the density functional theory BP86 approach coupled with CP correction. MP2 is the most economical post-Hartree-Fock method that accounts for the full range of intermolecular interactions including dispersion effects and is expected to yield good results for weakly bound systems. However, Becke[37] has found that transition metal chemistry is notoriously problematic for HF based theories, such as MP2, due to the importance of both dynamical and nondynamical correlation. Orbitals tend to be too localised on the metal atom or the ligands resulting in MP2 not fully capturing the effects of correlation in transition metal-ligand bonds. In particular, MP2 is known to overestimate the bond energies of transition metal carbonyls[37]. Furthermore, a comprehensive study of monometal (M = Cr, Mo, W, Fe, Ru, Os, Ni, Pd, Pt) carbonyls[38] found that the BP86 approach is superior to MP2, providing more reliable results at less computational costs that were in very good agreement with experimental data. BP86 has also been used successfully in recent times to attribute IR bands of metal dinitrogen complexes (M = Fe[39], Ti[40], Zr[40], Hf[40], Sc[41], La[42], Y[42]). Based on these previous studies of transition metal systems, BP86 may be more appropriate for describing the experimental spectra of the lanthanide containing Eu:CO and Eu:N_2 complexes. Both BP86 and MP2 and the hybrid B3LYP functionals are employed and compared for the systems studied in this thesis.

I.6 Luminescence Spectroscopy of Eu/RG Systems

Previous work by the Maynooth group focused on the luminescence of the following metals isolated in the RG's: cadmium[43], zinc[44], mercury[45] and magnesium[46,47] and more recently sodium[13] and manganese [3,48,49,50]. These systems all exhibit spherically symmetric ns^1 or ns^2 S ground states and involve excited np^1 and ns^1np^1 states reached in absorption. The most recent metal studied, Mn, is located in the centre of the transition metal series with a [Ar]$3d^5 4s^2$ ground state, the half filled d-orbital yielding the spherically symmetric ^6S ground state. Having studied Group I, II and transition metal systems the next logical progression of the study of metal atom luminescence is to investigate lanthanide metals. The f-block equivalent of manganese is europium, with a half-filled f-orbital it exhibits a fully relaxed electronic configuration of [Xe]$4f^76s^2$ and a spherically symmetric ^8S ground state. In correlation with the previously studied systems it has a $6s^16p^1$ excited electronic state accessible in absorption in the visible spectral region. The correlations between Mn and Eu led to it being chosen as the lanthanide system of study for this thesis.

Figure I.7 presents the complete UV/Vis energy level diagram of atomic Eu in the gas phase. It exists in a a^8S ground state. Electric dipole selection rules dictate that $\Delta L = 1$, i.e. S → P transitions will be allowed[51]. Combined with the spin selection rule[51] ($\Delta S = 0$) transitions to ^8P states will be fully allowed. Inspection of Figure I.7 show there are three ^8P states namely ^8P, y^8P and z^8P occurring at 333.5, 466.3 and 629.3 nm (29982.5, 21444.6 and 15890.5 cm^{-1}) in the gas phase[25].

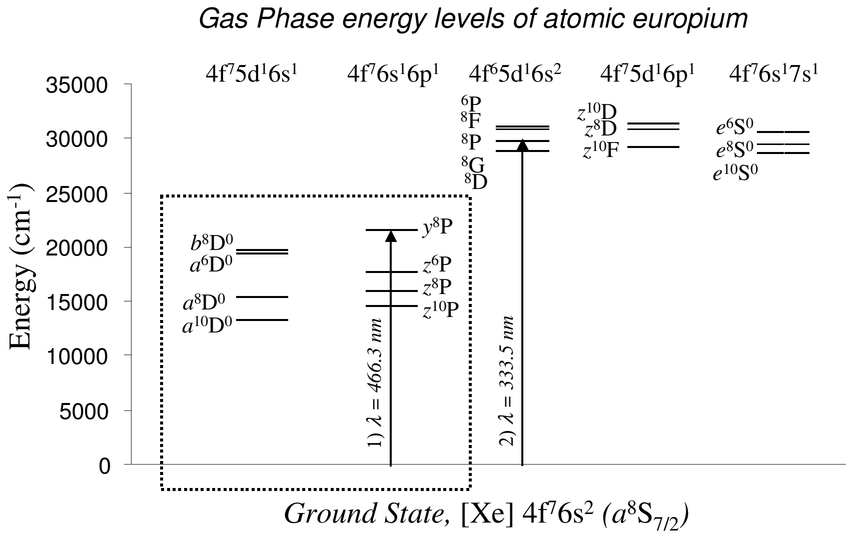

Figure I.7 Schematic representation of the energy levels of gas phase atomic europium. The transitions with large oscillator strengths in the gas phase, the allowed $y^8P_{5/2} \leftarrow a^8S_{7/2}$ and $^8P_{5/2} \leftarrow a^8S_{7/2}$ occurring at 21444.6 cm^{-1} (466.3 nm) and 29982.5 cm^{-1} (333.5 nm) respectively, are indicated by arrows[25]. The dashed rectangle highlights the region of interest in this study.

The UV f → d type absorption pertaining to the $^8P \leftrightarrow a^8S$ electronic transition of Eu/RG were identified and investigated before[6,7,8]. In this previous study, as expected for f → d transitions, these bands were narrow and unshifted[5] allowing easy identification and assignment. Emission in this region was observed from the ^8D state. The previous study performed absorption and emission spectroscopy only, the lack of capability to perform excitation spectra prevented any metal site occupancy identifications from being made. Chapter III of this thesis presents site-specific excitation spectra in this region augmenting the previous data.

Although the UV transitions have been investigated, to date no work has appeared in the literature pertaining to the complicated visible luminescence of Eu/RG. This thesis presents a complete spectroscopic study of this region. The transition with greatest oscillator strength in the gas phase is y^8P ↔ a^8S occurring at 466.3 nm. The aim of Chapter III is to assign absorption features to this s → p type electronic transition of atomic Eu. Following identification of the fully allowed y^8P ↔ a^8S transition, excitation spectra in this region resolve multiple site occupancies which are convoluted in absorption spectra. The subsequent chapter presents the site-specific luminescence spectroscopy of Eu/RG solids with resonant (y^8P) excitation with continuous and pulsed light sources. Time resolved emission spectra allow excited state lifetime measurements and relaxation processes to be probed. There are seven lower energy excited states of $6s^16p^1$ and $5d^16s^1$ electronic configurations below the y^8P state. These are highlighted in Figure I.7 by a dashed box and lead to complex relaxation pathways and numerous emission features which are investigated in Chapter IV.

In Chapter V the effects of prolonged resonant (y^8P) laser irradiation of the Eu/RG samples is presented. Atomic features are completely removed by this process and new absorptions to higher energy are formed. Excitation, emission and lifetime analysis of these new features are recorded and an attempt is made to identify the source of these features.

Once the complete visible luminescence of atomic Eu isolated in the solid RG's is achieved, the photoreactivity of europium with small molecules in the solid state is investigated in Chapter VI. Both UV/Vis and near-infrared absorption spectroscopy are utilised to study this interesting reactivity. Attempts are made to assign vibrational bands observed in the IR spectral region by comparison to DFT and *ab initio* post-Hartree-Fock vibrational energy calculations.

All of the experimental data reported in this thesis was recorded in the Low Temperature Laboratory in the Department of Chemistry, National University of Ireland Maynooth, Maynooth, County Kildare, Ireland. The details and specifications of the experimental apparatus and spectroscopic set-ups used to achieve these results are presented in Chapter II.

References

[1] C. Crepin-Gilbert and A. Tramer, International Reviews in Physical Chemistry **18**, 485 (1999).

[2] C. B. Moore, *George Claude Pimental 1922 - 1989 [and references within]*. (National Acadamy of Sciences, Washington D.C., 2007).

[3] M. A. Collier, O. Byrne, C. Murray and J. G. McCaffrey, The Journal of Chemical Physics **132** (16), 164512 (2010).

[4] H. J. Himmel and M. Reiher, Angewandte Chemie International Edition **45** (38), 6264 (2006).

[5] A. A. Belyaeva and Y. B. Predtechenskii, Opt. Spectrosc. (USSR) **60** (6), 700 (1986).

[6] M. Jakob, H. Micklitz and K. Luchner, Berichte Der Bunsen-Gesellschaft-Physical Chemistry Chemical Physics **82** (1), 32 (1978).

[7] M. Jakob, H. Micklitz and K. Luchner, Physics Letters A **61** (4), 265 (1977).

[8] M. Jakob, H. Micklitz and K. Luchner, Physics Letters A **57** (1), 67 (1976).

[9] S. Suzer and L. Andrews, The Journal of Chemical Physics **89** (9), 5514 (1988).

[10] W. E. Klotzbucher, M. A. Petrukhina and G. B. Sergeev, The Journal of Physical Chemistry A **101** (25), 4548 (1997).

[11] S. Cradock and A. J. Hinchcliffe, *Matrix Isolation, A technique for the study of reactive inorganic species*. (Cambridge University Press, 1975).

[12] C. Kittel, *Introduction to Solid State Physics*, 7th ed. (John Wiley & Sons Inc., 1996).

[13] M. Ryan, M. Collier, P. de Pujo, C. Crepin and J. G. McCaffrey, Journal of Physical Chemistry A **114** (9), 3011 (2009).

[14] H. E. Hallam, *Vibrational Spectroscopy of Trapped Species*. (Wiley - Interscience, New York, 1973).

[15] R. L. Fulton, The Journal of Chemical Physics **61** (10), 4141 (1974).

[16] T. Shibuya, The Journal of Chemical Physics **78** (8), 5175 (1983).

[17] The refractive indices of Ar, Kr and Xe are 1.29, 1.28 and 1.49 recorded at 60 K and λ = 488 nm from H. J. Jodl, *Solid State Aspects of Matrices in The Chemistry and Physics of Matrix-Isolated Species*. (North-Holland, 1989); The index of refraction used for solid Ar at 233 nm is 1.32 K at 6 K, that of Kr is 1.428 at 241 nm at 12 K. (P. Gurtler, unpublised results, 1996).

[18] M. Brith and O. Schnepp, The Journal of Chemical Physics **39** (10), 2714 (1963).

[19] R. L. Mowery, J. C. Miller, E. R. Krausz, P. N. Schatz, S. M. Jacobs and L. Andrews, The Journal of Chemical Physics **70** (8), 3920 (1979).

[20] J. Rose, D. Smith, B. E. Williamson, P. N. Schatz and M. C. M. O'Brien, The Journal of Physical Chemistry **90** (12), 2608 (1986).

[21] I. Bersuker, *The Jahn-Teller Effect*. (Cambridge University Press, 2006).

[22] J. M. Hollas, *Modern Spectroscopy*, 3rd ed. (John Wiley & Sons Inc. , 2002).

[23] E. S. J. Gauerke and M. L. Campbell, Journal of Chemical Education **71** (6), 457 (1994).

[24] *Atomic Spectroscopy, A Compendium of Basic Ideas, Notation, Data and Formulas. available: http://physics.nist.gov/Pubs/AtSpec/node09.html [2010, July 11]*. (National Institute of Standards and Technology, Gaithersburg, MD.).

[25] *NIST Atomic Spectra Database (version 3.1.5), available: http://physics.nist.gov/asd3 [2010, August].* (National Institute of Standards and Technology, Gaithersburg, MD).

[26] M. J. Frisch, G. W. Trucks, H. B. Schlegel, G. E. Scuseria, M. A. Robb, J. R. Cheeseman, J. A. Montgomery, T. Vreven, K. N. Kudin, J. C. Burant, J. M. Millam, S. S. Iyengar, J. Tomasi, V. Barone, B. Mennucci, M. Cossi, G. Scalmani, N. Rega, G. A. Petersson, H. Nakatsuji, M. Hada, M. Ehara, K. Toyota, R. Fukuda, J. Hasegawa, M. Ishida, T. Nakajima, Y. Honda, O. Kitao, H. Nakai, M. Klene, X. Li, J. E. Knox, H. P. Hratchian, J. B. Cross, V. Bakken, C. Adamo, J. Jaramillo, R. Gomperts, R. E. Stratmann, O. Yazyev, A. J. Austin, R. Cammi, C. Pomelli, J. W. Ochterski, P. Y. Ayala, K. Morokuma, G. A. Voth, P. Salvador, J. J. Dannenberg, V. G. Zakrzewski, S. Dapprich, A. D. Daniels, M. C. Strain, O. Farkas, D. K. Malick, A. D. Rabuck, K. Raghavachari, J. B. Foresman, J. V. Ortiz, Q. Cui, A. G. Baboul, S. Clifford, J. Cioslowski, B. B. Stefanov, G. Liu, A. Liashenko, P. Piskorz, I. Komaromi, R. L. Martin, D. J. Fox, T. Keith, A. Laham, C. Y. Peng, A. Nanayakkara, M. Challacombe, P. M. W. Gill, B. Johnson, W. Chen, M. W. Wong, C. Gonzalez and J. A. Pople, *Gaussian 03, Revision E.01.* (Gaussian Inc., Wallingford CT, 2004).

[27] C. Sonia, M. Domenico, G. Jurgen, H. Christof, H. Trygve and J. Poul, The Journal of Chemical Physics **123** (18), 184107 (2005).

[28] X. Cao and M. Dolg, Journal of Molecular Structure: THEOCHEM **581** (1-3), 139 (2002).

[29] X. Y. Cao and M. Dolg, Theoretical Chemistry Accounts **108** (3), 143 (2002).

[30] A. Buchachenko, G. Chałasiński and M. Szcześniak, Structural Chemistry **18** (6), 769 (2007).

[31] M. Dolg, H. Stoll and H. Preuss, The Journal of Chemical Physics **90** (3), 1730 (1989).

[32] S. Simon, J. Bertran and M. Sodupe, The Journal of Physical Chemistry A **105** (17), 4359 (2001).

[33] D. Hugas, S. Simon and M. Duran, Chemical Physics Letters **386** (4-6), 373 (2004).

[34] Nationmaster.com, *http://www.nationmaster.com/wikimir/images/upload.wikimedia.org/wikipedia/commons/thumb/7/7a/Morse-potential.png/400px-Morse-potential.png*. (Last accessed July 2010).

[35] C. N. Banwell and E. M. McCash, *Fundamentals of Molecular Spectroscopy*, 4th ed. (McGraw-Hill Publishing, 1993).

[36] J. Zheng, I. M. Alecu, B. J. Lynch, Y. Zhao and D. G. Truhlar, *Database of Frequency Scaling Factors for Electronic Structure Methods, available: http://comp.chem.umn.edu/database/freq_scale.htm*.

[37] E. R. Johnson and A. D. Becke, Canadian Journal of Chemistry **87**, 1369 (2009).

[38] V. Jonas and W. Thiel, Journal of Chemical Physics **102** (21), 8474 (1995).

[39] Z. H. Lu, L. Jiang and Q. Xu, The Journal of Physical Chemistry A **114** (5), 2157 (2010).

[40] G. P. Kushto, P. F. Souter, G. V. Chertihin and L. Andrews, The Journal of Chemical Physics **110** (18), 9020 (1999).

[41] G. V. Chertihin, L. Andrews and C. W. Bauschlicher, Journal of the American Chemical Society **120** (13), 3205 (1998).

[42] Y. L. Teng and Q. Xu, The Journal of Physical Chemistry A **112** (16), 3607 (2008).

[43] B. Healy and J. G. McCaffrey, The Journal of Chemical Physics **110** (8), 3903 (1999).

[44] V. A. Bracken, P. Gurtler and J. G. McCaffrey, The Journal of Chemical Physics **107** (14), 5290 (1997).

[45] M. A. Collier and J. G. McCaffrey, The Journal of Chemical Physics **119** (22), 11878 (2003).

[46] P. Kerins, B. Healy and J. G. McCaffrey, Low Temperature Physics **26** (9), 756 (2000).

[47] J. G. McCaffrey and G. A. Ozin, The Journal of Chemical Physics **101** (12), 10354 (1994).

[48] M. A. Collier and J. G. McCaffrey, Journal of Chemical Physics **122** (18) (2005).

[49] M. A. Collier and J. G. McCaffrey, Journal of Chemical Physics **122** (5) (2005).

[50] M. A. Collier, M. C. Ryan and J. G. McCaffrey, Journal of Chemical Physics **123** (4) (2005).

[51] A. Corney, *Atomic and Laser Spectroscopy*. (Clarendon Press and Oxford University Press, 1977).

Chapter II
Experimental

II.1 Introduction

As outlined in Chapter I the matrix-isolation technique involves co-condensing a gaseous mixture of substrate and host onto a cold sample window. In this project, the inert hosts were argon, krypton and xenon and the guest metal was europium. Molecular hosts used were dinitrogen (N_2) and carbon monoxide (CO). The following sections present and describe the experimental set-up and techniques used in order to form matrix-isolated samples of atomic europium in these hosts and the apparatus employed to spectrally characterise samples and reaction products. These experimental considerations are presented in the six sections which follow. Firstly the matrix-isolation equipment used to attain high vacuum and low sample temperatures is described. Then the components of the gas handling system employed to achieve high purity of hosts and matrix host mixtures are listed, followed by a description of the metal vaporisation technique used to form atomic Eu vapour and the matrix-isolation sample preparation procedure. The UV/Vis and Infrared spectroscopic set-ups and detection methods are then presented.

II.2 Matrix-isolation Apparatus

Matrix-isolated samples were formed in a high vacuum sample chamber on a calcium fluoride (CaF_2) substrate window held at 10 K. Vacuum in the region of low 10^{-8} mbar was achieved using a Speedivac oil diffusion pump supported by an Edwards rotary pump[1]. The vacuum was monitored with an Alcatel Penning Gauge (Model CF2P). A liquid nitrogen-filled cold trap at the top of the diffusion pump prevented cryo-pumping of boiling diffusion oil towards the sample chamber when working at low temperatures as laid out in Figure II.1 and listed in Table II.1.

The vacuum shroud of the sample chamber was custom built and supplied by APD cryogenics. The five-faced cube around the sample holder had a one-inch optical window on each of three of the sides and the sample window could be rotated 360^0 to allow for transmittance scans directly through the sample or excitation/emission scans recorded monitoring emission perpendicular to the excitation source as seen in Figure II.2. The fourth face is connected to an electron gun which produces a source of atomic europium metal vapour and the final face on the bottom is covered with a blank metal plate.

Table II.1 Manufacturers and relevant part numbers of components necessary to achieve high-vacuum in the region of low 10^{-8} mbar in the matrix-isolation apparatus.

Component	Manufacturer	Model/Part number
Quarter-Swing butterfly valve	Edwards	QSB2
Rotary Vacuum Pump	Edwards	RV3
Oil Vapour Diffusion Pump	Speedivac	E02

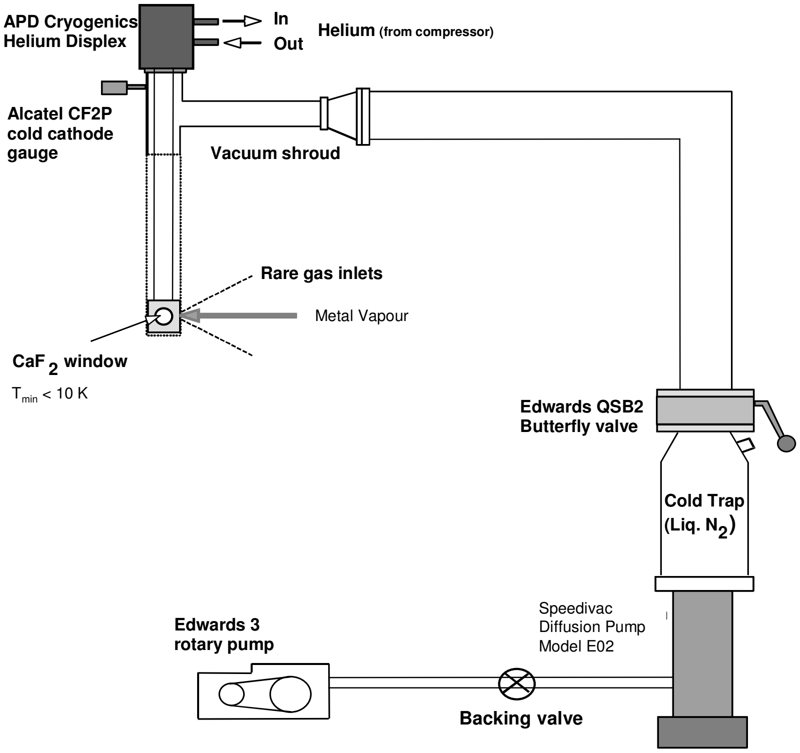

Figure II.1 Overview of the matrix-isolation apparatus showing the vacuum shroud and pumping set-up used.

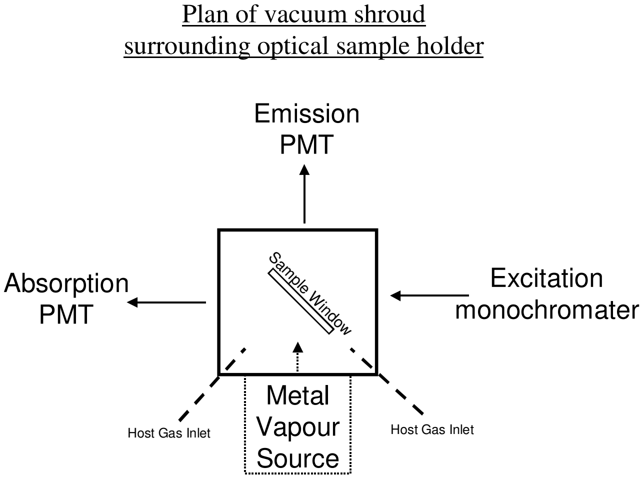

Figure II.2 Plan of the five-faced vacuum shroud surrounding the optical sample holder. Transmittance spectra are recorded directly through the sample while emission/excitation spectra are monitored perpendicular to the excitation source. Bottom face is covered with a blank metal plate.

The sample window was attached to the end of the second stage of an APD cryogenics closed-cycle refrigeration system, shown in Figure II.3, with a model DE-202 displex expander[2] operating on the Gifford-McMahon refrigeration cycle process using high pressure (260 psi) and high purity (99.995%) Helium.

The second stage of the expander was surrounded by a modified radiation shield which allowed temperatures of 10 K or below to be achieved at the sample window. Temperatures were controlled and monitored using a Scientific Instruments temperature control unit connected to a Silicon diode temperature sensor[3] located in the tip of the second stage, directly at the sample window. The details of these components are listed in Table II.2.

CaF_2 is chosen as the sample window material due to its wide optical transparency range (130-9000 nm) but also because this material is non-hygroscopic, extremely insoluble and quite chemically inert making these windows both unreactive and durable and thus very suitable for use as matrix-isolation substrates. Spectroscopy in the IR region was performed on a different matrix-isolation set-up equipped with a potassium bromide (KBr) window allowing transparency in the mid-IR range of interest, transmitting light from the near UV to the far-infrared. No radiation shield was employed on this system meaning the base temperature achievable was 13 K for infrared absorption experiments.

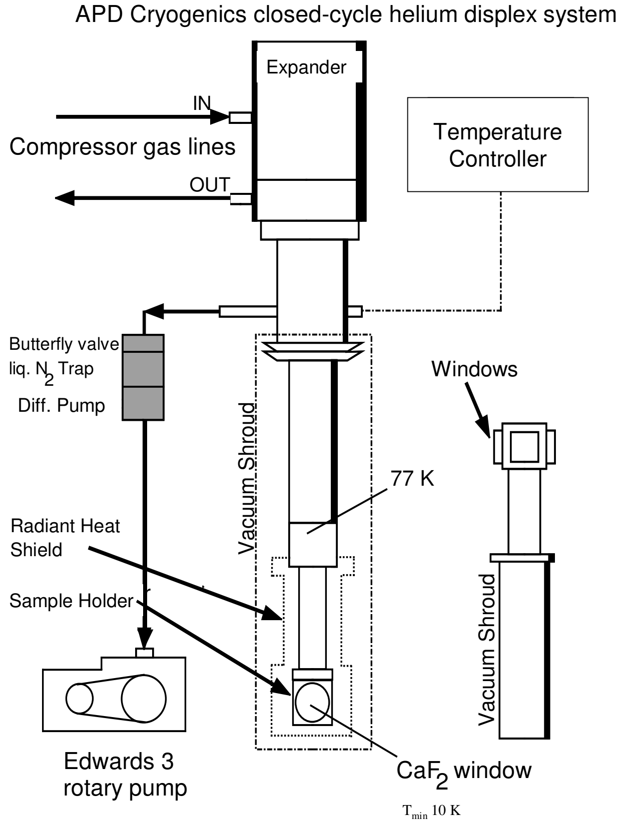

Figure II.3 Schematic of the matrix-isolation apparatus detailing the various stages of the cryogenic cooling system used to achieve temperatures of 10 K at the sample window.

Table II.2 Part numbers and manufacturers of the components necessary to achieve and monitor low temperatures (10 K) at the substrate window.

Component	Manufacturer	Model/Part number
Expander[2]	APD Cryogenics	DE-202
Helium compressor[4]	APD Cryogenics	HC-2D
Refrigerator[5]	APD Cryogenics	DMX-1AE
Silicon diode[3]	Scientific Instruments	SI-410A diode
Digital Temperature Controller[3]	Scientific Instruments	SI-9600-1

II.3 Gas handling system

The following section details the gas handling system (GHS) used. The GHS is a high vacuum chamber completely isolated from the matrix-isolation system. This allowed host gases and gas mixtures to be prepared for the next experiment while maintaining an already formed sample in the matrix-isolation sample chamber. Pressures in the GHS were maintained in the low 10^{-8} mbar region using a turbo-molecular pump[6]. A Granville-Phillips nude ionisation gauge coupled with a GP 307 series control unit[7] allowed monitoring of the vacuum in the GHS.

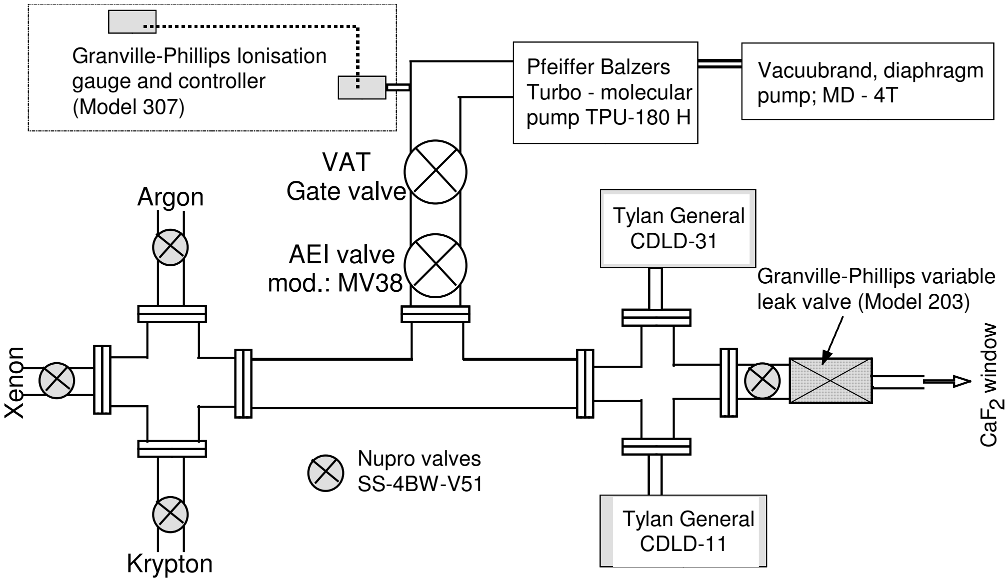

Figure II.4 A schematic of the various components comprising the Gas Handling System (GHS).

The pressure of host gas in the GHS before, during and after deposition were monitored using two Baratron gauges[8] working in the 0 to 10 Torr and 0 to 1000 Torr ranges. In particular, the 0 to 10 Torr sensitivity allowed the accurate formation of gas mixtures of low concentration ratios. A Granville-Phillips variable leak valve[9] (Model 203) allowed control of the rate of gas flow into the sample chamber and thus the rate of host flow during sample deposition to be known. A schematic of the GHS is presented in Figure II.4 along with a list of the individual components in Table II.3. A list of the matrix host gases used including their physical properties, purity and suppliers is detailed in Table II.4.

Table II.3 Details of the relevant parts composing the gas handling system (GHS).

Component	Manufacturer	Model/Part number
Turbo-molecular pump[6]	Pfeiffer	TPU-180H
Control unit[7]	Granville-Phillips	307 Series
Ion Gauge[7]	Granville-Phillips	274043
Baratron gauge (0-10 Torr)[8]	Tylan general	CDLD-11
Baratron gauge (1-1000 Torr)[8]	Tylan general	CDLD-31
Variable leak valve[9]	Granville-Phillips	Type 203

Table II.4 Matrix host gases, suppliers and purity. The melting point of each is listed in the rightmost column in Kelvin units.

Host Gas	Purity	Supplier	Melting point (K)[10]
Ar	99.998 %	BOC Gases	86.65
Kr	99.995 %	Linde Gas	116.64
Xe	99.999 %	Linde Gas	161.25
N_2	99.999 %	Linde Gas	63.15
CO	99.95 %	ISOTEC/Sigma-Aldrich	68.0

II.4 M/RG Sample Preparation

II.4.I Metal vaporisation

Europium metal vapour was produced by the electron bombardment technique using an Omicron (EFM3) electron gun coupled with an EVC 300 control unit[11]. The bulk metal (Eu chip, Sigma Aldrich[12]) was placed in a molybdenum crucible[13] held at high voltage while current was passed through a nearby filament, the details of which can be seen in Figure II.5, Figure II.6 and Table II.5. The voltage differential causes electrons from the filament to be accelerated towards the bulk metal in the crucible resulting in localised heating and metal vaporisation.

EFM evaporators are designed to effectively focus the heating power onto the evaporant with minimum heat dissipation. Heat radiation is absorbed by a water-cooled shroud surrounding the evaporant thus ensuring low background pressure (typically in the 10^{-10} mbar range) during evaporation and hence limiting impurities present in samples. By design the evaporant beam is precisely defined allowing highly uniform deposition of samples, the area of which can be controlled by varying the distance from the source to the sample window.

An integral flux monitor enables reproducible real-time monitoring of the amount of metal being vaporised. One can control the vaporisation rate by adjusting the crucible voltage and filament current on the front panel of the EVC 300 control unit while monitoring the response of the evaporant flux rate. However, in this case the flux monitor can act only as a guide to the amount of metal vaporisation as the irregular shape of the Eu chips meant the crucible packing between re-fills was not consistent. The quantity of metal contained in matrix-isolated samples was ascertained with more certainty by absorption spectroscopy upon completion of sample deposition. A built-in exit shutter with manual control allows one to stabilise the flux with the shutter closed before beginning sample deposition. Also, the EFM evaporator has a rear-loading feature which enabled crucibles to be re-filled without detaching the EFM from the vacuum chamber thus keeping the source alignment constant between crucible re-fillings.

Following each re-fill of the crucible a two-step outgassing procedure was performed before sample deposition in order to remove any adsorbed contaminants from the system. Initially, the filament was outgassed by passing a current through it without any voltage on the crucible. Secondly, any contaminants or europium oxides were outgassed from the surface of the bulk metal by evaporating the bulk metal with the shutter closed until no pressure rise was observed in the sample chamber i.e. no more vaporisation of contaminants. This process was aided by removal of some of the europium oxide layer by gentle filing with an abrasive surface before introducing the re-filled crucible to the vacuum system.

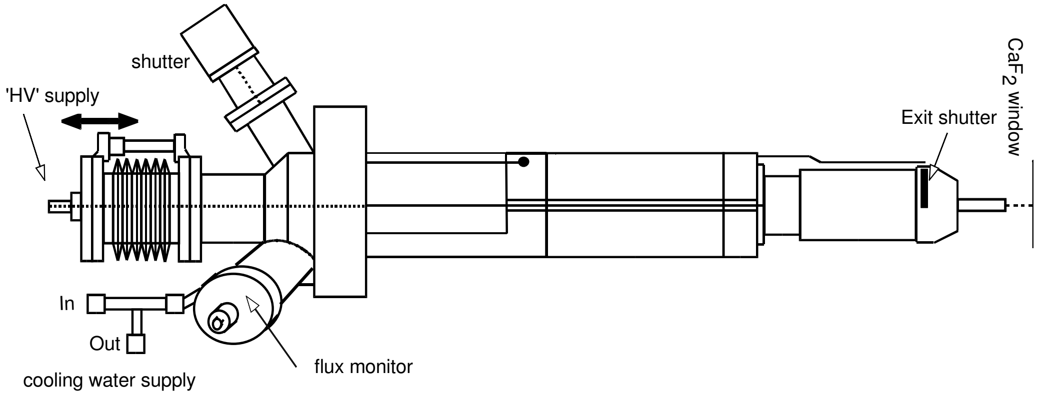

Figure II.5 Overview of the Omicron EFM3 electron gun.

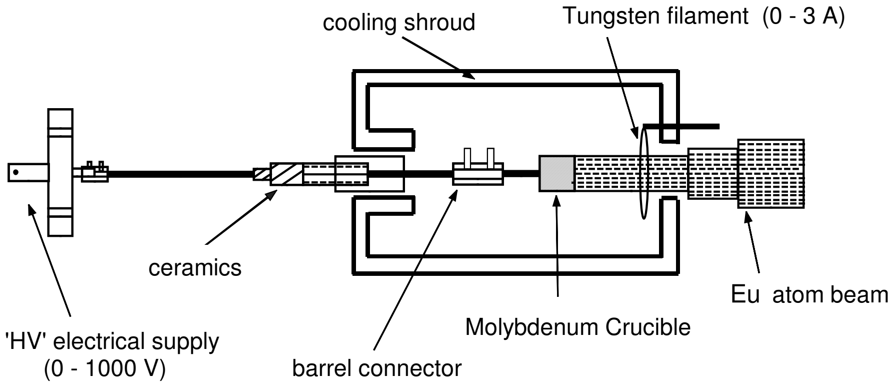

Figure II.6 Representation of the internal components of the EFM3 vaporisation source.

Table II.5 Details of the necessary parts involved in the formation of guest metal vapour.

Item	Manufacturer	Model	Details
Electron gun[11]	Omicron	UHV EFM3	Ifil 0-2.5 A
Control Unit[11]	Omicron	EVC 300	Voltage 0-1000V
Crucible[13]	Omicron	B000432-S	Outer diameter 8.0 mm Inner diameter 6.0 mm Capacity 250 mm^3 Temperature (max) 2200 ^{0}C
Europium[12]	Sigma Aldrich	457965-5G	Europium chip in mineral oil Purity 99.9 %, m.p. 822 ^{0}C[10]

II.4.II Sample Deposition

The procedure for sample formation is described in this section. Firstly the metal vaporisation rate is allowed to stabilise by monitoring the flux using the electron gun control unit. Once a steady atomic beam is attained a base layer of pure RG host without any guest atoms is deposited onto the sample window to limit metal aggregation and contamination of the window between depositions. Then the shutter of the electron gun is opened allowing metal vapour into the sample chamber while at the same time still flowing the RG host and thus co-condensing both on the cold window.

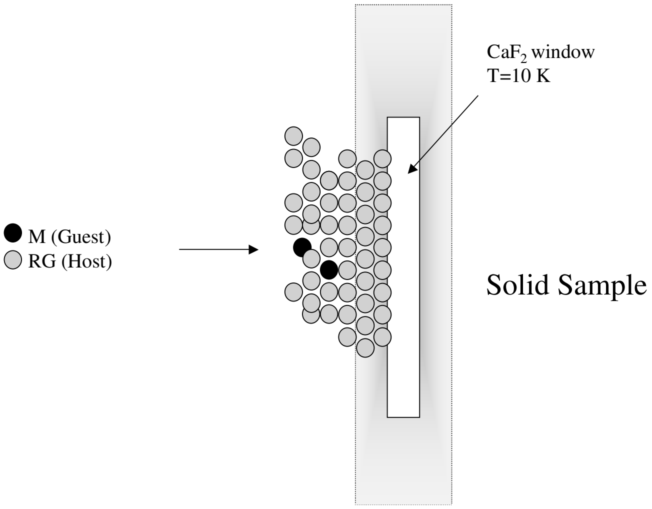

Figure II.7 Schematic representation of a M/RG matrix-isolated sample during deposition.

Typically voltages of 400 V and filament currents of 1.4 A were used to form samples containing isolated europium atoms. Continuity between samples was obtained by using the same metal fluxes and the same RG flow during depositions. The flow of host gas into the sample chamber from the GHS was regulated by the Granville-Phillips variable (Model 203)[9] leak valve.

II.5 Luminescence measurements

The spectroscopic set-up used to probe Eu/RG samples can be divided into two main sections depending on the spectral region being investigated. Both steady-state and time-resolved luminescence spectroscopy was performed in the UV/Vis spectral region. Fourier Transform absorption spectroscopy was recorded in the infrared spectral region.

II.5.I UV/Vis Spectroscopy

II.5.I.1Steady-state luminescence set-up

A schematic of the steady-state luminescence set-up used is presented in Figure II.8. Continuous lamp excitation was produced from a deuterium lamp (UV 180 to 400 nm range) and a tungsten lamp (UV/Vis 300 to 900 nm range). Upon deposition a transmittance spectrum of the matrix-isolated sample was recorded by passing the excitation light directly through the sample. Excitation wavelength selection was performed using a 0.30 m SpectraPro-300i monochromator[14] from Acton Research Corporation containing a 1200 grooves/mm diffraction grating blazed at 300 nm. Transmittance spectra were recorded by monitoring the light intensity on the transmittance PMT (Hamamatsu R928[15]) detector as the excitation monochromator scanned through the range of wavelengths. An absorption spectrum could then be created from the transmittance spectrum using the Beer-Lambert law (Equation II.1),

$$\text{Absorbance} = -\log_{10}(I/I_0) \qquad \textit{Equation II.1}$$

where the incident transmittance spectrum (I_0) is taken as the throughput of a blank matrix host sample i.e. a matrix containing only host atoms, no metal dopant. Assuming the same sample thickness for the M/RG sample and the corresponding RG blank, absorbance is calculated using Equation II.2. By dividing the sample transmittance ($I_{M/RG}$) by the blank transmittance (I_{Blank}) and taking negative log of this an absorption spectrum for a particular M/RG sample is produced.

$$\text{Absorbance} = -\log_{10}(I_{M/RG}/I_{Blank}) \qquad \textit{Equation II.2}$$

Once an absorption spectrum is obtained an emission spectrum is recorded monitored perpendicular to the excitation source. Again, the excitation wavelength is selected using the 0.30 m monochromator while the emission wavelength of interest was selected using a 0.50 m Spectra-Pro-500i monochromator[16] and the emission intensity was monitored using a Hamamatsu R928-P PMT[15] detector at – 20^0C in a Photocool S600 cooling housing[17]. Similarly, excitation spectra were recorded by monitoring the change in emission intensity at a particular emission wavelength while scanning the range of excitation wavelengths. Note, steady-state emission spectra could also be recorded using the iCCD detector by flipping the swing mirror in 0.5 m monochromator, as shown in Figure II.8.

Table II.6 Specifications of the SpectraPro-300i and -500i monochromators used to record steady-state and time-resolved emission spectra in the UV/Vis spectral region. # indicates the specifications refer to the 1200 grooves/mm gratings.

ARC Monochromator	SpectraPro-300i[14]	SpectraPro-500i[16]
Focal length (mm)	300	500
Wavelength range (nm)	180 nm – far infrared	180 nm – far infrared
Gratings(grooves/mm) / Blaze(nm)	1200 / 300	1200 / 300 600 / 600 150 / 300
Resolution (nm)#	0.1 @ 435.8 nm	0.05 @ 435.8 nm
Dispersion (nm/mm)#	2.7	1.7
Accuracy (nm)#	± 0.2	± 0.2

Table II.7 Details of the Photon-Multiplier Tube (PMT) detectors used to record steady-state spectra in the UV/Vis spectral region. The R928-P has much lower electronic noise and is used to record emission/excitation spectra.

Hamamatsu PMT	R928[15]	R928-P[15]
Range (nm)	185 – 900	185 – 900
Peak wavelength (nm)	400	400
Photo-cathode material	Multialkali	Multialkali
Window material	UV glass	UV glass

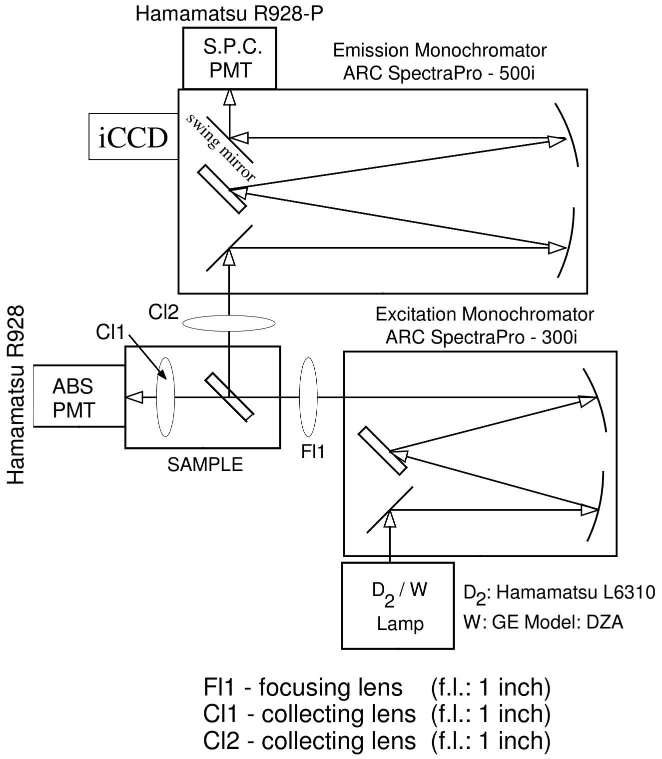

Figure II.8 Layout of the UV-Visible Luminescence set-up.

II.5.I.2 Time-resolved measurements

To perform time-resolved measurements a pulsed excitation source coupled with a time-gated sensor is needed. In this case, a pulsed dye laser and a time-gated iCCD for shorter lifetime measurement or the Multi Channel Scaling photon counting technique for longer lifetime measurements were employed.

The laser source was the output of a Quantel TDL90 Dye Laser[18] pumped by the second (532 nm) or third (355 nm) harmonics of a Nd:YAG laser operating at a repetition rate of 10 Hz (Quantel YG980E)[19]. The dye laser allowed tuneable excitation to be selected by choosing the correct organic dye for the spectral region of interest, details of dyes used are listed in Table II.8. Typical laser output powers of up to 5 μJ/mm^2 were obtained using the oscillator and pre-amplifier of the TDL90. Increased powers beyond 1 mJ/mm^2 could be obtained by pumping the amplifier dye cell.

Laser excitation wavelengths in the UV region were achieved by frequency mixing the fundamental of the YAG (1064 nm) with the output of a particular dye. Mixing was performed using KDP (Potassium diPhosphate) crystals [Quantel MCC1 Mixing crystal and Quantel QCC2 compensator to correct for the walk of the beam]. A Pellin-Broka prism at the output of the dye laser allowed the mixed UV output to be separated from the dye and YAG beams.

Table II.8 Spectral characteristics of the dye materials used in this study. All were dissolved in ethanol and manufactured by radiant dyes. The spectral ranges quoted are in methanol from LambdaChrome manual[20]. Pumped by: # = 3rd (355 nm), * = 2nd (532 nm) harmonic of Nd:YAG.

Dye Material	Absorption Maximum	Fluorescence Maximum	Dye Laser Range (nm)
Stilbene 3# (Stilbene 420) $C_{28}H_{20}O_6S_2$	350 nm	-	415 – 439 (λ_{max} = 428)
Coumarin 440# (Coumarin 120) $C_{10}H_9NO_2$	354 nm	435 nm	420 – 470 (λ_{max} = 440)
Coumarin 460# (Coumarin 47) $C_{14}H_{17}NO_2$	373 nm	450 nm	444 – 476 (λ_{max} = 460)
Coumarin 480# (Coumarin 102) $C_{16}H_{17}NO_2$	389 nm	465 nm	462 – 497 (λ_{max} = 480)
DCM* (LC 6500) $C_{19}H_{17}N_3$	472 nm	644 nm	615 – 666 (λ_{max} = 639)
Rhodamine 6G* (Rhodamine 590) $C_{28}H_{31}N_2O_3Cl$	530 nm	556 nm	555 – 580 (λ_{max} = 566)
Rhodamine B* (Rhodamine 610) $C_{28}H_{31}N_2O_3Cl$	552 nm	580 nm	584 – 619 (λ_{max} = 594)

II.5.I.3 Short-lived emission decay times

An Andor Technologies nanosecond time-gated iStar DH720 intensified charged-coupled device (iCCD) comprising of a CCD sensor connected to a gated image intensifier was used to record short-lived lifetimes. A PC installed with Andor iStar software and controller card (CCI-010) allowed control of the iCCD unit and ARC SpectraPro 500i monochromator via the RS232 port of a PC. The iCCD was maintained at –15^{o}C by an integrated Peltier cooling system. The image intensifier consists of three major components, a photocathode, a microchannel plate (MCP) and the output phosphor screen. The photocathode in front of the microchannel plate converts photons to electrons which are then multiplied by the MCP. After the MCP a phosphor screen converts the electrons back to photons which are fibre-optically guided to the CCD as displayed in Figure II.9.

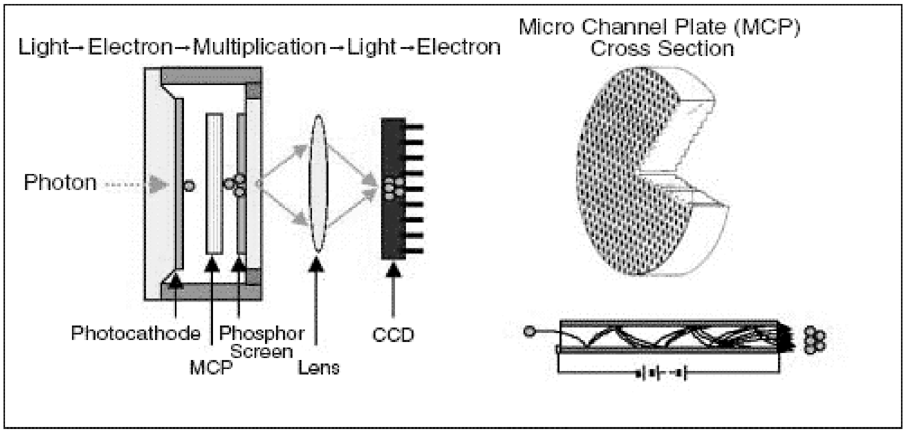

Figure II.9 Details of the light amplification process performed in the image intensifier of the iCCD[21]. To the left is shown the three main components of the image intensifier, the photocathode, the microchannel plate (MCP) and the phosphor screen. To the right is a detailed view of the MCP which consists of a thin disk of honeycombed glass. When a high potential is applied across it, the incident photoelectron cascades down the channel amplifying the number of exiting electrons.

The MCP consists of a thin disk of honeycombed glass with a high potential across it (500-1000 V) so that the photoelectron will cascade down the channel amplifying the number of exiting electrons. Varying the voltage enables an increase or decrease in the gain of the output towards the phosphor screen so that even single photon events can be detected. The presence of the MCP also allows the image intensifier to operate as a shutter. By switching the MCP high voltage on and off in a rapid fashion ultra fast shuttering occurs, permitting time-resolved measurements of events taking place on the nanosecond scale to be recorded. When the shutter is open i.e. high voltage applied across the MCP, the MCP input signal is allowed to fall on the CCD and data is acquired but when the applied voltage is removed the shutter is closed and no signal reaches the CCD.

The MCP is a key component of the image intensifier giving two main advantages to the CCD *a)* Increased sensitivity, single photon events can be detected and *b)* ultra fast shuttering, allowing gating periods and consequently time-resolution of events as short as 2 ns to be achieved.

Experimentally, short-lived fluorescence lifetimes were extracted from time-resolved emission spectra recorded using the iCCD triggered by an output pulse from the TDL90 laser. Laser powers employed were generally in the region of 1 to 5 $\mu J/mm^2$. The Andor software controlled the diffraction grating used in the 0.5 m monochromator to select desired resolution and spectral range.

II.5.I.4 Long-lived emission decay times (τ >10 μs)

Long-lived lifetime measurements were recorded using the Quantel laser system discussed previously as the excitation source but instead employing the photon counting multi-channel scaling (MCS) time analysis technique. The signal from a photon counting (R928-P) emission PMT[15] was amplified by an Ortec (Model VT120) fast-timing preamplifier[22] and to limit electronic noise relayed to an Ortec (Model 584) constant–fraction discriminator[23] (CFD). The output of the CFD was passed simultaneously to the stop-in on a 2 GHz multi-channel scalar[24] (Fast ComTec, Model 7886) and to an Ortec (Model 661) ratemeter[25]. The Q–switch pulse of the Nd:YAG was taken as the start pulse for the MCS unit.

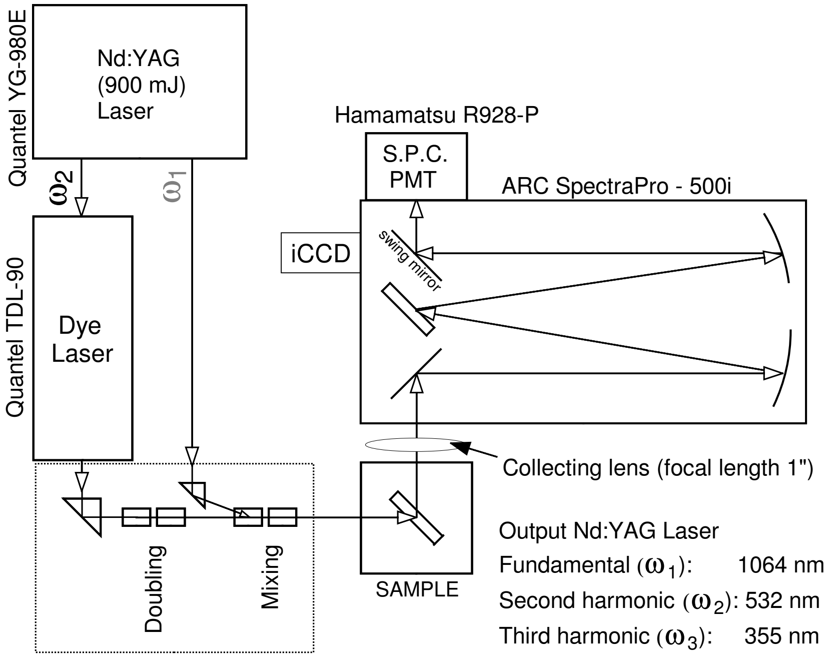

Figure II.10 Optical layout of the set-up employed for recording Time-resolved Emission Spectra (TRES).

II.5.I.5 Decay curve fitting

In both long and short-lived measurements, the change in intensity of a particular emission feature was monitored as a function of time. Long-lived lifetimes were extracted from the experimental data by fitting single or multiple exponential functions to the decay curves and performing a non-linear least squares fit analysis. The fits were generally performed over four orders of magnitude. In the case of short-lived emission features a trial fit function was fitted to the decay curve which included a re-convolution with the time profile of the laser excitation source. Once good agreement was achieved between the fit and the experimental decay curve, analysis of the portion of the fit deconvoluted from the laser profile allowed a lifetime of the emission feature to be extracted.

II.5.II Infrared Absorption Spectroscopy

In the case of europium reactivity with small molecules such as nitrogen (N_2) and carbon monoxide (CO), absorption spectra were recorded in the mid-infrared spectral region monitoring the change in vibrational frequency of the carbon-oxygen stretch in CO at 2140 cm^{-1} and the dinitrogen stretch of N_2 at 2330 cm^{-1}. Spectra in this region were recorded using a Bruker IFS 66/S spectrometer with a resolution of 0.5 cm^{-1} equipped with a DTGS (Deuterated Triglycine Sulfate) and a much more sensitive liquid nitrogen cooled MCT (Mercury-cadmium-telluride) detector, the specifications of which are listed in Table II.9[26]. The light sources (S) available were a Globar for the mid-IR range and a tungsten lamp for near-IR spectroscopy.

Instead of CaF_2 used during UV/Vis spectroscopy, KBr was the chosen material for the matrix sample window and the outer one-inch optical windows of the matrix-isolation apparatus. KBr has an increased infrared transparency range (7,500 - 370 cm^{-1})[27]. However, it is highly hydroscopic so measures were taken to ensure the system was not exposed to atmospheric water. The vacuum shroud was surrounded by a flow of dried, purged air supplied by a Peak Scientific Instruments Purge Gas Generator (Model PG28L).

Table II.9 Specifications of the infrared detectors available in the Bruker IFS 66/S infrared spectrometer.

Detector	Part No.	Range (cm^{-1})	Sensitivity/Noise	Operating Temperature
DTGS	D301	12000-250	$>4x10^8$ $cmHz^{1/2}W^{-1}$	Room Temperature
MCT	D315	12000-420	$>5x10^9$ $cmHz^{1/2}W^{-1}$	Liquid N_2 cooled

The Bruker IFS 66/S is a rapid scan Michelson Interferometer, a schematic of which is displayed in Figure II.11. Light originates from a broadband infrared source (S) whose output is collimated. This light beam then impinges upon a beamsplitter (BMS). The beamsplitter transmits 50 % of the light to one mirror and reflects 50 % of the light to a second mirror. The light reflected off these two mirrors is passed by the beamsplitter a second time and the two beams recombine on the other side of the beamsplitter after passing through the sample and are finally focused onto an IR detector (D). In the interferometer, one mirror (M1) is held in a fixed position relative to the beamsplitter during the measurement, and the second mirror (the moving mirror M2) scans back and forth relative to the beamsplitter.

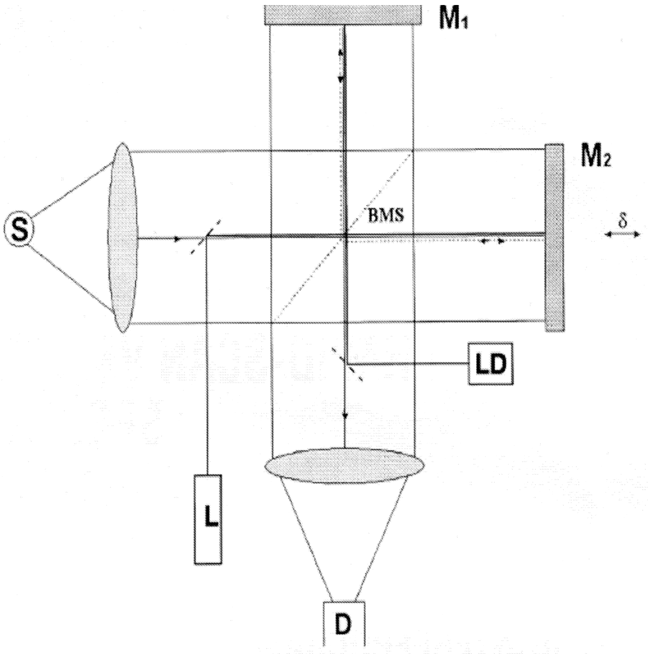

Figure II.11 Schematic of the Michelson interferometer with the HeNe laser running co-axial. S = source, BMS = beamsplitter, M = mirror, D = detector, L = Laser.[28]

In a rapid scan FT-IR spectrometer such as the Bruker IFS 66/S the moving mirror in the interferometer scans forward and backward in a rapid continuous fashion. During the mirror scan, the path length of the IR beam from the beamsplitter to the moving mirror changes relative to the path length of the IR beam to the fixed mirror. This path traversal difference for the light beams in the two arms of the interferometer is known as optical path difference (OPD) or optical retardation. When the two parts of the IR beam recombine on the other side of the beamsplitter and form an image at the detector the intensity of the composite beam is an interference pattern depending very strongly upon the optical path difference. The plot of this intensity variation as a function of optical retardation i.e. the intensity registered at the detector as a function of moving mirror position is known as an interferogram.

In addition to the IR source (S) a Helium-Neon (HeNe) laser beam (L) traverses the same optical path as the IR light. The monochromatic HeNe beam is split by the beamsplitter and the two beams recombine after passing through the two arms of the interferometer, travelling the same path as the IR beam. The HeNe laser light is monochromatic and the moving mirror moves at a constant velocity, thus one will observe a constant frequency and constant amplitude interferogram for a monochromatic source such as this. The HeNe laser interferogram is used by the FT-IR spectrometer to monitor the mirror position during the course of the scan, yielding a plot of intensity versus mirror position. This interferogram and the sample interferogram are then Fourier Transformed to yield a spectrum of intensity versus wavenumber.

References

[1] Edwards, *Rotary Vacuum Pumps E2M2,E1M5/E2M5, E1M8/E2M8*. (Edwards High Vacuum, 1983).

[2] *DE-202 Expander Technical Manual*. (APD Cryogenics Inc., May 1989 (257519A)).

[3] *Instruction Manual, Series 9600 microprocessor – based digital temperature indicators/controllers manual #A090-145*. (Scientific Instruments Inc., March 6th, 1990).

[4] *Helium Compressor HC-2D Technical Manual*. (APD Cryogenics Inc., Jan 1992, (256685A)).

[5] *Laboratory interface components Technical Manual, Models WMX, DMX, HMX, FMX.* (APD Cryogenics Inc., Aug 1990, (257692A)).

[6] *Operating Instructions, Turbo-molecular pump, TPU 180H, Ed. 3.* (Balzers).

[7] *307 Vacuum Gauge Controller Technical Manual*. (Granville-Phillips, 1993).

[8] *Technical Sheets, Capacitance Diaphragm Gauges CDL Series.* (Tylan General).

[9] *203 Variable Leak Valve, Technical Manual*. (Granville-Phillips, 1993).

[10] *CRC Handbook of Chemistry and Physics*, 76th ed. (CRC Press, 1995).

[11] Omicron, *Instruments for Surface Science, Instruction Manual UHV Evaporator, EFM 3/4, Version 2.0*. (1996).

[12] SigmaAldrich, *Europium Chips (5g in mineral oil) Catalogue Number 457965-5G*.

[13] Omicron, *EFM Evaporators, 'Ultra-Pure Submonolayer and multilayer thin film growth', Brochure 2008.*

[14] *SpectraPro – 300i, SP – 300i, Manual Rev. 997.1*. (Acton Research Corporation).

[15] Hamamatsu, *Data Sheet, Photomultiplier Tubes R928, R955*.

[16] *SpectraPro – 500i, 500i Manual V1097.1*. (Acton Research Corporation).

[17] *Photocool Series Power Supply, Instruction Manual, (Model PC177CE009 for R928).* (Products for Research, Inc.).

[18] *Quantel – TDL 90, Instruction Manual – Issue 1*. (Quantel).

[19] *Instruction Manual QUANTEL YG 980 Q-switched Nd:YAG laser, Doc. 980, Version #1, anglaise PM/DT (12.05.97).* (Quantel).

[20] U. Brackmann, *Lambdachrome Laser Dyes Catalogue*, 3rd ed. (Lambda Physik, 2000).

[21] Hamamatsu, http://sales.hamamatsu.com/assets/html/sd/images/ICCD-camera-fig6.gif. (Last accessed March 2010).

[22] Ortec, *Model VT120 Fast Timing Pre-Amplifier, Operating and Service Manual, Part No. 760360, Revision B.*

[23] Ortec, *Model 584, Constant - Fraction Discriminator, Operation and Service Manual, Part No. 733550, Revision B.*

[24] FastComTecGmbH, *2 GHz Fast Multiscalar, User Manual, Model 7886*.

[25] Ortec, *Model 661 Ratemeter, Operation and Service Manual, Part No. 740380, Revision B*.

[26] BrukerOptics, *DigiTect detectors for Bruker Optics VERTEX and TENSOR series FT-IR-spectrometers, Product Sheet*.

[27] BrukerOptics, *IFS 66/S User Manual*. (Bruker Optik GmbH, 2000).

[28] T. J. Johnson and G.Zachmann, *Introduction to Step-Scan FTIR*. (BrukerOptics).

Chapter III

Eu(y^8P)/RG Absorption and Excitation Spectroscopy

Sites of isolation in solid RG's and the observation of Eu dimers

III.1 Introduction

Absorption spectra of matrix-isolated atomic europium recorded in the UV/Vis spectral region exhibit two main absorption features. These are the 1) s → p type y^8P ($4f^7 6s^1 6p^1$) ← $a^8S_{7/2}$ transition observed in the visible region and, 2) the f → d type ^{8}P, ^{6}P ($4f^6 5d^1 6s^2$) ← $a^8S_{7/2}$ transitions occurring in the UV spectral region as shown in Figure III.1. The y^8P absorption dominates the spectrum due to its much larger oscillator strength. y^8P transition from the $a^8S_{7/2}$ ground state is ten times more intense than the ^{8}P ← $a^8S_{7/2}$ transition in the gas phase[1]. The following sections discuss in detail the previously unreported visible absorption features and identification of multiple metal trapping sites within the RG lattices (RG = Ar, Kr, Xe).

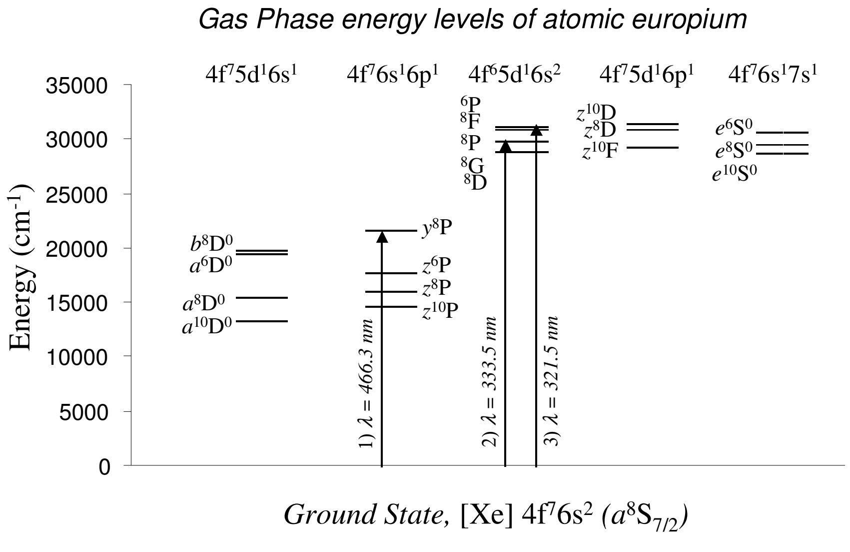

Figure III.1 Schematic representation of the energy levels of gas phase atomic europium. The $y^8P_{5/2}$ ← $a^8S_{7/2}$, $^8P_{5/2}$ ← $a^8S_{7/2}$ and $^6P_{5/2}$ ← $a^8S_{7/2}$ occurring at 21444.6 cm^{-1} (466.3 nm), 29982.5 cm^{-1} (333.5 nm) and 31107.3 cm^{-1} (321.5 nm) respectively, are indicated by arrows[1].

The work done on the y^8P state absorption will be presented as follows. Firstly, absorption features observed in RG matrix samples are assigned to electronic transitions of atomic Eu based on comparison to the gas phase energies and lifetime characteristics which will be presented in Chapter IV. An annealing study allows a thermally unstable site to be identified in all matrices. Next, absorption spectra of samples deposited at increased metal loading and increased deposition temperatures will be presented in an effort to observe Eu cluster formation.

y^8P state absorption and excitation spectroscopy of atomic Eu isolated in annealed rare gas solids allowed identification of multiple metal atom trapping sites within the RG matrices. Site occupancy could not be resolved through absorption alone, however excitation spectra monitoring site-specific emission features identified particular absorption features corresponding to atoms residing in a particular site within the matrix.

Analysis of these results allows sites occupied by Eu atoms in the RG solids to be identified. There are two thermally stable 'blue' and 'red' sites of isolation of atomic Eu in solid Ar and Kr and one thermally stable 'blue' site in Xe matrices. Site attributions are made based on use of a polarisability model on the $y^8\text{P} \leftarrow a^8\text{S}_{7/2}$ electronic transition of atomic Eu. This polarisability model was used in previous work by our group investigating sites of isolation of atomic Mn within the RG matrices[2]. An analysis of the gas phase to RG matrix frequency shifts observed for $\text{P} \leftarrow \text{S}$ type electronic transitions allows association of certain site types occupied by metal atoms in the rare gas solids.

The possible sites occupied by Eu atoms within RG matrices are discussed with comparison of Eu/RG to Na/RG. Sodium is chosen as a comparative system due to Eu and Na having similar polarisabilities and ionisation energies and both having spherical ground states, a^8S and ^{2}S respectively. Because of their spherically symmetric ground states Eu and Na atoms favour occupancy in spherical sites of isolation within the lattice.

In summation, complicated absorption spectra of Eu/RG are deconvoluted into multiple sites using excitation spectroscopy. A polarisability plot allows association of sites occupied and they are attributed to particular *fcc* lattice sites by comparison to Na/RG experimental and Molecular Dynamic calculations.

III.2 Eu/RG Absorption Spectroscopy

Absorption spectra of atomic europium isolated in the solid RG's recorded in the UV/Vis spectral range are analysed. Atomic transitions are assigned based on their spectral proximity to the gas phase transition since the weak van der Waals interaction between the guest metal atom and the RG host causes little change in the observed transition energy from that of the free metal atom. One expects the upper state is increasingly stabilised by heavier rare gases[3] and therefore a trend to lower absorption energy is expected in more polarisable RG hosts. This is precisely what is observed for the y^8P excited state of atomic Eu as the matrix host is changed from Ar to more polarisable Xe. Annealing effects on the absorption spectra allow identification of a thermally unstable site of isolation of atomic europium in the RG lattices present upon deposition.

III.2.I Eu/Ar

Atomic europium was successfully isolated in Ar matrices at 10 K. An absorption spectrum recorded in the UV/Vis spectral region is presented in Figure III.2 and shows two main absorption regions. Intense absorption is observed in the visible region at 450 nm and three weaker features occurring in the UV region centred at 309, 322 and 335 nm corresponding to absorption of the spin-orbit levels of the ^8P_J and ^6P_J electronic states.

Jakob *et al.* [4,5,6] have previously investigated these UV absorptions in RG matrices (RG = Ar, Kr and Xe). The dominance of the fully allowed $y^8P_{5/2} \leftrightarrow a^8S_{7/2}$ electronic transition occurring at 466.3 nm in the gas phase is not surprising considering it has a much greater oscillator strength than the ^{8}P state in the free atom. We now discuss the previously unreported y^8P state absorption of atomic Eu observed at 450 nm in solid argon.

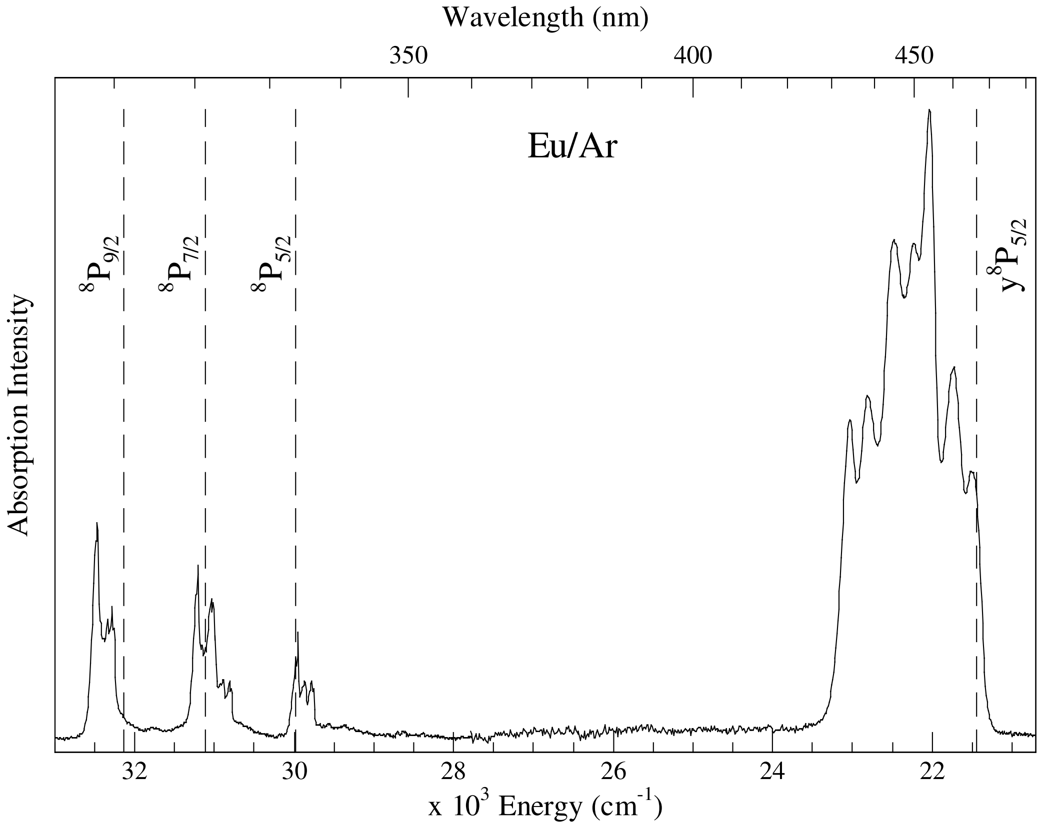

Figure III.2 Eu/Ar UV/Vis absorption spectrum recorded at 10 K following sample deposition at 10 K. Dashed vertical lines represent the gas phase transition energy positions of the labelled electronic states.

Top trace of Figure III.3 presents an expanded view of the absorption spectra of atomic Eu isolated in Ar in the y^8P spectral region. A broad, structured absorption profile is observed upon deposition centred at 450 nm, covering a spectral range of approximately 40 nm.

Annealing the Ar matrix has the effect of greatly reducing the two bands at 459.5 and 464.7 nm. These features, present on deposition, are clearly a thermally unstable site of isolation of Eu atoms in the Ar lattice. Lowest trace of Figure III.3 displays the inverted difference spectrum produced by annealing. The thermally unstable site displays threefold splitting with components at 453.2, 459.5 and 464.7 nm.

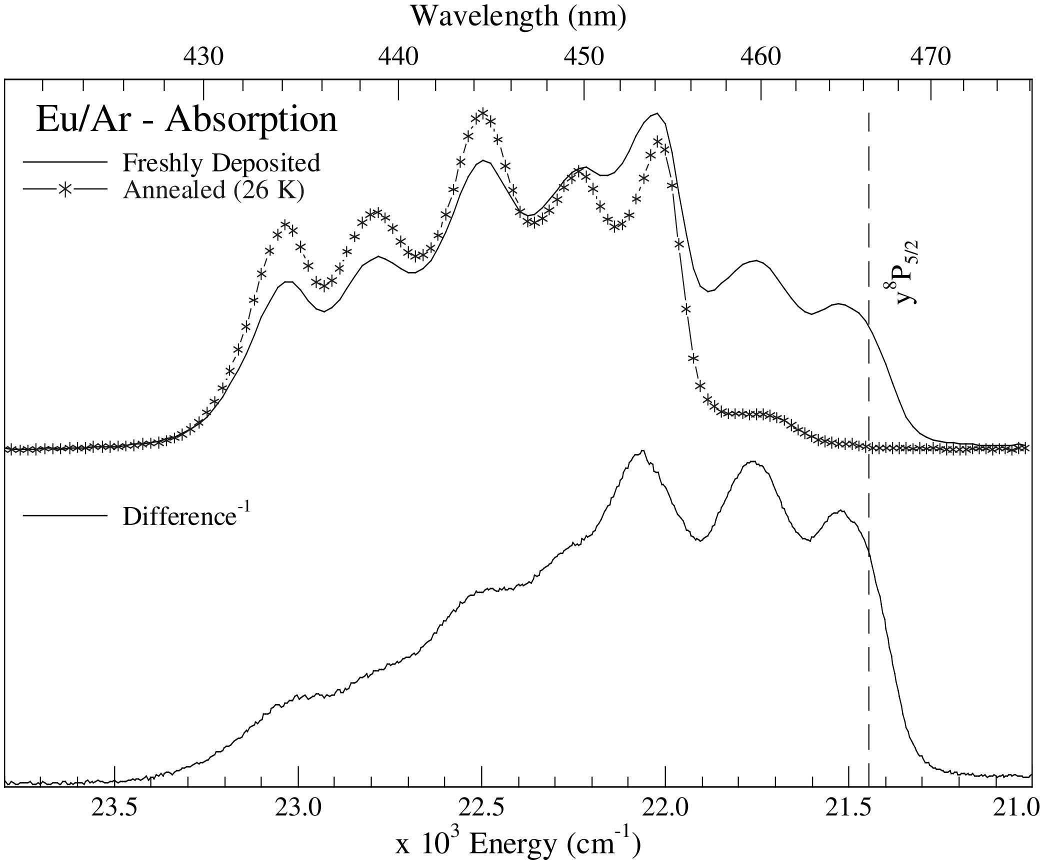

Figure III.3 Eu/Ar absorption spectra recorded at 10 K in the vicinity of the atomic Eu $y^8P_{5/2} \leftrightarrow a^8S_{7/2}$ transition. A comparison of the absorption recorded on deposition and following matrix annealing to 26 K is shown in top trace. An inverted difference spectrum indicates the removal of a thermally unstable site centred at 459.5 nm, shown lower trace.

The remaining structured absorption band centred at 445 nm exhibits resolved bands at 434.3, 439.0, 444.8, 450.1 and 454.3 nm. These five absorption features suggest the existence of two thermally stable sites of isolation of atomic Eu in the Ar matrix. In order to distinguish between the two different sites they are labelled ‘blue’ and ‘red’ sites, the blue site being of higher energy. Both exhibit Jahn-Teller (JT) threefold splitting where the lower energy Jahn-Teller component of the blue site overlays the high energy Jahn-Teller component of the red site at 444.8 nm. Thus five features are observed in the absorption spectrum instead of the expected six. This will be presented in more detail in Section III.4 using site-specific excitation spectroscopy.

III.2.II Eu/Kr

The absorption spectrum of atomic Eu isolated in solid krypton is presented in Figure III.4. As was the case for Eu/Ar, the spectrum is dominated by an absorption feature in the y^8P spectral region.

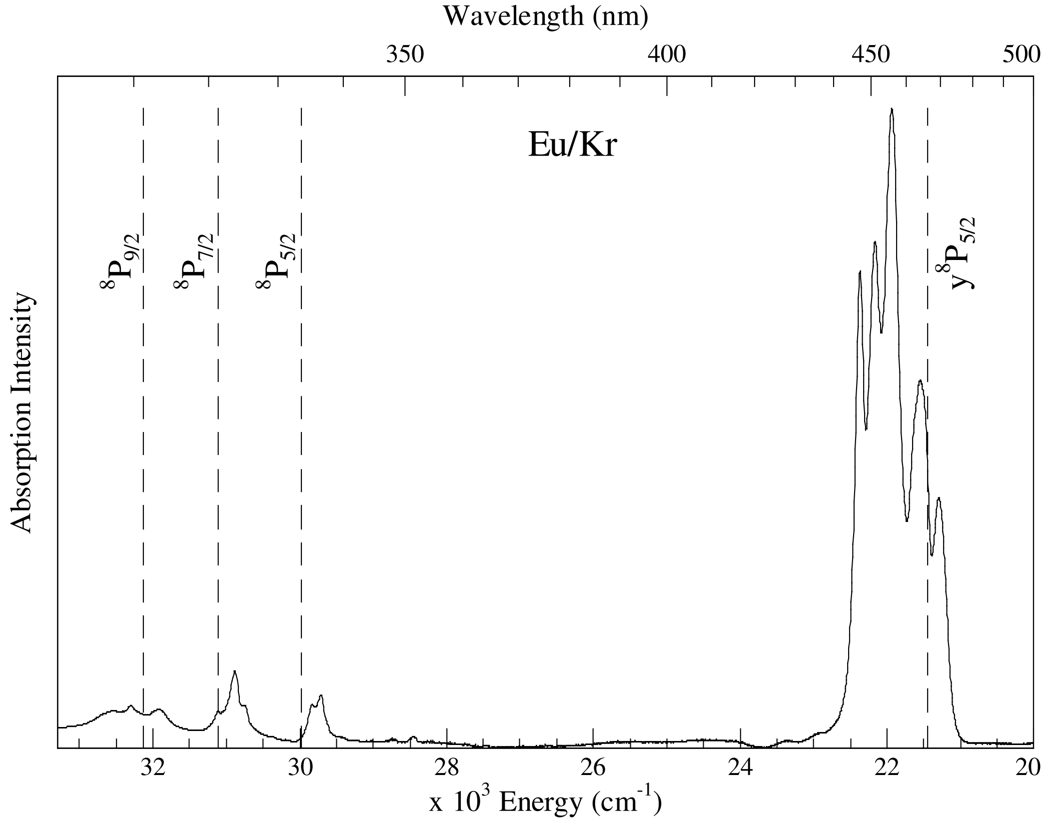

Figure III.4 Eu/Kr UV/Vis absorption spectrum recorded at 10 K following sample deposition at 10 K. Dashed vertical lines represent the gas phase positions of the labelled electronic states.

The dominant feature is a broad band centred at 460 nm, approximately 40 nm wide. Three features in the UV spectral region centred at 310, 324 and 336 nm corresponding to absorption into ^8P_J and ^6P_J spin-orbit levels are also identifiable[4,5,6]. The following section discusses the spectral characteristics of the y^8P absorption feature.

This 460 nm absorption feature exhibits five resolved features in freshly deposited samples located at 447.0, 451.4, 456.1, 464.0 and 469.7 nm as displayed in the top trace of Figure III.5. The red shoulder of the y^8P state absorption feature is most effected by annealing. Upon close inspection of Figure III.5, a decrease in the intensity of the red shoulder centred at 464 nm and complete removal of the absorption feature at 469.7 nm is seen. Lower trace of Figure III.5 presents an inverted difference spectrum following annealing. Three JT components pertaining to guest atoms isolated in a thermally unstable site are identified at 456.8, 464.0 and 469.7 nm.

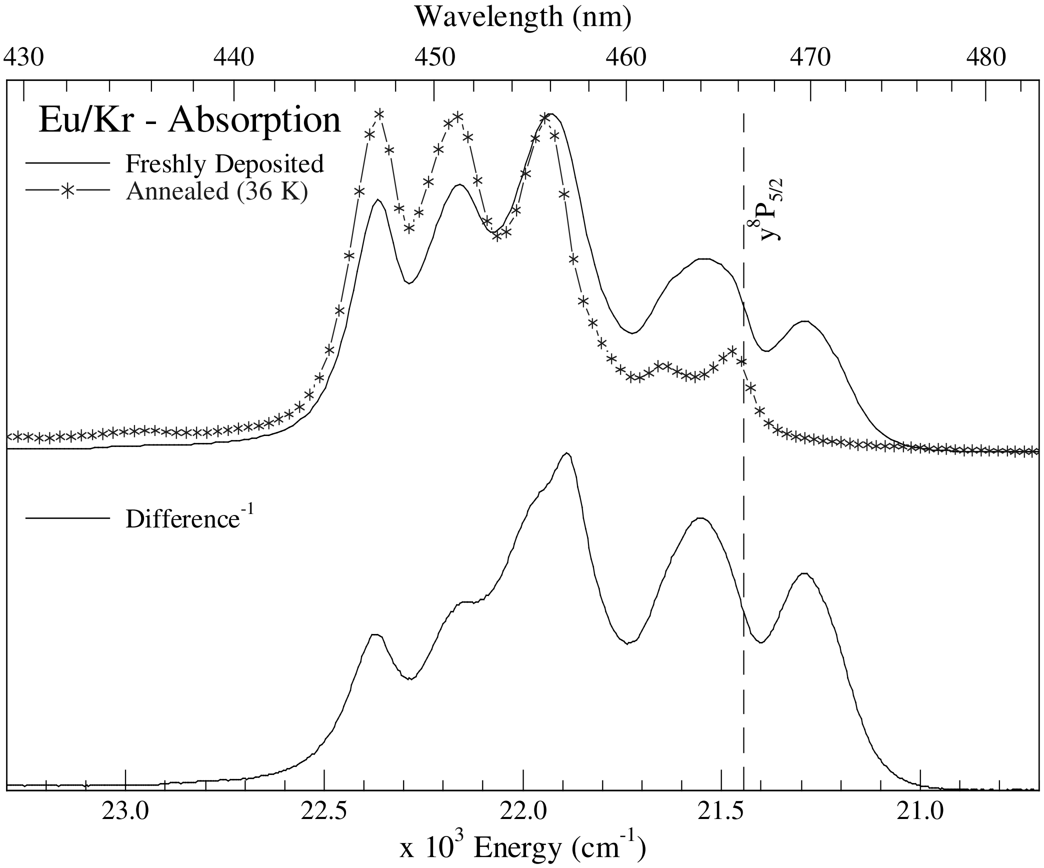

Figure III.5 Eu/Kr absorption spectra recorded at 10 K in the vicinity of the atomic Eu $y^8P_{5/2} \leftrightarrow a^8S_{7/2}$ transition. A comparison of the absorption recorded on deposition and following matrix annealing to 36 K is shown in top trace. An inverted difference spectrum indicates the removal of a thermally unstable site centred at 464 nm, shown lower trace.

Following annealing two thermally stable sites of isolation remain in the Kr matrix. A dominant blue site to higher energy exhibiting characteristic Jahn-Teller threefold splitting features at 447.0, 451.4 and 456.1 nm and a weaker red site of isolation with features centred at 461.9 and 465.7 nm. The red site is almost four times less intense than the blue site.

The removal of a thermally unstable site by sample annealing can be monitored by recording the changes in site-specific emission features at particular temperatures. Figure III.6 shows the effect of annealing on the y^8P state resonance fluorescence produced with y^8P state excitation at 453.5 nm in a Kr matrix. Two emission features are observed centred at 468 and 472 nm due to Eu atoms isolated in the red (R) and thermally unstable (U) sites of isolation respectively as will be discussed Chapter IV.

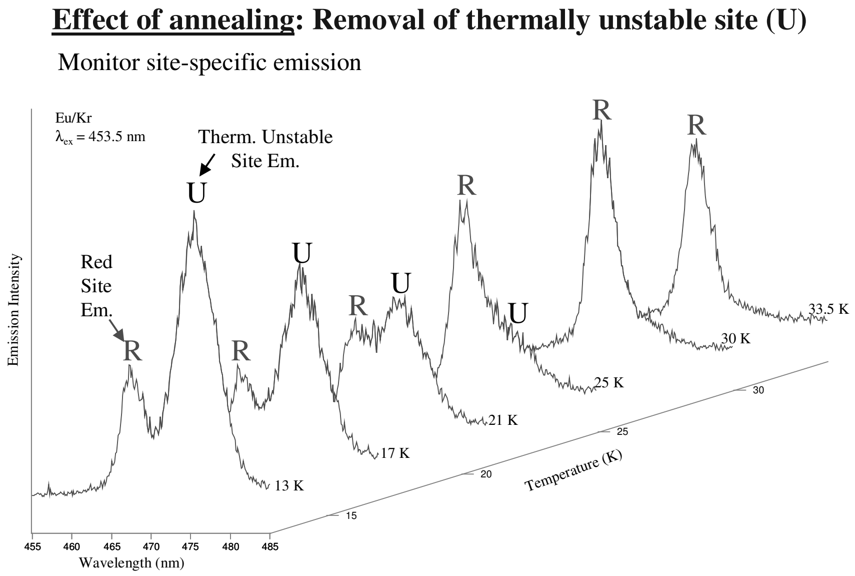

<u>Effect of annealing</u>: Removal of thermally unstable site (U)

Monitor site-specific emission

Figure III.6 Eu/Kr emission spectra, recorded during sample annealing, showing the increase in the red site emission feature at 468 nm (R) and a decrease of the thermally unstable site emission centred at 472 nm (U).

The first emission spectrum is recorded at 13 K in a freshly deposited sample and exhibits both R and U emission features. As the scan temperature is increased, the intensity of the thermally unstable feature, U, gradually decreases to zero while there is a corresponding increase in intensity of the red site emission feature, R. At 33.5 K only red site emission feature is observed and this is the case upon return to base temperature. This is in agreement with the change observed in the absorption spectrum following annealing i.e. the thermally unstable site absorption centred at 464 nm is completely removed.

III.2.III Eu/Xe

The UV/Vis absorption spectrum of matrix-isolated atomic Eu in solid Xe is presented in Figure III.7 with dashed vertical lines representing the gas phase energies of the labelled electronic transitions.

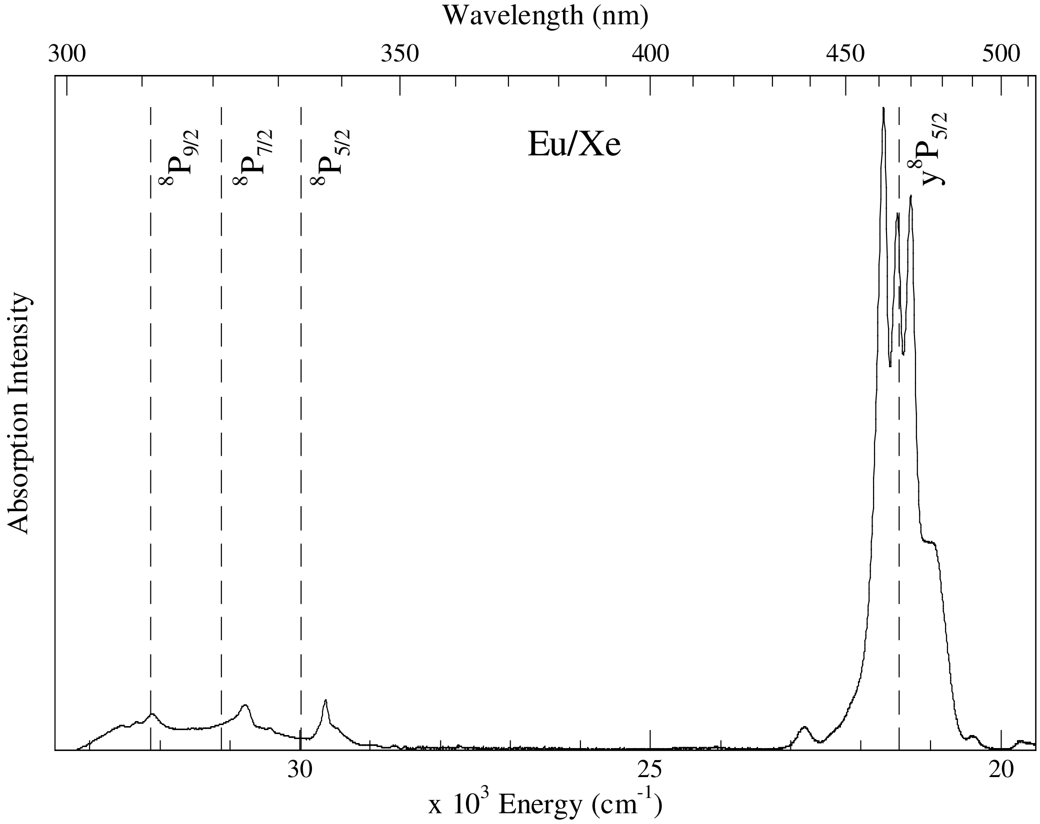

Figure III.7 Eu/Xe UV/Vis absorption spectrum recorded at 10 K following sample deposition at 10 K. Dashed vertical lines represent the gas phase positions of the labelled electronic states.

The absorption is dominated by the $y^8P \leftarrow a^8S_{7/2}$ transition centred at 468 nm. Also evident in the spectrum are the weaker UV absorptions centred at 308, 324 and 336 nm assigned and discussed by Jakob *et al.*[4,5,6] as absorptions from the $a^8S_{7/2}$ ground state into the spin-orbit levels of the ^8P_J and ^6P_J electronic states.

y^8P state absorption at 468 nm shows resolved features in freshly deposited samples. Three peaks at 461.2, 465.2 and 469.7 nm and a broad shoulder to lower energy, centred at 476.4 nm, can be seen in Figure III.8.

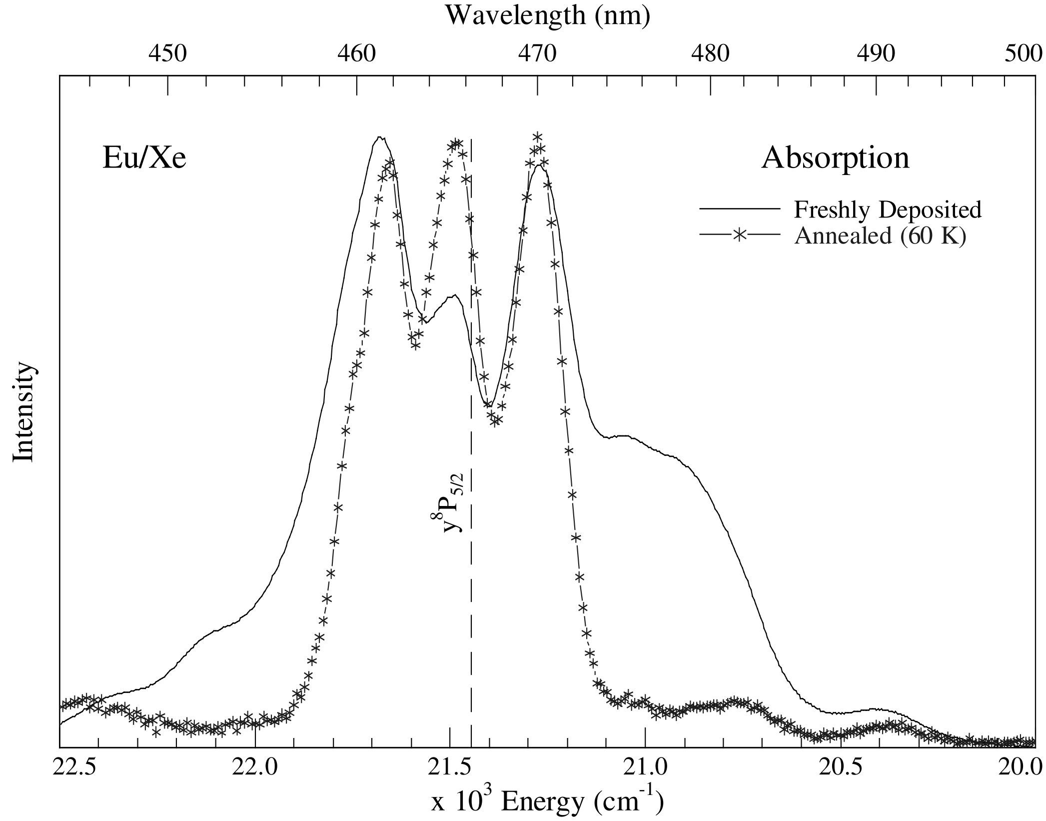

Figure III.8 Eu/Xe absorption spectra recorded at 10 K in the vicinity of the atomic Eu $y^8P_{5/2} \leftrightarrow a^8S_{7/2}$ transition. A comparison of the absorption recorded on deposition and following matrix annealing to 60 K is shown.

Annealing of the sample completely removes the red shoulder leaving three well resolved features at 461.2, 465.2 and 469.7 nm. This threefold splitting pattern of a P state absorption is characteristic of Jahn-Teller distortion and indicative of atomic Eu existing in a highly symmetric site within the lattice. The red shoulder centred at 476 nm, removed upon annealing, implies the existence of a thermally unstable site of isolation upon deposition.

III.2.IV Eu/RG Absorption Spectroscopy Summary

In summary, UV/Vis absorption spectra of atomic Eu isolated in the solid RG's shows two main features, 1) visible y^8P state absorption in the 450 nm spectral region and 2) UV ^8P_J, ^6P_J state absorptions into the individual spin-orbit levels. The previously unreported y^8P state absorption of matrix-isolated atomic Eu dominates the spectra, and is the focus of the current study.

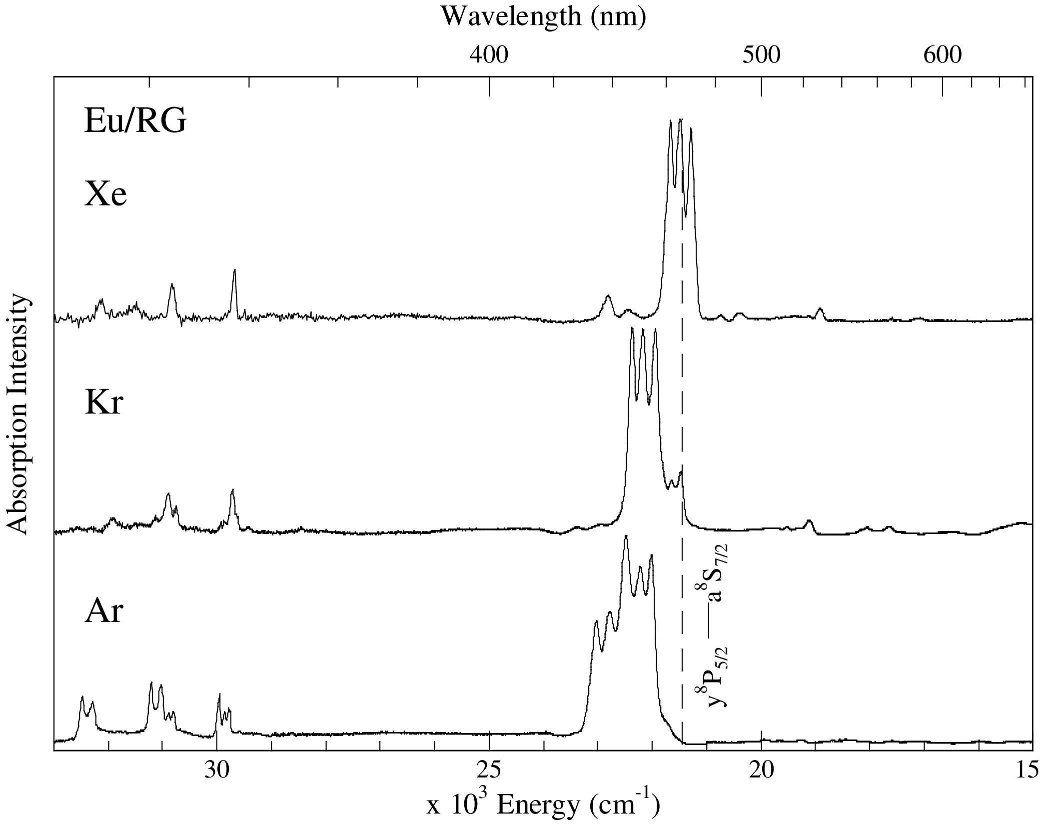

Figure III.9 Eu/RG UV/Vis absorption spectra recorded at 10 K following sample annealing. The gas phase position of the $y^8P_{5/2} \leftarrow a^8S_{7/2}$ transition is shown by the dashed vertical line[1].

Figure III.9 presents a summary of the UV/Vis absorption spectra of Eu atoms isolated in each of the RG matrices (RG = Ar, Kr and Xe) following sample annealing. It should be noted there is a progressive blue shift in absorption position of the y^8P state relative to the gas phase position as one changes from Xe to Kr to Ar, with Ar exhibiting the greatest shift from the gas phase.

Monitoring the visible y^8P state absorption feature before and after annealing suggested Eu atoms exist in multiple trapping sites in the RG lattices. In particular, it allowed identification of a thermally unstable site removed by sample annealing. It appears there exists two thermally stable sites of isolation in the Ar and Kr matrices and one single thermally stable site in solid Xe.

Table III.1 Spectral positions of the absorption features assigned to atomic europium isolated in solid RG's on deposition at 10 K. λ_{abs} indicates the position of the central threefold split component. The dominant/primary (1°) and secondary (2°) absorptions are labelled to reflect their relative absorption strengths. Features pertaining to the thermally unstable site removed by annealing are labelled U. The gas phase transition energies for the Eu atom are also presented. The gas phase – RG matrix shift is denoted by δ in wavenumber units.

Transition	Eu atom gas phase[1]		Eu/RG Absorption Features			
	λ (nm)	v (cm^{-1})	Host RG	λ_{Abs} (nm)	v (cm^{-1})	δ (cm^{-1})
$y^8P_{5/2} \leftrightarrow a^8S_{7/2}$	466.3	21444.58	Ar (2^0)	439.0	22779	+ 1334
			Ar (1^0)	450.1	22217	+ 773
			Ar (U)	459.5	21763	+ 318
			Kr (1^0)	451.4	22153	+ 709
			Kr (2^0)	465.7	21473	+ 29
			Kr (U)	464.0	21552	+ 107
			Xe (1^0)	465.2	21496	+ 52
			Xe (U)	476.4	20991	– 454

The spectral location of each sites' central Jahn-Teller component absorption feature relative to gas phase are listed in Table III.1. To further reinforce site assignments site-specific excitation spectra were recorded in the y^8P spectral region which allow deconvolution of congested absorption spectra and are presented in Section III.4.

III.3 Eu Dimer and Concentration Study

Before presenting excitation spectra and discussing in detail sites of isolation in the RG solids, evidence of europium aggregates is presented. The absorption spectra presented in the preceding section show good atomic isolation with little evidence of europium metal dimers or aggregates for matrix-isolated Eu/RG samples deposited at 10 K. This is not entirely surprising as Eu has an outer valence electron configuration of $4f^7 6s^2$, the half filled f-orbital and full s-orbital meaning any dimer formed will be a van der Waals type diatomic and thus of quite weak bond strength. This statement is supported by calculations by Cao *et al.*[7] who calculate a large bond length of 4.9 Å for Eu dimer using the CCSD(T) method.

Also, dimerisation is known to be less pronounced for heavier transition metals because heavier metals are more polarisable thus increasing the van der Waals type interaction with the matrix material and thereby tend to stabilise atoms rather than M_2 molecules. Europium is a significantly heavy metal (Atomic weight = 152 amu) thus this argument predicts matrix-isolated europium will not readily form any aggregates in the RG hosts. Both these factors predict low favourability of dimer formation. It is therefore not surprising that little or no dimer is observed in matrix-isolated samples of atomic Eu formed at 10 K.

To investigate the presence of perfectly isolated Eu atoms and the possible presence of Eu_2 dimer the following sections present concentration studies of matrix-isolated europium samples formed at 10 K. The appearance of new non-atomic absorption bands at increased metal loading allows one to assign these new spectral features to Eu aggregates. Concentration studies of samples formed during warm depositions were also pursued in an effort to favour dimer formation and hence aid identification of its absorption features. It is known that the deposition temperature strongly affects the yield of monomeric metal as compared to clusters. Only at very low temperatures is it possible to achieve high monomer yield; at higher temperatures self aggregation is severe even at very low concentrations[8].

The results are presented in the following sections. First the Ar system is discussed as it is the least polarisable host and will favour metal aggregation, giving the best conditions for observation of dimer absorption features. Following this, concentration studies in the Kr and Xe systems at low and high deposition temperatures are presented.

III.3.I Eu/Ar

The effects of increased metal loading on matrix-isolated samples formed at 10 K are presented in Figure III.10 for Eu in solid Ar. The dashed vertical line represents the gas-phase transition of the nearest atomic electronic state, namely the y^8P state.

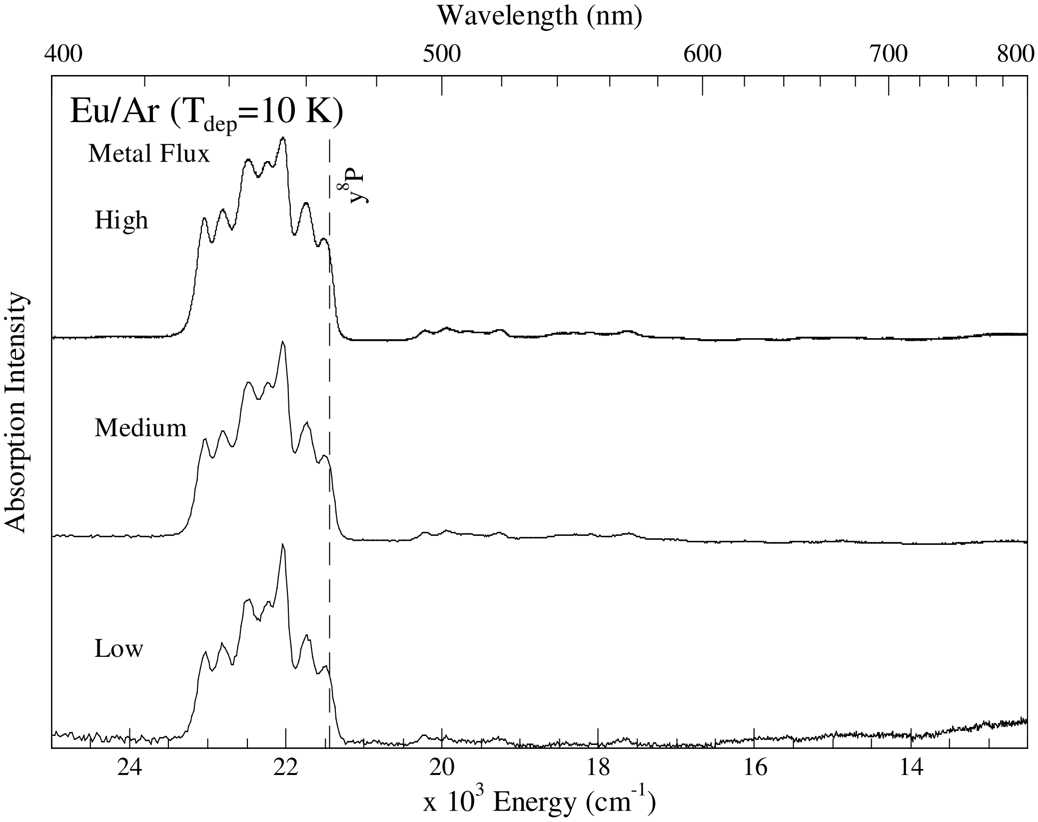

Figure III.10 Eu/Ar visible absorption spectra, normalised to the y^8P state absorption, recorded at 10 K following sample deposition at 10 K. The three spectra show the effects of increased metal flux, metal atom concentration.

The absorption spectra are normalised to the y^8P state absorption of atomic Eu centred at 454 nm. Even at high metal loading there is little evidence of any new non-atomic absorption features. There is no indication of dimer or aggregates being formed under these preparation conditions.

To promote cluster formation samples were prepared under the same metal loading conditions but deposited at a higher temperature of 16 K. The absorption spectra of europium in solid Ar formed at 16 K at various metal loadings are presented in Figure III.11. The gas phase positions of the y^8P and z^6P states observed in emission in Chapter IV are displayed as dashed vertical lines.

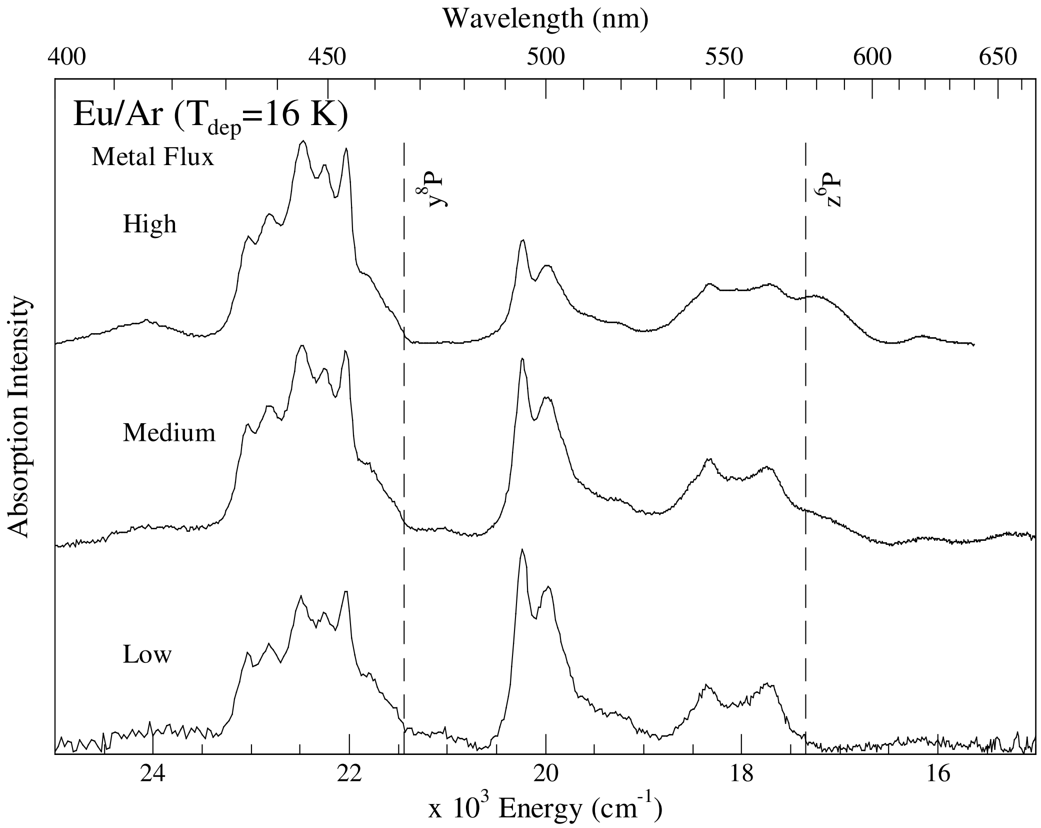

Figure III.11 Normalised Eu/Ar visible absorption spectra recorded at 10 K following sample deposition at 16 K. The three spectra shown indicate the changes in the relative intensities of the observed bands with increased metal flux, metal atom concentration. The noise on the lowest trace is due to weak absorption strength at low metal concentrations. The gas phase positions of the y^8P and z^6P states are shown as dashed vertical lines.

Two regions of the absorption spectrum show new features, a narrow doublet with peaks at 494.2 and 500.5 nm and a broader doublet with bands at 545.7 and 564.5 nm. These new non-atomic features must correspond to europium aggregates. The lowest trace represents a sample made with low metal loading. The doublet at 500 nm is the dominant feature of the spectrum. Use of these low metal fluxes implies it must correspond to the europium dimer.

At increasing metal concentrations the dimer band at 500 nm decreases relative to the atomic absorption while a shoulder at 580 nm becomes more prominent. This suggests that at higher concentrations, larger aggregates are being formed thus decreasing the dimer absorption at 500 nm and increasing the feature at 580 nm which must correspond to higher-order metal clusters i.e. $Eu_{x\ (x>2)}$.

A comparison of the absorption spectra in this region of samples formed with low metal flux at 10 and 16 K is presented in Figure III.12, normalised with respect to the y^8P state atomic absorption.

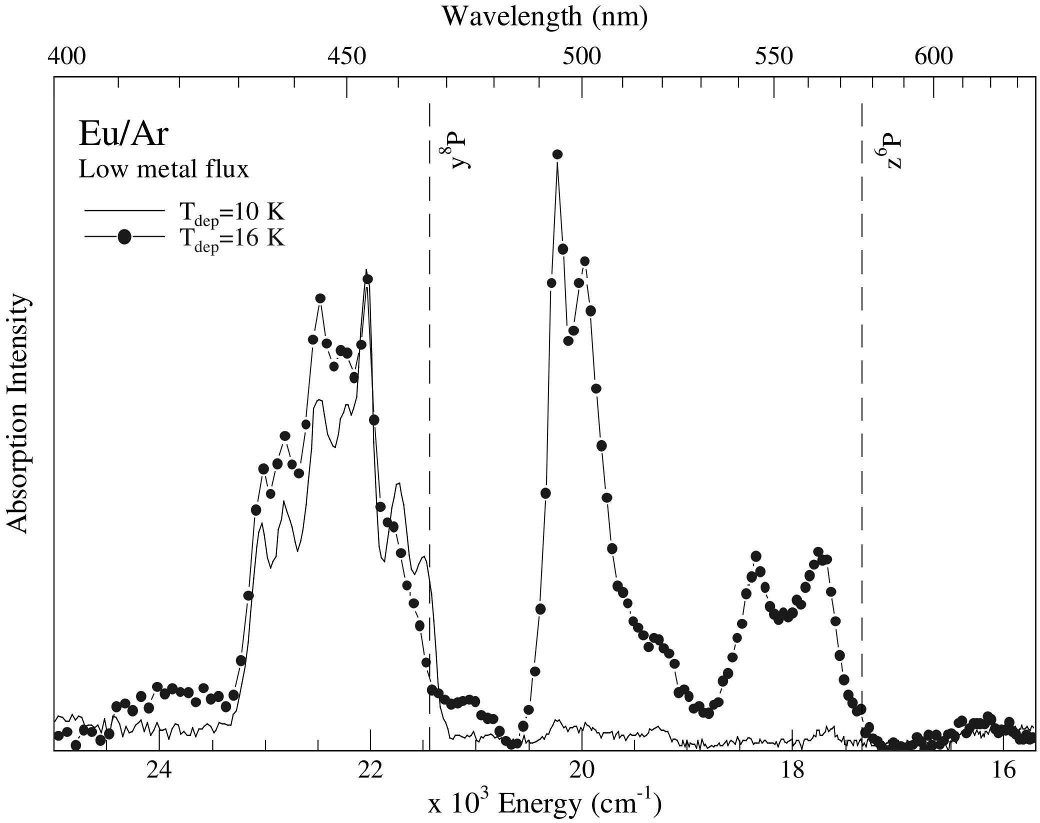

Figure III.12 Eu/Ar visible absorption spectra recorded at 10 K following sample deposition at 10 K (solid trace) and 16 K (dash and dot) with low metal fluxes. Spectra are presented normalised with respect to the y^8P state atomic absorption at 450 nm. The spectra indicate the changes in the relative intensities of the observed bands with increased deposition temperatures.

On close inspection one can see that the cluster features are much more significant in the sample formed at 16 K. It appears samples formed at 10 K exhibit some, but quite little, cluster concentrations. Aggregates are only observed when favourable conditions for cluster formation are deployed such as the higher deposition temperatures.

III.3.II Eu/Kr

Figure III.13 presents the normalised absorption spectra of atomic europium isolated in solid Kr in samples formed at 10 K with various metal concentrations. As was the case for the Ar system at these low deposition temperatures, there is little evidence of europium dimer formation.

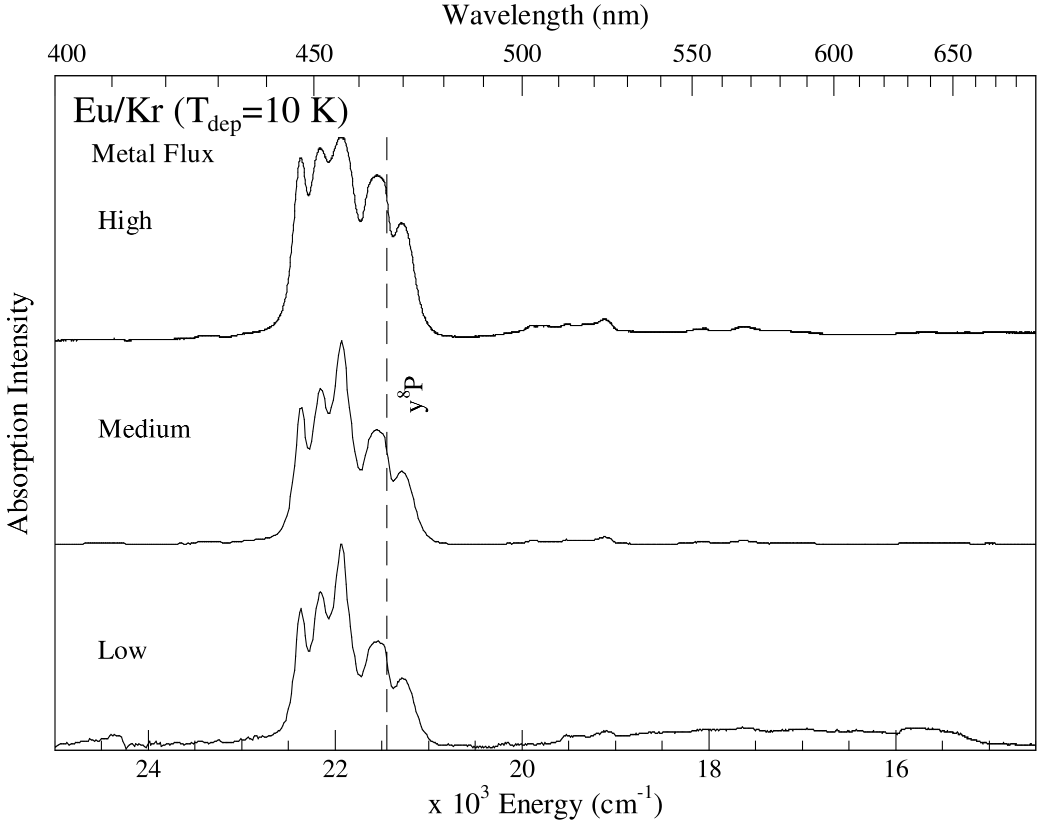

Figure III.13 Normalised Eu/Kr visible absorption spectra recorded at 10 K following sample deposition at 10 K. The three spectra show the effects of increased metal flux, metal atom concentration.

However, samples deposited at 22 K clearly exhibit new absorption features that are attributed to europium aggregates. Figure III.14 presents the absorption spectra of Kr matrices deposited at 22 K followed by cooling to 10 K at which temperature the presented spectra were recorded.

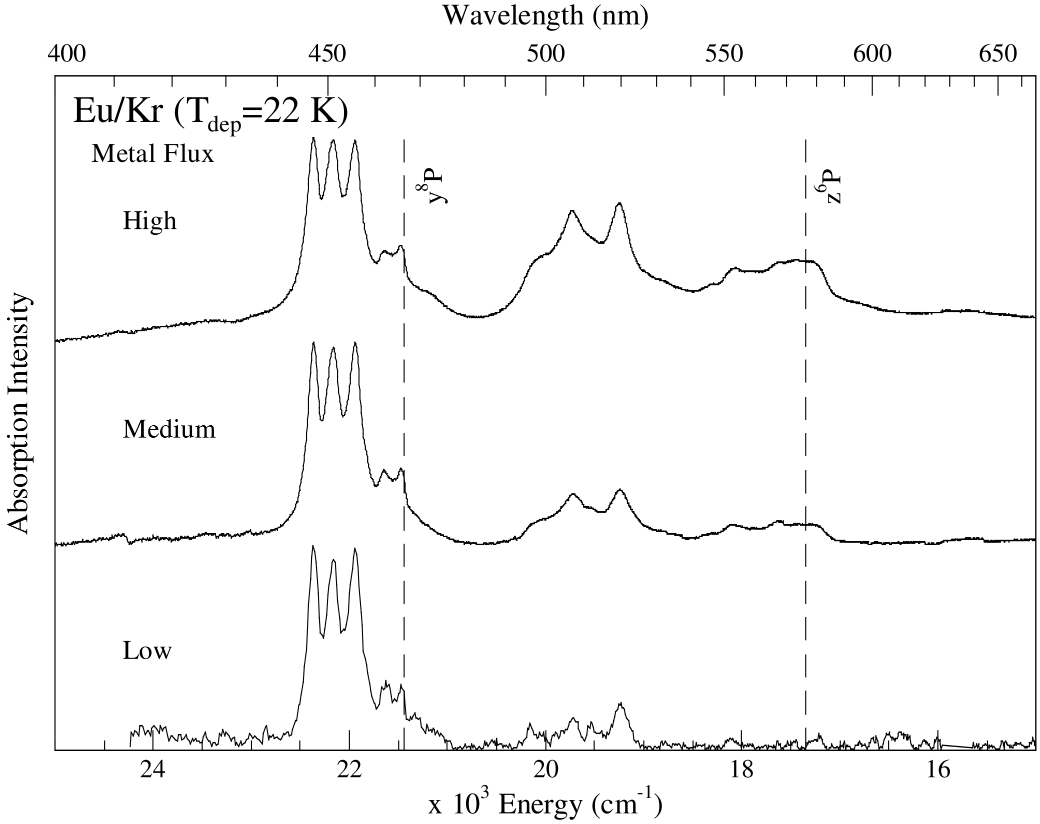

Figure III.14 Normalised Eu/Kr visible absorption spectra recorded at 10 K following sample deposition at 22 K. The three spectra shown indicate the changes in the relative intensities of the observed bands with increased metal flux, metal atom concentration. The noise on the lowest trace is due to weak absorption strength at low metal concentrations. The gas phase positions of the y^8P and z^6P states are shown as dashed vertical lines.

Under these warm deposition conditions new absorption features are observed in the 510 nm spectral region even at low metal loading (bottom trace). These features become more prominent at medium and high metal loading, their corresponding growth at increased metal fluxes is indicative of metal aggregates. Three features are identifiable in the 500 nm region at 498.8 (shoulder), 507.1 and 519.6 nm, and further absorption features are observed at 552.5, 567.0 and 579.6 nm at high metal loading.

As discussed for the Ar system, the non-atomic absorption features observed in samples formed with low metal loading are most likely due to europium dimer. Thus in this case the features in the 510 nm region are attributed to Eu_2, while the remaining features which increase at higher metal loading are indicative of higher aggregates i.e. $Eu_{x\ (x>2)}$.

III.3.III Eu/Xe

The absorption spectra of europium isolated in solid Xe with varying amounts of metal are presented in Figure III.15. In each case the spectrum is dominated by the y^8P state atomic absorption centred at 465.4 nm.

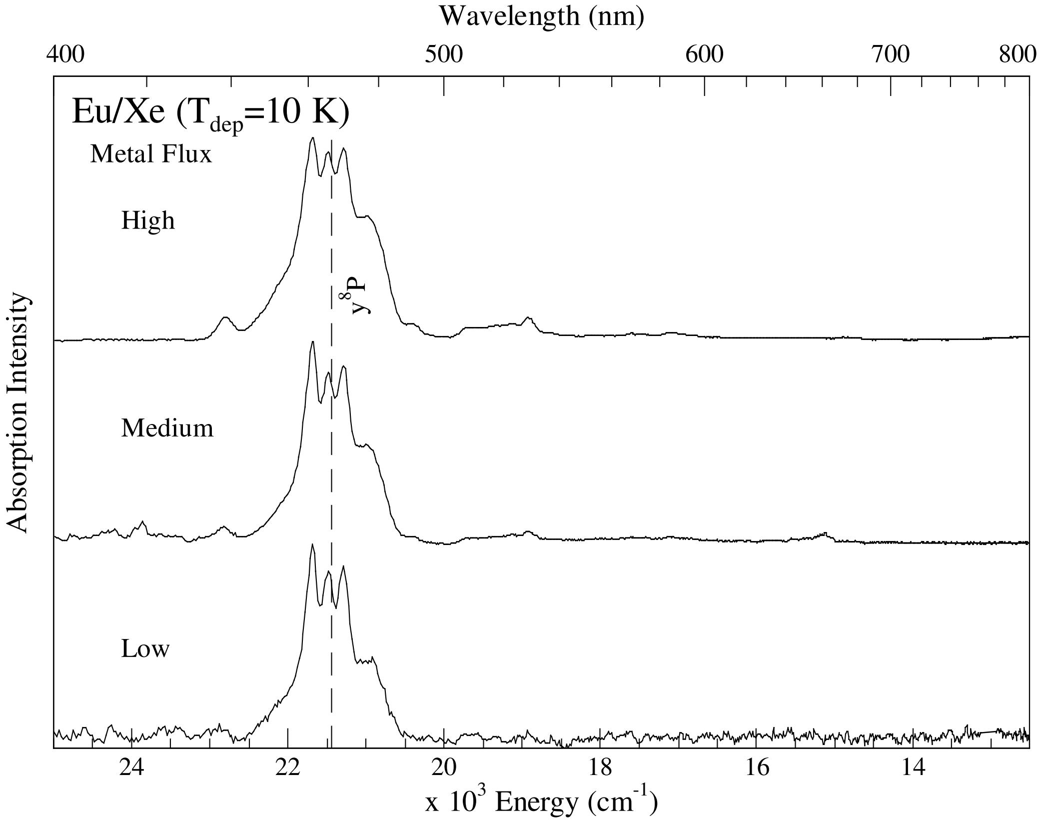

Figure III.15 Normalised Eu/Xe visible absorption spectra recorded at 10 K following sample deposition at 10 K. The three spectra show the effects of increased metal flux, metal atom concentration.

As was the case for Ar and Kr matrices, the concentration study of samples deposited at 10 K in solid Xe shows little evidence of europium dimer formed upon deposition.

The absorption spectra of samples deposited at 25 K in solid Xe are presented in Figure III.16. A broad absorption feature centred at 513 nm is observed to increase relative to the y^8P atomic absorption with increased metal loading. This effect is characteristic of a Eu dimer component band. No other new non-atomic absorption features are identified implying no higher aggregates of $Eu_{x\ (x>2)}$ are formed in the Xe matrix under these conditions. This is reasonable considering Xe is the most polarisable of the three RG hosts. Xe will have the greatest attractive interaction with the guest species and hence the greatest Eu-RG binding energy. When a guest atom arrives at the growing Xe sample during deposition it is bound to the lattice to a much greater extent than in the Ar and Kr hosts. This allows less diffusion towards another metal atom in solid Xe, thus stabilising atoms more so than forming M_x molecules.

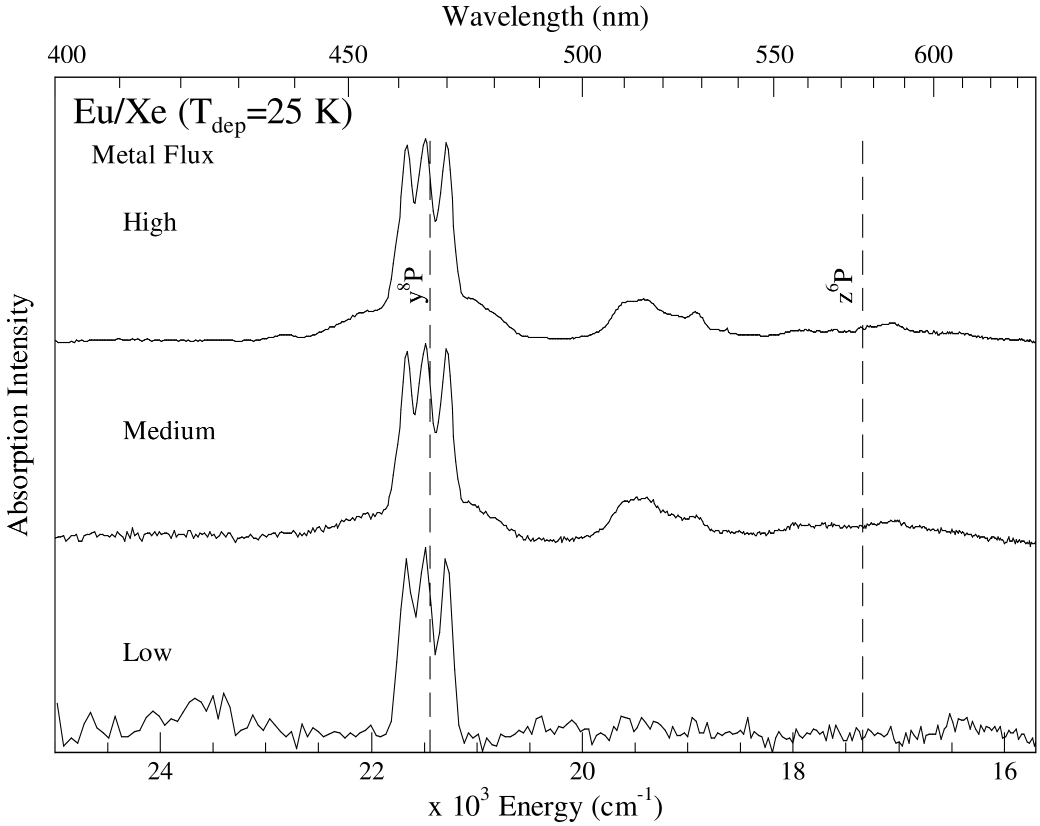

Figure III.16 Normalised Eu/Xe visible absorption spectra recorded at 10 K following sample deposition at 25 K. The three spectra shown indicate the changes in the relative intensities of the observed bands with increased metal flux, metal atom concentration. The noise on the lowest trace is due to weak absorption strength at low metal concentrations. The gas phase positions of the y^8P and z^6P states are shown as dashed vertical lines.

III.3.IV Eu/RG Dimer formation Summary

Presented in Figure III.17 is a comparison of the absorption spectra recorded in the three RG's (RG = Ar, Kr and Xe) formed with high metal loading and warm deposition. These conditions promote dimer and aggregate formation.

Clearly identifiable is the $y^8P \leftarrow a^8S$ electronic transition of atomic europium in the 450 nm spectral region, the gas phase position of which is marked by the dashed vertical line. Also, shown here for comparison is the gas phase position of the

z^6P state which is observed in emission in Chapter IV. Additional non-atomic absorption features present in the 495 to 520 nm and 540 to 580 nm spectral regions were assigned in the preceding sections as being due to matrix-isolated europium dimers and aggregates. A summary of the spectral locations of these features is presented in Table III.2. In each case europium dimer is observed to absorb in the 495 to 520 nm region while higher aggregates are identified at longer wavelengths centred in the 540 to 580 nm spectral range.

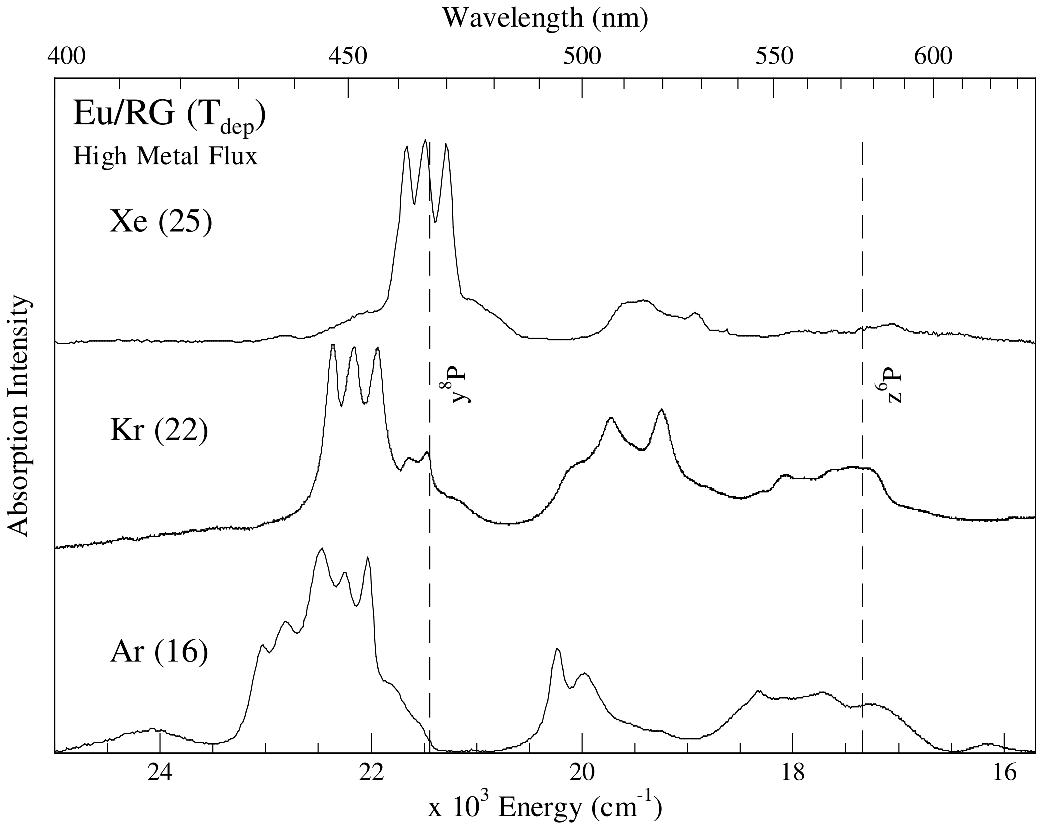

Figure III.17 Eu/RG visible absorption spectra recorded at 10 K following high temperature sample depositions with high metal fluxes. The gas phase position of the $y^8P_{5/2}$, $z^6P_{7/2} \leftarrow {}^8S_{7/2}$ transitions are shown by the dashed vertical lines.

A curious observation is that the relative abundance of dimer with respect to atom goes down with respect to increased Eu concentration in Ar, yet in Kr the reverse is seen. This can be rationalised based on kinetics of stepwise addition of atoms. It suggests that the dimer formation is slow. This is to be expected given that it is forming a weak van der Waals bond. Once the dimer is formed however, addition of further atoms to form Eu clusters occurs rapidly.

1) $Eu + Eu \rightarrow Eu_2$ *slow*

2) $Eu_2 \rightarrow Eu_3$ *fast*

Ar being the least rigid matrix readily forms dimers as seen by their large concentration in samples with low amounts of metal. The slow dimer formation step is readily overcome in Ar. The second, higher cluster forming, step leads to the observed decrease of relative abundance of dimer at higher metal concentrations as the dimer is rapidly used to form larger aggregates. Conversely, in Kr the dimer formation step is slower due to the increased rigidity of the host. The second, higher cluster forming, step is thereby inhibited in this host which is evidenced by the much lower concentrations of larger metal aggregates in the Kr solid.

Table III.2 The spectral location of europium dimer and higher aggregate's visible absorption features (λ_{Abs}) in nanometre units for each of the three RG's (RG = Ar, Kr and Xe).

	Eu/RG, λ_{Abs} (nm)		
Assignment	Ar	Kr	Xe
Eu_2	494.2 500.5	498.8 507.1 519.6	513 (broad)
$Eu_{x\ (x>2)}$	545.7	552.5	
	564.5	567	
	580.5	579.9	

Europium is surprising as previous metal systems studied by the Maynooth group (Ca [Ar]4s^2, Mn [Ar]4s^{2}3d^5) readily form van der Waals metal dimers even with low temperature deposition conditions[9]. However, europium proved to self-aggregate to a much lesser extent in the matrix. This may be due to the larger mass of this guest which is three times heavier than any metal previously studied. The increased mass means atoms have less momentum upon arrival at the growing sample limiting their movement towards another europium atom and decreasing the probability of dimer formation.

Since the absorption features observed at 450 nm in the RG matrices can be definitively attributed to atomic absorption features, namely the y^8P state, excitation spectra recorded in this region will now be presented to allow deconvolution of congested y^8P state absorption spectra and identification of multiple metal atom trapping sites in the solid RG's.

III.4 Eu(y^8P)/RG Excitation Spectroscopy

The absorption spectra of matrix-isolated atomic Eu suggest the presence of two thermally stable sites of isolation in Ar and Kr matrices. In this section the excitation spectra recorded by monitoring the atomic emission features produced with excitation of the $y^8P \leftarrow a^8S$ transition in all Eu/RG systems are presented. Monitoring site-specific emission features allows particular absorption features to be attributed to distinct metal atom trapping sites within the RG matrices.

III.4.I Eu/Ar

Excitation spectra recorded in the y^8P spectral region monitoring site-specific emission features in an annealed argon matrix are presented in Figure III.18. Overlapped also in Figure III.18 is the absorption spectrum recorded in this region.

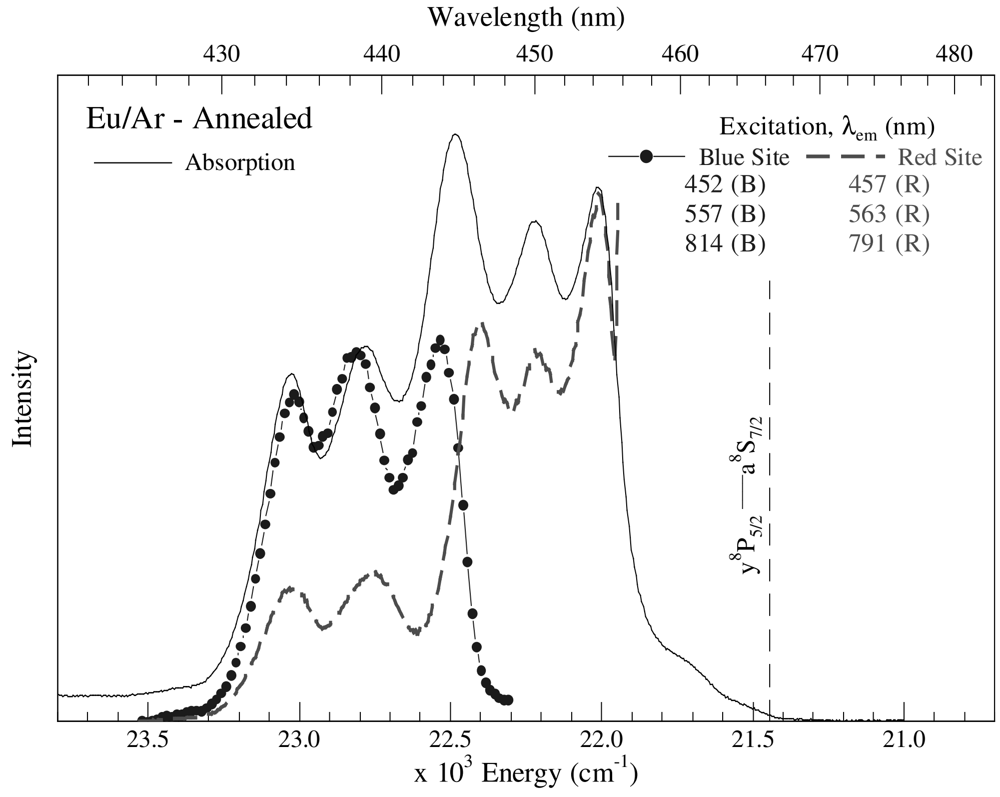

Figure III.18 Site-Specific excitation spectra recorded in the region of the $y^8P_{5/2} \leftrightarrow a^8S_{7/2}$ transition at 10 K in an annealed Eu/Ar sample. The absorption spectrum in this region is overlaid for comparison (solid trace). Two sites of isolation are identified, a higher energy blue site centred at 438.4 nm (dash-and-dot) and a lower energy red site located at 450.1 nm (dashed trace).

The excitation spectra show two clearly identifiable sites of isolation in the Ar matrix. A higher energy 'blue site' shown as a dashed-and-dotted line and a lower energy 'red site' displayed as a dashed trace. The excitation spectra of atoms in the two sites accounts fully for all features present in the absorption spectrum. Each site consists of a threefold Jahn-Teller splitting pattern indicative of Eu atoms isolated in a site of high symmetry. The spectral characteristics of the excitation features of each site are listed in Table III.3.

Table III.3 Photophysical characteristics of the sites of isolation (red and blue) of Eu/RG revealed in the excitation spectra of the y^8P ($4f^7 6s^1 6p^1$) ↔ $a^8S_{7/2}$ ($4f^7 6s^2$) transition of atomic europium. The dominant/primary (1^o) and secondary (2^o) sites are labelled to reflect their relative absorption strengths. The spectral position, v, and average linewidth (fwhm) of the three excitation components, Δ_{AV}, are quoted in wavenumber units. Gas phase to matrix frequency shifts are presented for the atomic Eu $y^8P_{5/2} \leftarrow a^8S_{7/2}$ transition[1] (G.P.: 21445 cm^{-1}) as δ in wavenumber units. (* represents Δ_{AV} was calculated using only two JT components as the third one was not fully resolved).

Eu(y^8P)/RG Excitation Features

Eu/RG Site	Component	λ (nm)	v (cm^{-1})	Δ_{AV} (cm^{-1})	δ (cm^{-1})
Argon	1	446.4	22400		955
Red (1^0)	2	450.1	22219	168*	774
	3	454.4	22008		564
	1	434.0	23044		1600
Blue (2^0)	2	438.4	22808	200	1364
	3	443.6	22542		1098
Krypton	1	446.6	22392		948
Blue (1^0)	2	450.9	22180	208	735
	3	455.5	21957		513
	1	458.5	21809		364
Red (2^0)	2	462.0	21644	88*	200
	3	466.1	21455		10
Xenon	1	461.5	21669		225
(1^0)	2	465.2	21496	137	51
	3	469.6	21296		–149

The three excitation components of the blue site exhibit an average width (fwhm) of 200 cm^{-1} and a blue matrix shift from the gas phase value of the $y^8P_{5/2} \leftarrow a^8S_{7/2}$ atomic transition of 1364 cm^{-1} from the central Jahn-Teller component. Red site excitation features yield a slightly smaller average width of 168 cm^{-1} and smaller matrix shift of 774 cm^{-1} to higher energy, the details of which are listed in Table III.3.

III.4.II Eu/Kr

Site-selective excitation spectra of atomic europium isolated in the Kr matrix recorded in the vicinity of the $y^8P \leftarrow a^8S$ transition allow identification of two distinct metal atom trapping sites in solid Kr.

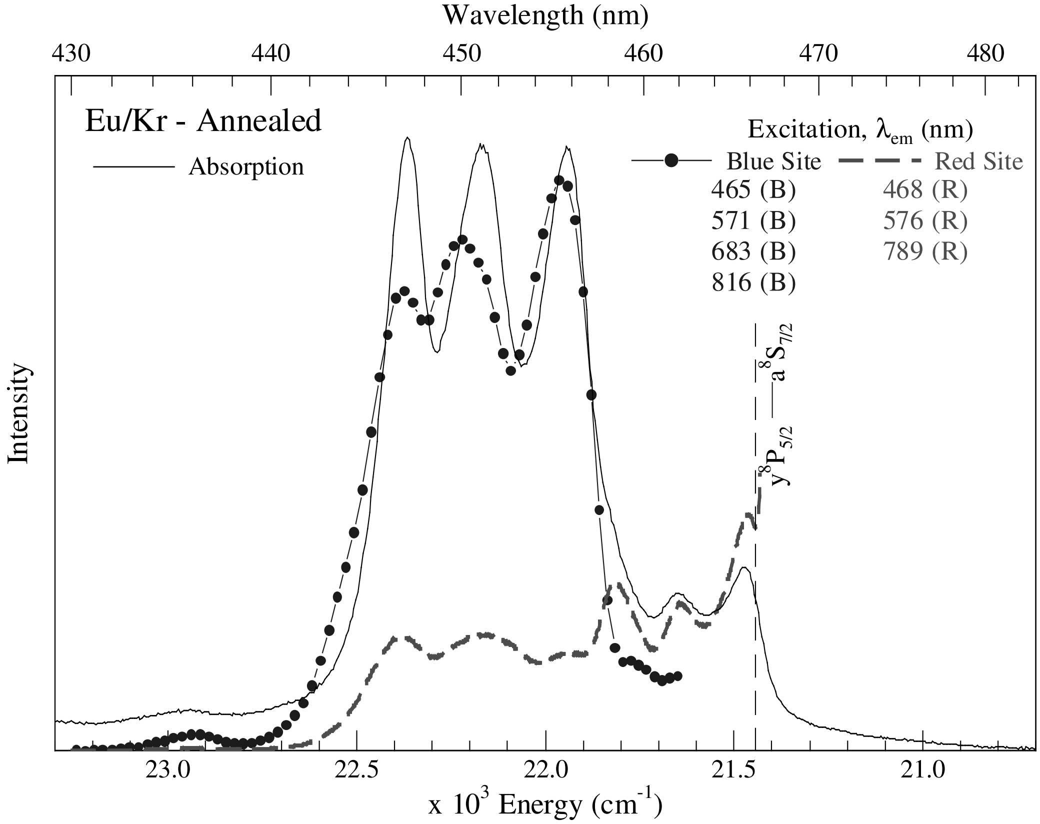

Figure III.19 Site-Specific excitation spectra recorded in the region of the $y^8P_{5/2} \leftrightarrow a^8S_{7/2}$ transition at 10 K in an annealed Eu/Kr sample. The absorption spectrum in this region is overlaid for comparison (solid trace). Two sites of isolation are identified, a higher energy blue site centred at 450.9 nm (dash-and-dot) and a lower energy red site located at 462 nm (dashed trace).

Figure III.19 presents the excitation spectra overlapped with the absorption spectrum recorded in this region. Three main absorption peaks at 447, 451 and 455 nm corresponding to one particular site are identified and the shoulder absorbing to lower energy is due to existence of a weaker red site in the Kr matrix also exhibiting threefold splitting in the excitation spectrum with features at 459, 462 and 466 nm. The characteristics of the three components in each excitation spectrum are collated in Table III.3.

The blue site excitation components in solid Kr display an average width of 208 cm^{-1} and matrix shift of 735 cm^{-1} to the gas phase value of the $y^8P_{5/2} \leftarrow a^8S_{7/2}$ electronic transition. Europium atoms isolated in the red site in the Kr matrix exhibit a smaller component width of 88 cm^{-1} and a shift of only 200 cm^{-1} to higher energy from the gas phase atomic transition position.

III.4.III Eu/Xe

Excitation spectra in the RG's are recorded by monitoring change in emission intensity at a particular wavelength while scanning through a range of excitation wavelengths. One can present an excitation spectrum as a three-dimensional plot of excitation wavelength versus emission wavelength versus intensity (z-axis) as exampled in Figure III.20 for a sample of matrix-isolated europium in xenon. By taking a two-dimensional slice at a particular emission wavelength an excitation spectrum is produced. In this example, a two-dimensional slice is taken at emission wavelengths 590 and 823 nm. This yields plots of emission intensity versus excitation wavelength i.e. an excitation spectrum in the y^8P spectral region.

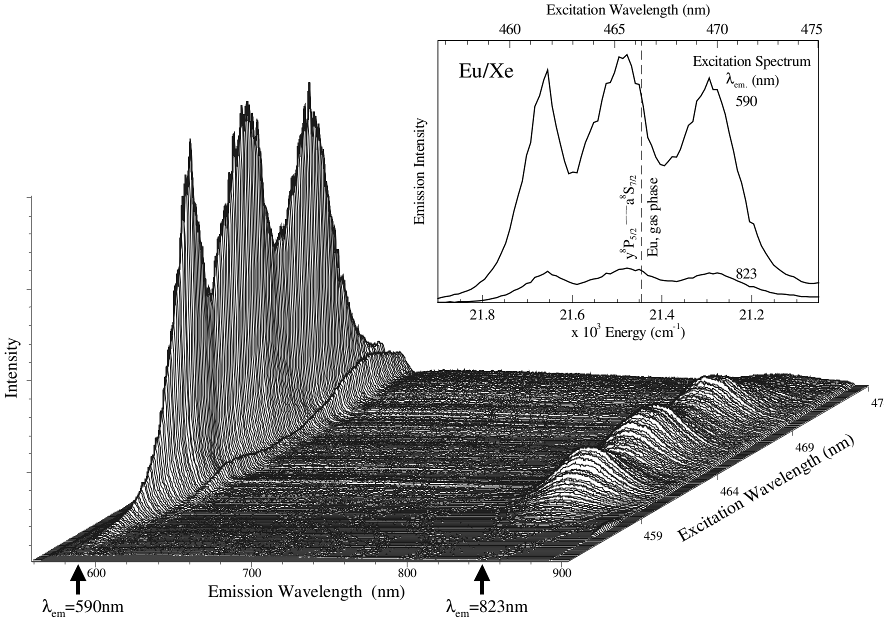

Figure III.20 Three-dimensional plot of excitation wavelength versus emission wavelength versus intensity (z-axis). A two-dimensional slice taken at emission wavelengths 590 and 823 nm is shown in inset yielding a plot of emission intensity versus excitation wavelength i.e. an excitation spectrum in the y^8P spectral region.

The absorption spectrum of Eu/Xe is much simpler than that of Ar or Kr, consisting of three resolved absorption features at 462, 466 and 470 nm in the y^8P spectral region. Excitation spectra recorded in this region in solid Xe are consistent with this. Figure III.21 presents an overlap of the excitation and absorption spectra in this region recorded in an annealed Xe sample. The absorption spectrum is completely accounted for, confirming there exists only one thermally stable site of isolation in the Xe matrix.

Eu/Xe y^8P state excitation components comprise of an average linewidth (fwhm) of 137 cm^{-1} and exhibit a blue matrix shift of 51 cm^{-1} from the gas phase $y^8P_{5/2} \leftarrow a^8S_{7/2}$ atomic transition to the central Jahn-Teller component, the details of which are listed in Table III.3.

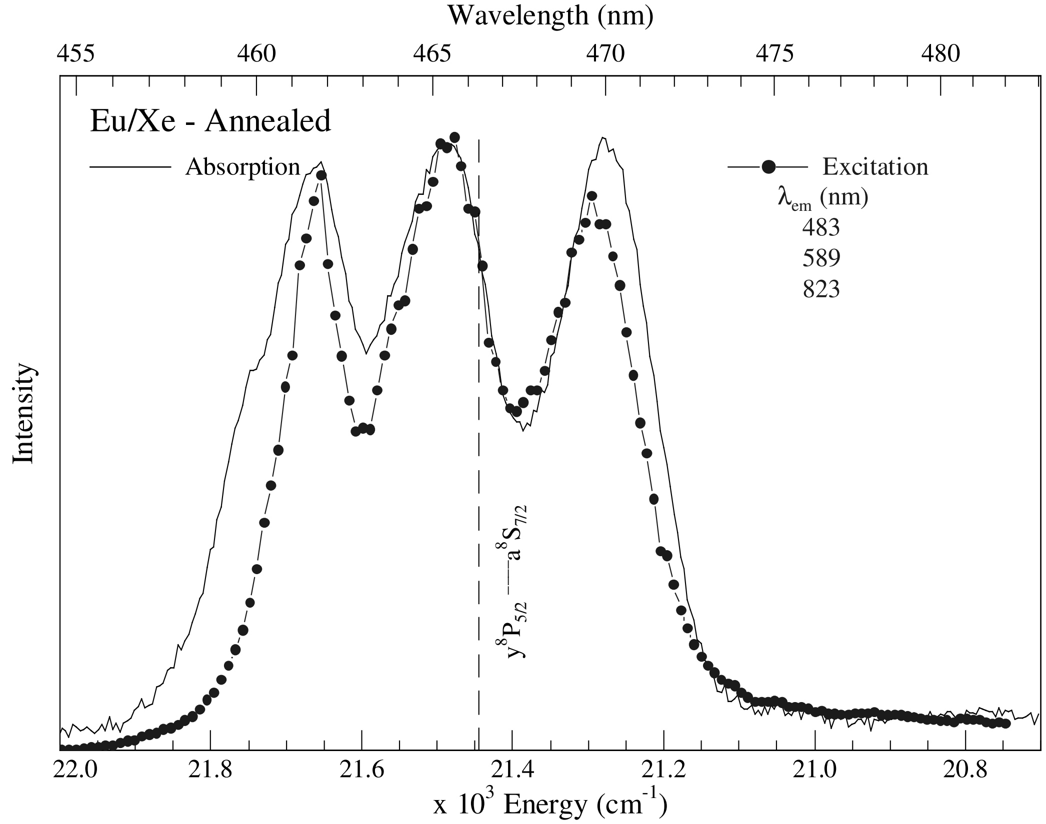

Figure III.21 Excitation spectrum (dash-and-dot) recorded in the region of the $y^8P_{5/2} \leftrightarrow a^8S_{7/2}$ transition at 10 K in an annealed Eu/Xe sample. The absorption spectrum in this region is overlaid for comparison (solid trace). One site of isolation is identified centred at 465.2 nm.

III.4.IV Eu/RG Excitation Summary

In summary, excitation spectra allow resolution of distinct sites of isolation for atomic Eu isolated in the three RG's which are congested in absorption spectra. The excitation spectra reveal the presence of threefold split patterns for each of the sites identified in the RG solids attributed to the Jahn-Teller effect which is indicative of Eu atoms occupying highly symmetric matrix environments. There exists two thermally stable sites in Ar matrices labelled the blue and red sites centred at 438.4 nm and 450.1 nm respectively. Two thermally stable sites in Kr are centred at 450.9 nm and 462 nm. One single thermally stable site of isolation is identified in Xe centred at 465.2 nm.

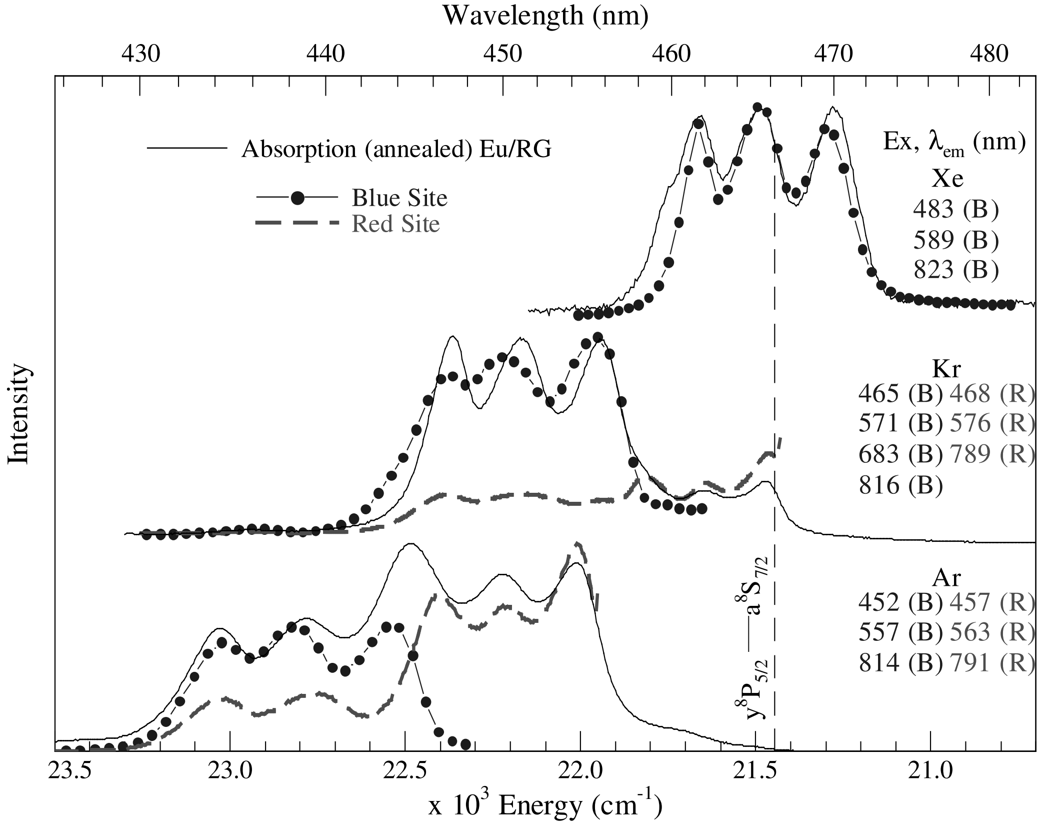

Figure III.22 Eu/RG absorption and site-specific excitation spectra in the region of the $y^8P_{5/2} \leftarrow {}^8S_{7/2}$ transition recorded at 10 K following sample annealing.

Figure III.22 presents a summary of the absorption and excitation spectra recorded in the y^8P spectral region in the solid RG's. Excitation spectroscopy allows clear identification of two distinct metal trapping sites in the Ar and Kr matrices. Absorption spectra are completely explained by the existence of these two sites suggesting no other site of isolation of atomic Eu exists in these annealed RG matrices. On the other hand, in the Xe matrix there exists one thermally stable site of isolation of atomic Eu.

A summary of the excitation features of the y^8P state atomic europium isolated in the solid RG's is available in Table III.3. Inspection of Table III.3 and Figure III.22 reveals there is little shift between the spectral location of the red site in Ar and the blue site in Kr. A progressive blue shift to higher energy is observed for a particular site type as one moves to a less polarisable RG host i.e. from Xe to Kr to Ar.

III.5 Polarisability study – site assignments

Laursen and Cartland[3] showed for group 12 metal atoms (Hg, Cd and Zn) the matrix shift from the gas phase atomic position for P ← S transitions is approximately linear when plotted against the polarisability of the RG's. This was also proved to be the case for matrix-isolated Mn by Collier and McCaffrey[2]. A plot of RG polarisability versus shift from gas phase allowed association of certain site types occupied by metal atoms in the rare gas solids. For metal atoms 'trapped' in a particular site type, a linear dependence of the matrix shifts versus rare gas polarisability is expected.

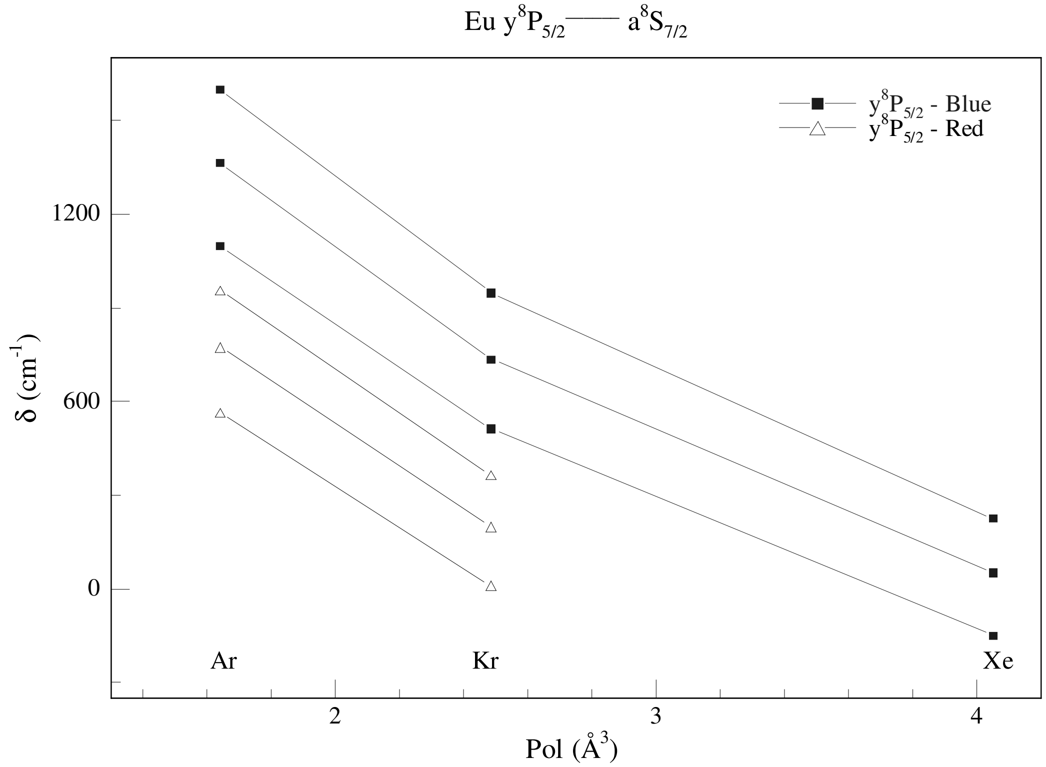

Figure III.23 A plot of the gas phase to Eu/RG matrix frequency shifts (δ cm^{-1}) observed for each of the Jahn-Teller components of the blue and red sites identified for the $y^8P_{5/2} \leftarrow a^8S_{7/2}$ transition of atomic europium versus the RG host polarisabilities. The filled squares (connected by the solid line) highlights the linear correlation between the frequency shifts and rare gas polarisability observed for the Eu $y^8P_{5/2} \leftarrow a^8S_{7/2}$ transition occurring within the blue sites of isolation.

In the case of atomic Eu isolated in the RG's a plot of matrix shift from the gas phase $y^8P_{5/2} \leftarrow a^8S_{7/2}$ transition is plotted against the RG polarisability for both the blue and red sites and is displayed in Figure III.23. In this plot the gas phase to matrix frequency shift is calculated from each of the threefold components of both of the thermally stable red and blue sites. It is clear an approximately linear correlation exists between the single thermally stable site of isolation in Xe and the blue sites in Ar and Kr. This suggests atomic Eu is trapped in the same site type in the blue site in Ar and Kr and the sole site in Xe.

To the best of our knowledge no Eu-RG diatomic bond length data is available either experimentally or from *ab initio* calculations so attempts were made to calculate an estimate of the Eu-RG diatomic bond length. Sodium was chosen as a comparative system as it has distinctly similar physical characteristics to atomic Eu. Both have polarisability and ionisation potentials of the same order of magnitude as shown in Table III.4. Furthermore both Na and Eu have spherical ground electronic states, ^2S and a^8S respectively, so they will show preference for spherical sites of isolation in the solid RG's.

In order to estimate the magnitude of the Eu-RG van der Waals diatomic bond length the Luiti-Pirani (LP) technique was employed. It is a modification of the London-Drude model (Equation III.1). Relying only on the ionisation potential (I) and polarisability (α), it is used specifically to predict intermolecular forces of van der Waals diatomics yielding expressions for bond length (R_e) and dissociation energies (D_e)[10].

$$U_{disp} = -\frac{3}{2}\left(\frac{I_1 I_2}{I_1 + I_2}\right)\frac{\alpha_1 \alpha_2}{R^6} \qquad \textit{Equation. III.1}$$

The Na-RG diatomic bond lengths are well known from very accurate, high-resolution experiments by Zimmermann *et al.*[11,12,13] and are listed in Table III.4. When compared to results for Na-RG calculated with the LP method there is good agreement. Differences in the range of 1 to 4 % are observed, confirming the LP method will calculate a diatomic bond length of correct order of magnitude for a S state metal atom-RG van der Waals 'bond'. The Eu-RG diatomic bond lengths were then computed by the LP technique, the results of which are presented in Table III.4.

The LP predicted Eu-RG bond lengths are of the same order of magnitude as Na-RG, approximately 0.1 Å longer than the sodium diatomics in all cases. It is thus suggested Eu will exhibit similar trapping site preferences as atomic Na in the RG matrices i.e. Eu atoms will exist in the same site of isolation as Na in the RG host lattices.

Table III.4 Leftmost section contains a comparison of the ground states (G.S.) of atomic Na and Eu with their polarisability (α) and ionisation potentials (I.P.). The central section displays the Na-RG diatomic bond lengths calculated using the Luiti-Pirani (LP) technique versus the experimental (exp) Na-RG distances in Angstrom (Å) and the percentage difference between both. The rightmost column presents the Eu-RG diatomic bond lengths calculated with the LP technique.

	G.S.	α[14] (Å^3)	I.P.[14] (eV)	Na-RG	R_e (Å) exp	R_e (Å) LP	%	Eu-RG	R_e (Å) LP
Na	$^2S_{1/2}$	24.1	5.14	Ar	5.01	5.07	1.2	Ar	5.17
Eu	$^8S_{7/2}$	27.7	5.67	Kr	4.92	5.08	3.3	Kr	5.18
				Xe	4.95	5.13	3.6	Xe	5.21

Recent experimental and molecular dynamic simulations[15] attribute the red and blue sites of atomic Na in Ar and Kr matrices observed upon deposition as hexa-vacancy (hv) and tetra-vacancy (tv) sites respectively. Sodium shows a preference for the hv in solid Ar thus the dominant site of isolation of atomic Eu in Ar may be expected to be a hv site also. The red site in Eu/Ar is thus attributed to hv occupancy. Sodium displays a slight preference for the tv site (56 %) in solid Kr, allowing the dominant blue site of isolation of Eu in the Kr lattice to be attributed to a tv. The polarisability model of Eu/RG allowed association of the blue sites of isolation in the RG's as the same site type so these sites in the three RG's are attributed to tetra-vacancies, whilst the red sites present in Ar and Kr are hexa-vacancies. The sizes of the available spherical vacancies in the *fcc* RG lattices along with the LP predicted Eu-RG diatomic bond lengths are listed in Table III.5 for comparison purposes.

Table III.5 Site sizes in Angstrom units (Å) for specific spherically symmetric site types in the solid rare gases. Also shown is the lattice parameter, *a*, of each *fcc* solid. The details of these sites were presented in Chapter I. In addition, the LP calculated Eu($^8S_{7/2}$)-RG diatomic ground state bond lengths are presented.

RG	*a* (Å)[16]	I_{oh} (Å)	sv (Å)	tv (Å)	hv (Å)	Eu-RG (Å)
Ar	5.31	2.655	3.755	4.403	4.598	5.17
Kr	5.64	2.822	3.988	4.676	4.884	5.18
Xe	6.13	3.065	4.330	5.083	5.308	5.21

In summary, two thermally stable sites of atomic Eu are identified in the solid RG's by monitoring site-specific excitation spectra in the region of the y^8P electronic state. The blue site observed in the three RG's is attributed to atomic Eu occupying a tetra-vacancy site whilst the red site present in Ar and Kr is a larger hexa-vacancy. Europium atoms exist in both sites in solid Ar and Kr exhibiting a slight preference for the hv site in the Ar lattice while tv occupancy dominates considerably in the Kr matrix.

III.6 UV Absorption Features

At this point with knowledge of the sites of isolation of atomic Eu in the RG's and the ability to perform site-specific excitation spectra it is worth briefly re-visiting the UV absorption features. These were investigated in the 1970's by Jakob *et al.*[4,5,6] in samples formed at 4 K and annealed to 0.3 of the hosts' melting point. The absorption spectra were recorded at a resolution of 10 cm^{-1} and revealed quite complex and structured absorption features of the ^{6}P, ^{8}P ← a^8S transitions.

Figure III.24 presents UV absorption spectra recorded in the present study of annealed Eu/RG samples. There are five known spin-orbit levels in this region in the gas phase, ^8P_J (J = 5/2, 7/2, 9/2) and ^6P_J (J = 5/2 and 7/2). Their locations are identified in Figure III.24 with dashed vertical lines. It is not possible to achieve as high a resolution of these features with the current experimental set-up, but broadly speaking the spectral features are consistent with the results of Jakob *et al.* as seen for Eu/Ar in Figure III.26. In particular, in the $^8P_{5/2}$ region of Eu/Ar three absorption peaks observed at 333.8, 334.9 and 335.8 nm in this study correspond to the three more resolved absorption bands observed in the previous work[4,5,6].

Steady-state excitation spectra recorded in the current study monitoring the intense y^8P state visible fluorescence (~ 450 nm) in the region of these ^{6}P and ^{8}P states (300 to 330 nm) in annealed samples allowed site-specific features to be identified and are presented in Figure III.25. Clearly the assignments of Jakob *et al.* of these spectral features originating from absorption into the individual J-levels of the ^6P_J and ^8P_J states is correct. However this data can now be extended to attribute individual features to atomic Eu occupying a particular site of isolation, namely the red hv or blue tv sites, both of which are of *cubic* symmetry.

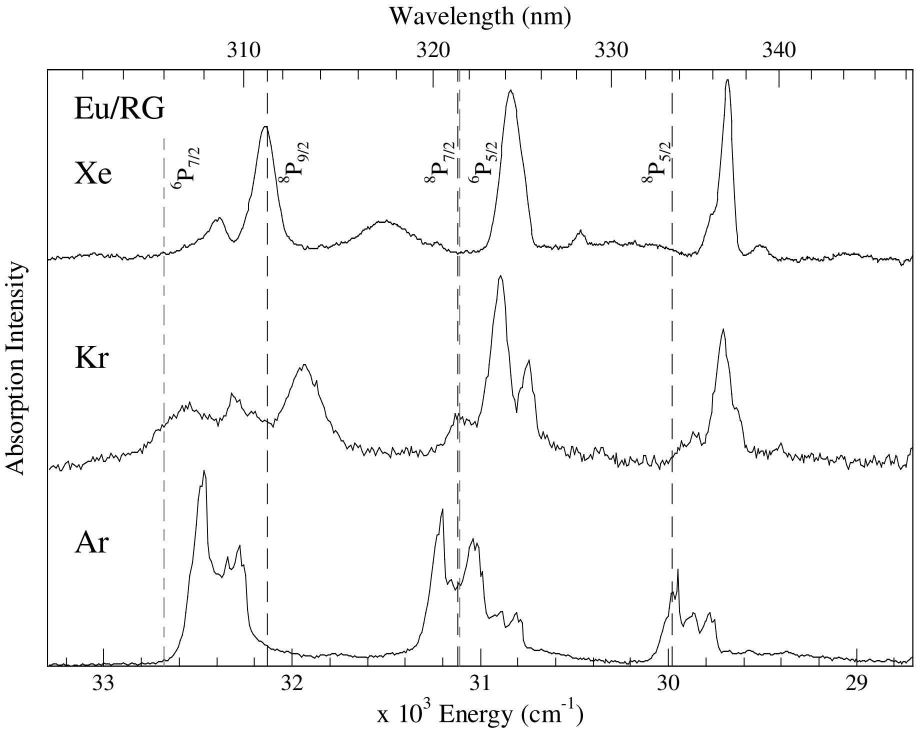

Figure III.24 Eu/RG UV absorption spectra recorded at 10 K following sample annealing. The gas phase positions of the ^6P_J, $^8P_J \leftarrow a^8S_{7/2}$ transitions are shown by the dashed vertical lines.

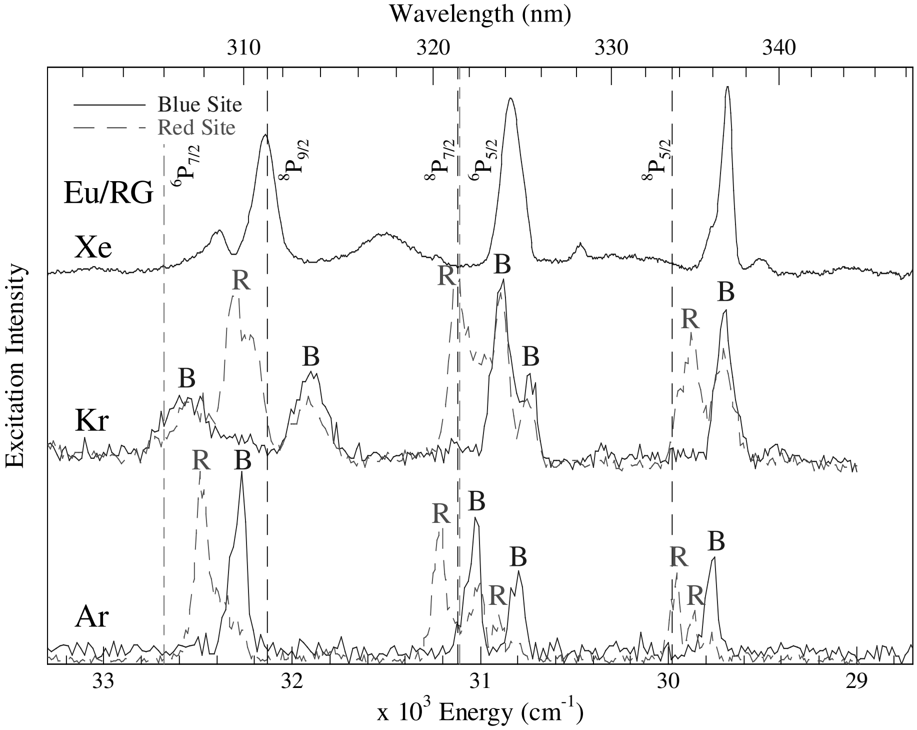

Figure III.25 Eu/RG site-specific excitation spectra in the UV spectral region recorded at 10 K following sample annealing. Two sites of isolation are identified, the blue site (B, solid trace) and the red site (R, dashed trace). The gas phase positions of the ^6P_J, $^8P_J \leftarrow a^8S_{7/2}$ transitions are identified by the dashed vertical lines.

The $^8P_{5/2}$ absorption region was presented in detail in Ar matrices by Jakob *et al.*[6] and suggested the complex structure of the absorption spectrum was a result of crystal field (CF) splitting of the $^8P_{5/2}$ state. Temperature dependence studies of the absorption spectra identified three zero phonon lines (ZPL's), each with a high energy phonon-sideband. It was assumed the Eu atom existed in one site of *non-cubic* symmetry in the Ar lattice. The three ZPL's were thus proposed as arising from individual weak field states of the J = 5/2 level split by a *non-cubic* crystal field.

A comparison with the current Eu/Ar data is presented in Figure III.26. With the attribution of site types occupied and site-specific absorption features identified, the data of Jakob *et al.* is reanalysed. The effect of the *cubic* CF experienced in the hexa-vacancy (hv) and tetra-vacancy (tv) lattice sites on the $^8P_{5/2}$ level is considered. A *cubic* CF is predicted to split the J = 5/2 spin-orbit level into two weak field components of intensity ratio 2:1[17,18].

This is precisely as is observed in Figure III.26 for atoms in the red site of isolation. Two ZPL features of intensity 2:1 are located at 333.8 and 334.9 nm. However, only one blue site ZPL of much weaker intensity is identifiable at 336 nm. There is evidence of the second blue site CF state at 334.7 nm to higher energy of the red site 334.9 nm ZPL but it is difficult to identify conclusively without the complete temperature study of Jakob *et al.* performed at high-resolution.

Absorption features in the 322 and 309 nm regions contain much more structure. Without the temperature dependence study performed at high-resolution over this whole spectral region, it is impossible to accurately assign which features are due to ZPL's and which are sideband structures. The absorptions here are also complicated by the fact there are two distinct P states occurring in these regions. In the 322 nm spectral region both the $^6P_{5/2}$ and $^8P_{7/2}$ transitions occur while in the 310 nm spectral region $^6P_{7/2}$ and $^8P_{9/2}$ absorb. Notwithstanding this, it is possible to develop the previous work of Jakob *et al.* with site-specific excitation spectra and assign particular features in each of the RG lattices to atomic Eu isolated in a particular site. Table III.6 lists the site-specific absorption features identified in this study. They are displayed for Eu/Ar with the data of Jakob *et al.* in Figure III.26. Features corresponding to the red and blue sites are labelled R and B respectively. Notably, the blue site features occur to lower energy than the red site in this region. This is an energy reversal compared to the y^8P state where the blue site features occur to higher energy than the red site.

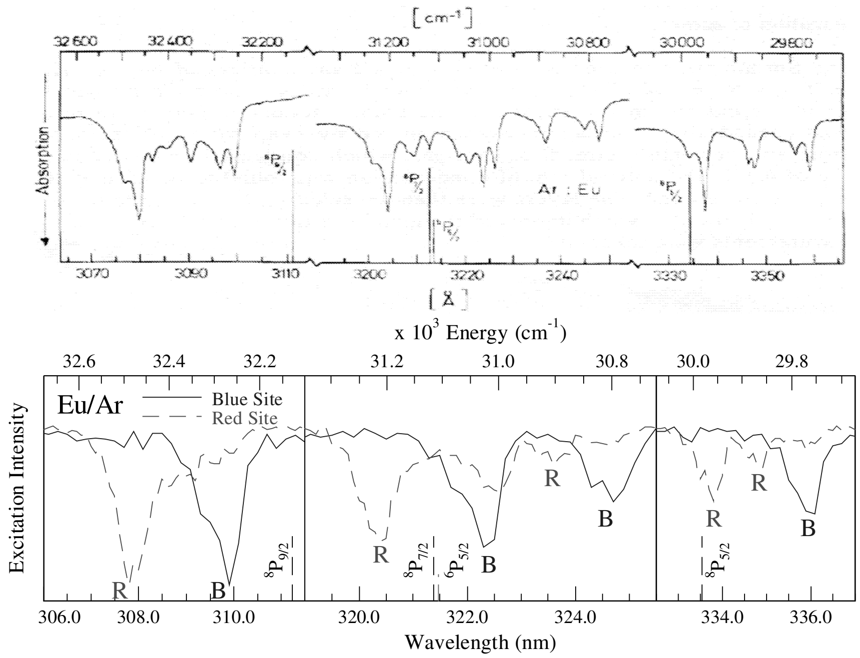

Figure III.26 Top panel presents high-resolution UV absorption spectra of an annealed Eu/Ar sample recorded in a previous study[6]. Bottom panel displays the site-specific excitation spectra obtained in the current study allowing absorption features to be attributed to Eu atoms trapped in a particular site within the *fcc* lattice.

In summary, absorption features in the UV spectral region relating to f → d type ^{8}P, ^{6}P ($4f^65d^16s^2$) ← $a^8S_{7/2}$ transitions are observed in agreement with earlier studies in this region. Site-specific excitation spectra develop previous assignments and allow identification of absorption features pertaining to Eu atoms isolated in different sites within the RG lattices. Notably the $\Delta J = 0, \pm 1$ selection rule is obeyed for all transitions in this region. Absorption from the $a^8S_{7/2}$ ground state to J = 5/2, 7/2, 9/2 levels is observed. There is no evidence of the $^6P_{3/2}$ state absorption which is unidentified in the gas phase also.

Table III.6 Spectral locations of the site-specific features (red and blue) revealed in the UV excitation spectra of Eu/RG. The spectral positions of the components are presented in nanometre and (wavenumber units) alongside the gas phase values of the ^6P_J, ^8P_J ← $a^8S_{7/2}$ transitions. The spectral position of the $^6P_{3/2}$ state is unknown in the gas phase.

Gas Phase[1]	Spectral Location, nm (cm^{-1})		
^6P_J	J = 7/2	J = 5/2	J = 3/2
	305.99 (32681)	321.5 (31107)	-
^8P_J	J = 9/2	J = 7/2	J = 5/2
	311.23 (32130)	321.37 (31116)	333.53 (29982.5)

	Eu/Ar		
Blue	309.9 (32269)	322.2 (31036) 324.6 (30807)	335.8 (29780)
Red	307.8 (32489)	320.4 (31211) 323.6 (30902)	333.8 (29958) 334.9 (29860)

	Eu/Kr		
Blue	307 (32573) 313.4 (31908)	323.8 (30888) 325.4 (30731)	336.6 (29709)
Red	309.7 (32295) 310.4 (32216)	321.4 (31114)	334.7 (29878)

	Eu/Xe		
Blue	308.8 (32383) 311.1 (32144) 317.4 (31506)	324.3 (30835)	336.8 (29691)

III.7 Conclusion

Absorption spectra of matrix-isolated atomic europium recorded in the UV/Vis spectral region is dominated by the s → p type y^8P ($4f^7 6s^1 6p^1$) $\leftarrow a^8S_{7/2}$ transition observed in the 450 nm spectral region. Absorption and excitation spectroscopy recorded for atomic Eu isolated in the solid rare gases (Ar, Kr and Xe) identified several trapping sites within RG matrices.

Annealing effects attributed the lowest energy absorption features to a thermally unstable site of isolation present in each RG matrix upon deposition. Excitation spectroscopy identified multiple thermally stable metal atom trapping sites within the rare gas matrices.

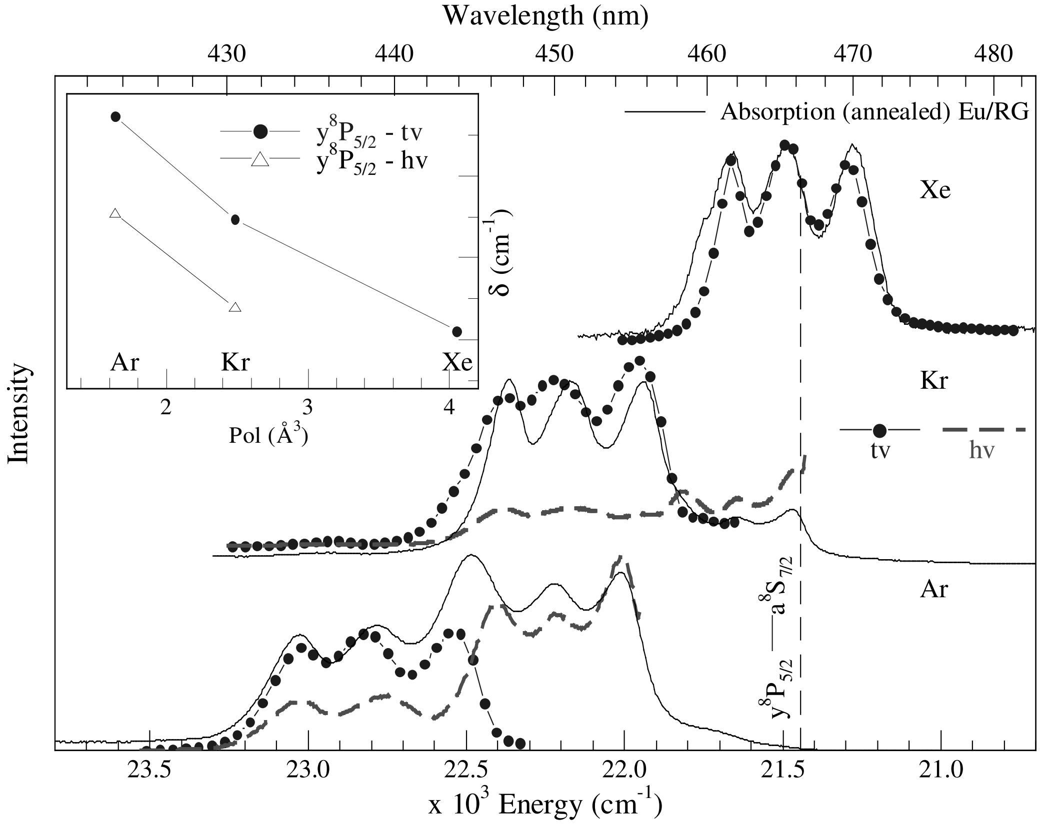

Figure III.27 Eu/RG absorption and site-specific excitation spectra in the region of the $y^8P_{5/2} \leftarrow {}^8S_{7/2}$ transition recorded at 10 K following sample annealing. Inset is a plot of the gas phase to matrix frequency shifts (δ cm^{-1}) observed for the central Jahn-Teller component of the blue (tv) and red (hv) sites versus the RG host polarisabilities. The circles (connected by the solid line) plotted in the inset highlights the linear correlation between the frequency shifts and rare gas polarisability observed for the Eu $y^8P_{5/2} \leftarrow a^8S_{7/2}$ transition occurring within the blue (tv) sites of isolation in each RG.

Two distinct thermally stable metal atom trapping sites labelled blue and red were identified. y^8P state excitation spectra reveal the presence of threefold split excitation patterns for each of these sites attributed to Jahn-Teller distortion which is indicative of Eu atoms occupying a highly symmetric matrix environment. Absorption spectra in this region were completely explained by the existence of these two sites as seen in Figure III.27.

Site associations were made based on application of the polarisability model to the $y^8P_{5/2} \leftarrow a^8S_{7/2}$ electronic transition of atomic Eu and use of the Luiti-Pirani method complemented by comparison to Na/RG. The site types occupied by Eu atoms within the matrix are proposed as a tetra-vacancy (tv) blue site and a hexa-vacancy (hv) red site. That is to say, atomic Eu exists solely in a tetra-vacancy site of isolation in the larger xenon matrix while both the tetra-vacancy and hexa-vacancy sites are populated in solid Ar and Kr. The tv site dominates in the krypton matrix and the hv site is slightly more prominent in solid argon.

Furthermore, knowledge of the site occupancy allowed assignment of absorption features observed in the UV spectral region as transitions from the ground state to each of the J spin-orbit levels of the ^{6}P and ^{8}P states of Eu atoms isolated in a particular site and leads to an interesting comment on the different excited states observed. The visible y^8P state has three spin-orbit levels with a splitting in the region of 160 cm^{-1} between each in the gas phase but exhibits a Jahn-Teller threefold splitting pattern when isolated in solid RG's. The splitting between the individual J-levels of the ^{6}P and ^{8}P states is a much larger value in the region of 1000 cm^{-1} as seen in Table III.7. This allows absorption into each of the individual spin-orbit levels, with no evidence of JT distortion on these P states, to be identified in the RG lattices.

Table III.7 Gas phase positions of the individual spin-orbit levels of P states of atomic Eu observed in the solid RG's in wavenumber units. The spacing between each J-level is denoted as Δ. The spectral position of the $^6P_{3/2}$ state is unknown in the gas phase.

Gas phase positions of P states of atomic Eu[1]

y^8P [Xe]$4f^7 6s^1 6p^1$			**^{8}P** [Xe]$4f^6 5d^1 6s^1$			**^{6}P** [Xe] $4f^6 5d^1 6s^1$		
J	ν (cm^{-1})	Δ (cm^{-1})	J	ν (cm^{-1})	Δ (cm^{-1})	J	ν (cm^{-1})	Δ (cm^{-1})
5/2	21444.6	160.6	5/2	29982.5	1133.9	3/2	-	-
7/2	21605.2	156.1	7/2	31116.4	1013.9	5/2	31107.3	1573.8
9/2	21761.3		9/2	32130.3		7/2	32681.1	

Bersuker states that sufficiently large spin-orbit coupling can completely reduce Jahn-Teller distortions[19]. The Eu/RG system allows one to observe both extremes of this Jahn-Teller effect, when spin-orbit splitting is small (y^8P) the JT distortion dominates and threefold splitting of P states is observed, whilst when spin-orbit splitting is large (^{8}P, ^{6}P) spin-orbit effects dictate and individual J-levels of the P state are observed with no evidence of any JT effects.

References

1 *NIST Atomic Spectra Database (version 3.1.5), available: http://physics.nist.gov/asd3 [2010, August]*. (National Institute of Standards and Technology, Gaithersburg, MD).

2 M. A. Collier and J. G. McCaffrey, Journal of Chemical Physics **122** (5) (2005).

3 S. L. Laursen and H. E. Cartland, Journal of Chemical Physics **95** (7), 4751 (1991).

4 M. Jakob, H. Micklitz and K. Luchner, Berichte Der Bunsen-Gesellschaft-Physical Chemistry Chemical Physics **82** (1), 32 (1978).

5 M. Jakob, H. Micklitz and K. Luchner, Physics Letters A **61** (4), 265 (1977).

6 M. Jakob, H. Micklitz and K. Luchner, Physics Letters A **57** (1), 67 (1976).

7 X. Y. Cao and M. Dolg, Theoretical Chemistry Accounts **108** (3), 143 (2002).

8 Y. Haas and U. Samuni, Progress in Reaction Kinetics and Mechanism **23** (4), 211 (1998).

9 M. Collier, *Ph.D. Thesis, National University of Ireland Maynooth (2004).* (http://eprints.nuim.ie/154/1/MartinCollierThesis.pdf).

10 R. Cambi, D. Cappelletti, G. Liuti and F. Pirani, Journal of Chemical Physics **95** (3), 1852 (1991).

11 R. Bruhl, J. Kapetanakis and D. Zimmermann, Journal of Chemical Physics **94** (9), 5865 (1991).

12 D. Schwarzhans and D. Zimmermann, European Physical Journal D - Atoms, Molecules, Clusters & Optical Physics **22** (2), 193 (2003).

13 E. Zanger, V. Schmatloch and D. Zimmermann, Journal of Chemical Physics **88** (9), 5396 (1988).

14 *CRC Handbook of Chemistry and Physics*, 76th ed. (CRC Press, 1995).

15 M. Ryan, M. Collier, P. de Pujo, C. Crepin and J. G. McCaffrey, Journal of Physical Chemistry A **114** (9), 3011 (2009).

16 H. E. Hallam, *Vibrational Spectroscopy of Trapped Species*. (Wiley - Interscience, New York, 1973).

17 O. Byrne, M. A. Collier, M. C. Ryan and J. G. McCaffrey, Low Temperature Physics **36** (5), 417 (2010).

18 M. A. Collier, O. Byrne, C. Murray and J. G. McCaffrey, The Journal of Chemical Physics **132** (16), 164512 (2010).

19 I. Bersuker, *The Jahn-Teller Effect*. (Cambridge University Press, 2006).

Chapter IV

Luminescence spectroscopy of the y^8P state of atomic europium isolated in rare gas solids, (RG = Ar, Kr and Xe).

IV.1 Introduction

Very little of the luminescence of atomic europium (Eu) isolated in the rare gases (RG's) is available in published journals. In fact, the reported luminescence of any lanthanide isolated in RG matrices is quite limited. The absorption of atomic Eu occurs in two major spectral regions, the near-UV centred at 320 nm and the visible region occurring at approximately 450 nm. These absorptions arise from the ^{8}P, ^{6}P ← $a^8S_{7/2}$ and y^8P ← $a^8S_{7/2}$ transitions respectively.

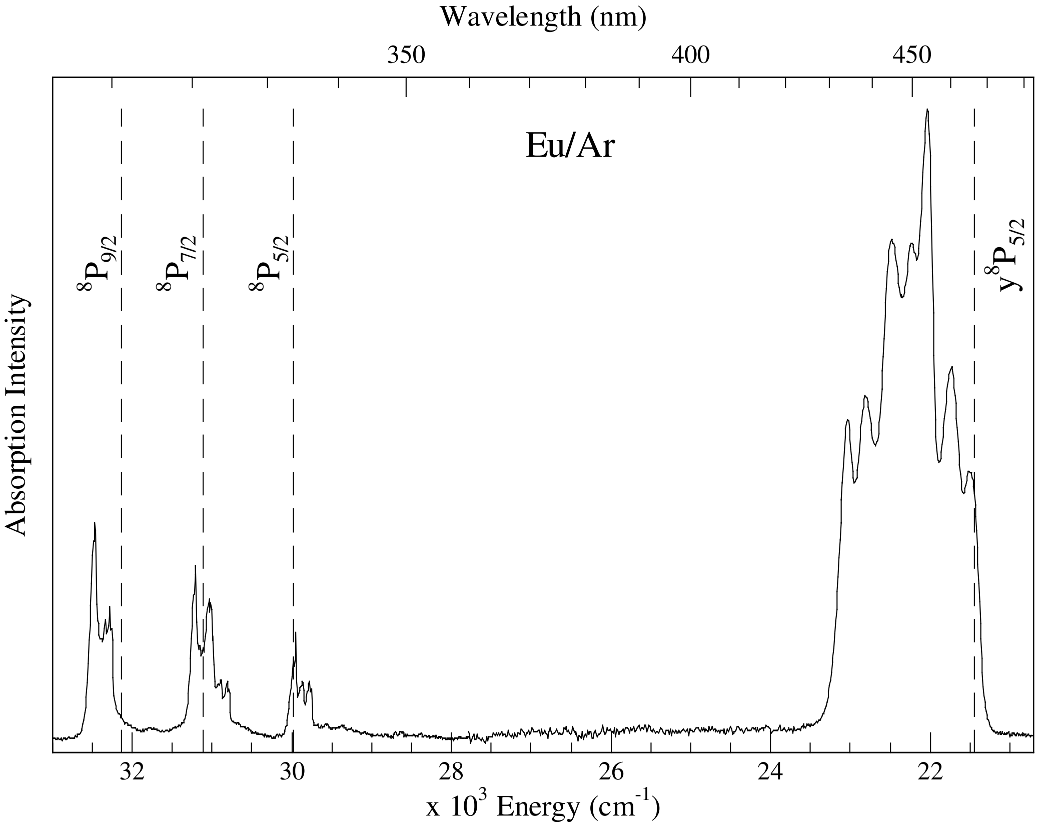

Figure IV.1 Eu/Ar UV/Vis absorption spectrum recorded at 10 K following sample deposition at 10 K. The spectral position of the gas phase transitions of atomic Eu are shown by the dashed vertical lines[1].

A previous study in the 1970's investigated the absorption and emission produced in the UV region[2,3,4] but to the best of our knowledge, nothing of the more accessible visible luminescence has been published. This situation is surprising considering the visible absorption dominates, having an oscillator strength ten times that of the UV transition in the gas phase[1]. As can be clearly seen in Figure IV.1 the visible absorption is also the feature of greatest intensity in the solid state.

The following sections discuss the luminescence produced in the visible region with y^8P state excitation. In Chapter III, absorption and excitation spectra for Eu/RG recorded in this region allowed the identification of multiple metal atom trapping sites within the RG matrices. Upon annealing one thermally unstable site was removed leaving the Eu atom in one site in the Xe matrix and two thermally stable sites within the Ar and Kr lattices.

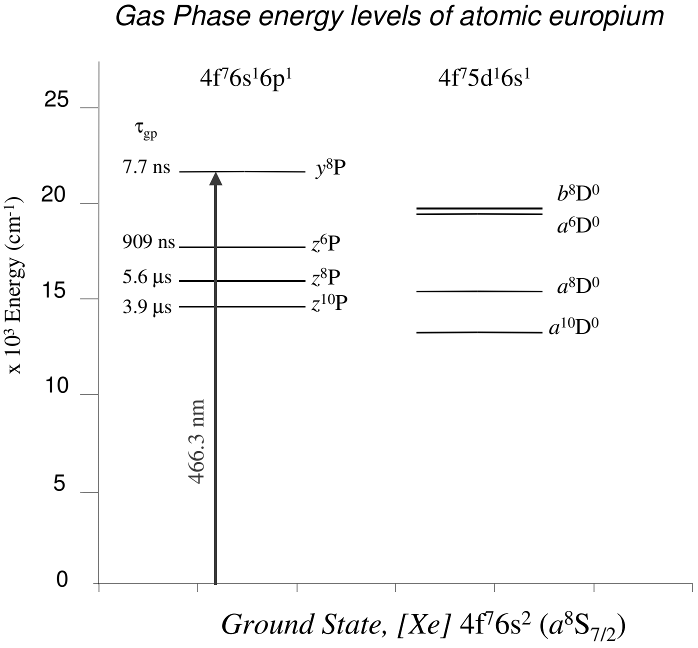

Figure IV.2 Schematic representation of the energy levels of gas phase atomic europium in the visible spectral region under investigation in this study. The fully allowed y^8P ← $a^8S_{7/2}$ transition occurring at 21444.6 cm^{-1} (466.3 nm) is indicated by the arrow[1].

Site-selective excitation of the y^8P state in each of the RG's using both lamp and pulsed laser excitation yield site-specific steady-state emission spectra and decay profiles which are presented in the following sections. Temperature effects on the lifetimes and emission profiles were also investigated allowing comment on the excited states involved. Examination of the energy level diagram of gas phase atomic Eu in Figure IV.2 show there are seven lower energy excited states below the y^8P state.

The presentation of results is structured in the following manner. Firstly, the luminescence produced with site-selective y^8P red and blue site excitation of atomic Eu isolated in solid Ar will be presented. Then the y^8P luminescence from both sites in Kr is discussed and finally the luminescence of the less complicated case of Xe. This is followed by a comparison of the luminescence from sites of the same type and finally, trends observed in each of the RG's are highlighted and discussed. Atomic Eu isolated in annealed RG hosts yields four emission features. State assignments of the emission will be made on the basis of spectral location and recorded emission decays.

IV.2 Eu(y^8P)/Ar Luminescence

The luminescence spectra produced with y^8P state excitation of Eu atoms isolated in Ar matrices are presented in the following sections. Two thermally stable sites, the blue site centred at 438.3 nm and the red site centred at 450.1 nm remain following annealing as shown in the absorption spectra in the left panel of Figure IV.3.

Right panel of Figure IV.3 presents the emission spectra produced with site-selective excitation of the $y^8P \leftarrow a^8S_{7/2}$ transition in an annealed sample. Inspection of the emission spectra reveal four bands from atoms isolated in each of the sites. The following sections aim to assign each of these bands to a particular electronic transition of atomic Eu.

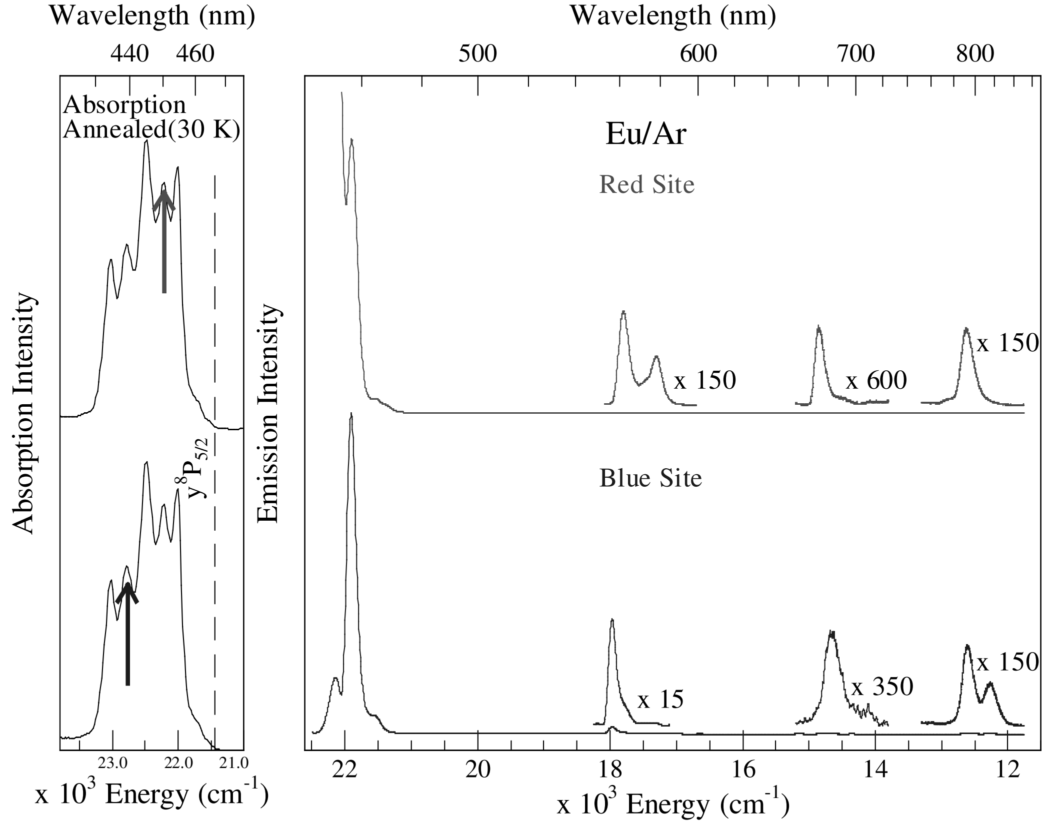

Figure IV.3 Absorption and emission spectra of Eu/Ar in the visible spectral region at 10 K following sample deposition at 10 K and sample annealing to 30 K. Left panel displays the y^8P absorption spectra, arrows indicate the site-specific excitation wavelength used to produce the emission spectra seen in right panel.

IV.2.I. Eu/Ar - $\lambda_{Em.} \approx 455$ *nm*

IV.2.I.I Red site

In this section the red site emission feature centred at 457.3 nm (21867 cm^{-1}) is discussed. The nearest gas phase electronic transition is the $y^8P_{5/2} \leftrightarrow a^8S_{7/2}$ occurring at 466.32 nm (21444.58 cm^{-1}) suggesting the emission observed at 457 nm is y^8P state resonance fluorescence exhibiting a blue matrix shift of + 422 cm^{-1}. A plot of the excitation spectrum recorded monitoring the 457 nm emission feature is overlapped with the absorption spectrum in this region and presented in Figure IV.4. A Stokes shift of 351 cm^{-1} is identified giving a measure of the extent of interaction of the excited state with the surrounding lattice in this site.

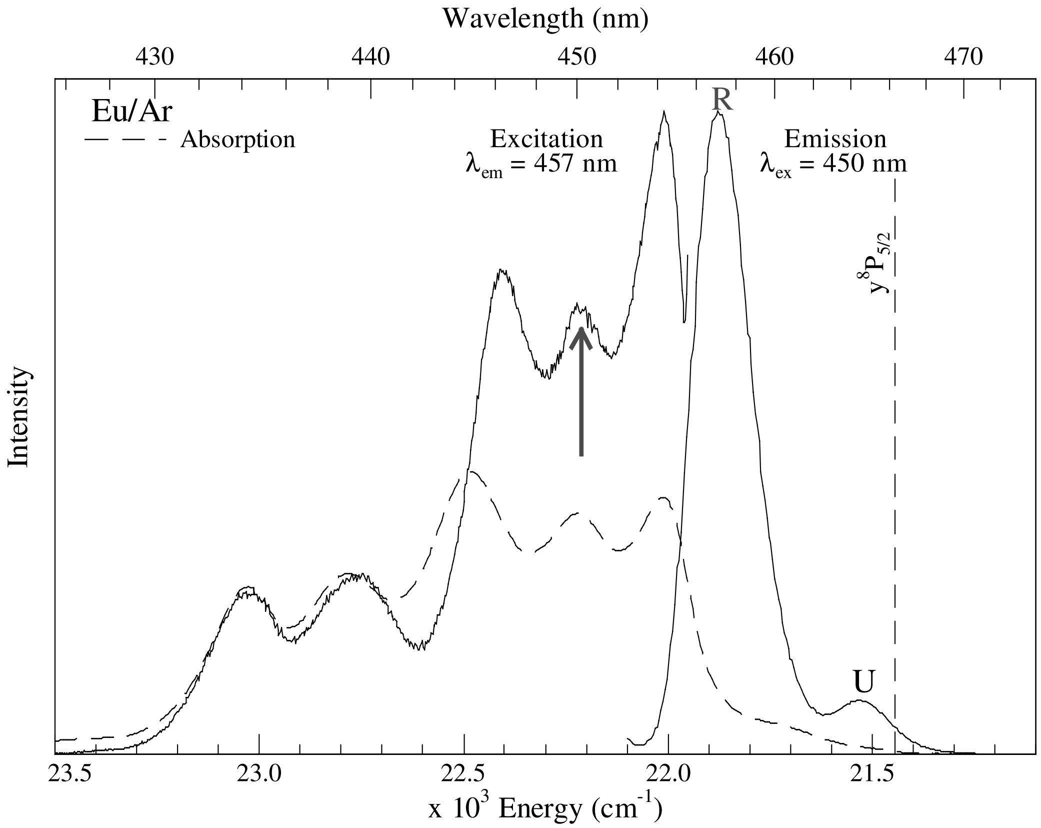

Figure IV.4 Absorption, excitation and emission spectra of Eu/Ar in the red site of isolation in the y^8P spectral region at 10 K following sample deposition at 10 K and sample annealing to 30 K. A minor amount of thermally unstable site emission (U) is observed due to some residual atoms remaining in this site following sample annealing.

The decay characteristics of this emission feature were recorded with excitation at 450 nm while monitoring emission at 457 nm in solid Ar. A single exponential decay convoluted with the laser profile is shown in Figure IV.5. The agreement with the fit yielding a lifetime of 3.5 ns for this electronic transition in the Ar matrix.

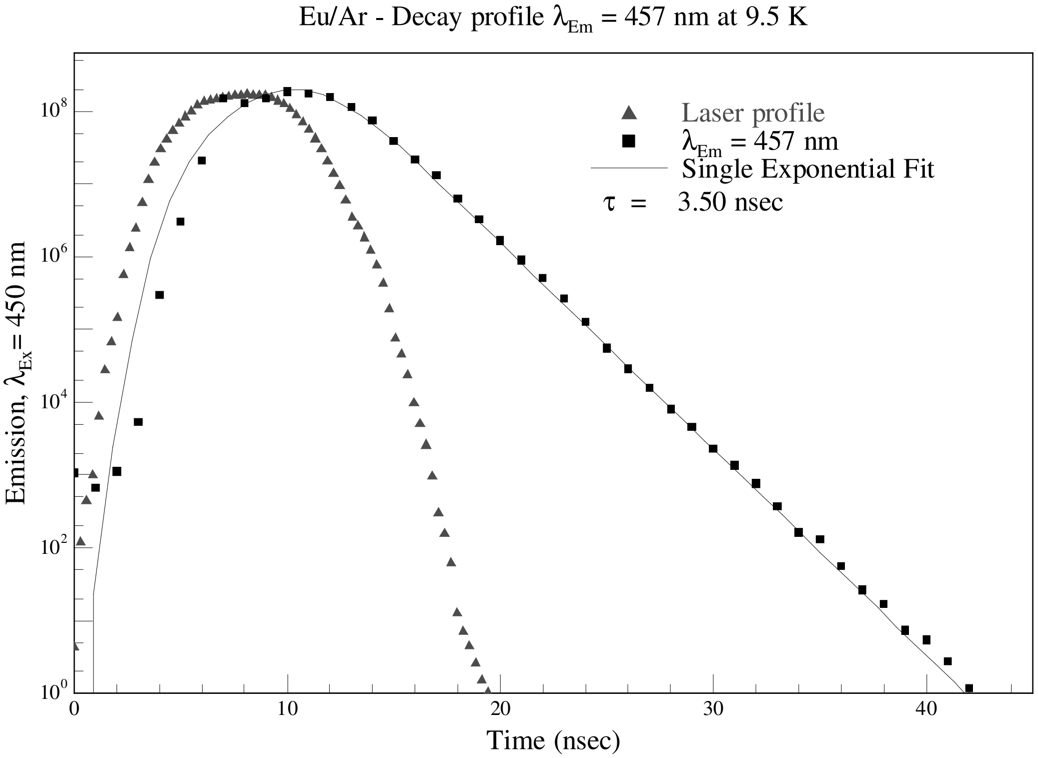

Figure IV.5 Decay profile of the Eu/Ar red site emission at 457 nm recorded at 10 K in an annealed sample. The decay profile is convoluted with the temporal profile of the laser excitation source at 450 nm.

In an attempt to assign the radiative lifetime of the 457 nm emission feature, decay profiles were recorded at various temperatures. Left panel of Figure IV.6 shows no temperature dependence in the range 9.5 to 16 K, thus the radiative lifetime is observed and assigned as 3.5 ns. When corrected for the effective field of the surrounding RG lattice, the matrix lifetime becomes 7.2 ns which compares very favourably to the gas phase $y^8P_{5/2} \leftrightarrow a^8S_{7/2}$ value of 7.7 ns[1]. This agreement allows confident assignment of this emission feature as y^8P state resonance fluorescence.

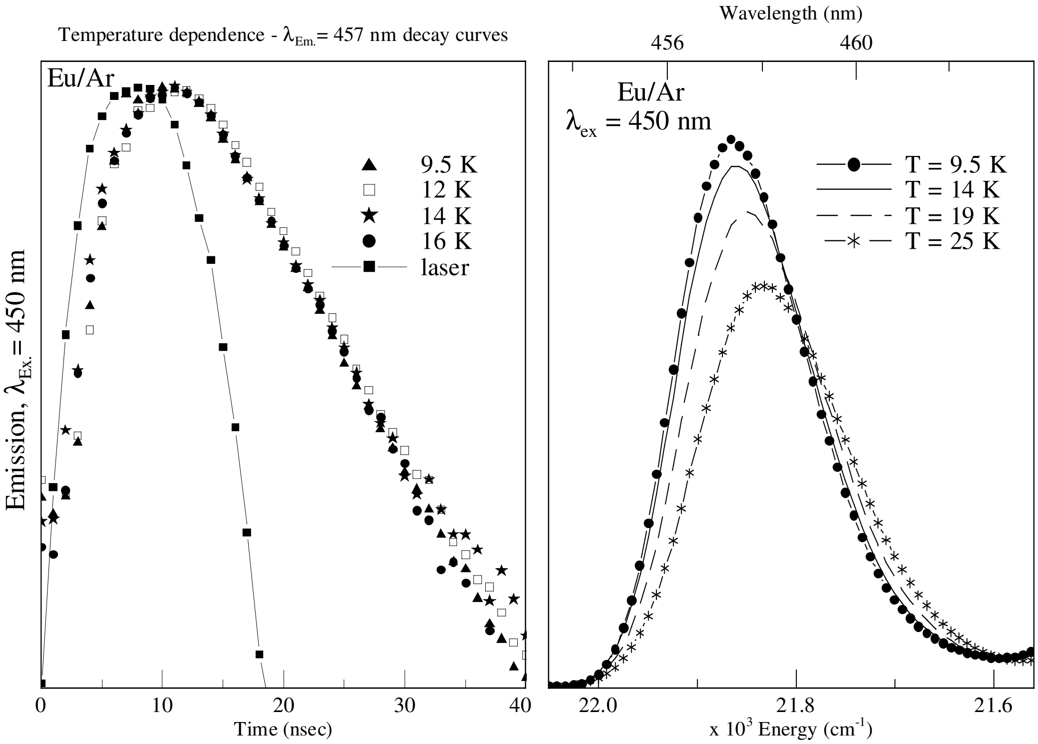

Figure IV.6 Left panel displays the decay profiles of the Eu/Ar red site emission at 457 nm recorded at elevated temperatures in an annealed sample. Right panel presents steady-state emission spectra recorded with y^8P ← $a^8S_{7/2}$ excitation at 450 nm at various temperatures.

Temperature effects on the steady-state emission spectra show little change in emission strength up to 16 K and hence no change in the decay profiles as seen in left panel of Figure IV.6. However, at higher temperatures a progressive red shift and decrease in emission intensity occurs due to activation of a competitive non-radiative relaxation step as seen in right panel of Figure IV.6.

IV.2.I.II Blue site

Blue site y^8P state excitation of the highest energy Jahn-Teller component at 434 nm, a value chosen to minimise any concurrent red site excitation, produces three emission features in this region centred at 452 (B), 457 (R) and 465 (U) nm, as shown in Figure IV.7. Excitation spectra assign these features as resulting from the blue, red and the thermally unstable sites of isolation respectively, as displayed in Figure IV.7. A minor amount of thermally unstable site emission (U) is observed due to some residual atoms remaining in this site following sample annealing.

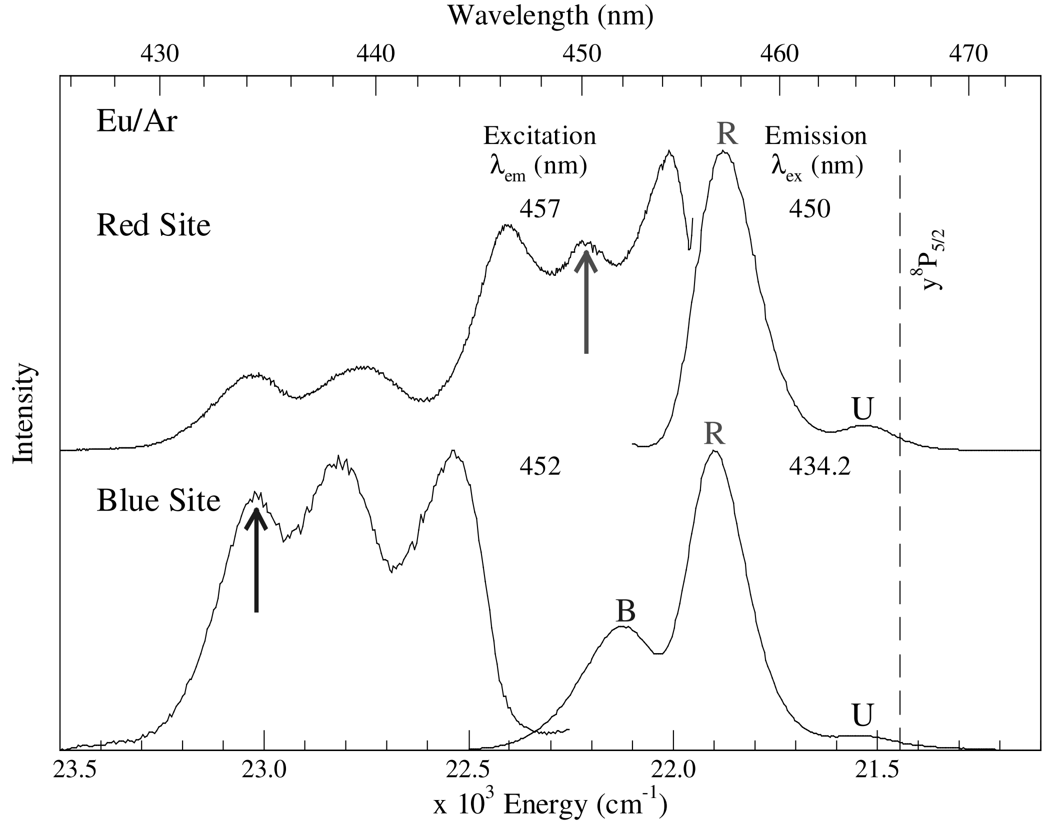

Figure IV.7 Site-specific excitation and emission spectra of Eu/Ar in the y^8P spectral region at 10 K following deposition at 10 K and sample annealing to 30 K. Arrows indicate the excitation wavelengths producing the observed emission spectra. A minor amount of thermally unstable site emission (U) is observed due to some residual atoms remaining in this site. The spectral position of the gas phase y^8P transition of atomic Eu is shown by the dashed vertical line[1].

The only electronic state in this spectral region in the gas phase is the y^8P state with its lowest spin-orbit level occurring at 466.32 nm (21444.58 cm^{-1}), suggesting the emission observed at 451.6 nm (22141 cm^{-1}) originates from the $y^8\text{P} \rightarrow a^8\text{S}$ transition exhibiting a blue matrix shift of + 697 cm^{-1} from the gas phase and a Stokes shift of 674 cm^{-1}.

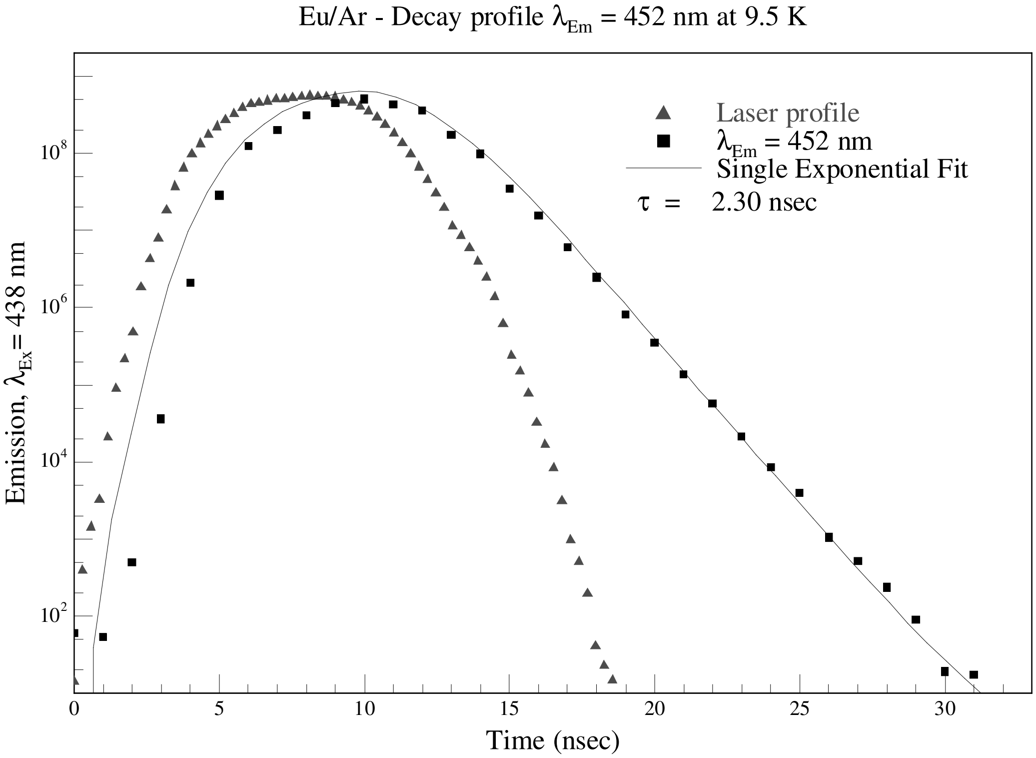

Figure IV.8 Decay profile of the Eu/Ar blue site emission at 452 nm recorded at 10 K in an annealed sample. The decay profile is convoluted with the temporal profile of the laser excitation source at 438 nm.

The temporal decay profile of this feature at 9.5 K is presented in Figure IV.8. The emission is short-lived and a lifetime of 2.3 ns is extracted. In an effort to identify the true radiative lifetime of this transition in solid Ar, the effects of temperature on its decay profile were also investigated and are presented in left panel of Figure IV.9. Figure IV.9 shows that even in the temperature range 9.5 to 12 K there is a change in decay profile. Thus the radiative lifetime is not identified in the present work. However, this lifetime of 2.3 ns at 10 K is in agreement with assignment of the emission as $y^8\text{P} \rightarrow a^8\text{S}$ relaxation which has a comparable value of 3.5 ns in the red site.

Strong temperature dependence is also evident in the emission intensity in steady-state spectra as presented in right panel of Figure IV.9. There is an obvious decrease in the emission strength at increasing temperatures, most likely due to enhancement of a relaxation process competing with the $y^8\text{P} \rightarrow a^8\text{S}$ electronic transition.

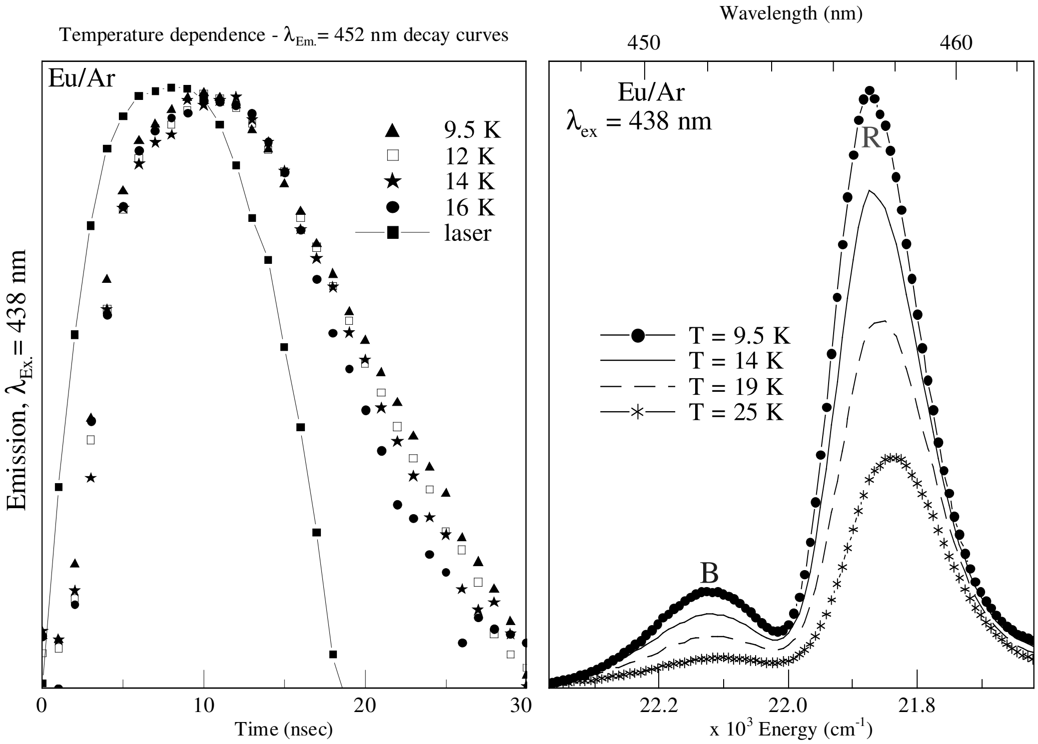

Figure IV.9 The decay profiles of the Eu/Ar blue site emission at 452 nm recorded at elevated temperatures in an annealed sample are displayed in left panel. Right panel presents steady-state emission spectra recorded with y^8P ← $a^8S_{7/2}$ excitation at 438 nm at various temperatures.

IV.2.I.III Indirect red site emission – 457 nm

Upon inspection of bottom trace of Figure IV.7, red site (457 nm) emission is observed with blue site excitation implying there is either *a)* re-absorption caused by the spectral overlap between blue site emission feature centred at 452 nm and red site absorption feature centred at 450.1 nm, or *b)* the excitation wavelength of 434 nm is exciting some atoms isolated in the red site. The latter possibility seems unlikely as the excitation wavelength selected was the highest energy JT component of the blue site to minimise any concurrent red site excitation.

To investigate possibility *a)* the decay profile of the red emission feature observed at 457 nm (R) produced indirectly with blue site y^8P state excitation is presented in Figure IV.10. It exhibits a double exponential decay curve with components of 2.3 and 3.5 ns. The 2.3 ns component is a risetime feature as evidenced by its negative amplitude. This is the same value as the lifetime of the blue site 452 nm emission, whilst the major 3.5 ns component has a lifetime value the same as the red site fluorescence. This behaviour implies this decay profile is composed of two steps, blue site emission followed by red site re-absorption and emission.

To further probe the origin of this multi-component relaxation step, decay profiles were recorded at increased temperatures. At 16 K the major lifetime component remains constant, just as the direct red site fluorescence does, whilst the risetime exhibits a value of 1.4 ns, the same value as blue site y^8P state emission at this temperature confirming each step relates to red and blue site emission respectively.

Based on the spectral overlap between the blue site emission feature and the red site absorption profile, the multi-component decay and the identification of a risetime it can be definitively assigned that red site re-absorption of blue site y^8P state emission is the source of the emission observed at 457 nm produced indirectly with blue site excitation in solid Ar.

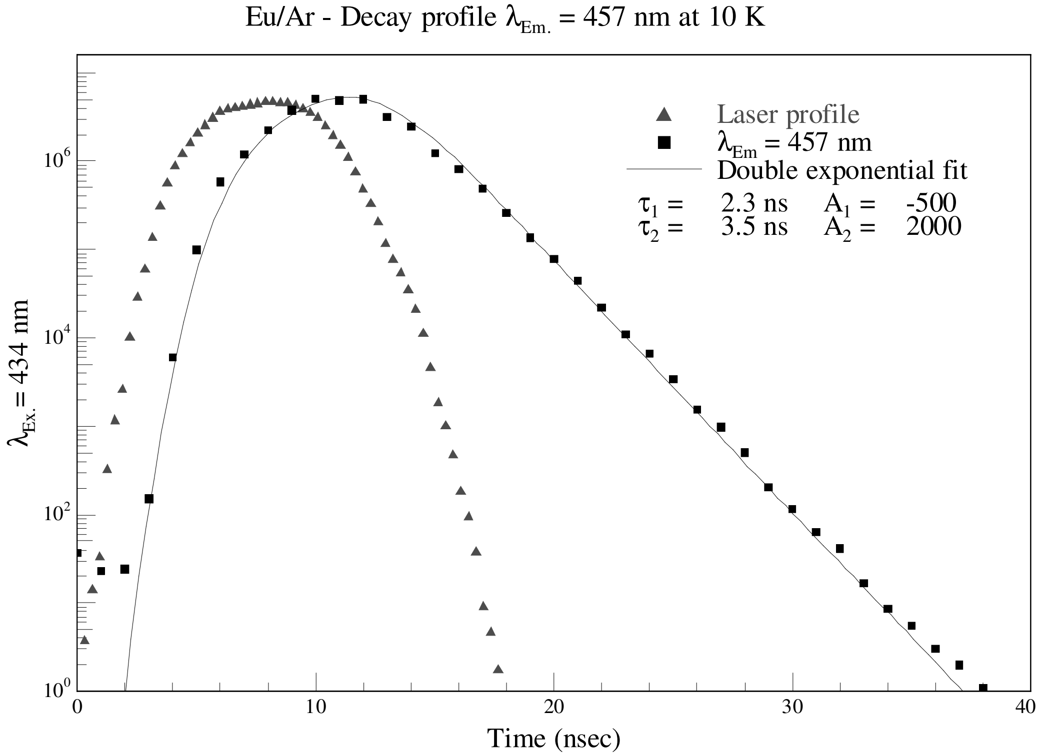

Figure IV.10 Decay profile of the Eu/Ar red site emission at 457 nm recorded at 10 K in an annealed sample. The emission was produced indirectly with blue site excitation at 434 nm. The decay profile is convoluted with the temporal profile of the laser excitation source.

IV.2.I.IV Eu/Ar ($y^8P \rightarrow a^8S$) Summary

In summary, $y^8\mathrm{P} \rightarrow a^8\mathrm{S}$ emission is observed from atomic Eu in both sites of solid Ar at 452 and 457 nm. A corrected lifetime of 7.2 ns for the red site is attained which compares very favourably to the gas phase value of this transition (7.7 ns). Emission from both sites displays an intensity decrease at elevated temperatures implying competitive non-radiative steps are becoming activated. Stokes shifts of 351 cm^{-1} in the red site and 674 cm^{-1} in the blue site show the excited state has a greater interaction with the surrounding lattice in the blue site of isolation.

IV.2.II Eu/Ar - $\lambda_{Em.} \approx 560$ nm

The emission feature of second greatest intensity in the Ar matrix is observed in the 560 nm spectral region. Emission from the red site occurs at 563 nm whilst blue site emission is observed at 557 nm.

IV.2.II.I Red site

Red site emission produced with y^8P state excitation is observed at 562.9 nm (17767 cm^{-1}) exhibiting a bandwidth of 144 cm^{-1}. To assign the electronic state producing this feature, its temporal profile was recorded with y^8P state excitation. The decay profile at 9.5 K is fitted with a double exponential curve revealing lifetime components of 72 and 280 ns with amplitudes of 1450 and 1050 respectively as shown in Figure IV.11.

The short lifetime of this feature suggests it results from an electric-dipole allowed transition i.e. a P → S transition. A comparison with the energy level diagram for atomic Eu in Figure IV.2 shows there are three lower energy P states below the y^8P electronic state, namely the z^6P, z^8P and z^{10}P states, with the lowest spin-orbit state of each occurring at 17340.7, 15890.5 and 14067.9 cm^{-1} respectively in the gas phase. The nearest transition in the gas phase is $z^6\mathrm{P}_{7/2} \rightarrow a^8\mathrm{S}_{7/2}$ suggesting the observed emission is due to relaxation from the z^6P state with a matrix shift of 426 cm^{-1}. The lifetime of these three P → S type electronic transitions are known in the gas phase and listed in Table IV.1. The $z^6\mathrm{P}_{7/2} \rightarrow a^8\mathrm{S}_{7/2}$ transition has a lifetime of 909 ns. This is of a similar order of magnitude as the lifetime recorded for the 563 nm transition in solid Ar thus further re-enforcing the attribution of the z^6P state as being the source of this emission feature.

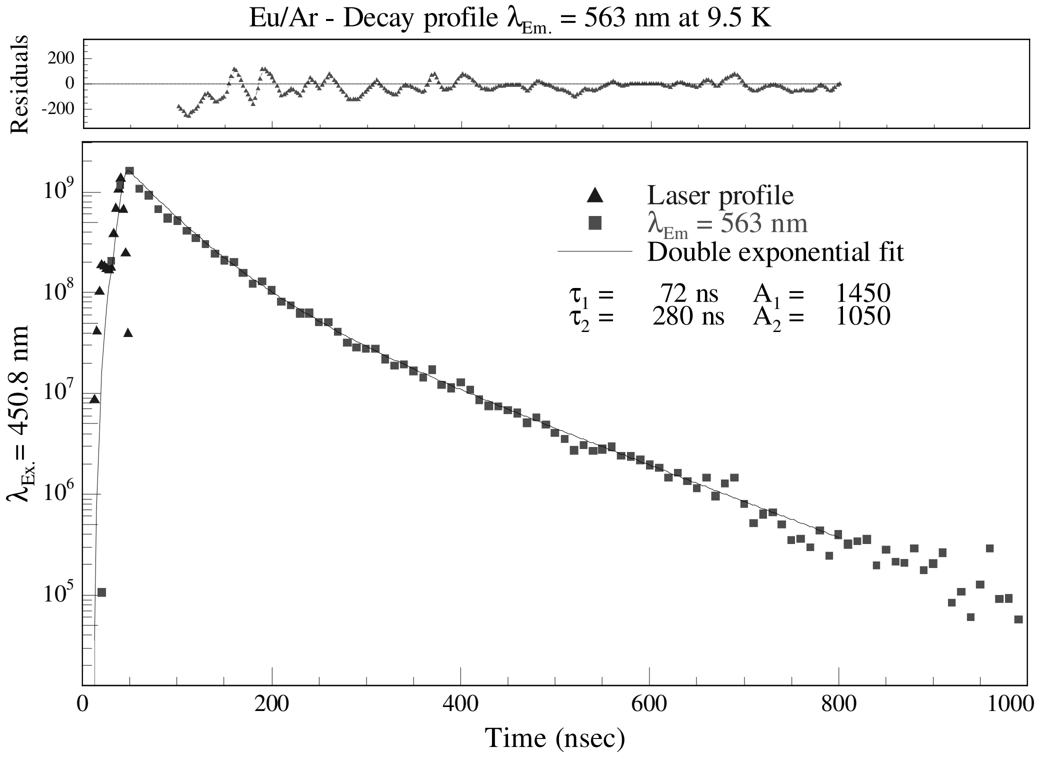

Figure IV.11 Decay profile of the Eu/Ar red site emission at 563 nm recorded at 10 K in an annealed sample. The decay profile is convoluted with the temporal profile of the laser excitation source at 450.8 nm. The residual shown represents the difference between the recorded decay and the double exponential fit.

Table IV.1 Photophysical characteristics of the lowest energy spin-obrit levels of the P ($4f^76s^16p^1$) ↔ a^8S ($4f^76s^2$) type electronic transitions of atomic europium occurring at $\lambda > 500$ nm in the gas phase.

Gas Phase P → S type transitions[1]

Transition	λ (nm)	ν (cm^{-1})	τ
$z^6P_{7/2} \leftrightarrow a^8S_{7/2}$	576.68	17340.65	909.1 ns
$z^8P_{5/2} \leftrightarrow a^8S_{7/2}$	629.31	15890.53	5.56 μs
$z^{10}P_{7/2} \leftrightarrow a^8S_{7/2}$	710.84	14067.86	3.85 μs

Presented in left panel of Figure IV.12 is an analysis of the effects of varying temperature on the lifetime. The emission decay curves are temperature independent in the range 9.5 to 16 K, indicating the radiative lifetime has been identified. When corrected for the effective field of the surrounding matrix, values of 147 and 575 ns are obtained which are in even closer agreement with the gas phase value (909 ns) allowing assignment of this feature as z^6P state emission. The source of the two lifetime components in the solid state is not clear but may be due to inaccuracies of the lifetime values recorded in the gas phase to date. This is discussed in more detail in Section IV.6.

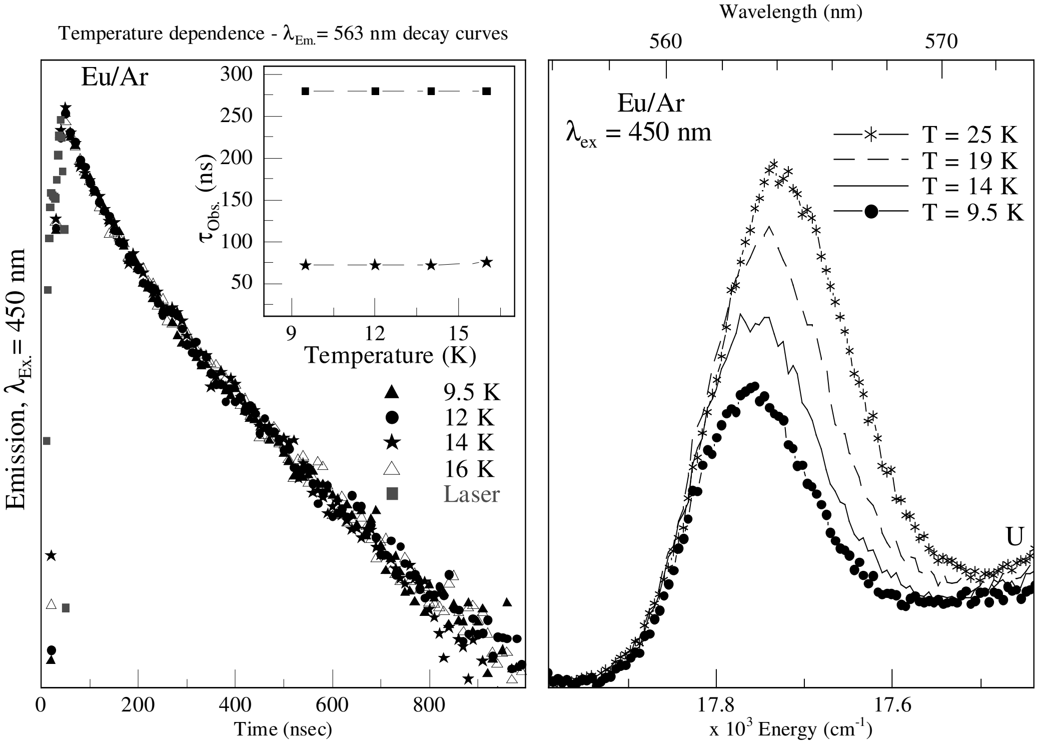

Figure IV.12 Left panel displays the decay profiles of the Eu/Ar red site emission at 563 nm recorded at elevated temperatures in an annealed sample. Inset plots the lifetime components of these decay profiles versus temperature. The right panel presents steady-state emission spectra recorded with $y^8P \leftarrow a^8S_{7/2}$ excitation at 450 nm at various temperatures. The high baseline to lower energy of this 563 nm emission feature is due to a minor amount of thermally unstable site emission (U) which can be seen clearly in Figure IV.16.

The effects of temperature on the steady-state emission spectra show a gradual increase in intensity is observed with increasing temperature steps of 14, 19 and 25 K. This implies enhancement of non-radiative feeding from the higher y^8P state occurs at elevated temperatures. These effects are completely reversible and the original spectrum is obtained on returning to 9.5 K again.

IV.2.II.II Blue site

The corresponding emission feature produced with blue site excitation is observed centred at 557 nm. A gaussian lineshape analysis of the emission profile produced with blue site y^8P state excitation is presented in Figure IV.13.

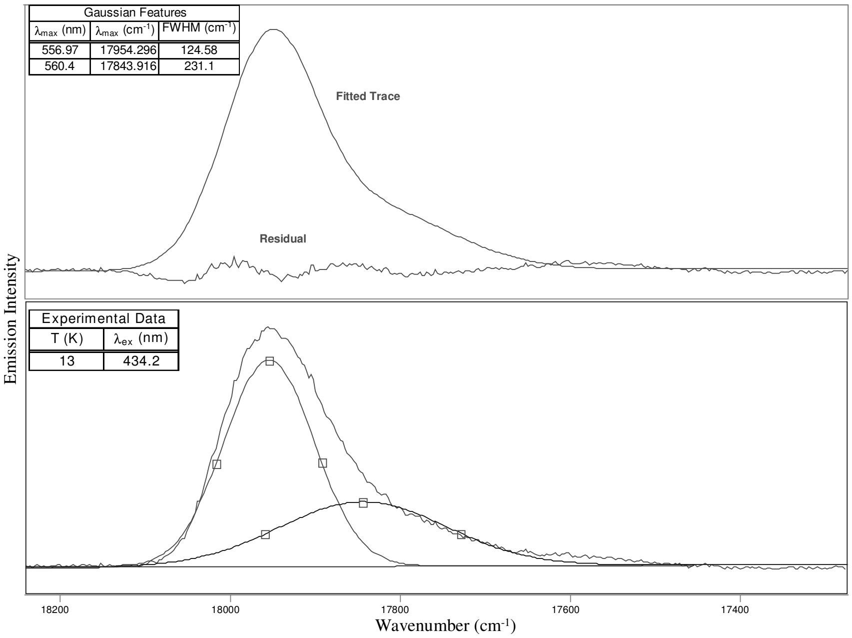

Figure IV.13 Gaussian lineshape analysis of the 557 nm emission observed for Eu/Ar. The upper panel shows an acceptable fit of the emission spectrum recorded at 10 K, where the simulated emission band and the residual is shown. Two broad Gaussian functions were required to completely represent the 10 K spectrum (lower trace) the weak lower energy shoulder pertaining to emission from Eu in the red site of isolation.

Two gaussian curves resulting from emission of both sites are necessary to reproduce the observed emission band shape. Excitation spectra in the y^8P state region confirm the higher intensity more dominant component centred at 557 nm originates from atomic Eu isolated in the blue site of isolation in the Ar matrix, whilst the red site appears as a weak lower energy shoulder caused by red site re-absorption in the y^8P state spectral region. Blue site $z^6\text{P} \rightarrow a^8\text{S}$ emission occurs at 557 nm (17954 cm^{-1}), exhibiting a bandwidth of 125 cm^{-1} and matrix shift of + 614 cm^{-1} in solid Ar. Its temporal characteristics support this assignment and are presented in Figure IV.14.

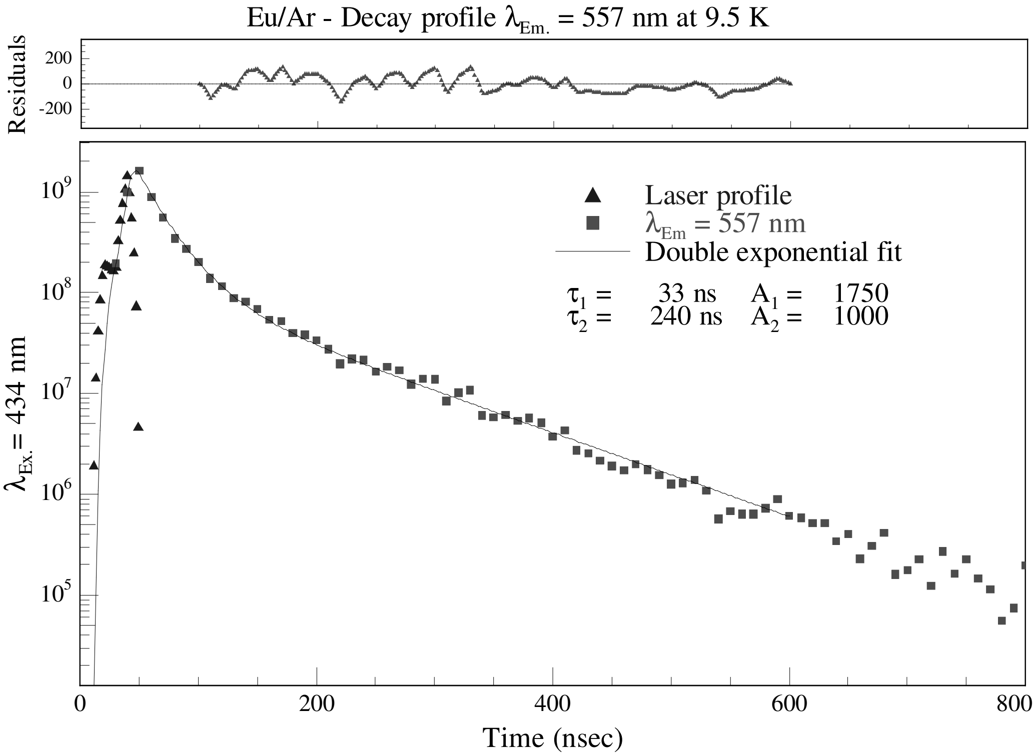

Figure IV.14 Decay profile of the Eu/Ar blue site emission at 557 nm recorded at 10 K in an annealed sample. The decay profile is convoluted with the temporal profile of the laser excitation source. The residual shown represents the difference between the recorded decay and the double exponential fit.

A lifetime consisting of two components $\tau_1 = 33$ and $\tau_2 = 240$ ns is identified at 9.5 K. The shorter component dominates the decay profile as indicated by its larger amplitude. In an attempt to identify the radiative lifetime of the 557 nm emission feature, temperature effects on the decay profile were investigated. Presented in the left panel of Figure IV.15 is the effect of increasing temperature on the decay profile. Inset of Figure IV.15 is a plot of lifetime components versus temperature. The shorter 33 ns component is unaffected by temperature change in the range 9.5 to 16 K. This indicates its true radiative lifetime is identified. However, the longer component shows a gradual decrease in magnitude at increased temperatures.

Steady-state emission spectra recorded at various temperatures show an unusual trend. From 9.5 to 14 K there is an increase in intensity followed by a decrease at higher temperatures. This may be due to activation of a non-radiative feeding step from the y^8P state up to 14 K followed by enhancement of other relaxation processes competing with the $z^6\text{P} \rightarrow a^8\text{S}$ electronic transition at T > 14 K.

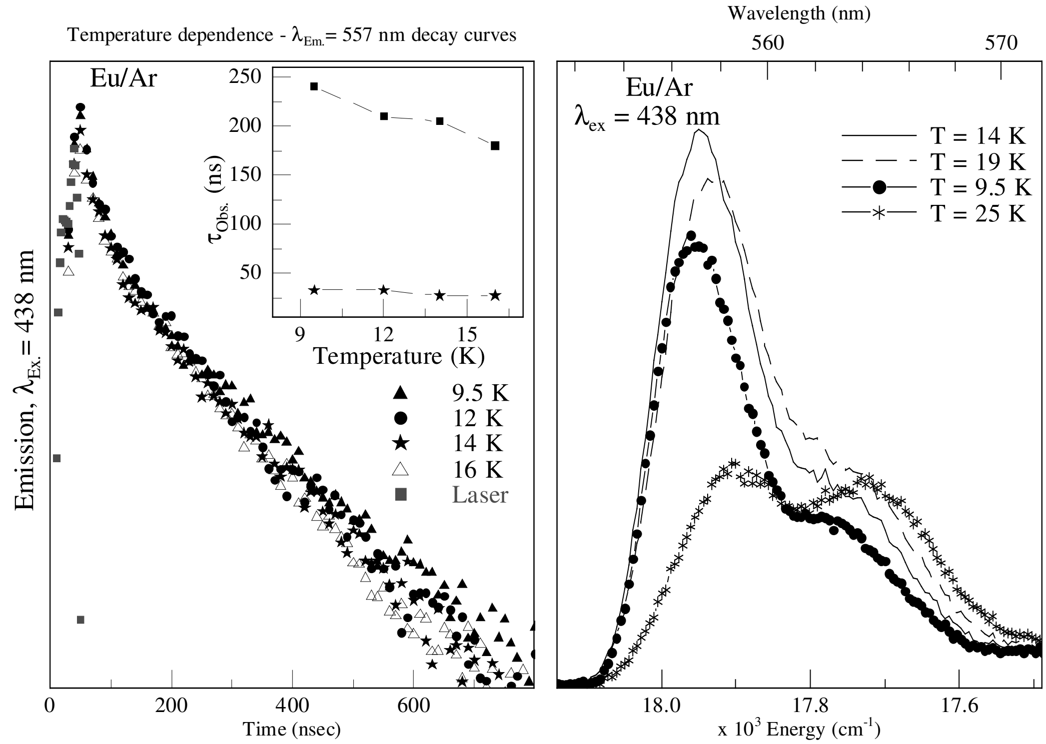

Figure IV.15 The decay profiles of the Eu/Ar blue site emission at 557 nm recorded at elevated temperatures in an annealed sample are displayed in left panel. Inset plots the lifetime components of these decay profiles versus temperature. The right panel presents steady-state emission spectra recorded with $y^8\text{P} \leftarrow a^8\text{S}_{7/2}$ excitation at 438 nm at various temperatures. The shoulder to lower energy at 563 nm is due to guest atoms occupying the red site of isolation.

IV.2.II.III Eu/Ar ($z^6P \rightarrow a^8S$) Summary

A comparison of the red and blue site z^6P emission is presented in Figure IV.16 along with the gas phase position of this electronic transition (dashed vertical line). The feature at approximately 17350 cm^{-1} (U) is due to some Eu atoms remaining in the thermally unstable site.

Based on its proximity to the gas phase transition and comparable lifetime values the emission features of atomic Eu observed at 563 and 557 nm in solid Ar are assigned as z^6P state relaxation exhibiting matrix shifts of + 426 and + 614 cm^{-1} with lifetime components of 72 and 280 ns and 33 and 240 ns respectively.

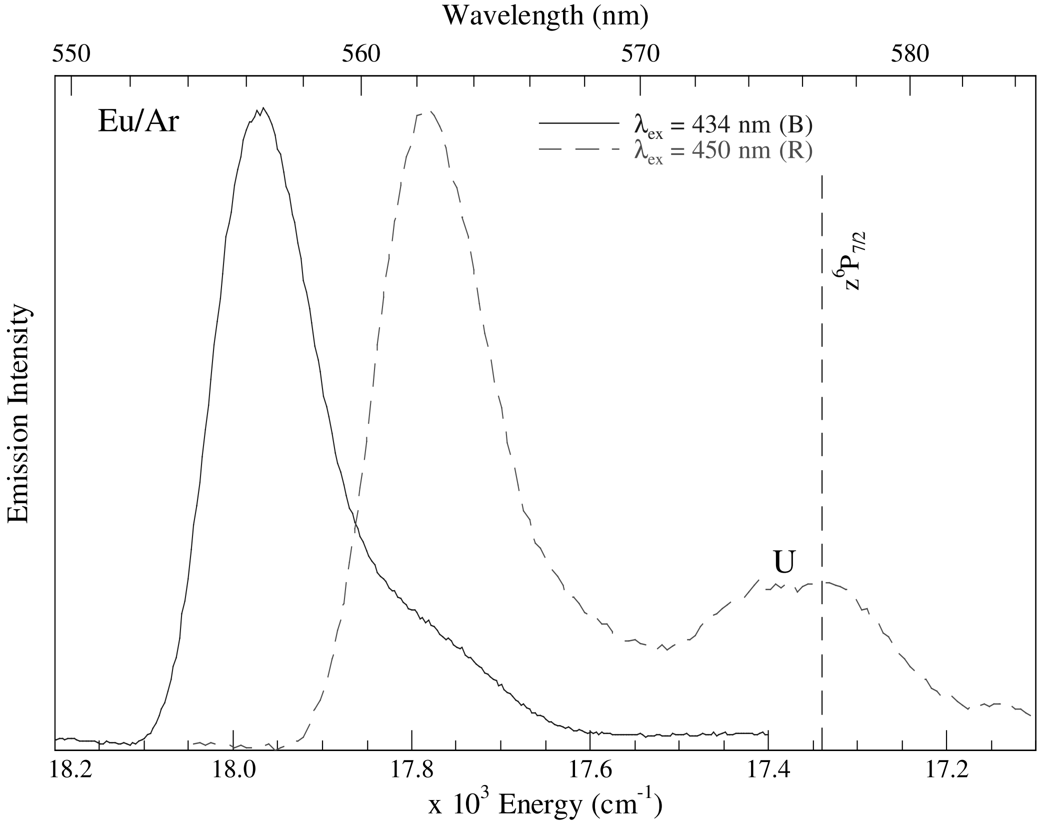

Figure IV.16 Emission spectra produced in the 560 nm spectral region with site-specific y^8P state excitation of Eu/Ar at 10 K following deposition at 10 K and sample annealing to 30 K. A minor amount of thermally unstable site emission (U) is observed due to some residual atoms remaining in this site. The gas phase position of the nearest P → S type electronic transition of atomic Eu, $z^6P_{7/2}$, is shown by the dashed vertical line.

IV.2.III Eu/Ar - $\lambda_{Em.} \approx 679$ nm

The emission features of lowest intensity from both sites in solid Ar are observed in the 679 nm spectral region and are presented in Figure IV.17. The blue site emission is centred at 682.6 nm (14650 cm^{-1}) with a bandwidth of 285 cm^{-1} while red site emission is centred at 675 nm (14815 cm^{-1}) exhibiting a bandwidth of 274 cm^{-1}. Interestingly, the blue site emission feature occurs to lower energy than the red site.

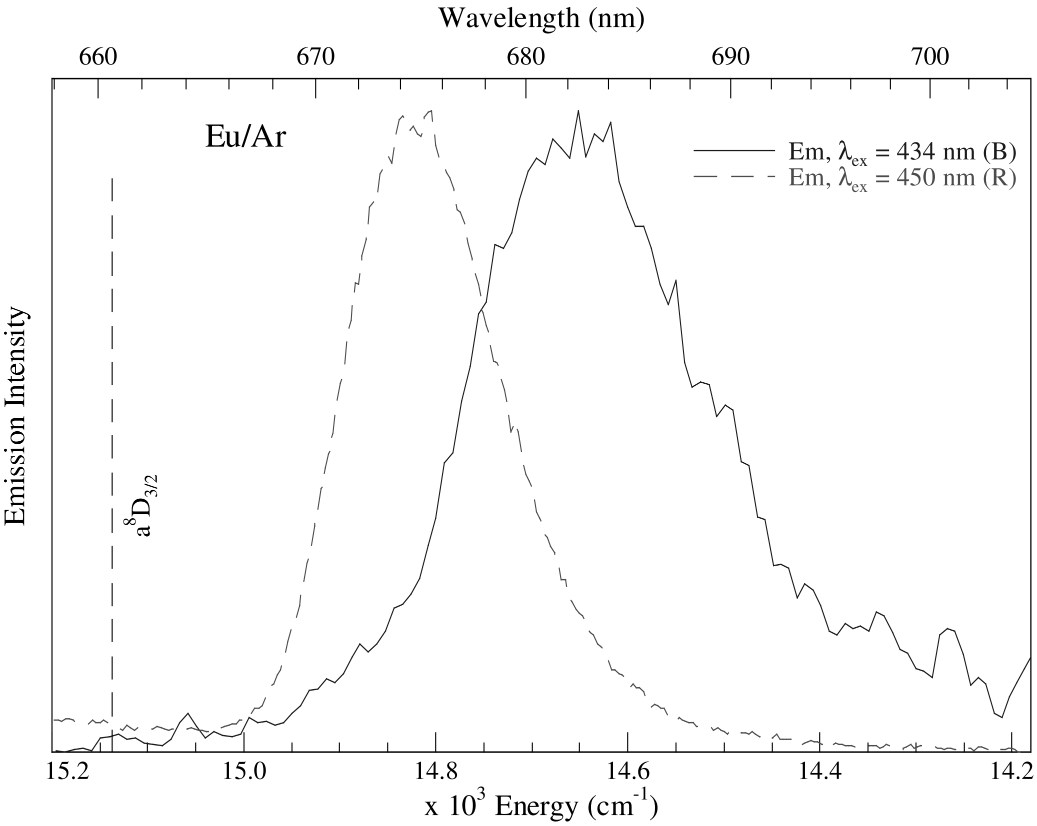

Figure IV.17 Emission spectra produced in the 679 nm spectral region with site-specific y^8P state excitation of Eu/Ar at 10 K following deposition at 10 K and sample annealing to 30 K. The spectral position of the nearest D → S type gas phase transition of atomic Eu, $a^8D_{3/2}$, is indicated by the dashed vertical line.

IV.2.III.I Red site

To assign this 675 nm emission its decay curve was recorded at 9.5 K and is presented in Figure IV.18. It exhibits a double exponential decay profile with lifetime components of 39 and 561 μs and amplitudes of 1382 and 162 respectively. Furthermore, its decay curve was recorded at elevated temperatures as presented in left panel of Figure IV.19. The shorter component dominates the decay, exhibiting larger amplitudes at both temperatures.

The right panel of Figure IV.19 presents the effect of increased temperature on the steady-state emission spectra. A gradual decrease in intensity is observed at increased temperatures, implying non-radiative feeding steps to lower energy excited states become activated.

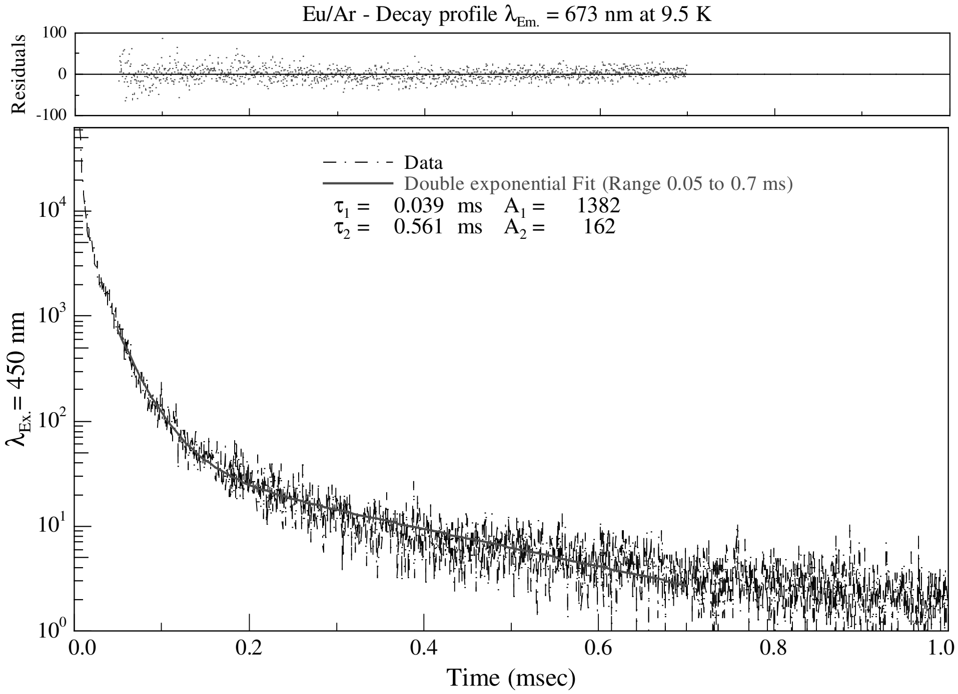

Figure IV.18 Decay profile of the 673 nm emission recorded at 10 K using the Single Photon Counting technique with red site y^8P state excitation at 450 nm. The residuals display the difference between the double exponential fit and the decay recorded.

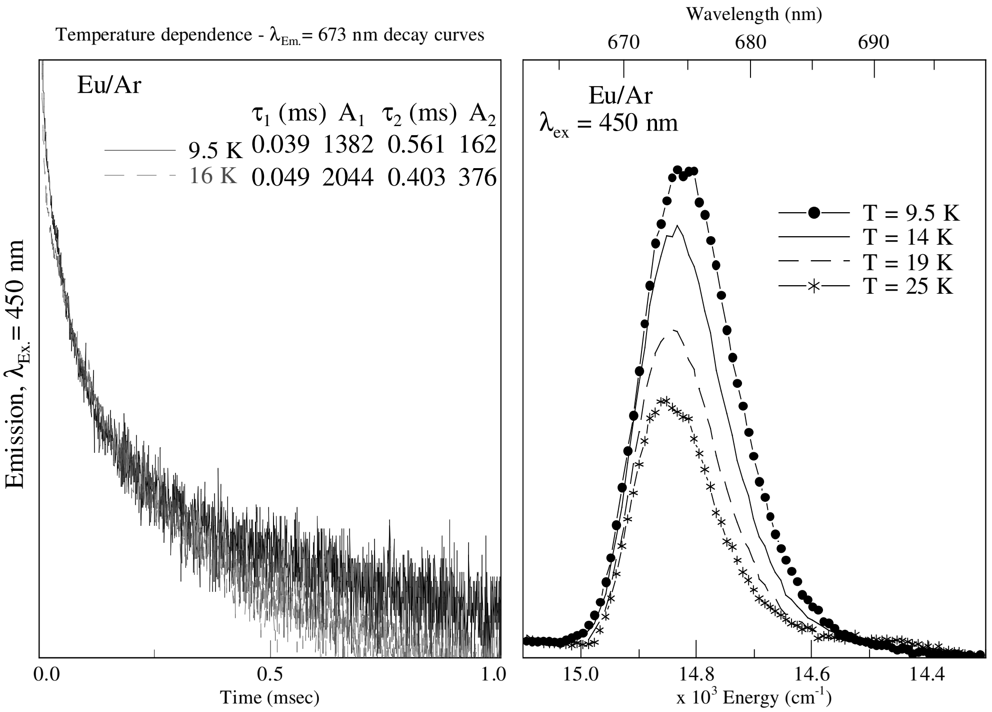

Figure IV.19 The decay profiles of the Eu/Ar red site emission at 673 nm recorded at 10 and 16 K in an annealed sample are displayed in left panel. Details of the double exponential fit components are shown inset. The right panel presents steady-state emission spectra recorded with $y^8\text{P} \leftarrow a^8\text{S}_{7/2}$ excitation at various temperatures.

IV.2.III.II Blue site

The corresponding blue site feature in the Ar matrix is observed at 683 nm. The temporal profile of this emission feature exhibited a double exponential lifetime with decay components of 52 and 199 μs at 9.5 K as shown in Figure IV.20.

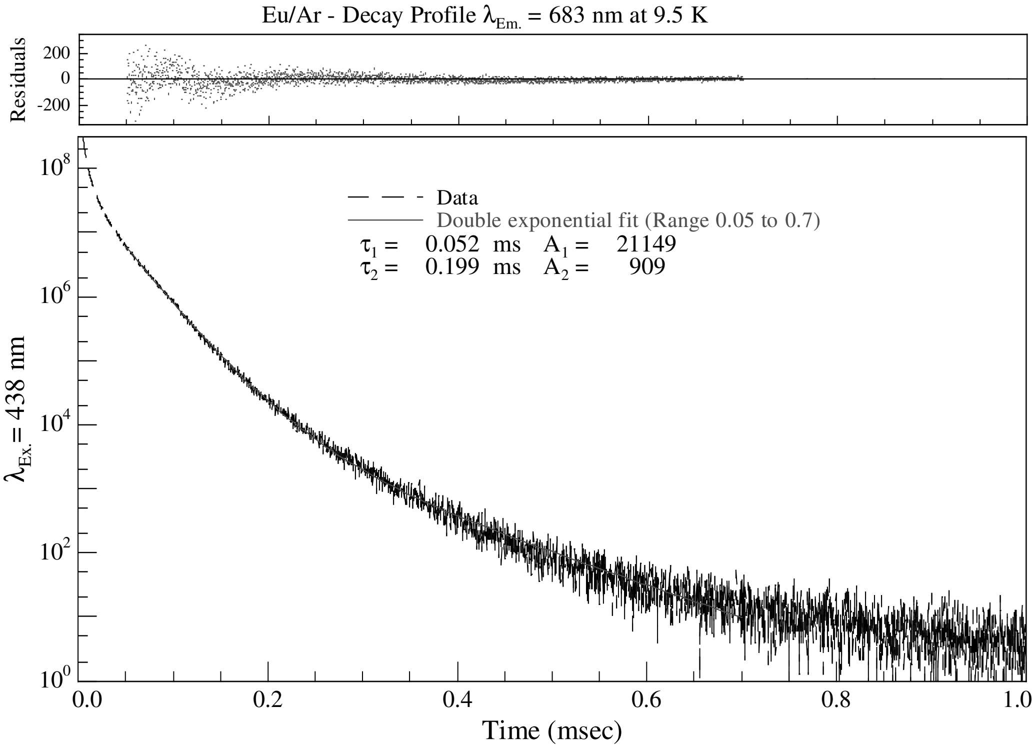

Figure IV.20 Decay profile of the 683 nm emission recorded at 10 K with blue site y^8P state excitation at 438 nm. The residuals present the difference between the double exponential fit and the recorded decay.

Also investigated was the effect of increased temperature on the decay profile as presented in Figure IV.21. There is no temperature dependence exhibited by the major lifetime component in the range 10 to 16 K. Thus a radiative lifetime of 52 μs is identified in solid Ar. Contrary to the red site emission, right panel of Figure IV.21 shows the blue site steady-state spectra display a progressive increase in emission intensity at higher temperatures.

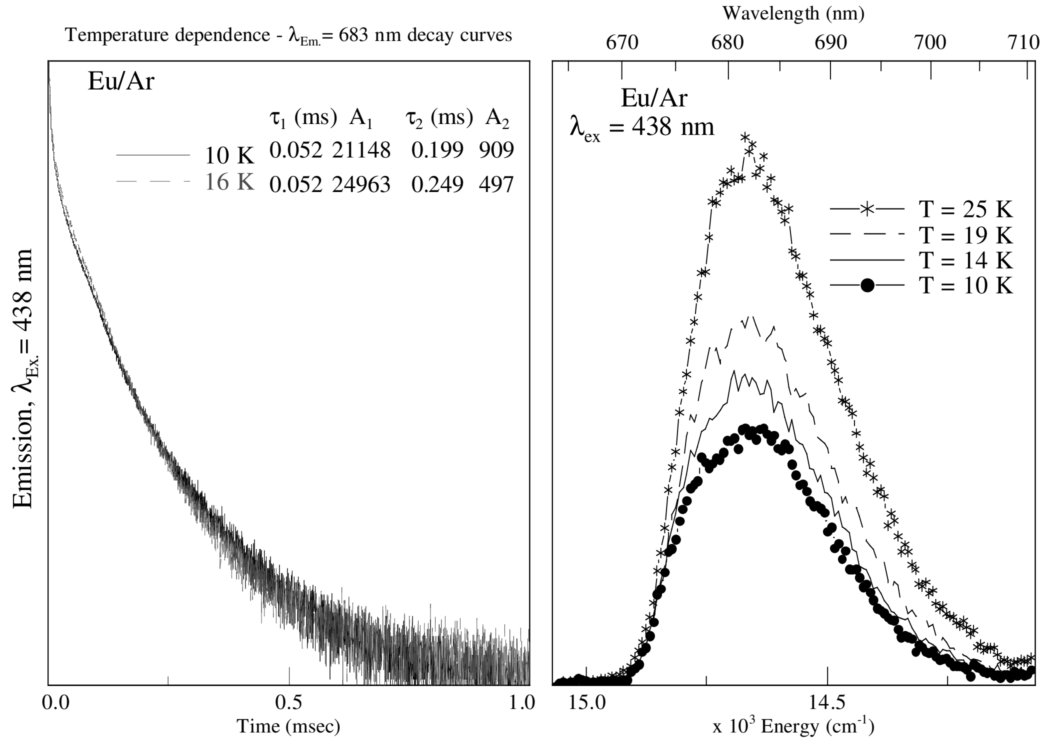

Figure IV.21 The decay profiles of the Eu/Ar blue site emission at 683 nm recorded at 10 and 16 K in an annealed sample are displayed in left panel. Details of the double exponential fit components are shown inset. The right panel presents steady-state emission spectra recorded with $y^8\mathrm{P} \leftarrow a^8\mathrm{S}_{7/2}$ excitation at various temperatures.

IV.2.III.III Eu/Ar ($a^8D \rightarrow a^8S$) Summary

The emission observed in solid Ar at 675 and 682.6 nm is long-lived, much longer lived than any P → S type transition in this region as evidenced by comparison with Table IV.1. This suggests it is an electric-dipole forbidden D → S transition. The nearest such type in the gas phase is $a^8\mathrm{D}_{3/2} \rightarrow a^8\mathrm{S}_{7/2}$ occurring at 660.6 nm (15137.7 cm^{-1}). Based on its temporal characteristics and spectral position this emission is assigned to the $a^8\mathrm{D} \rightarrow a^8\mathrm{S}$ transition of atomic Eu exhibiting double exponential decay profiles. Blue site emission from this D state occurs to lower energy than the red site, an energy reversal when compared to the P state emissions discussed earlier.

IV.2.IV Eu/Ar - $\lambda_{Em.} \approx 800$ *nm*

The final emission features observed in solid Ar occur in the 800 nm spectral region. Presented in Figure IV.22 is an overlap of the steady-state emission spectra in this region produced with both blue and red site y^8P state excitation. Excitation spectra confirm the 791 nm emission feature originates from Eu atoms isolated in the red site whilst the second band centred at 814 nm occurs from the blue site of isolation in the Ar matrix.

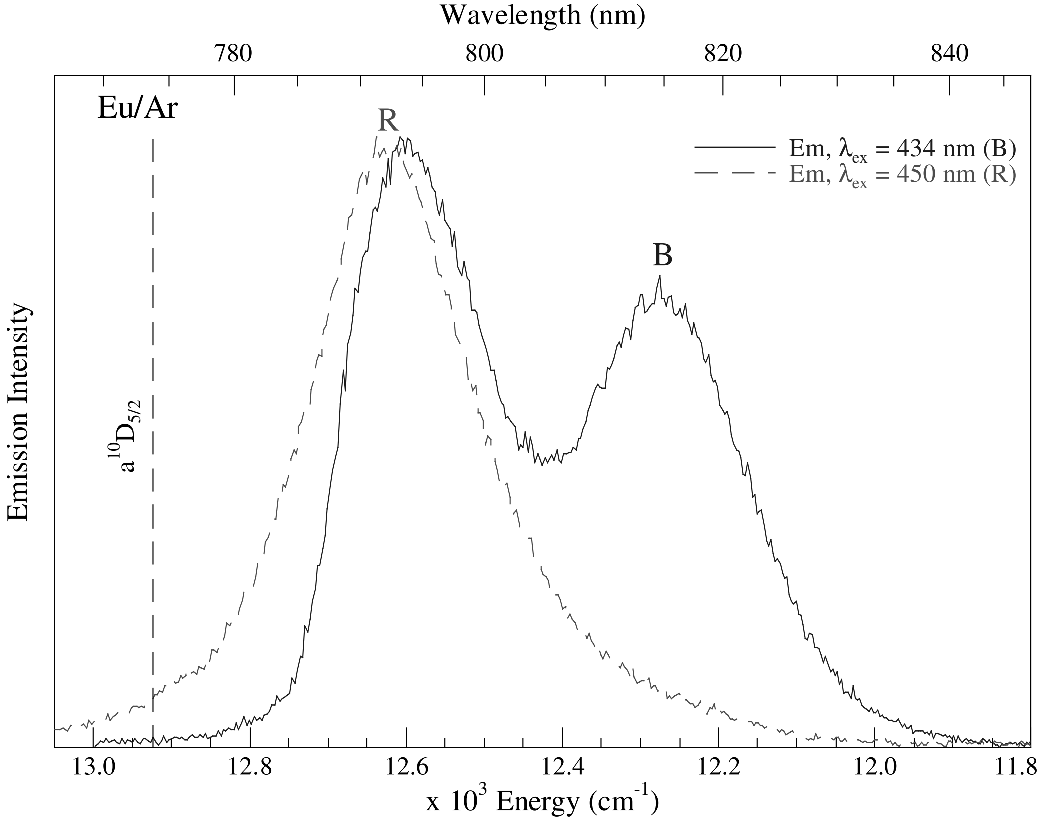

Figure IV.22 Emission spectra of Eu/Ar at 10 K following deposition at 10 K and sample annealing to 30 K produced in the 800 nm spectral region with site-specific y^8P state excitation. The spectral position of the nearest gas phase transition of atomic Eu, $a^{10}D_{5/2}$, is indicated by the dashed vertical line.

IV.2.IV.I *Red site*

The nearest gas phase electronic transition to the 791 nm emission is the metastable $a^{10}D_{5/2} \leftrightarrow a^8S_{7/2}$ occurring at 773.77 nm (12923.72 cm^{-1}). The decay characteristics of this emission feature in the matrix were recorded and exhibit a long-lived double exponential profile as presented in Figure IV.23.

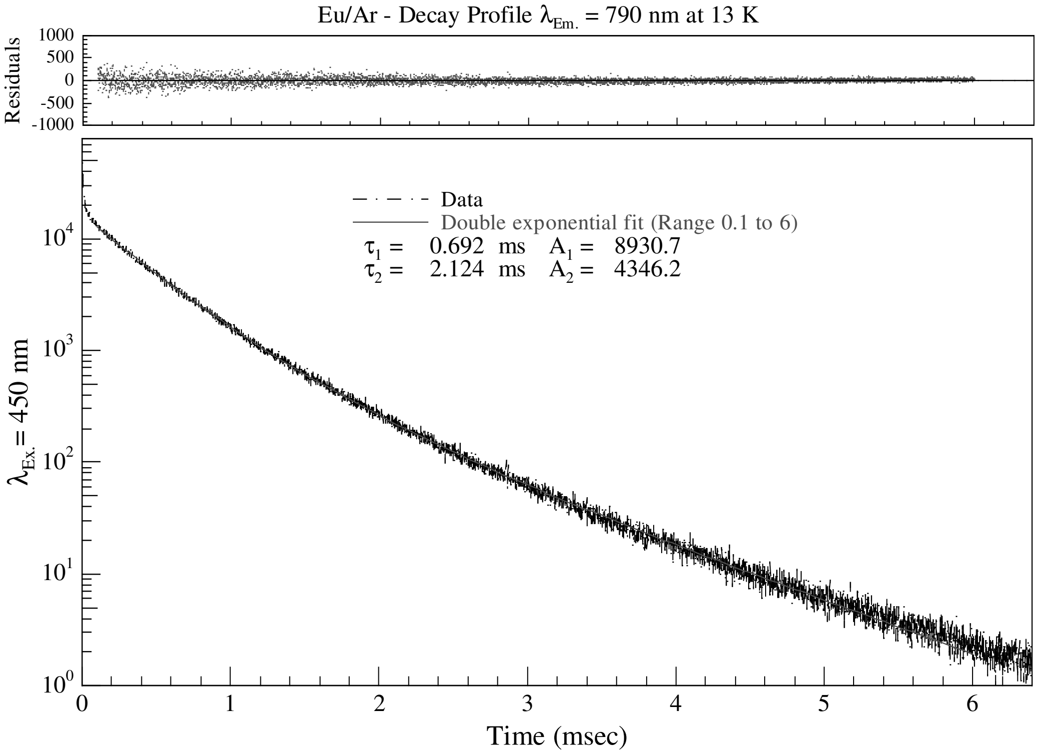

Figure IV.23 Temporal profile of the 790 nm emission recorded with red site y^8P state excitation. The residuals present the difference between the double exponential fit and the recorded decay.

The major component yields a lifetime of 0.69 ms and the minor component one of 2.12 ms. This long-lived nature is characteristic of an electric-dipole forbidden transition, such as a D → S type electronic transition, further suggesting the a^{10}D state as the source of the observed emission. As seen in left panel of Figure IV.24 the decay profile is completely temperature independent up to 27 K, thus the radiative lifetime of the 791 nm emission is identified in solid Ar yielding matrix corrected lifetime components of 1.4 and 4.3 ms.

Presented in right panel of Figure IV.24, increased temperature causes an increase in 791 nm emission feature's intensity. This originates from the fact that the a^{10}D state is the lowest energy excited state above the ground state and is populated by relaxation from the upper y^8P state. Increasing the temperature improves the efficiency of internal conversion/intersystem crossing occurring in the relaxation process to this metastable a^{10}D state thus increasing its emission intensity.

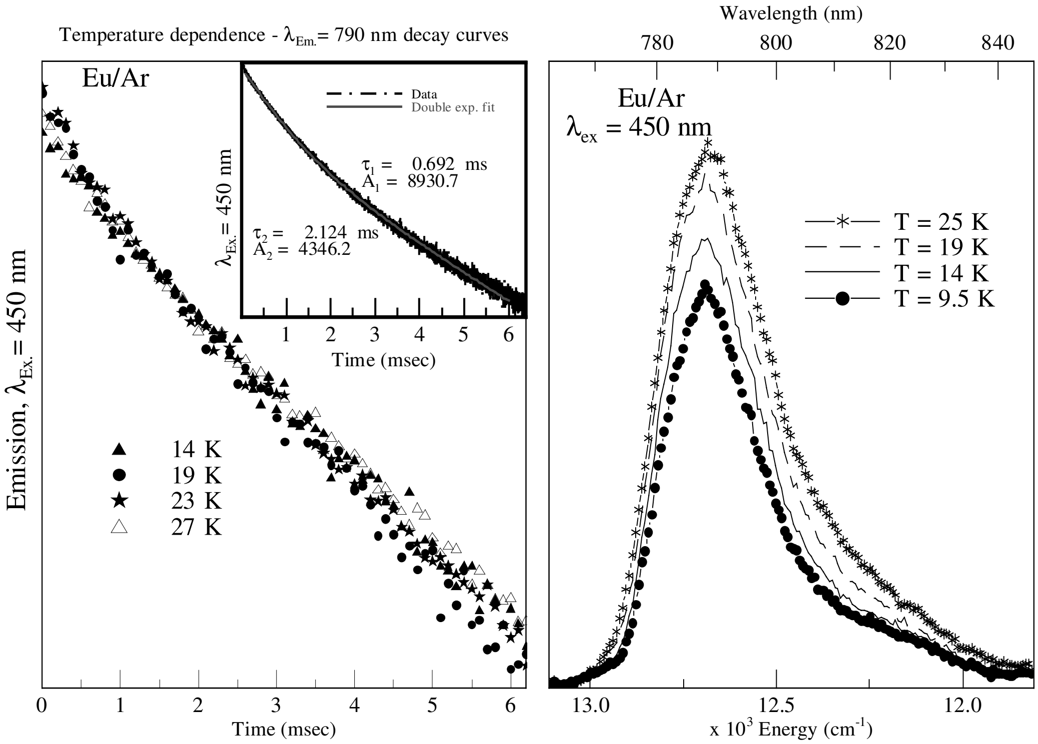

Figure IV.24 Left panel displays the decay profiles of the Eu/Ar red site emission at 790 nm recorded at elevated temperatures in an annealed sample. Inset shows the double exponential fit overlaid with the experimental data. The right panel presents steady-state emission spectra recorded with y^8P ← a^8S$_{7/2}$ excitation at various temperatures.

IV.2.IV.II Blue site

To verify the assignment of the corresponding blue site emission feature observed at 814 nm its decay characteristics were recorded. Figure IV.25 presents the decay profile overlapped with a double exponential fit yielding a lifetime made up of two components of 0.413 and 1.343 ms with amplitudes of 4770 and 4042 respectively. The very long-lived nature of the 814 nm emission feature in solid Ar again supports assignment of this feature as resulting from a^{10}D → a^8S relaxation.

Presented in left panel of Figure IV.26 are the effects of temperature on the emission decay profile. The temporal profile is not effected by temperature change in the range up to 19 K thus indicating the true radiative lifetime of the transition is observed in the Ar matrix. Similar to the case for the corresponding red site emission there is a progressive increase in emission intensity at higher temperatures due to enhanced relaxation to the metastable state from higher energy excited states as seen in right panel of Figure IV.26.

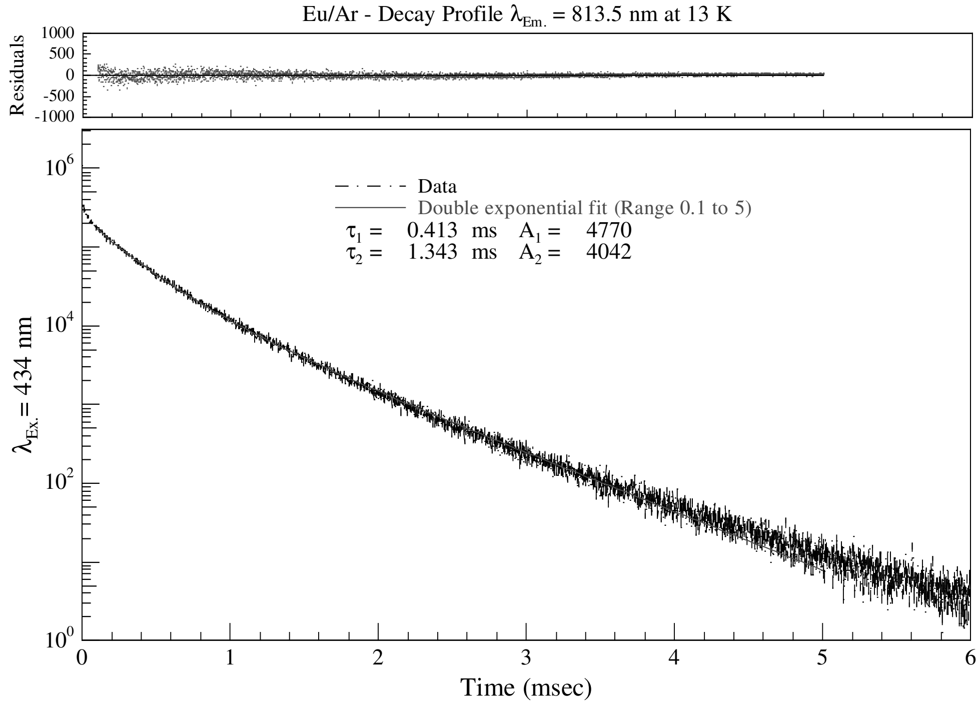

Figure IV.25 Decay profile of the 814 nm emission recorded with blue site y^8P state excitation. The residuals present the difference between the double exponential fit and the recorded decay.

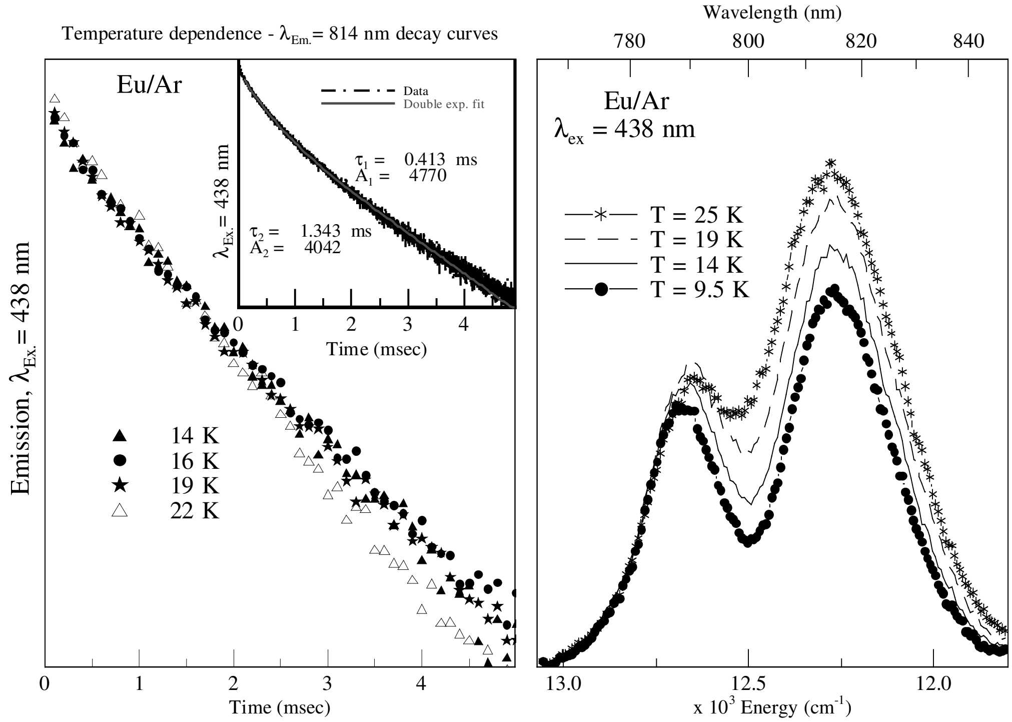

Figure IV.26 The decay profiles of the Eu/Ar blue site emission at 819 nm recorded at elevated temperatures in an annealed sample are displayed in left panel. Inset shows the double exponential fit overlaid with the experimental data. The right panel presents steady-state emission spectra recorded with y^8P state excitation at various temperatures.

IV.2.IV.III Eu/Ar ($a^{10}D \rightarrow a^8S$) Summary

The lowest energy emission feature in solid Ar is observed from the red and blue sites at 791 and 814 nm respectively and displayed in Figure IV.22. Both exhibit long-lived double exponential decays implying a forbidden D → S transition as the source. Based on their spectral location they are assigned as emission from the a^{10}D metastable state. Consistent with previous D state emission features, the blue site is observed to emit to lower energy than the red site for the ^{10}D state.

IV.2.V Eu(y^8P)/Ar Luminescence Summary

A summary of the luminescence of Eu atoms in the two thermally stable sites of isolation in solid Ar is presented in Figure IV.27. Dashed vertical lines represent the gas phase position of each of the assigned electronic transitions for comparison purposes.

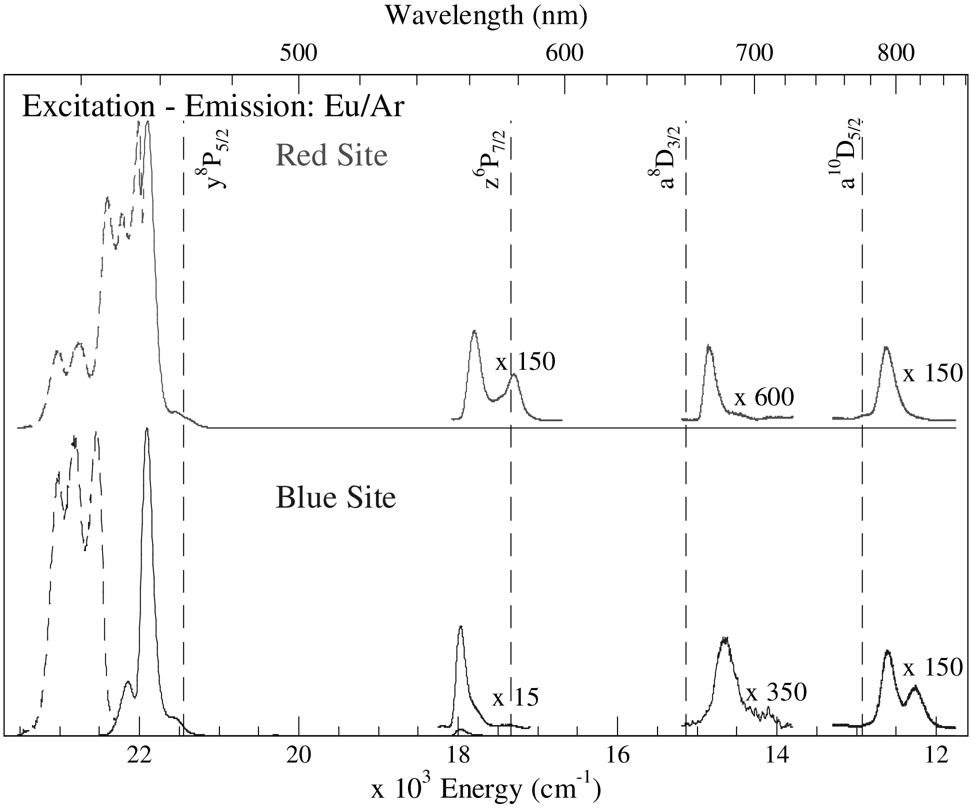

Figure IV.27 Emission spectra recorded at 10 K for the Eu/Ar system with site-selective lamp excitation of the Eu y^8P ← $a^8S_{5/2}$ transition. The excitation spectra were recorded by monitoring emission at 457 / 563 / 675 / 791 nm (top) and 452 / 557 / 683 / 814 nm (bottom) for the red and blue sites respectively and are shown by the dashed traces to the left. Spectra were recorded following Eu/Ar sample deposition at 10 K and matrix annealing to 30 K. The spectral positions of the assigned gas phase transitions of atomic Eu are shown by the dashed vertical lines.

Four emission features are produced with both blue and red site y^8P state excitation. They are centred at 452, 557, 683 and 814 nm for the blue site and 457, 563, 675 and 791 nm for the red site. These emission bands are assigned as resonance fluorescence from the y^8P state and optical relaxation of the z^6P and a^8D states to the ground state and emission from the metastable a^{10}D state respectively. The spectral and temporal characteristics of these emissions are presented in Table IV.2 with their state assignments. These assignments are made based on each feature's proximity to the corresponding transition in the gas phase and lifetime measurements.

Table IV.2 Photophysical characteristics of the emission features of the thermally stable sites of isolation (Red and Blue) in Eu/Ar revealed in the site-specific luminescence study of the y^8P ($4f^7 6s^1 6p^1$) state of atomic europium. The spectral position, λ, is quoted in nanometres (nm) and wavenumber (cm^{-1}) units. The bandwidth (full width at half maximum, *fwhm*) is denoted as Δ in wavenumber units. Gas phase to matrix frequency shifts for the assigned atomic Eu transition, δ, are displayed in wavenumber units. The observed lifetimes recorded in the matrix at 10 K are labelled τ_{10K}.

Gas Phase[1]		Eu(y^8P)/Ar Matrix Emission Features							
		Red Site				Blue Site			
Transition (nm / cm^{-1})	τ_{gp} (ns)	λ_{em} (nm / cm^{-1})	Δ (cm^{-1})	δ (cm^{-1})	τ_{10K}	λ_{em} (nm / cm^{-1})	Δ (cm^{-1})	δ (cm^{-1})	τ_{10K}
$y^8P_{5/2} \leftrightarrow a^8S_{7/2}$ 466.3 21444.58	7.7	457.3 21867	167	+ 422	3.5ns	451.6 22141	192	+ 697	2.3ns
$z^6P_{7/2} \leftrightarrow a^8S_{7/2}$ 576.68 17340.65	909.1	562.9 17767	144	+ 427	**72ns** 280ns	557 17954	125	+ 614	**33ns** 240ns
$a^8D_{3/2} \leftrightarrow a^8S_{7/2}$ 660.6 15137.7	-	675 14815	274	– 323	**39 μs** 561μs	682.6 14650	285	– 488	**52 μs** 199 μs
$a^{10}D_{5/2} \leftrightarrow a^8S_{7/2}$ 773.77 12923.7	-	790.6 12649	203	– 275	**0.7ms** 2.1ms	814.3 12281	281	– 643	**0.4ms** 1.3ms

IV.3 Eu(y^8P)/Kr Luminescence

Absorption and excitation spectra of atomic Eu isolated in solid Kr recorded in the region of the gas phase $y^8P \leftarrow a^8S_{7/2}$ transition allowed the identification of three sites of isolation in freshly deposited Kr samples. A higher energy blue site centred at 450.8 nm (22182 cm^{-1}) and a red site centred at 462 nm (21645 cm^{-1}) are present following annealing as seen in left panel of Figure IV.28.

Right panel of Figure IV.28 presents the emission spectra produced with site-selective excitation of the $y^8P \leftarrow a^8S_{7/2}$ transition in an annealed sample. Inspection of the emission profiles reveal four features at 465, 571, 683 and 816 nm from guest atoms isolated in the blue site and three features centred at 468, 576 and 789 nm pertaining to the red site. The following sections assign the observed emission to electronic transitions of atomic Eu isolated in solid Kr.

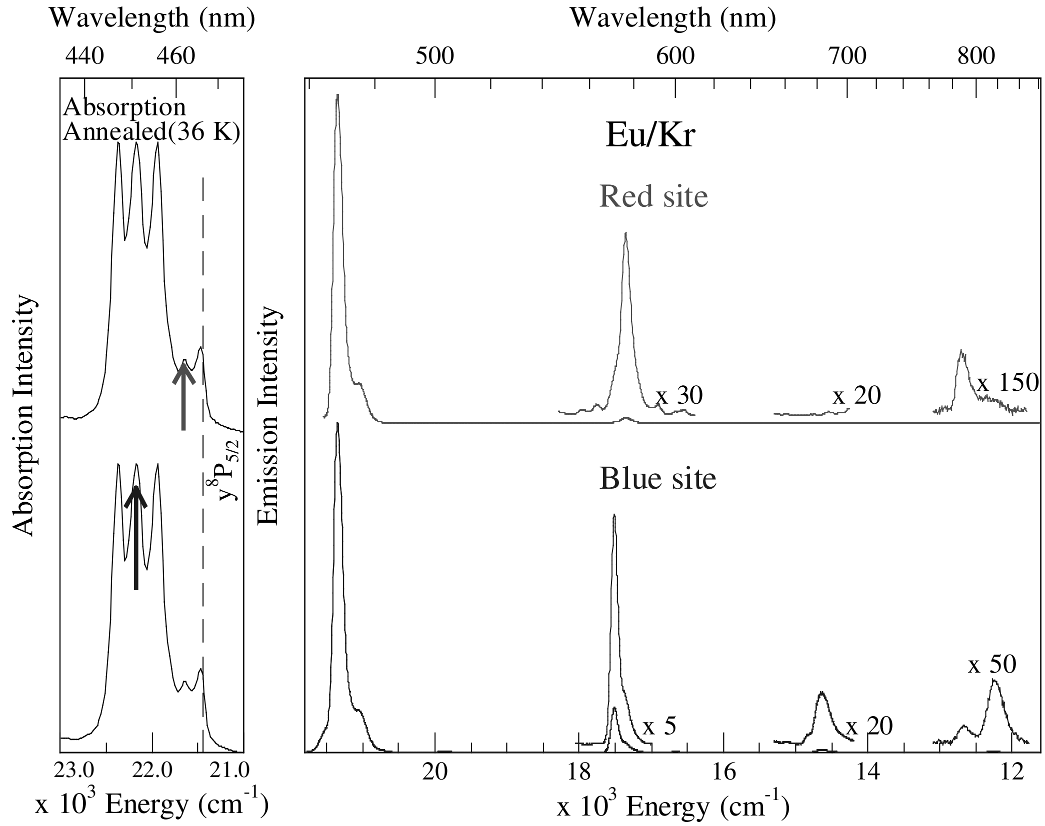

Figure IV.28 Absorption and emission spectra of Eu/Kr in the visible spectral region at 10 K following sample deposition at 10 K and sample annealing to 36 K. The spectral position of the gas phase y^8P state transition of atomic Eu is shown by the dashed vertical line. Left panel displays the y^8P state absorption spectra, arrows indicate the site-specific excitation wavelengths used to produce the emission spectra seen in right panel.

IV.3.I Eu/Kr - $\lambda_{Em.} \approx 467$ nm

Three emission bands are observed in this region centred at 465, 468 and 474 nm. Excitation spectra, as seen in Figure IV.29, attribute these features as resulting from the blue (B), red (R) and the thermally unstable (U) sites of isolation respectively.

The blue feature exhibits a Stokes shift of 657 cm^{-1}, much larger than the corresponding red site's value of 292 cm^{-1}, suggesting a larger repulsive interaction of the excited state in the blue site. As was the case in Ar matrices, blue site excitation causes emission from all three sites in this region due to the spectral overlap of the blue site emission centred at 465 nm and red site absorption feature centred at 468 nm. Some thermally unstable site emission (U) is also observed due to re-absorption of red site emission by a minimum amount of metal atoms remaining in the thermally unstable site.

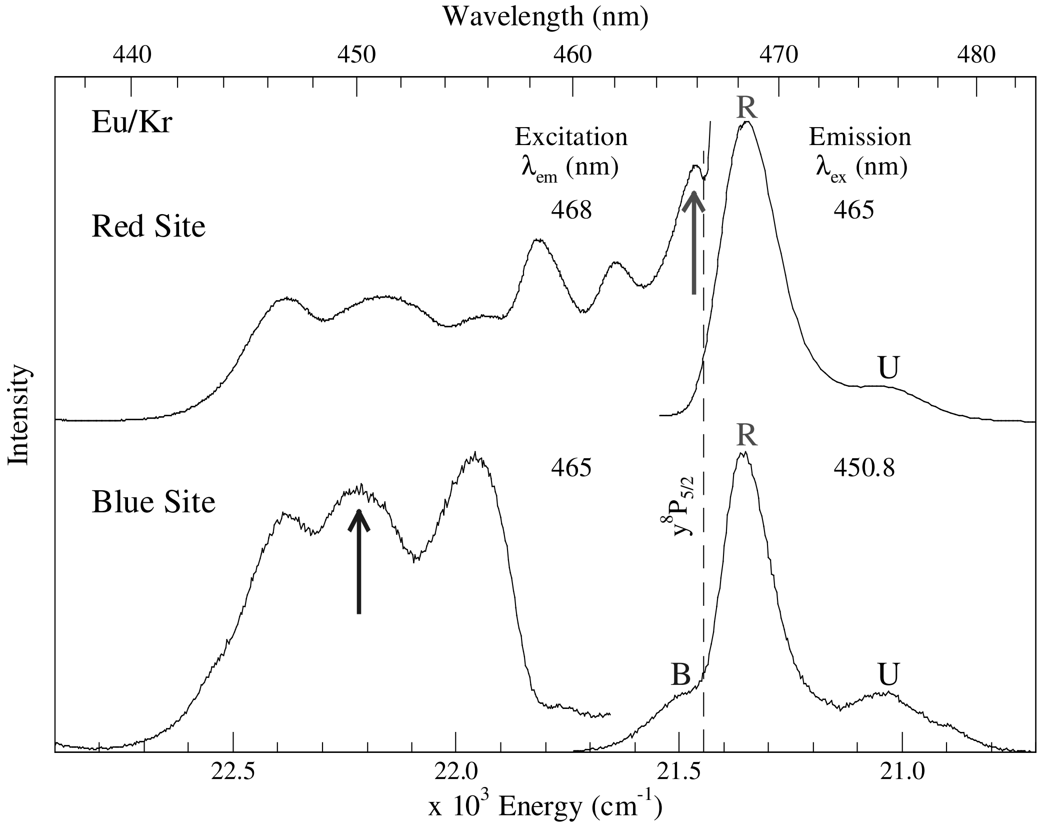

Figure IV.29 Site-specific excitation and emission spectra of Eu/Kr in the y^8P spectral region at 10 K following deposition at 10 K and sample annealing to 36 K. Arrows indicate the excitation wavelengths producing the observed emission spectra. A minor amount of thermally unstable site emission (U) is observed due to some residual atoms remaining in this site. The spectral position of the gas phase y^8P state transition of atomic Eu is shown by the dashed vertical line.

IV.3.I.I Red site

The red-site emission feature is observed at 468.3 nm (21352 cm^{-1}). The nearest gas phase electronic transition is the $y^8P_{5/2} \leftrightarrow a^8S_{7/2}$ transition occurring at 466.32 nm (21444.58 cm^{-1}) suggesting $y^8P \rightarrow a^8S$ relaxation is the source of this emission in solid Kr exhibiting a red matrix shift of – 92 cm^{-1}. The temporal profile of this emission feature is presented in Figure IV.30.

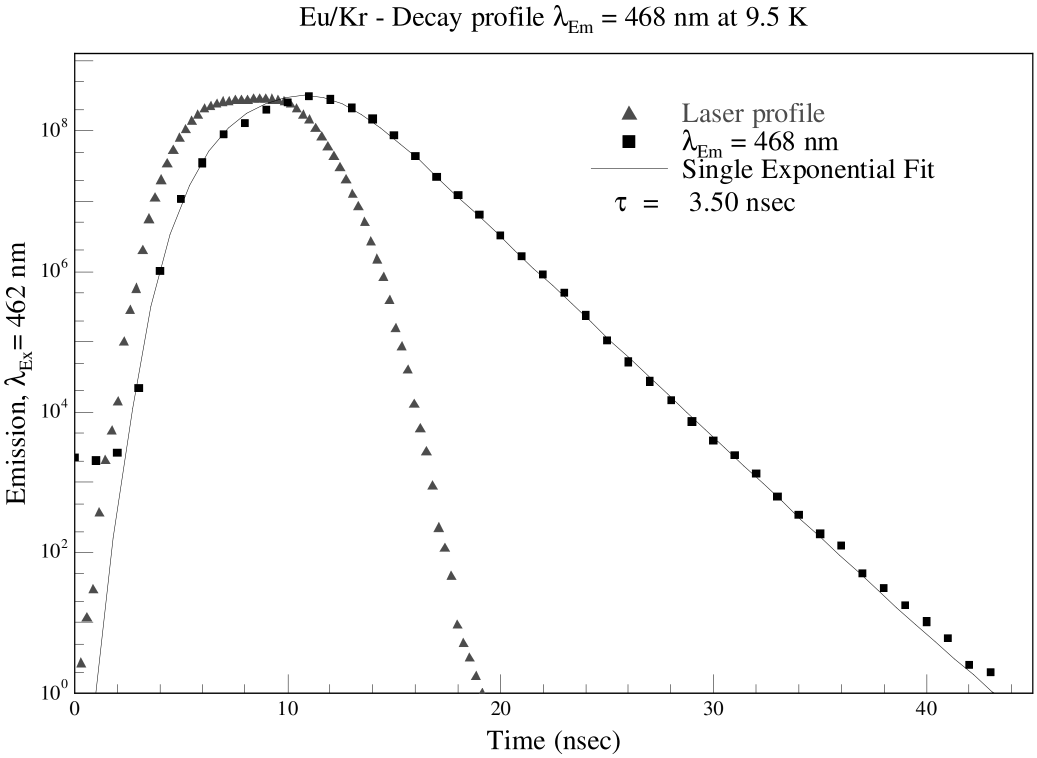

Figure IV.30 Decay profile of the Eu/Kr red site emission at 468 nm recorded at 10 K in an annealed sample. The decay profile is convoluted with the temporal profile of the laser excitation source at 462 nm.

A lifetime of 3.5 ns is extracted at 9.5 K which compares favourably to the known gas phase lifetime of 7.7 ns for the $y^8P_{5/2} \leftrightarrow a^8S_{7/2}$ transition. It is observed in left panel of Figure IV.31 that the decay profile is unaffected by temperature changes in the 9.5 to 16 K range. Thus the true radiative lifetime has been identified in solid Kr to be 3.5 ns. When corrected for the effective field of the surrounding matrix, a lifetime of 9.1 ns is obtained which is in good agreement with the gas phase value and establishes assignment of this feature to the $y^8P \rightarrow a^8S$ transition. Furthermore, temperature effects on the steady-state emission spectra show little change in intensity up to 16 K. However, at further elevated temperatures a gradual decrease in emission intensity occurs, as seen in right panel of Figure IV.31, suggesting activation of other non-radiative relaxation processes.

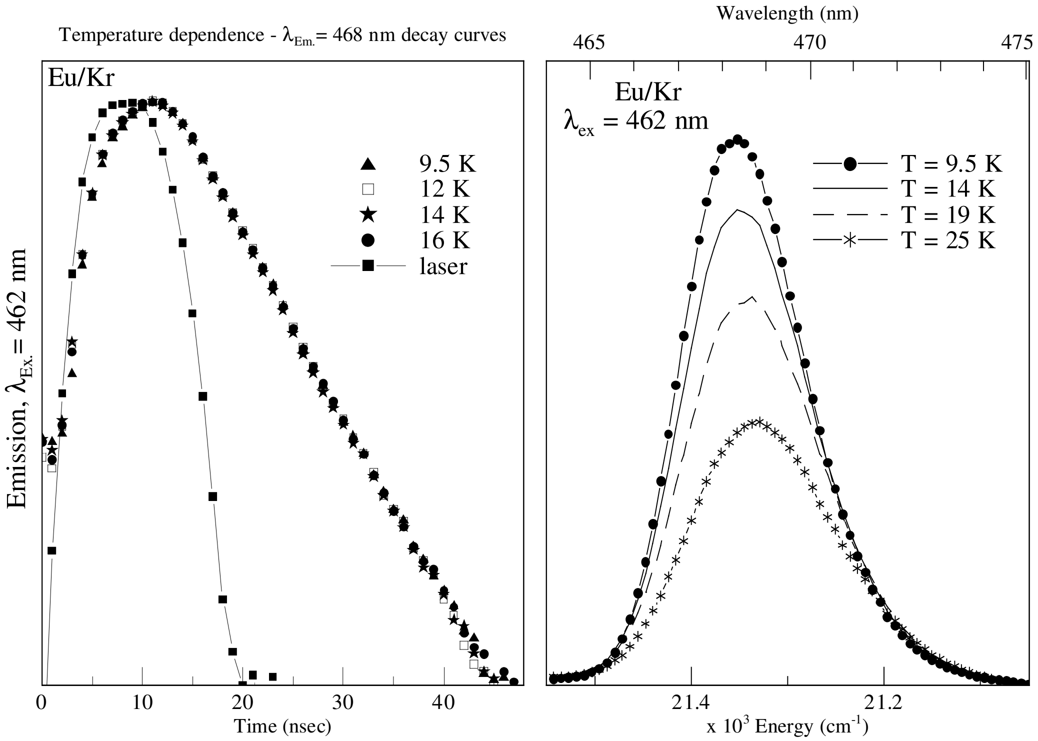

Figure IV.31 Left panel displays the decay profiles of the Eu/Kr red site emission at 468 nm recorded at elevated temperatures in an annealed sample. Right panel presents steady-state emission spectra recorded with y^8P ← a^8S$_{7/2}$ excitation at 462 nm at various temperatures.

IV.3.I.II Blue site

In this section the corresponding blue-site emission feature centred at 464.6 nm (21523 cm^{-1}) is assigned. To aid in the assignment of this emission feature its temporal characteristics with direct y^8P state blue site excitation were recorded and are presented in Figure IV.32.

A lifetime of 1.65 ns is extracted at 9.5 K. This value compares very well to the y^8P state lifetime observed in the red site of solid Kr (3.5 ns). In an attempt to identify the radiative lifetime of this feature the effects of increased temperature on the decay profile were investigated and are presented in left panel of Figure IV.33. Even in the temperature range 9.5 to 12 K the radiative lifetime has not been identified implying some non-radiative process is competing quite significantly with the electronic transition at these low temperatures.

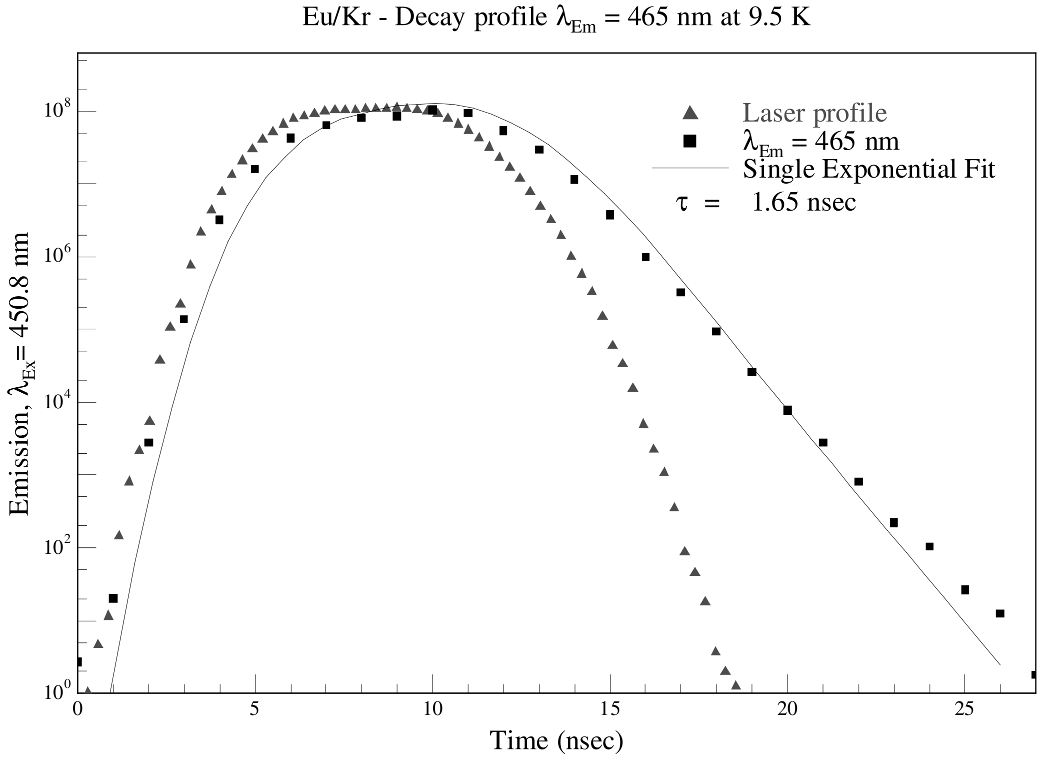

Figure IV.32 Decay profile of the Eu/Kr blue site emission at 465 nm recorded at 10 K in an annealed sample. The decay profile is convoluted with the temporal profile of the laser excitation source at 450.8 nm.

Steady-state emission spectra recorded at increasing temperatures showed a gradual decrease in emission strength at steps of 14, 19 and 25 K as seen in right panel of Figure IV.33. This effect was completely reversible and the original spectrum was obtained again upon returning to 9.5 K implying a feeding step to lower energy level(s) is activated at higher temperatures.

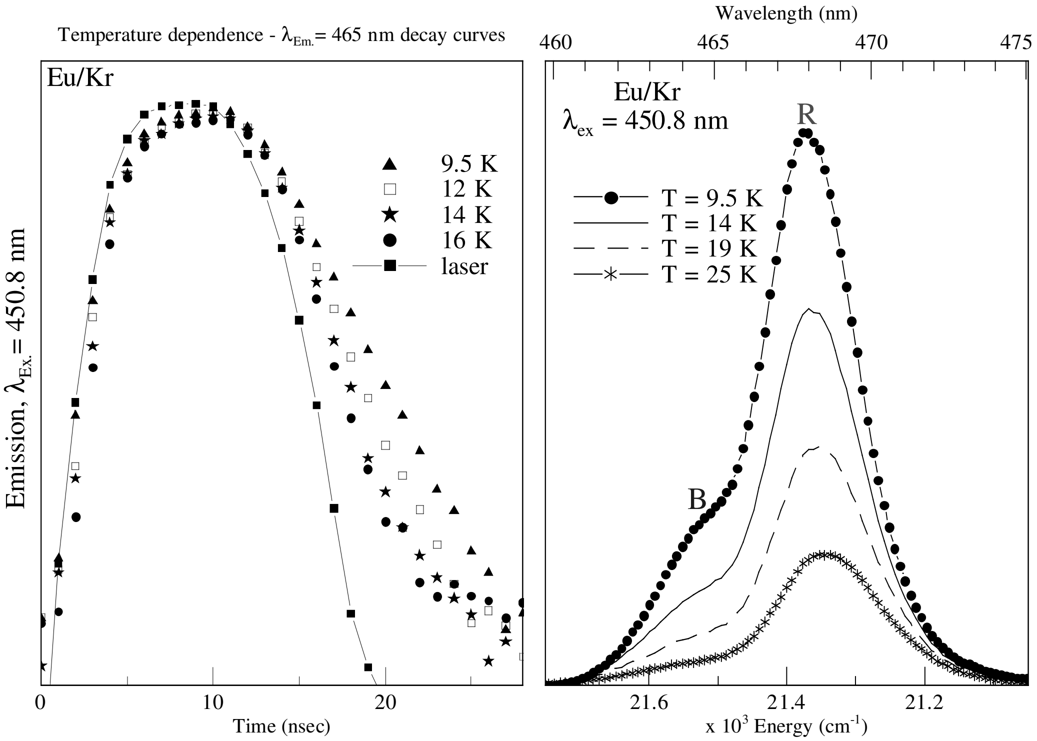

Figure IV.33 Decay profiles of the Eu/Kr blue site emission at 465 nm recorded at elevated temperatures in an annealed sample are displayed in left panel. Right panel presents steady-state emission spectra recorded with $y^8P \leftarrow a^8S_{7/2}$ excitation at 450.8 nm at various temperatures.

IV.3.I.III Eu/Kr ($y^8P \rightarrow a^8S$) Summary

In summary, y^8P state excitation produces emission features at 465 and 468 nm in solid Kr. Based on their spectral location and lifetime values these features are assigned as $y^8P \rightarrow a^8S_{7/2}$ resonance fluorescence of atomic Eu occurring from both the red and blue sites of isolation in the solid. Steady-state emission spectra show a decrease in intensity at elevated temperatures due to activation of non-radiative relaxation processes competing with the electronic transition. The blue site emission exhibits a Stokes shift value almost twice that of the red site implying the y^8P excited state experiences a much stronger repulsive interaction with the surrounding lattice in the blue site of isolation.

IV.3.II Eu/Kr - $\lambda_{Em.} \approx 573$ nm

The emission feature of second-greatest intensity in the Kr matrix is located in the 573 nm spectral region. Two site-specific emission features are observed as presented in Figure IV.34.

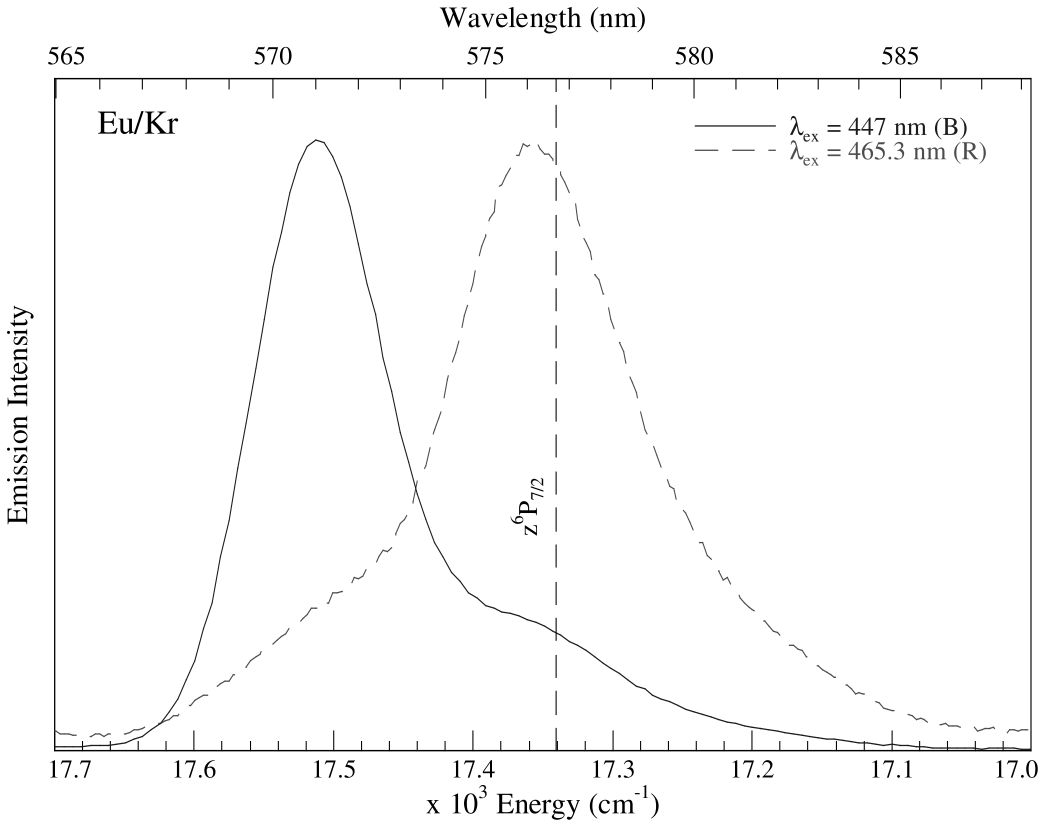

Figure IV.34 Emission spectra produced in the 573 nm spectral region with site-specific y^8P state excitation of Eu/Kr at 10 K following deposition at 10 K and sample annealing to 36 K. The spectral position of the nearest P → S type gas phase transition of atomic Eu, $z^6P_{7/2}$, is shown by the dashed vertical line.

Excitation spectra recorded in the region of the $y^8P \leftarrow a^8S$ transition indicate the high energy feature centred at 570.9 nm is due to emission from Eu atoms isolated in the blue site and the feature located at 576 nm results from atoms in the red site in solid Kr.

IV.3.II.I Red site

The red site emission centred at 576.3 nm displays a bandwidth of 176 cm^{-1}. The nearest gas phase transition in this region is the $z^6P_{7/2} \rightarrow a^8S_{7/2}$ electronic transition occurring at 576.68 nm (17340.65 cm^{-1}) representing a blue matrix shift of 10 cm^{-1}. In order to assign the electronic state producing this emission, its temporal profile was recorded with y^8P state excitation and is presented in Figure IV.35.

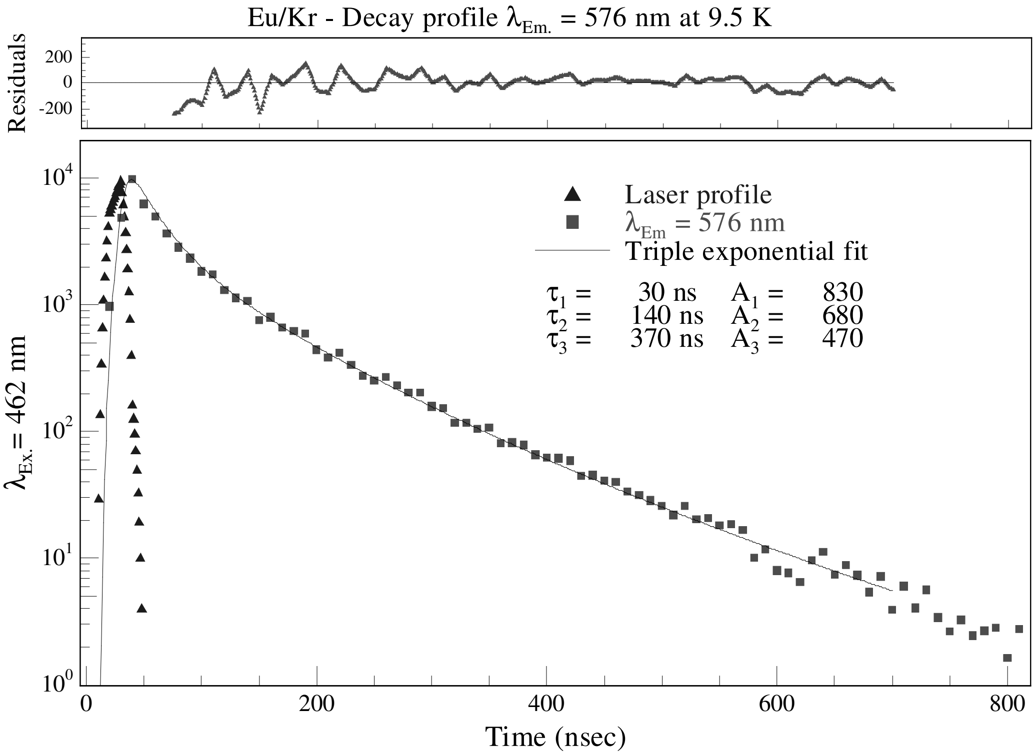

Figure IV.35 Decay profile of the Eu/Kr red site emission at 576 nm recorded at 10 K in an annealed sample. The decay profile is convoluted with the temporal profile of the laser excitation source at 462 nm. The residual shown represents the difference between the recorded decay and the triple exponential fit.

The recorded emission decay is complex, a triple exponential fit was required. A satisfactory fit was obtained with three lifetime components of 30, 140 and 370 ns and amplitudes of 830, 680 and 470 respectively. In an attempt to identify the radiative lifetime of this emission feature its decay profile was recorded at increased temperature and is observed to be temperature independent in the range 9.5 to 16 K as shown in Figure IV.36. The radiative lifetime is identified allowing matrix corrected values of 78, 362 and 958 ns to be obtained. A comparison with the gas phase z^6P$_{7/2}$ ↔ a^8S$_{7/2}$ transition reveals a lifetime of similar magnitude of 909.1 ns, thus allowing assignment of this emission as resulting from z^6P state relaxation to the ground state.

Also, the effects of increased temperature on the steady-state emission spectra showed a gradual increase in intensity at steps of 14, 19 and 25 K. This is most likely caused by the feeding step from the upper y^8P state becoming activated at higher temperature.

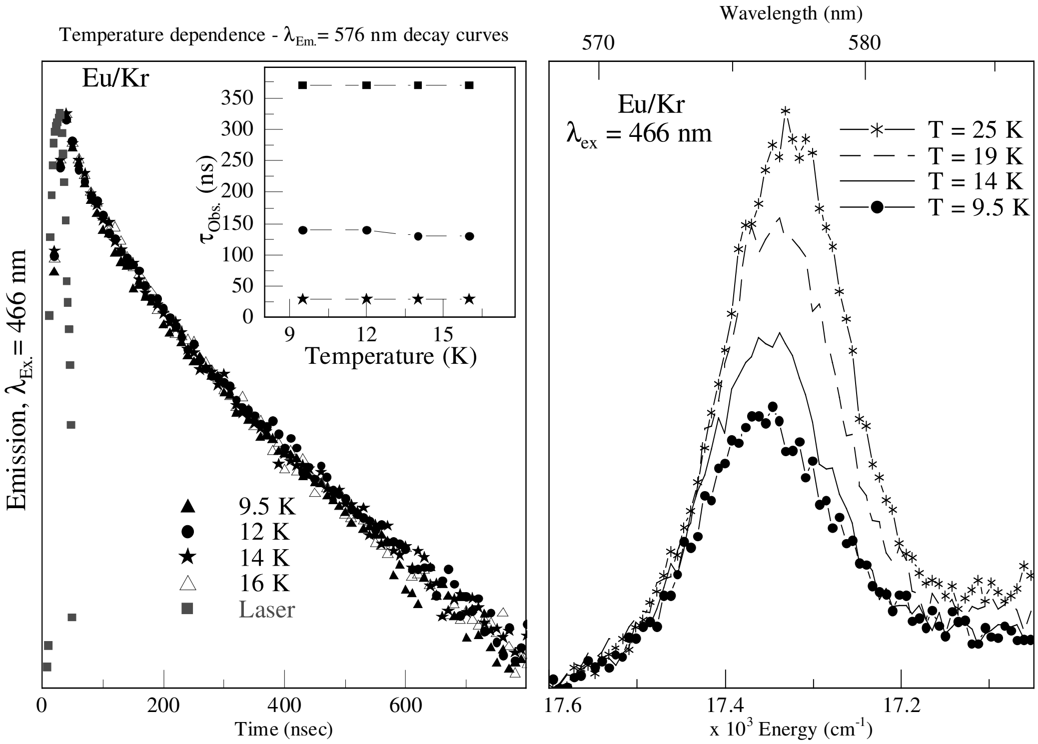

Figure IV.36 Left panel displays the decay profiles of the Eu/Kr red site emission at 576 nm recorded at elevated temperatures in an annealed sample. Inset plots the lifetimes of these decay profile components versus temperature. The right panel presents the steady-state emission spectra recorded with y^8P ← a^8S$_{7/2}$ excitation at 466 nm at various temperatures.

IV.3.II.II Blue site

The corresponding blue site emission is centred at 570.9 nm (17515 cm^{-1}) with a bandwidth of 103 cm^{-1}. Some red site emission is also observed as a weak shoulder at 576 nm due to re-absorption of blue site emission in the y^8P state spectral region as discussed earlier. A gaussian lineshape analysis of the observed emission profile is displayed in Figure IV.37. To allow state assignment of this 571 nm emission feature its temporal characteristics were investigated. The resulting decay profile is presented in Figure IV.38.

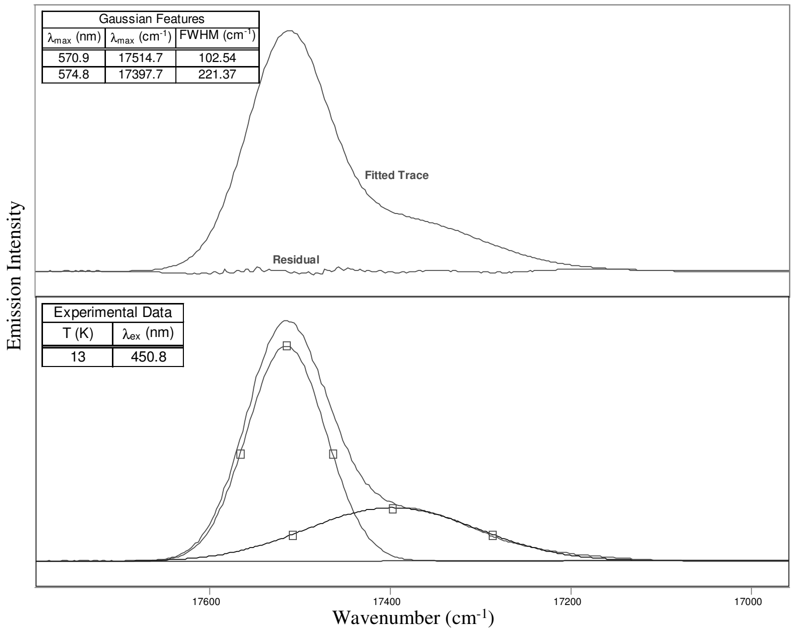

Figure IV.37 Gaussian lineshape analysis of the 571 nm emission observed for Eu/Kr. The upper panel shows an acceptable fit of the emission spectrum recorded at 10 K, where the simulated emission band and the residual is displayed. Two broad Gaussian functions were required to completely represent the 10 K spectrum (lower trace). The weak lower energy shoulder pertains to emission from the red site of isolation.

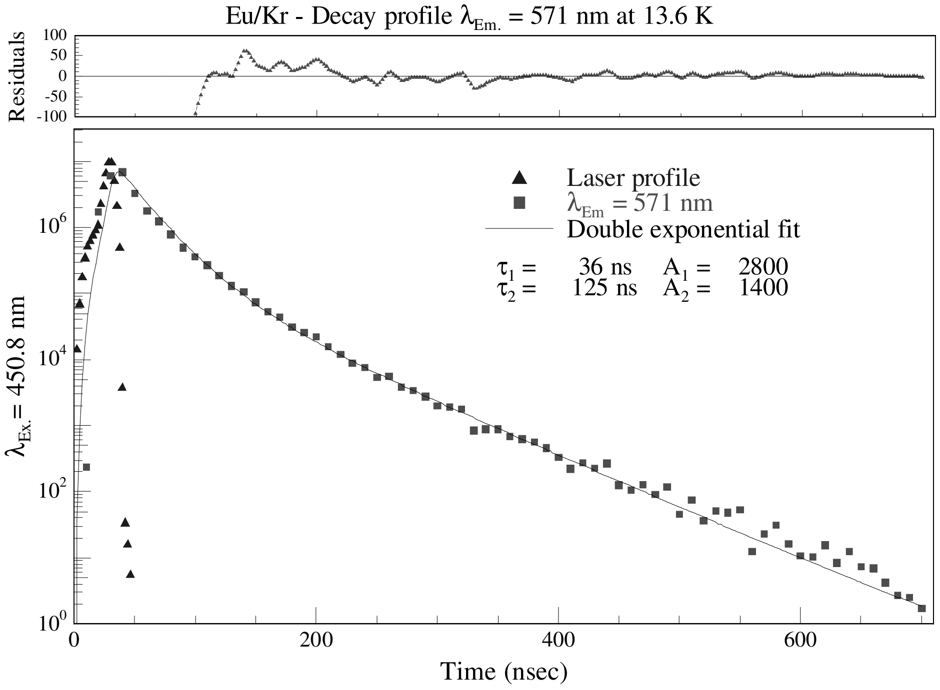

Figure IV.38 Decay profile of the Eu/Kr blue site emission at 571 nm recorded at 10 K in an annealed sample. The decay profile is convoluted with the temporal profile of the laser excitation source. The residual shown represents the difference between the recorded decay and the double exponential fit.

A lifetime consisting of two components $\tau_1 = 36$ and $\tau_2 = 125$ ns is extracted. The shorter component has a larger amplitude of 2800. The left panel of Figure IV.39 presents the effect of increasing temperature on the decay profile. It can be seen from inset of Figure IV.39 that the lifetime components do not change in the temperature range up to 19 K indicating the true radiative lifetime of this transition is observed in solid Kr, yielding matrix corrected lifetimes of 93 and 324 ns. These values compare well to the gas phase $z^6P_{7/2} \leftrightarrow a^8S_{7/2}$ transition, allowing assignment of this feature as resulting from z^6P state relaxation.

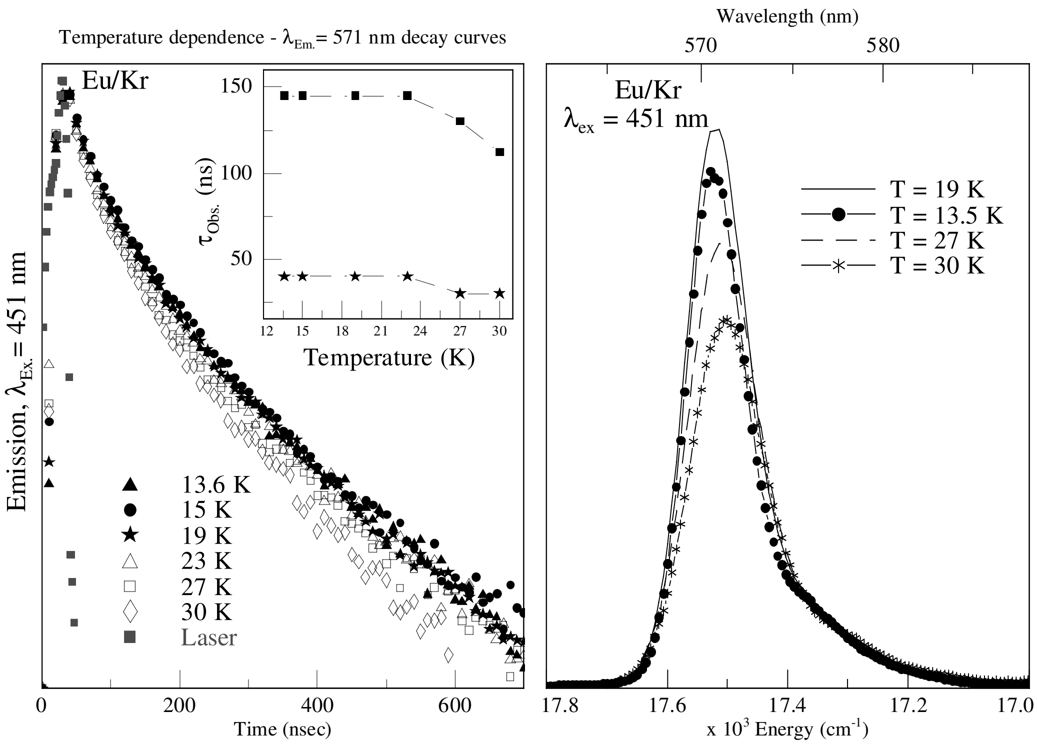

Figure IV.39 The decay profiles of the Eu/Kr blue site emission at 571 nm recorded at elevated temperatures in an annealed sample are displayed in left panel. Inset plots the lifetime components of these decay profiles versus temperature. The right panel presents steady-state emission spectra recorded with $y^8P \leftarrow a^8S_{7/2}$ excitation at 451 nm at various temperatures.

Presented in right panel of Figure IV.39 are the steady-state emission spectra recorded with y^8P state excitation at various temperatures. An unusual trend is observed, up to 19 K there is an increase in emission intensity caused by promotion of the feeding rate from the upper y^8P state. Then from 19 to 30 K there is a gradual decrease in emission strength most likely due to the enhancement of competing relaxation processes other than the $z^6P \rightarrow a^8S$ transition.

IV.3.III Eu/Kr - $\lambda_{Em.} \approx 683$ nm

The lowest intensity emission band observed in the Kr matrix is centred at 683 nm (14641 cm^{-1}) displaying a bandwidth of 236 cm^{-1}. This feature seems to originate from Eu atoms isolated in the blue site of isolation only. Red site excitation does not produce any emission features in this region. To aid in assignment of this band its temporal characteristics were recorded and are presented in Figure IV.40.

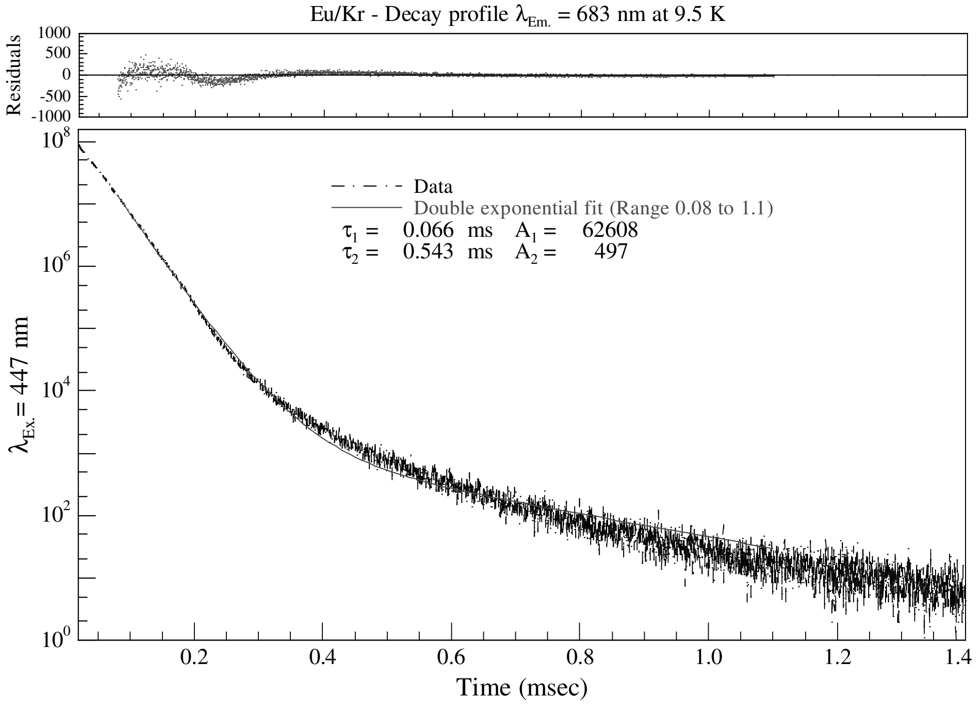

Figure IV.40 Decay profile of the 683 nm emission recorded at 10 K using Single Photon Counting technique with blue site y^8P state excitation at 447 nm. The residuals present the difference between the double exponential fit and the decay recorded.

The decay profile is made up of two components yielding lifetimes of 66 and 543 μs with amplitudes of 62608 and 497 respectively. These values are much longer lived than any P → S transitions suggesting it is an electric-dipole forbidden D → S transition. The nearest such type in the gas phase is the $a^8D_{3/2} \leftrightarrow a^8S_{7/2}$ transition occurring at 660.6 nm (15137.72 cm^{-1}). Allowing assignment of a^8D state relaxation as the source of this 683 nm emission in solid Kr exhibiting a matrix shift of – 496 cm^{-1}. Temporal profiles recorded at increased temperatures as seen in left panel of Figure IV.41 show little temperature dependence.

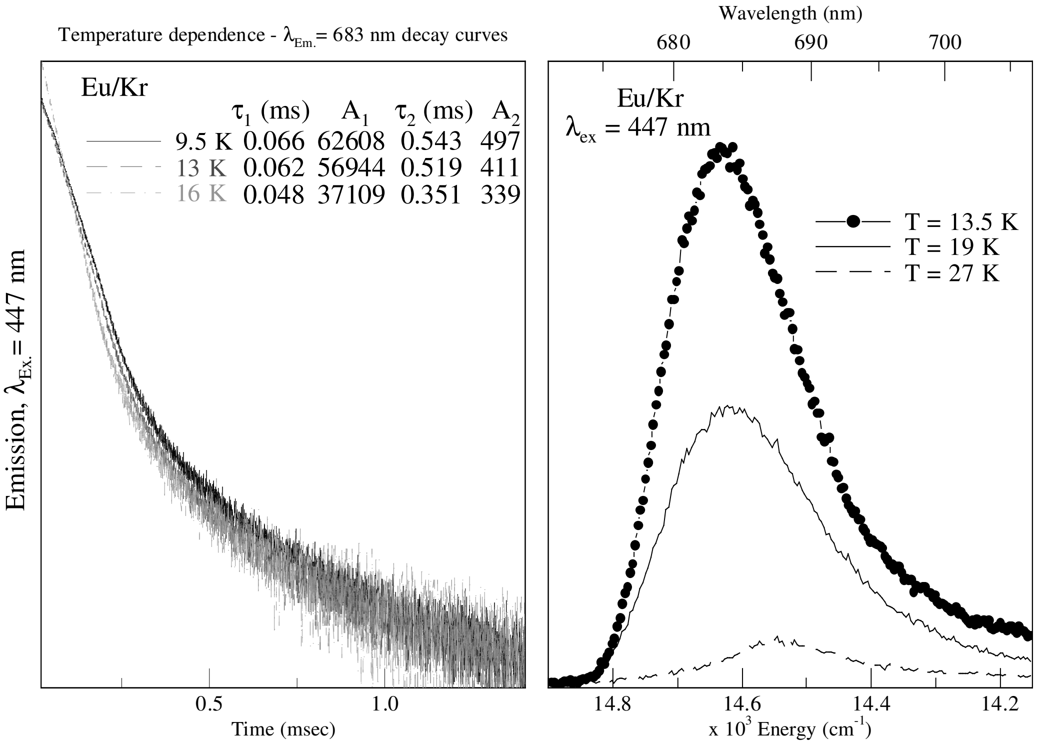

Figure IV.41 The decay profiles of the Eu/Kr blue site emission at 683 nm recorded at 10, 13 and 16 K in an annealed sample are displayed in left panel. Details of the double exponential fit components are shown inset. The right panel presents steady-state emission spectra recorded with y^8P ← $a^8S_{7/2}$ excitation at various temperatures.

Right panel of Figure IV.41 presents the steady-state emission spectra recorded in this region at temperatures up to 27 K. There is a gradual decrease in intensity implying a non-radiative process competing with the a^8D → a^8S electronic transition becomes activated at these higher temperatures.

IV.3.IV Eu/Kr - $\lambda_{Em.} \approx 800$ *nm*

The lowest energy emission features in solid Kr are observed in the 800 nm spectral region. Figure IV.42 presents the emission profiles produced with y^8P state excitation of guest atoms in each of the thermally stable sites. The blue site emission occurs at 816 nm while red site is observed at 789 nm.

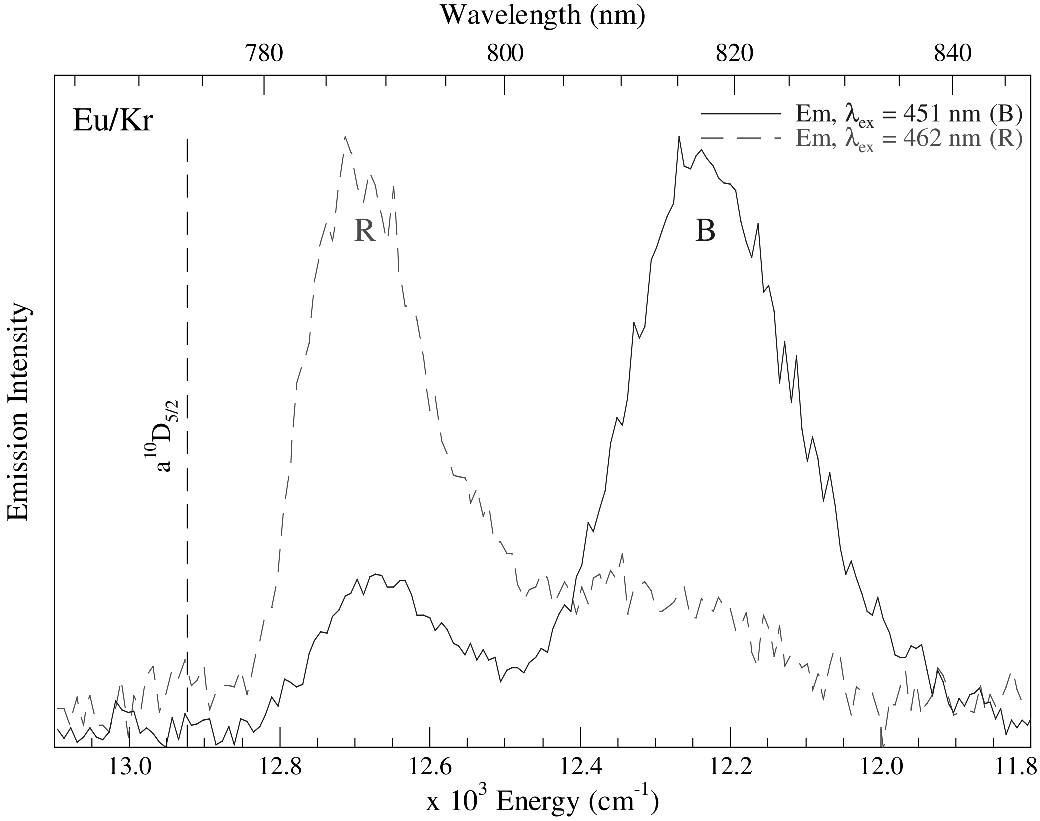

Figure IV.42 Emission spectra of Eu/Kr at 10 K following deposition at 10 K and sample annealing to 36 K produced in the 800 nm spectral region with site-specific y^8P state excitation. The spectral position of the nearest gas phase transition of atomic Eu, $a^{10}D_{5/2}$, is indicated by the dashed vertical line.

IV.3.IV.I Red site

The red site feature centred at 789.2 nm (12671 cm^{-1}) is in close proximity with the gas phase $a^{10}D_{5/2} \leftrightarrow a^8S_{7/2}$ transition occurring at 773.77 nm (12923.72 cm^{-1}) suggesting this emission arises from the a^{10}D state exhibiting a matrix shift of 253 cm^{-1}. In order to identify the excited state causing this emission its decay profile was recorded and is displayed in Figure IV.43. The temporal profile is double exponential, dominated by the shorter decay component with a lifetime of 0.82 ms. The long-lived millisecond nature of this emission feature supports its assignment as $a^{10}D \rightarrow a^8S$ relaxation in solid Kr. Presented in left panel of Figure IV.44, the temporal profile remains unchanged by temperature up to 16 K thus the radiative lifetime of this emission feature is identified yielding a matrix corrected value of 2.1 ms. A gradual increase in emission intensity is observed with increased sample temperature as seen in right panel of Figure IV.44. Indicating that feeding processes to the metastable a^{10}D lowest excited state are enhanced at higher temperatures.

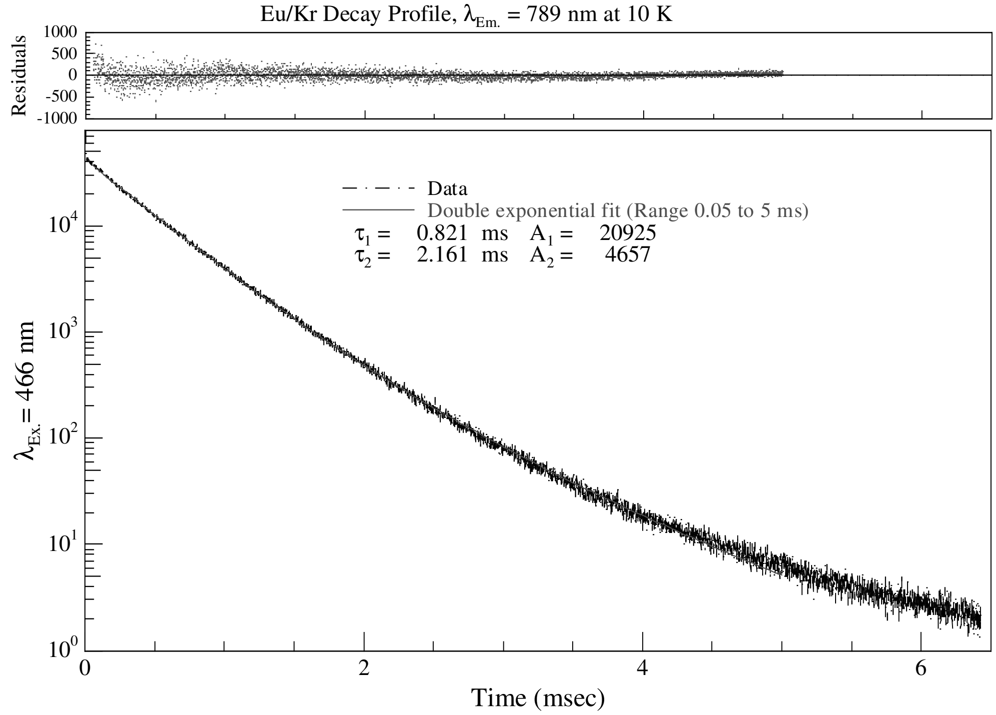

Figure IV.43 Temporal profile of the 789 nm emission recorded with red site y^8P state excitation at 466 nm. The residuals present the difference between the double exponential fit and the recorded decay.

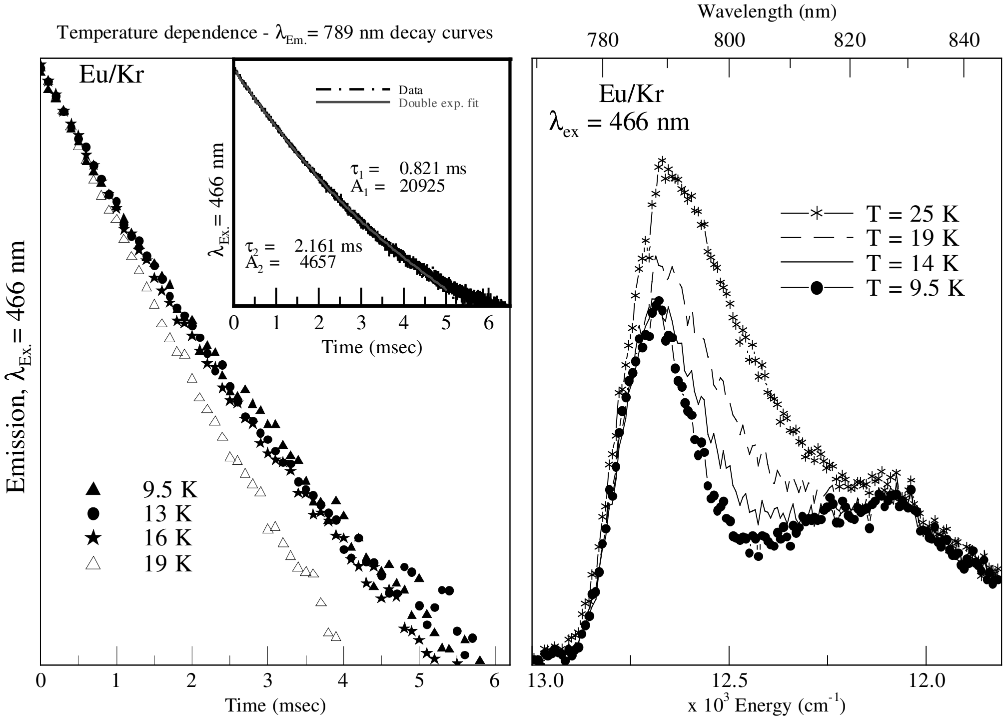

Figure IV.44 Left panel displays the decay profiles of the Eu/Kr red site emission at 789 nm recorded at elevated temperatures in an annealed sample. Inset shows the double exponential fit overlaid with the experimental data at 10 K. The right panel presents steady-state emission spectra recorded with y^8P ← $a^8S_{7/2}$ excitation at various temperatures.

IV.3.IV.II Blue site

The corresponding blue site emission occurs at 815.5 nm (12262 cm^{-1}) with a bandwidth of 285 cm^{-1}. The decay profile of this feature is presented in Figure IV.45.

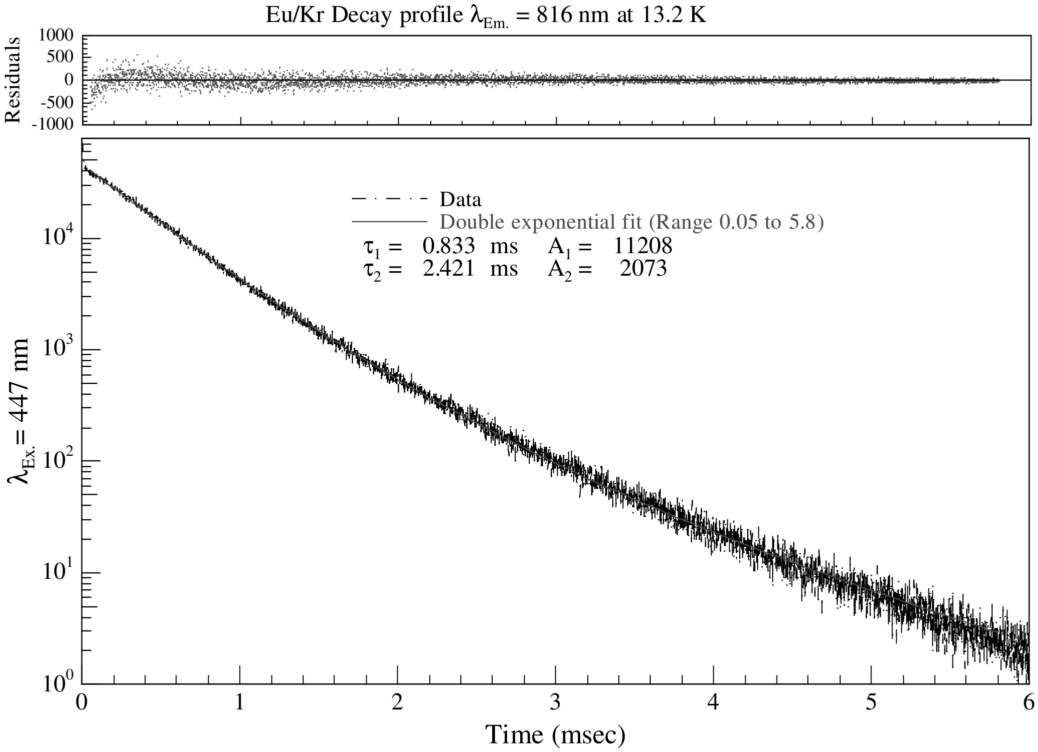

Figure IV.45 Decay profile of the 816 nm emission recorded with blue site y^8P state excitation at 447 nm. The residuals present the difference between the double exponential fit and the recorded decay.

Analysis of the temporal profile reveals two decay components yielding lifetimes of 0.833 and 2.421 ms with amplitudes of 11208 and 2073 respectively. The major component with a lifetime of 0.833 ms dominates the decay. Again, its long-lived nature suggests it is due to an electric-dipole forbidden transition. This feature is assigned as arising from $a^{10}D \rightarrow a^8S$ relaxation exhibiting a matrix shift of 662 cm^{-1} to lower energy. A temperature dependence study of the temporal profile is presented in left panel of Figure IV.46. The decay appears to be unaffected up to 15 K suggesting the radiative lifetime of this feature in the Kr matrix is identified.

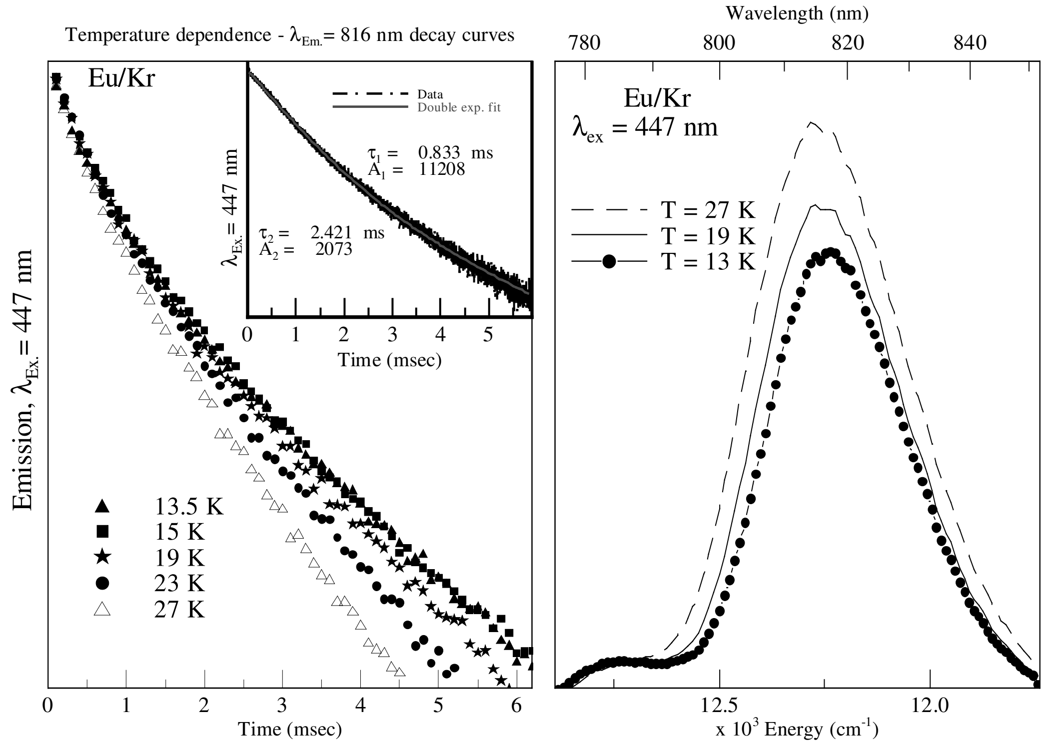

Figure IV.46 The decay profiles of the Eu/Kr blue site emission at 816 nm recorded at elevated temperatures in an annealed sample are displayed in left panel. Inset shows the double exponential fit overlaid with the experimental data. The right panel presents steady-state emission spectra recorded with y^8P ← $a^8S_{7/2}$ excitation at various temperatures.

As seen in the right panel of Figure IV.46, steady-state emission spectra at elevated temperatures show an increase in intensity indicating that feeding processes to the metastable a^{10}D state are being enhanced

IV.3.IV.III Eu/Kr ($a^{10}D \rightarrow a^8S$) Summary

The $a^{10}D_{5/2} \rightarrow a^8S_{7/2}$ electronic transition occurring at 773.77 nm in the gas phase is observed from Eu atoms isolated in the blue and red sites of isolation in Kr matrices at 816 and 789 nm respectively, representing matrix shifts of – 662 and – 253 cm^{-1}. Both emissions exhibit long-lived lifetimes confirming the a^{10}D state as the source of the emission. The intensity increase observed at elevated temperatures is due to enhancement of non-radiative relaxation processes feeding to this metastable state. The D → S type emissions from the red site occur to higher energy than the blue site, this was also the case for D state emission in solid Ar,

IV.3.V Eu(y^8P)/Kr Luminescence Summary

Presented here is a summary of the y^8P state luminescence of atomic Eu isolated in the two thermally stable sites of isolation in the Kr matrix. The gas phase position of the assigned electronic transitions are represented by dashed vertical lines.

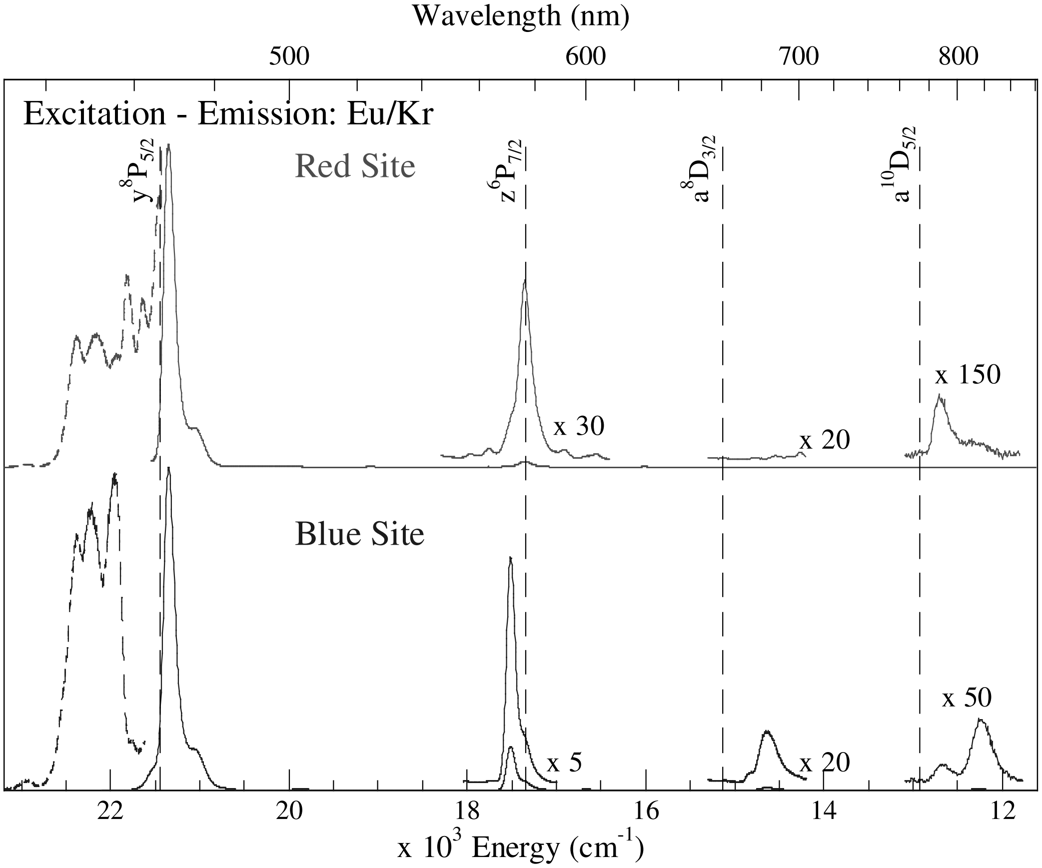

Figure IV.47 Emission spectra of the Eu/Kr system with site-selective lamp excitation of the Eu $y^8P \leftarrow a^8S_{5/2}$ transition. The excitation spectra were recorded by monitoring emission at 468 / 576 / 789 nm (top) and 465 / 571 / 683 / 816 nm (bottom) for the red and blue sites respectively and are shown by the dashed traces to the left. Spectra were recorded following Eu/Kr sample deposition at 10 K and matrix annealing to 36 K. The spectral positions of the assigned gas phase transitions of atomic Eu are shown by the dashed vertical lines.

Four emission features produced with blue site y^8P state excitation are observed at 465, 571, 683 and 816 nm and assigned as resulting from the y^8P, z^6P, a^8D and a^{10}D excited states respectively. These assignments are made based on proximity to the gas phase positions and lifetime measurements, the values of which are collated with the red site emission feature's spectral characteristics in Table IV.3.

Table IV.3 Photophysical characteristics of the emission features from the thermally stable sites of isolation (Red and Blue) in Eu/Kr revealed in the site-specific luminescence study of the y^8P ($4f^7 6s^1 6p^1$) state of atomic europium. The spectral position, λ, is quoted in nanometres (nm) and wavenumber (cm^{-1}) units. The bandwidth (full width at half maximum, *fwhm*) is denoted as Δ in wavenumber units. Gas phase to matrix frequency shifts for the assigned atomic Eu transition, δ, are displayed in wavenumber units. The observed lifetimes recorded in the matrix at 10 K are labelled τ_{10K}.

Gas Phase[1]		Eu(y^8P)/Kr Matrix Emission Features							
		Red Site				Blue Site			
Transition (nm / cm^{-1})	τ_{gp} (ns)	λ_{em} (nm / cm^{-1})	Δ (cm^{-1})	δ (cm^{-1})	τ_{10K}	λ_{em} (nm / cm^{-1})	Δ (cm^{-1})	δ (cm^{-1})	τ_{10K}
$y^8P_{5/2} \leftrightarrow a^8S_{7/2}$ 466.3 21444.58	7.7	468.3 21352	127	− 92	3.5 ns	464.6 21523	108	+ 78	1.65ns
$z^6P_{7/2} \leftrightarrow a^8S_{7/2}$ 576.68 17340.65	909.1	576.3 17351	176	+ 10	**30ns** 140ns 370ns	570.9 17515	103	+ 174	**36ns** 125ns
$a^8D_{3/2} \leftrightarrow a^8S_{7/2}$ 660.6 15137.7	-	-	-	-	-	683 14641	236	− 496	**60 μs** 543 μs
$a^{10}D_{5/2} \leftrightarrow a^8S_{7/2}$ 773.77 12923.7	-	789.2 12671	217	− 253	**0.8ms** 2.2ms	815.5 12262	285	− 662	**0.8ms** 2.4ms

IV.4 Eu(y^8P)/Xe Luminescence

Eu/Xe absorption spectra recorded in the region of the gas phase y^8P ↔ a^8S transition allowed the identification of two sites of isolation in freshly deposited Xe samples. A single thermally stable site of isolation, corresponding to the blue site in Ar and Kr, is centred at 465.2 nm (21496 cm^{-1}) as seen in the left panel of Figure IV.48.

Figure IV.48 also presents the emission spectrum resulting from excitation of the y^8P ← a^8S transition at 465.2 nm in an annealed sample. It reveals three emission features centred at 483, 589 and 823 nm. The following sections aim to assign each of these emission bands to a particular electronic transition of atomic Eu.

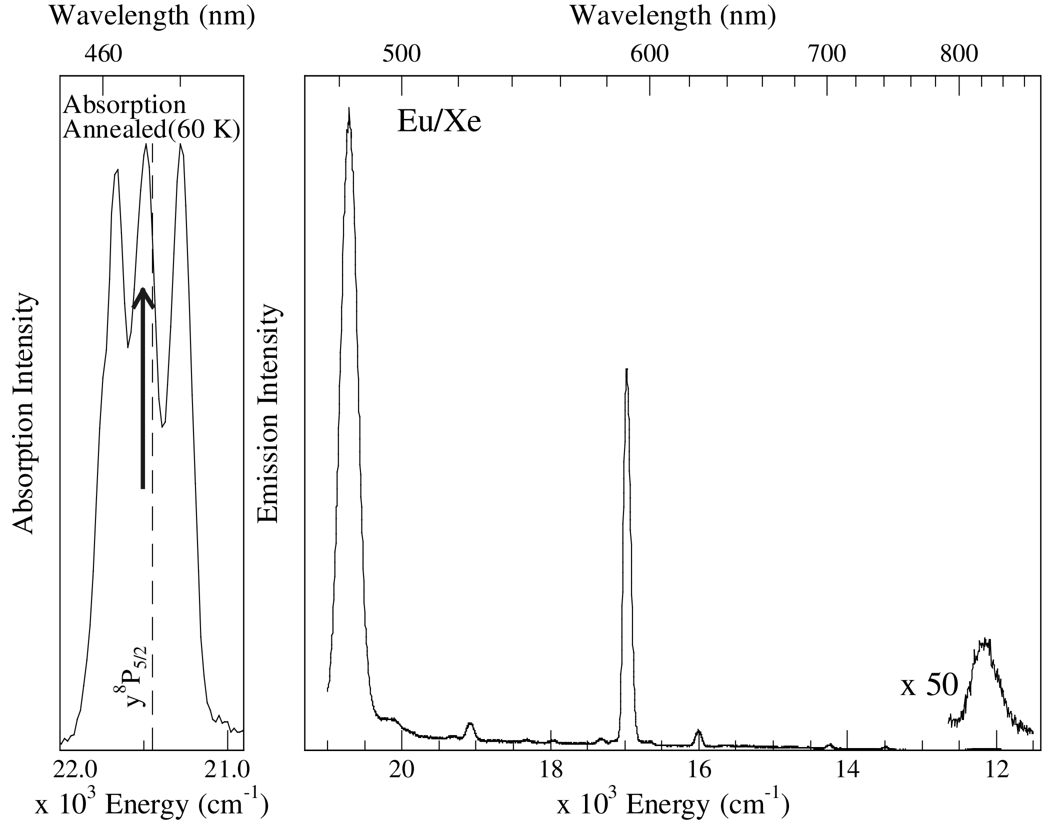

Figure IV.48 Absorption and emission spectra of Eu/Xe in the visible spectral region at 10 K following sample deposition at 10 K and sample annealing to 60 K. Left panel displays the y^8P state absorption spectrum. The arrow indicates the excitation wavelength used to produce the emission spectrum seen in right panel. The low intensity features at 16000 and 19000 cm^{-1} are due to contaminants on the sample window and are obvious here due to the weak emission strength in Eu/Xe.

IV.4.I Eu/Xe - $\lambda_{Em.} \approx 483$ nm

The emission feature of greatest intensity in the Xe matrix is located at 483 nm exhibiting a Stokes shift of 769 cm^{-1}. An expanded view of this region is displayed in Figure IV.49 along with its excitation spectrum. The y^8P state is the only gas phase electronic state in this range suggesting emission originates from the $y^8\text{P} \rightarrow a^8\text{S}$ transition representing a red matrix shift of 737 cm^{-1} and demonstrating a bandwidth of 268 cm^{-1} in the matrix. To aid in the assignment of this feature, its temporal profile was recorded and is displayed in Figure IV.50. A short lifetime of 2.8 ns is extracted which is on the same scale as the $y^8\text{P} \rightarrow a^8\text{S}$ transition identified in solid Ar and Kr.

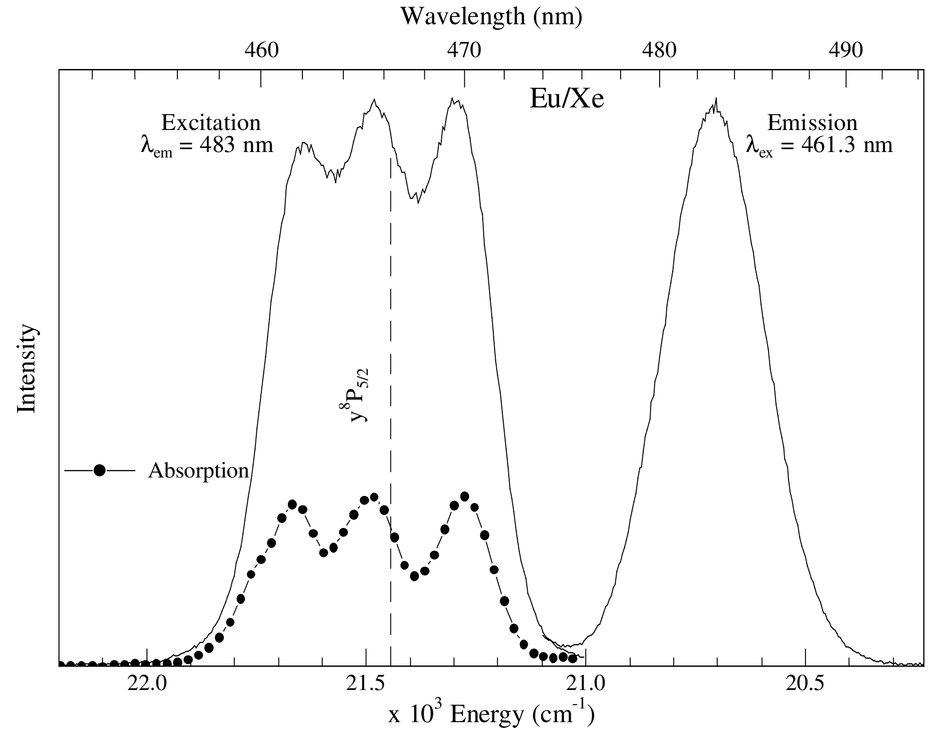

Figure IV.49 Absorption, excitation and emission spectra of Eu/Xe in the single thermally stable blue site of isolation in the y^8P state spectral region at 10 K following sample deposition at 10 K and sample annealing to 60 K. The spectral position of the gas phase y^8P transition of atomic Eu is shown by the dashed vertical line.

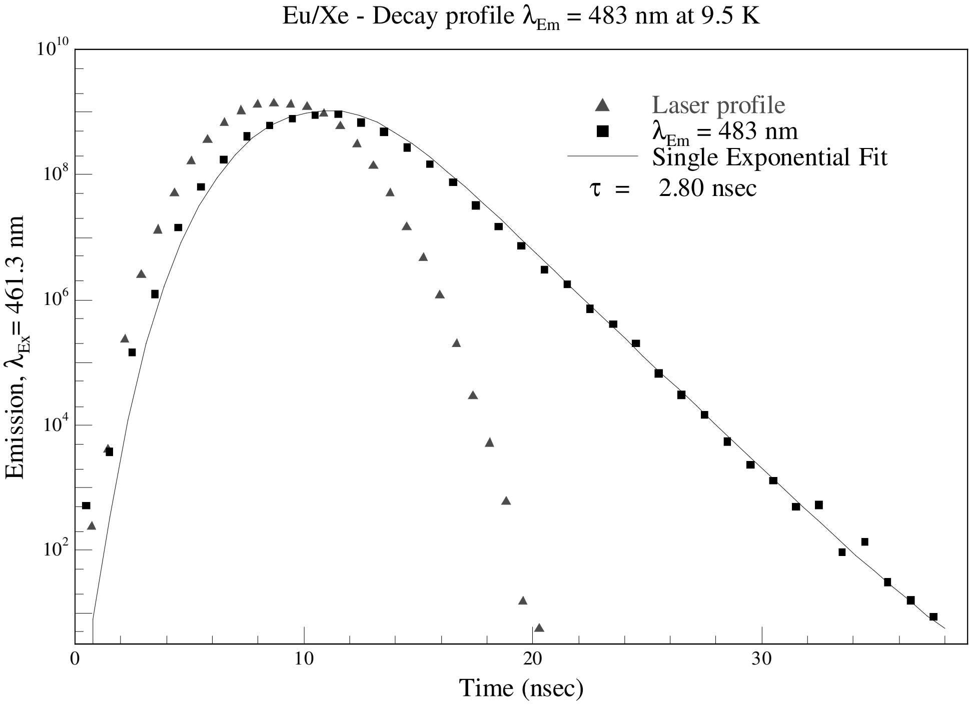

Figure IV.50 Decay profile of the Eu/Xe emission at 483 nm recorded at 10 K in an annealed sample. The decay profile is convoluted with the temporal profile of the laser excitation source at 461.3 nm.

In an attempt to identify the radiative lifetime of the excited state involved in the transition the decay characteristics were recorded at various temperatures and are presented in left panel of Figure IV.51. A temperature dependence is observed even over the short 9.5 to 11 K range, indicating that the radiative decay time has not been identified in the matrix. The trends of shortening decay time with increasing temperature for the 483 nm band indicates a non-radiative process is involved in this excited state decay. Steady-state emission spectra at elevated temperatures support this statement, showing a gradual decrease in intensity, due to relaxation processes competing with the y^8P state electronic transition becoming enhanced. This is seen in right panel of Figure IV.51.

Due to its spectral location and short-lived decay time, the observed 483 nm emission feature produced with y^8P state excitation in solid Xe is assigned as resonance fluorescence from the y^8P excited state of atomic Eu exhibiting a red matrix shift of 737 cm^{-1} and Stokes shift of 769 cm^{-1} with an observed lifetime in the matrix of 2.8 ns.

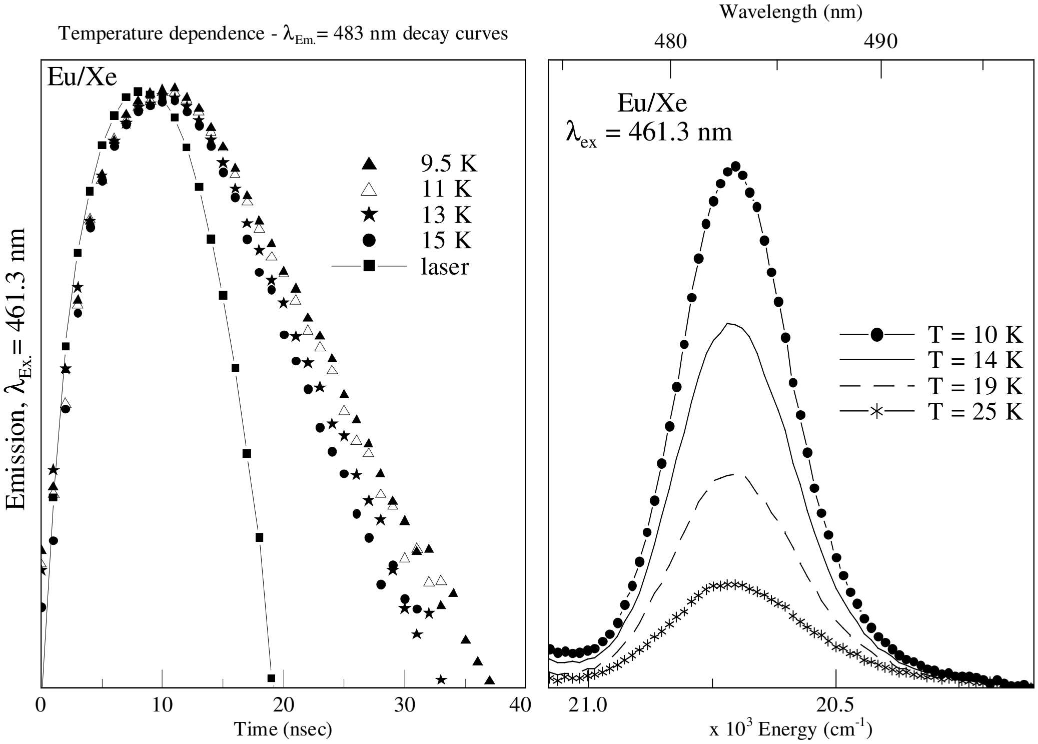

Figure IV.51 Decay profiles of the Eu/Xe emission at 483 nm recorded at elevated temperatures in an annealed sample are displayed in left panel. Right panel presents steady-state emission spectra recorded with y^8P ← a^8S$_{7/2}$ excitation at 461.3 nm at various temperatures.

IV.4.II Eu/Xe - $\lambda_{Em.} \approx 589$ *nm*

The emission feature of second greatest intensity in the Xe matrix is observed at 589.3 nm (16969 cm^{-1}) displaying a bandwidth of 110 cm^{-1}. To probe its source, its temporal characteristics were recorded and are displayed in Figure IV.52.

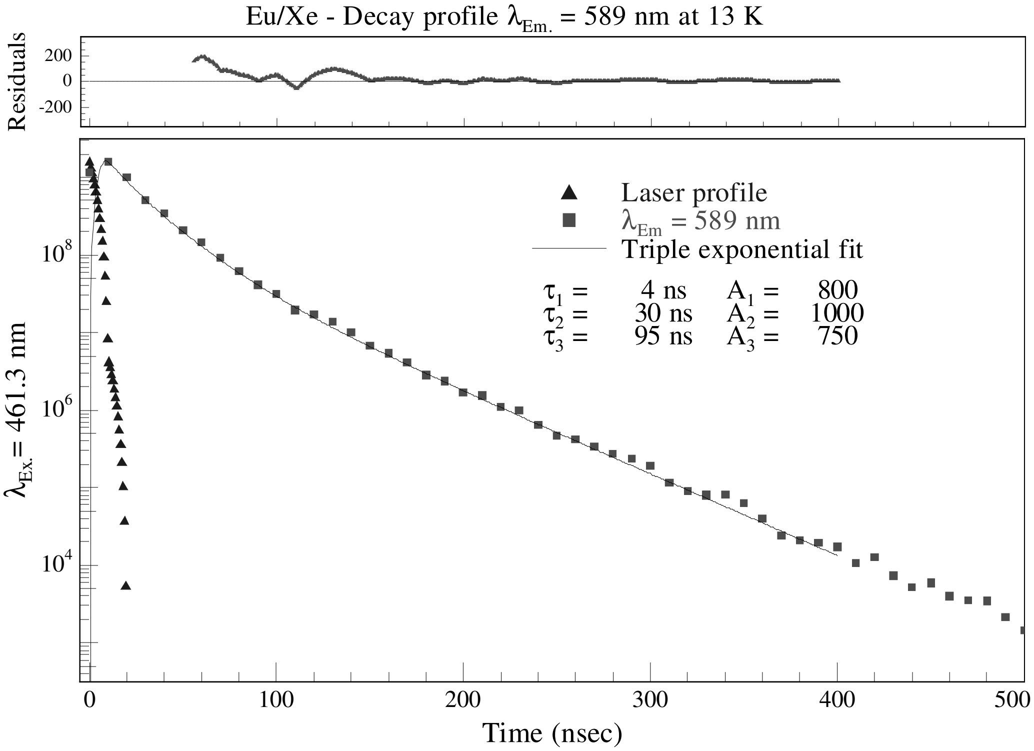

Figure IV.52 Decay profile of the Eu/Xe emission at 589 nm recorded at 10 K in an annealed sample. The decay profile is convoluted with the temporal profile of the laser excitation source at 461.3 nm. The residual shown represents the difference between the recorded decay and the triple exponential fit.

An adequate fit of the decay curve requires a triple exponential function yielding a lifetime with three components of $\tau_1 = 4$ ns, $\tau_2 = 30$ ns and $\tau_3 = 95$ ns with amplitudes of 800, 1000 and 750 respectively. As for the corresponding feature in Ar and Kr matrices discussed earlier, the nanosecond lifetime suggests it results from the z^6P → a^8S transition. Furthermore, the nearest gas phase transition is $z^6P_{7/2} \rightarrow a^8S_{7/2}$ implying this emission feature is due to relaxation from the z^6P state with a matrix shift of 372 cm^{-1}.

An analysis of the effects of varying temperature on the lifetime of the 589 nm emission in the Xe matrix is displayed in left panel of Figure IV.53. The inset of

Figure IV.53 presents the decay components' values at specified temperatures. The 30 ns component has the largest amplitude at all temperatures. There is no change in any of the three lifetime components up to 16 K. In fact, only the longer lifetime component becomes temperature dependent above 16 K. The shorter components remain unaffected by temperature. The radiative lifetime of this transition is identified yielding matrix corrected lifetime values of 12, 89 and 280 ns.

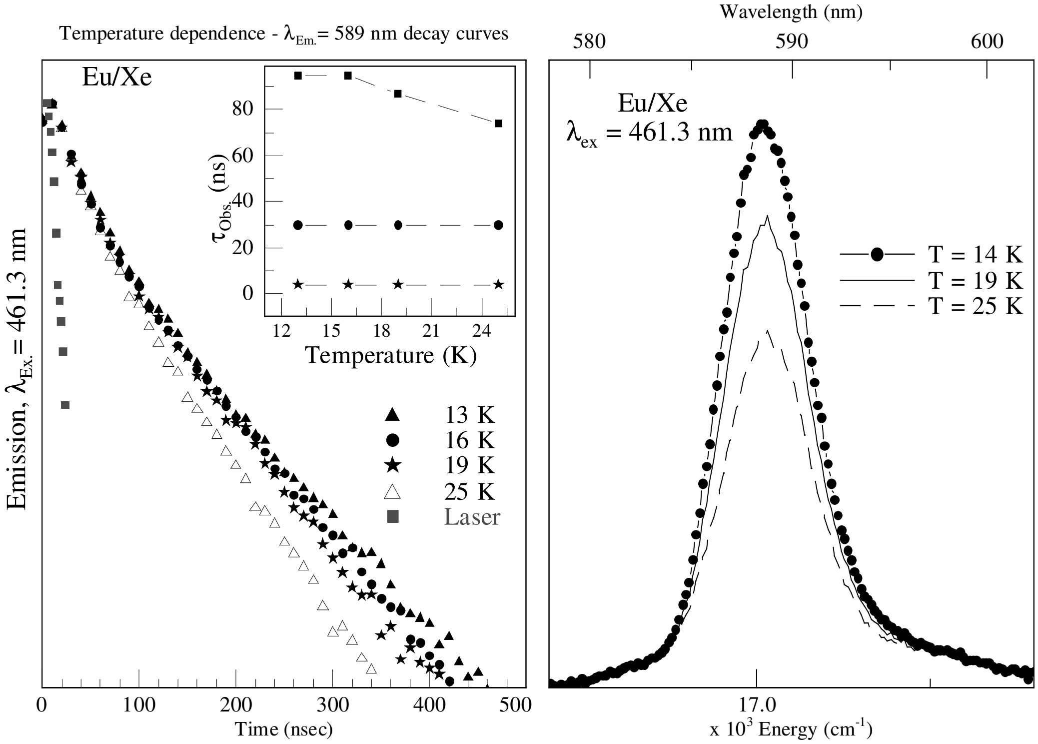

Figure IV.53 Left panel displays the decay profiles of the Eu/Xe emission at 589 nm recorded at elevated temperatures in an annealed sample. Inset plots the lifetime components of these decay profiles versus temperature. The right panel presents steady-state emission spectra recorded with y^8P ← $a^8S_{7/2}$ excitation at 461.3 nm at various temperatures.

Steady-state emission spectra of this feature show a noticeable decrease in intensity at elevated temperatures as displayed in right panel of Figure IV.53. This implies other non-radiative relaxation processes actively compete with the electronic transition causing a reduction in emission intensity.

Based on its spectral position and short lifetime components, which both compare favourably to the gas phase $z^6P_{7/2} \rightarrow a^8S_{7/2}$ transition, the emission observed at 589.3 nm in solid Xe is assigned as resulting from z^6P state relaxation of atomic Eu.

IV.4.III Eu/Xe - $\lambda_{Em.} \approx 823$ *nm*

The final emission feature observed in Xe is centred at 823 nm with a bandwidth of 367 cm^{-1}. The nearest gas phase transition of atomic Eu is $a^{10}D_{5/2} \rightarrow a^8S_{7/2}$ occurring at 773.77 nm (12923.72 cm^{-1}) which would represent a matrix shift of 779 cm^{-1}.

To complete the assignment of this emission band, decay characteristics were recorded and are presented in Figure IV.54. A single exponential fit consisting of a 1.22 ms lifetime was required to reproduce the decay profile. The long-lived nature implies an electric-dipole forbidden electronic transition is the origin of this feature, supporting its assignment as the $a^{10}D \rightarrow a^8S$ electronic transition. As displayed in left panel of Figure IV.55, there is no temperature dependence of the decay profile up to 18 K. The radiative lifetime of the excited state involved is identified, yielding a matrix corrected value of 3.5 ms.

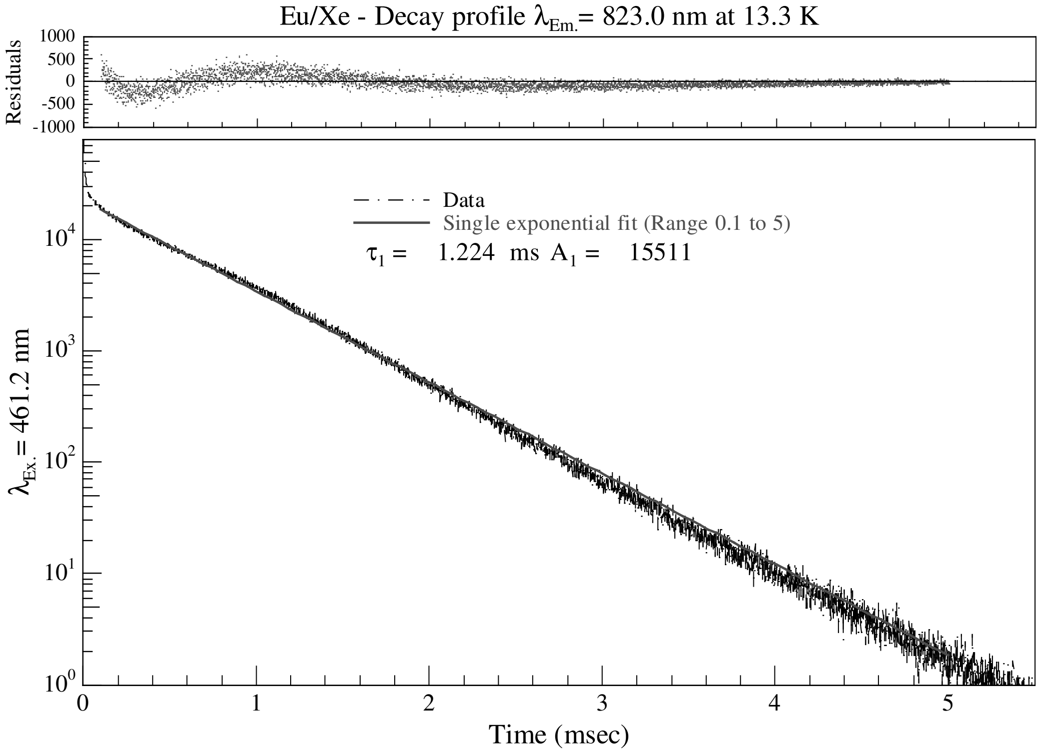

Figure IV.54 Temporal profile of the 823 nm emission recorded with y^8P state excitation at 461.2 nm. The residuals present the difference between the single exponential fit and the recorded decay.

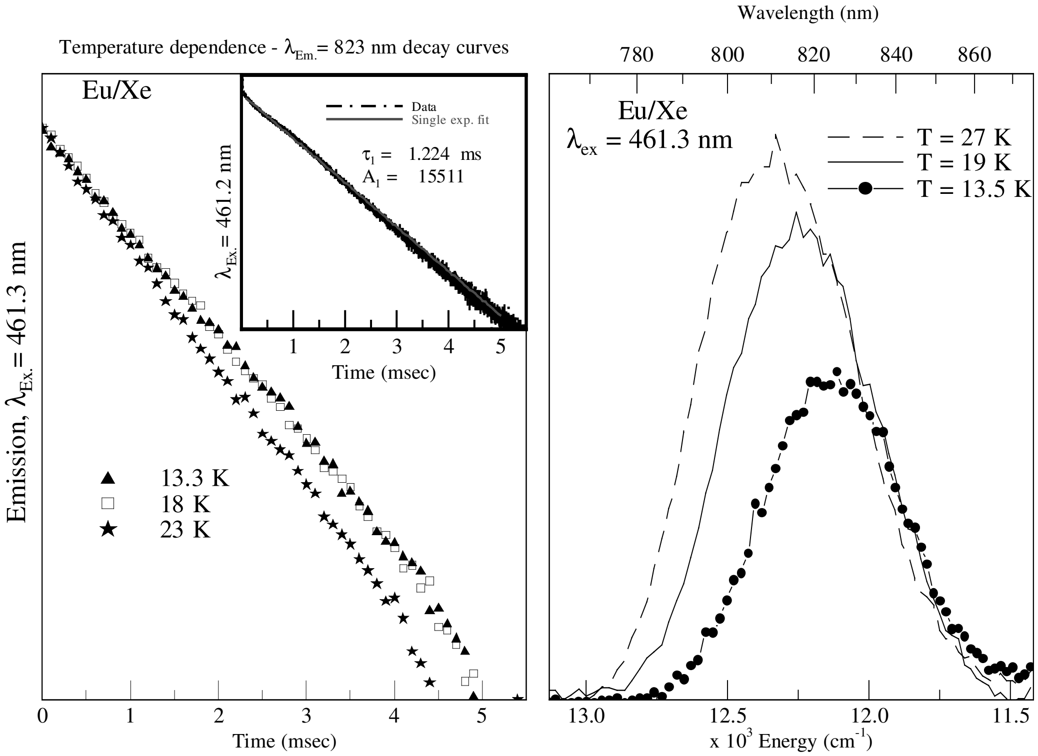

Figure IV.55 Left panel displays the decay profiles of the Eu/Xe emission at 823 nm recorded at elevated temperatures in an annealed sample. Inset shows the single exponential fit overlaid with the experimental data. The right panel presents steady-state emission spectra recorded with $y^8\text{P} \leftarrow a^8\text{S}_{7/2}$ excitation at various temperatures.

Steady-state emission spectra recorded at various temperatures showed a progressive blue shift in the observed band maximum and an increase in intensity with increasing scan temperature as shown in right panel of Figure IV.55. The shift observed was completely reversible and the original spectrum was obtained upon returning to base temperature. This is most likely due to improved efficiency of the feeding processes to the a^{10}D state.

In conclusion, the feature at 823 nm can be assigned as emission from the a^{10}D metastable state with a radiative lifetime of 1.2 ms in solid Xe.

IV.4.IV Eu(y^8P)/Xe Luminescence Summary

A summary plot of the luminescence of atomic Eu isolated in the thermally stable blue site in the Xe matrix is presented in Figure IV.56. Dashed vertical lines represent the gas phase positions of each of the assigned electronic transitions, the spectral and temporal characteristics of which are listed in Table IV.4. Notably, a^8D state emission which was present in Ar and Kr was not observed in the Xe lattice.

Table IV.4 Photophysical characteristics of the emission features from the thermally stable blue site of isolation in Eu/Xe revealed in the luminescence study of the y^8P ($4f^7 6s^1 6p^1$) state of atomic Eu. The spectral position, λ, is quoted in nanometres (nm) and wavenumber (cm^{-1}) units. The bandwidth (full width at half maximum, *fwhm*) is denoted as Δ in wavenumber units. Gas phase to matrix frequency shifts for the assigned atomic Eu transition, δ, are in wavenumber units. The lifetimes recorded in the matrix at 10 K are labelled τ_{10K}.

Gas Phase[1]		Eu(y^8P)/Xe Matrix Emission Features			
Transition (nm / cm^{-1})	τ_{gp} (ns)	λ_{em} (nm / cm^{-1})	Δ (cm^{-1})	δ (cm^{-1})	τ_{10K}
$y^8P_{5/2} \leftrightarrow a^8S_{7/2}$ 466.3 21444.58	7.7	483 20707	268	– 737	2.8 ns
$z^6P_{7/2} \leftrightarrow a^8S_{7/2}$ 576.68 17340.65	909.1	589.3 16969	110	– 372	4 ns **30 ns** 95 ns
$a^{10}D_{5/2} \leftrightarrow a^8S_{7/2}$ 773.77 12923.7	-	823.4 12145	367	– 779	1.2 ms

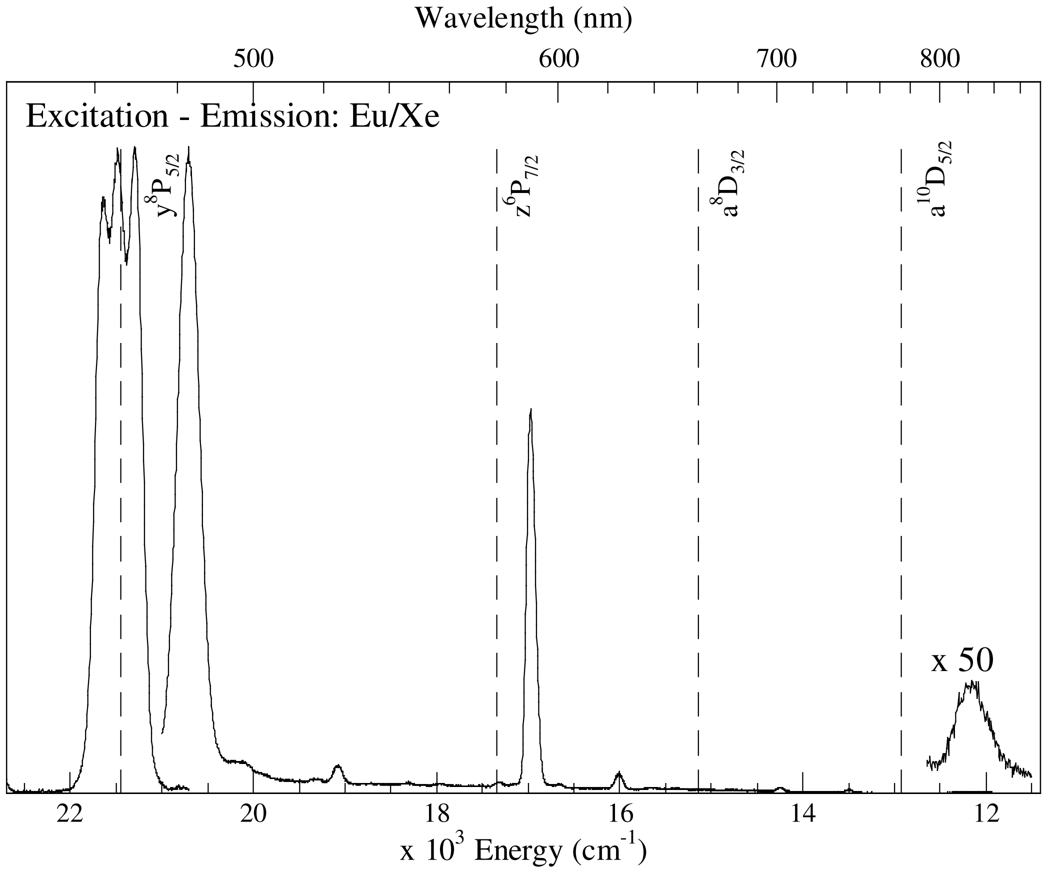

Figure IV.56 Emission spectrum recorded at 10 K for the Eu/Xe system with excitation of the y^8P state. The excitation spectrum recorded by monitoring emission at 483 / 589 / 823 nm is shown to the left. Spectra were recorded following Eu/Xe sample deposition at 10 K and matrix annealing to 60 K. The spectral positions of the assigned gas phase transitions of atomic Eu are shown by the dashed vertical lines.

IV.5 Eu(y^8P)/RG Luminescence

The luminescence study of atomic Eu isolated in the solid RG's was presented in the preceding sections. The differences and similarities observed in each of the RG's are now compared and contrasted. y^8P state excitation of Eu/RG samples produces four emission features assigned as y^8P resonance fluorescence, emission from the z^6P and a^8D excited states to the ground state and emission of the metastable a^{10}D electronic state.

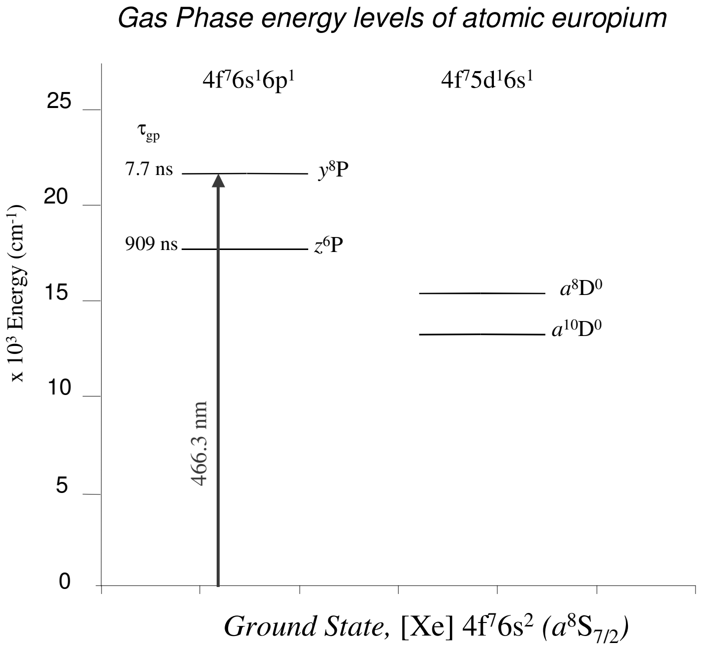
Gas Phase energy levels of atomic europium

Figure IV.57 Simplified schematic representation of the energy levels of gas phase atomic europium in the visible spectral region presenting only the excited states observed in emission in the RG solids. The fully allowed $y^8\text{P} \leftarrow a^8\text{S}_{7/2}$ transition occurring at 21444.6 cm^{-1} (466.3 nm) is indicated by the arrow[1].

Figure IV.2 presented the complete energy level diagram of atomic Eu in the visible spectral region. A simplified energy level diagram presenting only the excited states observed in emission in the RG solids is displayed in Figure IV.57. The spectral and temporal characteristics of each of these four emission features in both sites of isolation are listed in Table IV.5. Clearly identifiable in Figure IV.57 are two different electronic configurations that are accessed in the excited states. The y^8P and z^6P states exhibiting a 4f^{7}6s^{1}6p^1 configuration while the a^8D and a^{10}D states exist in a 4f^{7}5d^{1}6s^1 arrangement. In both cases a previously unoccupied orbital is filled leading one to expect broad and shifted spectral features[5]. The characteristic P and D type emissions are discussed in detail in Sections IV.5.I.I and IV.5.I.II but firstly, a comparison of the luminescence produced from the different sites in the RG solids is presented.

IV.5.I Red and Blue site Luminescence

A summary of the luminescence of atomic Eu isolated in the blue site of isolation in each of the three RG's is presented in Figure IV.58.

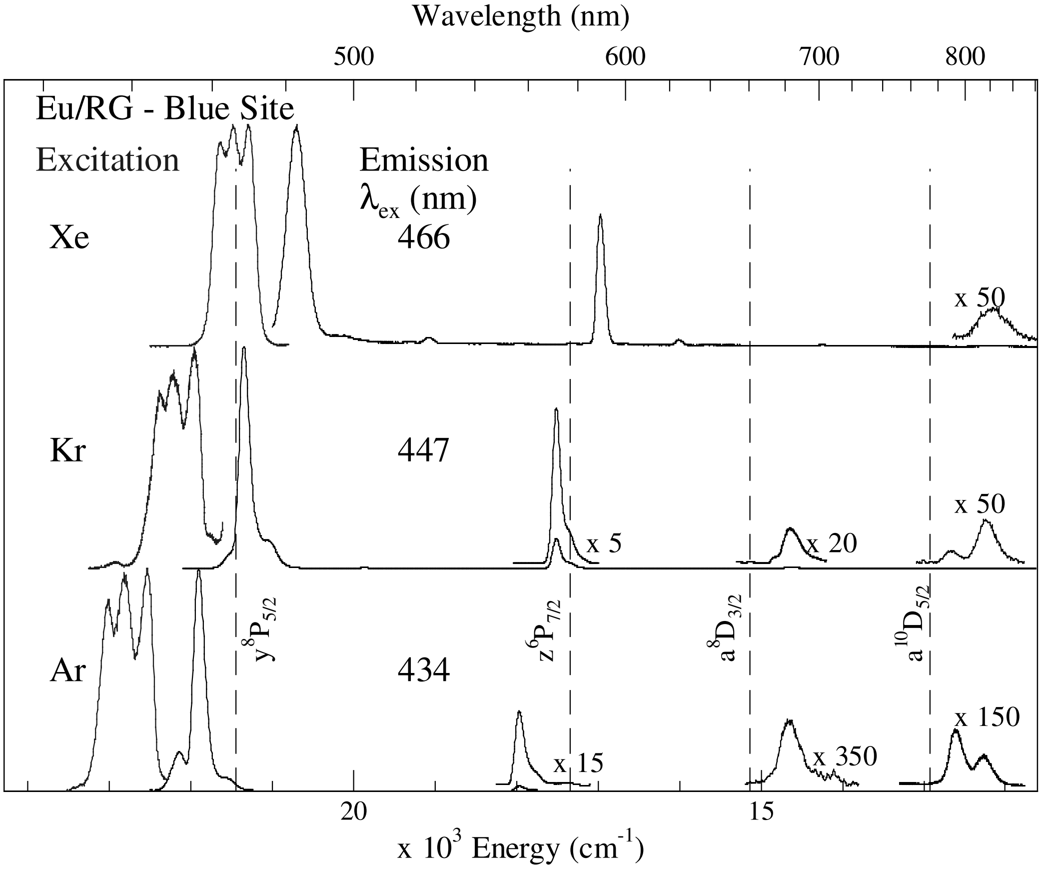

Figure IV.58 Emission spectra recorded at 10 K for Eu/Ar, Eu/Kr and Eu/Xe systems with site-selective lamp excitation of the high energy blue site corresponding to the Eu $y^8P \leftarrow a^8S_{5/2}$ transition. The excitation wavelengths used are shown as λ_{ex} (nm). The excitation spectra are shown to the left. All spectra were recorded following Eu/RG sample deposition at 10 K and matrix annealing. The gas phase spectral positions of the assigned transitions of atomic Eu are shown by the dashed vertical lines[1].

Table IV.5 Photophysical characteristics of the emission features of the Red and Blue sites of isolation in Eu/RG revealed in the luminescence study of the y^8P ($4f^7 6s^1 6p^1$) state of atomic Eu. The spectral position is quoted in λ (nm) and ν (cm^{-1}). The bandwidth (*fwhm*) is denoted as Δ. Gas phase to matrix frequency shifts for the assigned atomic Eu transition, δ, are displayed in wavenumber units. The observed lifetimes recorded in the matrix at 10 K are labelled τ_{10K}.

State	ν (cm^{-1})	λ (nm)	Δ (cm^{-1})	δ (cm^{-1})	τ_{10K}
Eu gas phase					
$y^8P_{5/2}$	21444.58	466.3	-	-	7.7 ns
$z^6P_{7/2}$	17340.65	576.68	-	-	909.1
$a^8D_{3/2}$	15137.7	660.6	-	-	-
$a^{10}D_{5/2}$	12923.7	773.77	-	-	-
Eu/Ar red (1°) site					
$y^8P_{5/2}$	21867	457.3	167	+ 422	3.5 ns
$z^6P_{7/2}$	17767	562.9	144	+ 427	**72 ns** 280 ns
$a^8D_{3/2}$	14815	675	274	– 323	**39 µs** 561 µs
$a^{10}D_{5/2}$	12649	790.6	203	– 275	**0.7 ms** 2.1 ms
Eu/Ar blue (2°) site					
$y^8P_{5/2}$	22141	451.6	192	+ 697	2.3 ns
$z^6P_{7/2}$	17954	557	125	+ 614	**33 ns** 240 ns
$a^8D_{3/2}$	14650	682.6	285	– 488	**52 µs** 199 µs
$a^{10}D_{5/2}$	12281	814.3	281	– 643	**0.4 ms** 1.3 ms
Eu/Kr red (2°) site					
$y^8P_{5/2}$	21352	468.3	127	– 92	3.5 ns
$z^6P_{7/2}$	17351	576.3	176	+ 10	**30 ns** 140 ns 370 ns
$a^{10}D_{5/2}$	12671	789.2	217	– 253	**0.8 ms** 2.2 ms
Eu/Kr blue (1°) site					
$y^8P_{5/2}$	21523	464.6	108	+ 78	1.65 ns
$z^6P_{7/2}$	17515	570.9	103	+ 174	**36 ns** 125 ns
$a^8D_{3/2}$	14641	683	236	– 496	**60 µs** 543 µs
$a^{10}D_{5/2}$	12262	815.5	285	– 662	**0.8 ms** 2.4 ms
Eu/Xe					
$y^8P_{5/2}$	20707	483	268	– 737	2.8 ns 4 ns
$z^6P_{7/2}$	16969	589.3	110	– 372	**30 ns** 95 ns
$a^{10}D_{5/2}$	12145	823.4	367	– 779	1.2 ms

Figure IV.58 shows there is a progressive red shift of P → S type electronic transitions (i.e. y^8P, z^6P → a^8S) on going to more polarisable hosts. This is due to the electronic configuration involved in the transition, the 6p-orbital that is populated in these excited states has a spatial occupancy beyond the outer 6s-shell thus allowing interaction with the RG host in the excited state. The magnitude of the shift observed for these two P states is discussed in more detail in Section IV.6.

It is observed that D state transitions (a^8D, a^{10}D → a^8S) are not so susceptible to matrix host changes, with only minor spectral shifts seen when the matrix solid is changed. This effect is rationalised by considering the electronic configuration of these D states. The 5d-orbitals occupied in the excited state remain spatially enclosed within the outer 6s-orbital thus shielded from the effects of changing lattices.

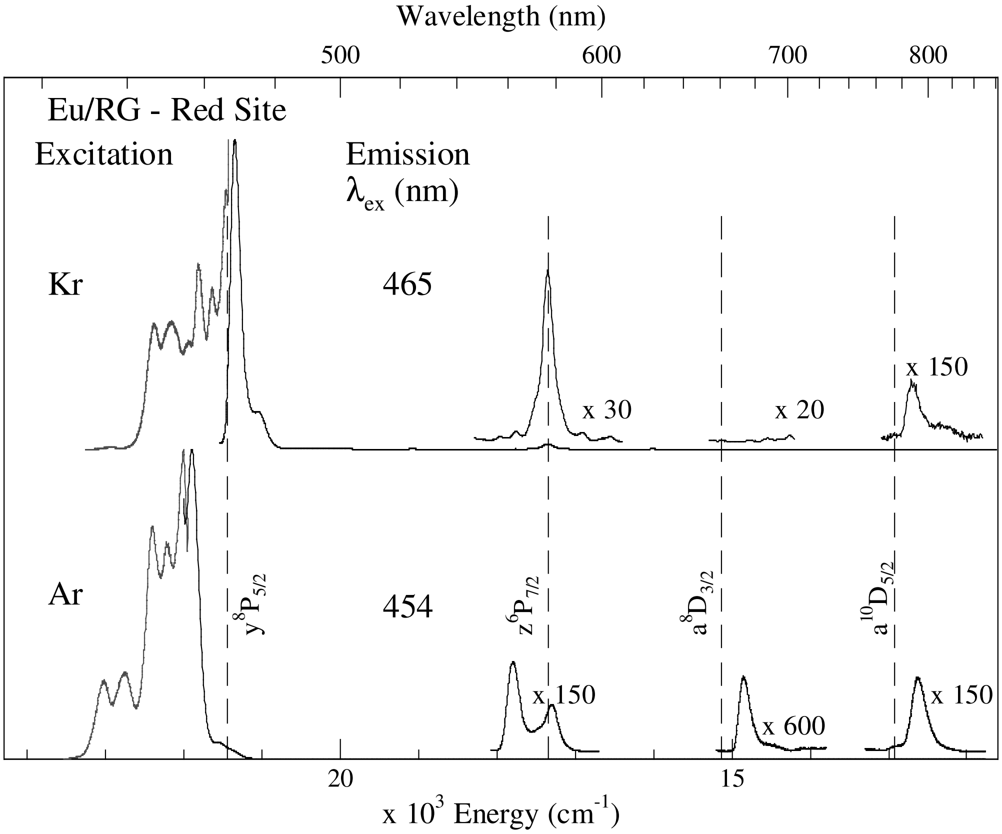

Figure IV.59 Emission spectra recorded at 10 K for Eu/Ar and Eu/Kr systems with site-selective lamp excitation of the low energy red site corresponding to the Eu y^8P ← $a^8S_{5/2}$ transition. The excitation wavelengths used are shown as λ_{ex} (nm). The excitation spectra are shown to the left. All spectra were recorded following Eu/RG sample deposition at 10 K and matrix annealing. The gas phase spectral positions of the assigned transitions of atomic Eu are shown by the dashed vertical lines[1].

Figure IV.59 presents a summary of the luminescence produced from Eu atoms isolated in the red site of isolation in the Ar and Kr matrices. Again, P → S type transitions are most effected by changing the RG host and shift to lower energies in the more polarisable Kr. As expected, the D state emission identified in both hosts is unaffected by changing the lattice material.

IV.5.I.I y^8P resonance fluorescence

By focusing on the y^8P resonance fluorescence, statements may be made regarding the effects of the different site types on the europium atom in the solid hosts. Firstly, Table IV.6 collates the spectral and temporal properties of the y^8P state transition in all sites and lattices.

Table IV.6 Photophysical characteristics of the y^8P state emission features from the thermally stable blue and red sites of isolation in Eu/RG. The spectral position is quoted in λ (nm) and ν (cm^{-1}). The bandwidth (*fwhm*) is denoted as Δ. Gas phase to matrix frequency shifts for the assigned transition, δ, are displayed in wavenumber units. The observed lifetimes recorded in the matrix at 10 K are labelled τ_{10K} and where the radiative lifetime is identified (τ_{rad}) values are corrected for the effective field of the surrounding matrix (τ_{Cor}). The magnitude of the Stokes shift (SS) between the central Jahn-Teller excitation component and the emission band is quoted in cm^{-1}.

Eu/RG - $\boldsymbol{y^8}$**P** resonance fluorescence

Host	ν (cm^{-1})	λ (nm)	Δ (cm^{-1})	δ (cm^{-1})	τ_{10K} (ns)	τ_{rad} (ns)	τ_{Cor} (ns)	SS (cm^{-1})
Gas Phase[1]	21444.58	466.3	-	-	7.7	7.7	7.7	-
				Red Site				
Ar	21867	457.3	167	+ 422	3.5 ns	✓	7.2	351
Kr	21352	468.3	127	– 92	3.5 ns	✓	9.1	292
				Blue Site				
Ar	22141	451.6	192	+ 697	2.3 ns	*X*	-	674
Kr	21523	464.6	108	+ 78	1.65 ns	*X*	-	657
Xe	20707	483	268	– 737	2.8 ns	*X*	-	769

The major point of note is the magnitude of the Stokes shift (SS) observed in each site type. The Stokes shift from emission band maximum to central Jahn-Teller excitation component of Eu isolated in the blue site is twice that of atoms in the red site of isolation. This indicates a greater interaction of the y^8P excited state with the surrounding host for atomic Eu isolated in the blue site. This effect is in complete agreement with the attribution in Chapter III of blue sites being tetra-vacancies (tv) and red sites as larger hexa-vacancies (hv). The site sizes available in the RG *fcc* lattices are listed in Table III.5. Clearly the tv site is smaller, thus a greater interaction of the atom with the surrounding host would be expected which manifests itself as a larger Stokes shift in this smaller site of isolation.

Also of note, the radiative lifetime of the y^8P fluorescence was identified for Eu isolated in the red site yielding lifetimes, which when corrected for the effective field of the surrounding matrix, were in very good agreement with the gas phase value of the $y^8\text{P} \leftrightarrow {}^8\text{S}$ transition. This can be seen in Figure IV.60 when a λ^3 extrapolation of the gas phase value is overlaid with the matrix corrected lifetimes.

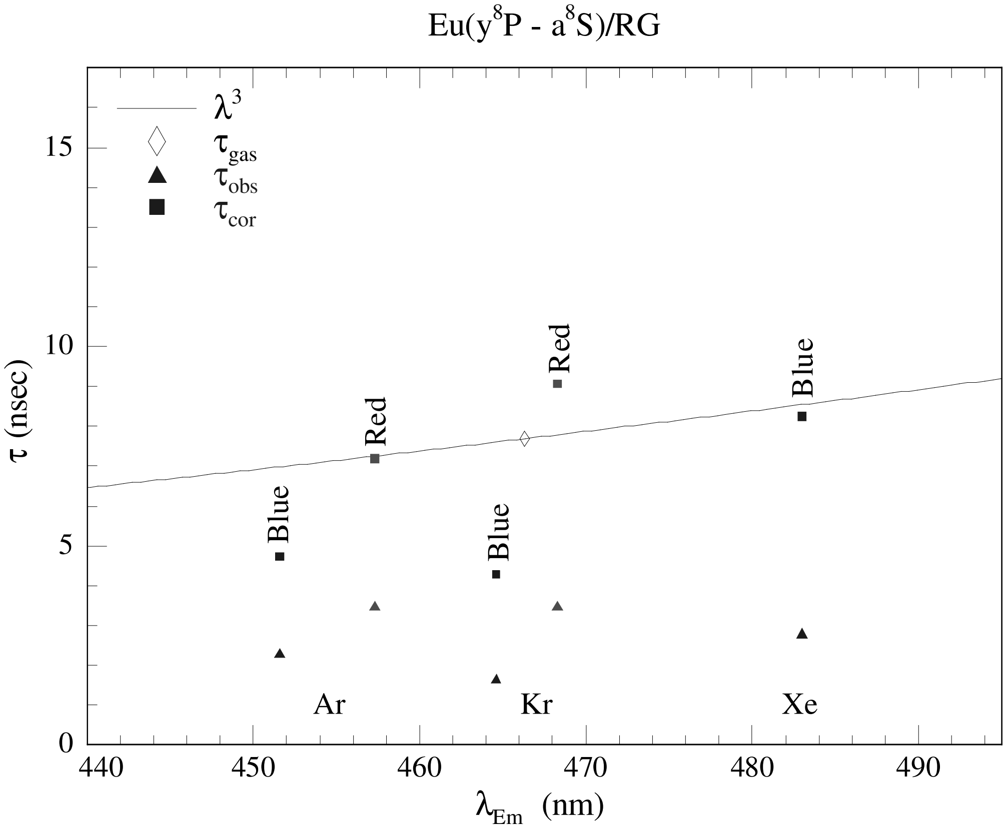

Figure IV.60 A comparison of the lifetimes recorded at 10 K for the Eu($y^8\text{P} \rightarrow a^8\text{S}$) emission features in Ar, Kr and Xe and a λ^3 extrapolation of the gas phase lifetime of the y^8P state of atomic Eu. The uncorrected and the data corrected for the effective fields are shown by filled triangles and closed squares respectively.

However, the radiative lifetime of the y^8P transition in the blue site of isolation could not be identified. This implies that even at 10 K non-radiative relaxation processes are competing quite significantly with the y^8P electronic transition which is obvious in the strength of the z^6P, a^8D and a^{10}D → a^8S features that are of much greater intensity in the blue sites of the RG's.

The enhanced relaxation to lower energy excited states in the blue site is also evident in y^8P fluorescence spectra recorded at increased temperatures and presented in Figure IV.61. The rate of decrease in emission band area is much greater in the blue site of isolation, implying non-radiative relaxation pathways are involved to a larger extent compared to the red site. For example, there is a 1 % decrease in emission strength when the sample temperature is raised from 10 K to 14 K for guest atoms in the red site. Blue site isolated Eu atoms lose y^8P state emission intensity by a factor of thirty three times more than this. This shows that even in this small 4 K temperature range, non-radiative relaxation pathways competing with the y^8P → a^8S electronic transition are much more involved for atoms in the blue site of isolation hence not allowing the radiative lifetime to be identified.

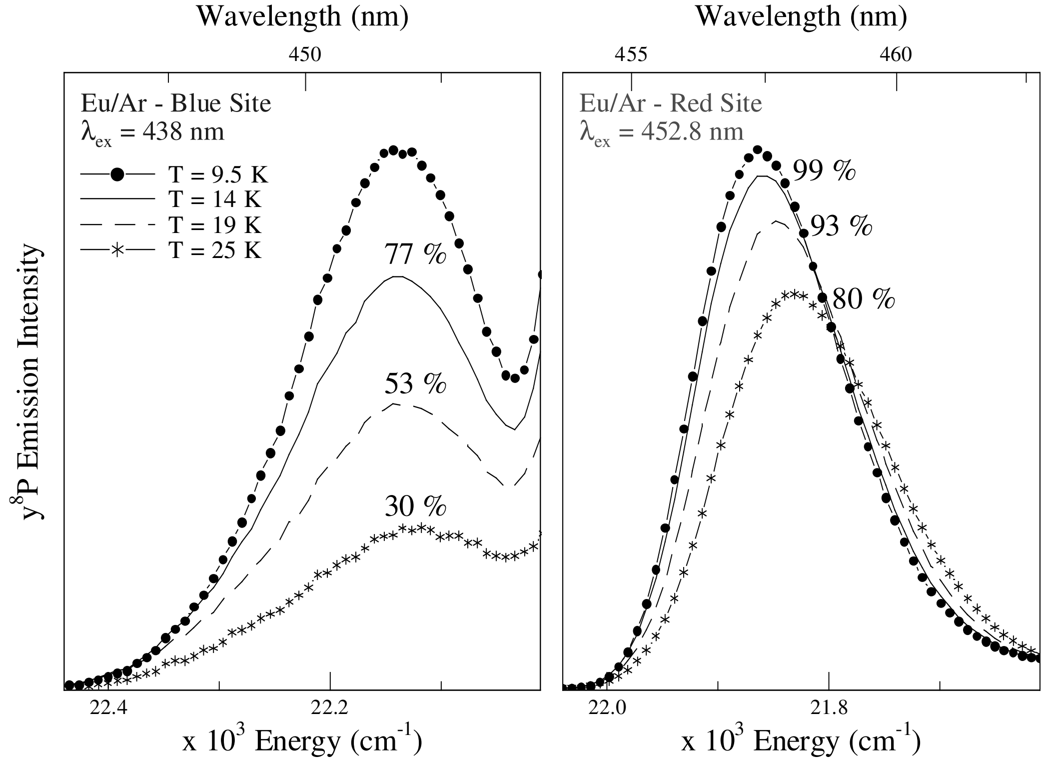

Figure IV.61 y^8P state site-specific emission spectra of Eu/Ar at various temperatures. The areas of the emission bands are quoted in terms of percentages relative to the original 10 K scan.

Finally, the effect of different hosts on the y^8P → a^8S transition is presented in Figure IV.62 for the blue site of isolation. Eu/RG spectral features are plotted versus their shift from the position of the y^8P → a^8S transition in the gas phase. Short range repulsive interactions are greatest for hosts with smaller vacancies and the long range Eu-RG attractive interactions increase with increasing host polarisability. These effects are the source of the greatest matrix shift to higher energy observed in the smaller, least polarisable Ar lattice. The larger, more polarisable xenon host exhibits very little matrix shift, the central JT excitation feature corresponds almost exactly with the y^8P → a^8S transition in the gas phase.

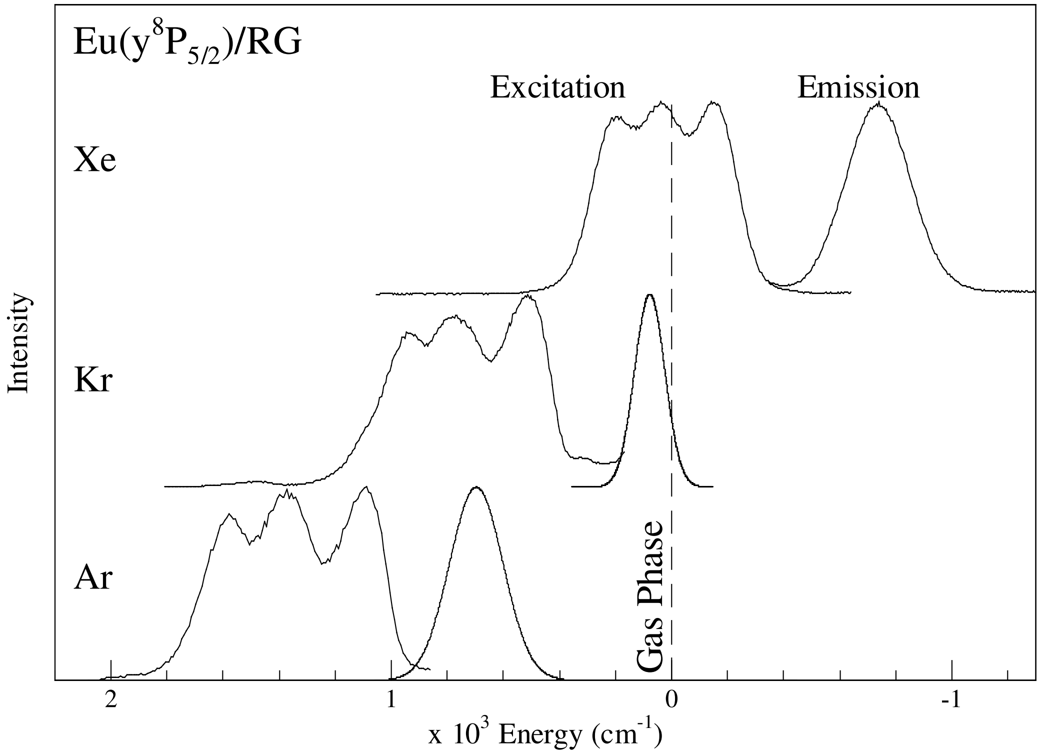

Figure IV.62 Excitation and emission spectra of the y^8P state recorded in the blue site of the Eu/RG's. Note the spectra are shown relative to the gas phase transition where the zero position represents the gas phase transition.

IV.5.I.II D State Emission

A comparison can be made for D → S type emissions observed from both sites in the solid RG's. Relaxation from the metastable a^{10}D state to the ground state is the best case for comparison as it is observed and identified in both sites in all hosts. Table IV.7 collates the spectral and temporal data of the a^{10}D state emission.

Evident for the emission from each site is the negligible spectral shift and similar bandwidths between Ar and Kr. Emission occurs at 790 nm with a width of approximately 210 cm^{-1} in the red site. There is also little difference in spectral location and bandwidths for a^{10}D state features from guest atoms isolated in the blue site in the Ar and Kr hosts. Bandwidths of 280 cm^{-1} and emission maxima at 815 nm are observed. However, a^{10}D state emission in Xe does not follow this trend. It yields a broader emission feature which is slightly red shifted compared to the corresponding Ar and Kr emission. This shift to lower energy is an effect of the increased stabilisation of the D state in the much larger and more polarisable Xe lattice.

Table IV.7 Photophysical characteristics of the a^{10}D state emission features of the thermally stable blue and red sites of isolation in Eu/RG. The spectral position is quoted in λ (nm) and ν (cm^{-1}). The bandwidth (*fwhm*) is denoted as Δ. Gas phase to matrix frequency shifts for the assigned transition, δ, are displayed in wavenumber units. The observed lifetimes recorded in the matrix at 10 K are labelled τ_{10K}.

Eu/RG – $\boldsymbol{a^{10}D \rightarrow a^{8}S_{7/2}}$ phosphorescence

Host	ν (cm^{-1})	λ (nm)	Δ (cm^{-1})	δ (cm^{-1})	τ_{10K} (ms)
Gas Phase[1]	12923.7	773.77	-	-	-
		Red Site			
Ar	12649	790.6	203	– 275	**0.7** 2.1
Kr	12671	789.2	217	– 253	**0.8** 2.2
		Blue Site			
Ar	12281	814.3	281	– 643	**0.4** 1.3
Kr	12262	815.5	285	– 662	**0.8** 2.4
Xe	12145	823.4	367	– 779	1.2

An essential difference regarding the solid state luminescence of D → S type emissions of atomic Eu compared with P → S is that the blue site features occur to lower energy than the corresponding red site D → S emission. The occupied lattice sites are labelled blue and red as monitored in the y^8P spectral region where they occur at higher and lower energy respectively. However, D state emission shows a reversal to this. Figure IV.63 displays a representative potential energy diagram of these excited states of atomic Eu in solid Ar, showing the relative shift of the P and D states in each site. Shown to the left of Figure IV.63 is the gas phase positions of the y^8P and a^{10}D states. For a metal atom in the gas phase, absorption and emission occur at exactly the same energy. For the $y^8\text{P} \rightarrow a^8\text{S}$ transition in the matrix, however, the metal atom remains isolated in a spherical site within the lattice while transitions between a ground state configuration with a spherical symmetry and that involving an anisotropic p-orbital occur. The excited atom is effectively larger than the ground state atom but the lattice site remains the same size. The excited guest experiences greater short range repulsive interactions with the host atoms thereby shifting its potential. These repulsive forces are larger in the smaller tetra-vacancy blue site causing the greatest potential shift. This results in blue site $\text{P} \rightarrow \text{S}$ transitions which occur to higher energy than the red site. However, transitions from the a^{10}D state involve occupancy of a d-orbital which is shielded from the repulsive forces of the surrounding hosts atoms by the outer 6s-orbital. This causes there to be little shift in the D state potentials compared to the ground state.

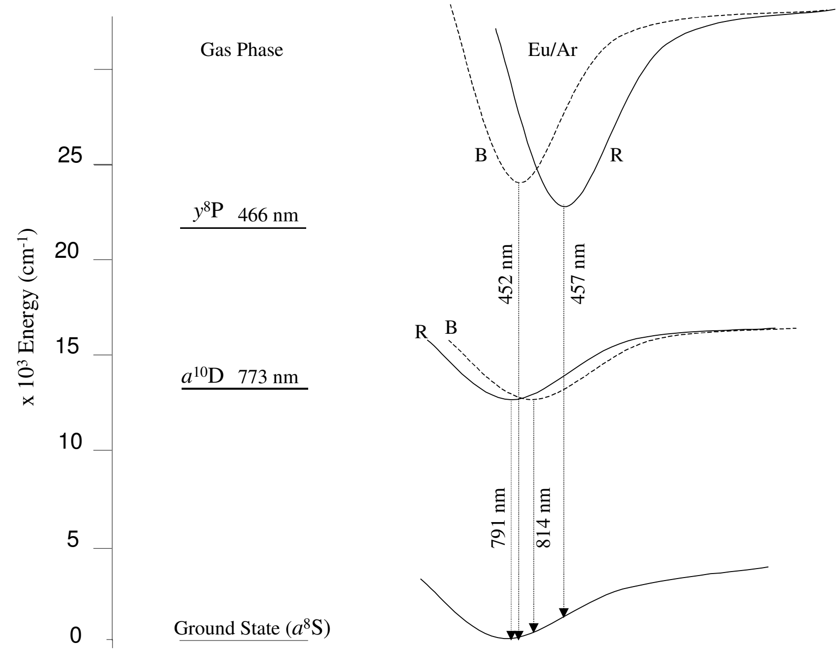

Figure IV.63 Representative potential energy diagram of the a^8S, y^8P and a^{10}D states in the red (R) and blue (B) sites of Eu/Ar versus the gas phase energies.

Another comment regarding D state luminescence of atomic Eu isolated in the solid RG's is the fact that these emissions are broadened and considerably shifted from the gas phase position of the corresponding electronic transition. Although D → S transitions are historically expected to be narrow, a study of the D state luminescence of atomic manganese isolated in the solid RG's has shown that the site size available plays an important role in defining its spectral characteristics[5].

In the case of atomic Mn isolated in solid krypton, two thermally stable sites of isolation are occupied in the *fcc* structured lattice, a single-vacancy (sv) site of size 3.99 Å and a larger tetra-vacancy (tv) with a size of 4.68 Å. The Luiti-Pirani method predicts a Mn-Kr van der Waals diatomic bond length of 4.54 Å. The tv site can easily accommodate the Mn atom with little distortion of the lattice site. Conversely, when the Mn atom exists in the sv site, considerable distortion is necessary to accommodate the guest atom causing interaction between the guest Mn and the surrounding lattice. The differing strengths of the Mn-RG interaction in each of these spatially very different lattice surroundings manifests itself in the luminescence observed from D type excited states. When the guest atoms cause little lattice distortion, D states show the classically expected narrow and unshifted spectral features. Thus for Mn(^{6}D)/Kr in a tv, a narrow bandwidth of 65 cm^{-1} and small matrix shift of –18 cm^{-1} is observed. However, Mn(^{6}D)/Kr sv site emission is considerably broadened and shifted, a bandwidth of 260 cm^{-1} and matrix shift of –1097 cm^{-1} are identified. When these observations are applied to the case of Eu/RG, neither the blue or red sites proposed to be tv and hv sites can accommodate the Eu guest without significant site distortion. This can be seen by consulting Table III.5 in Chapter III. Based on these considerations, the broadened and shifted atomic Eu D state emission in the RG's is to be expected for Eu/RG.

IV.5.II Temperature Effects

Steady-state spectra recorded for the Eu/RG emission profiles show a temperature dependence and this was used to probe the behaviour of the excited states involved and identify relaxation processes. There are clear similarities between atoms in the same site so results are discussed in these terms. In all cases, the y^8P fluorescence showed a decrease in emission strength with increasing temperatures. This is an indication of non-radiative relaxation processes competing with the y^8P → a^8S electronic transition becoming enhanced at higher temperatures and implies feeding steps to lower energy level(s) are thermally activated. It should be noted z^6P, a^8D and a^{10}D state emission is produced with y^8P state excitation even at 10 K so there is already some interaction between the y^8P state and these emitting states at this low temperature. Summary plots of the effects of increased temperature are presented as simplified energy level diagrams in Figure IV.64 and Figure IV.65.

IV.5.II.I *Red Site*

A summary of the effects of temperature on the emission profiles of atomic Eu isolated in the red site of isolation is presented in Figure IV.64. In conjunction with a decrease in emission strength of the y^8P state fluorescence at increased temperature, a gradual increase in emission intensity of the z^6P state occurs implying there is enhancement of the non-radiative feeding rate from the upper y^8P state to the z^6P state caused by crossing of the y^8P and z^6P potential energy surfaces.

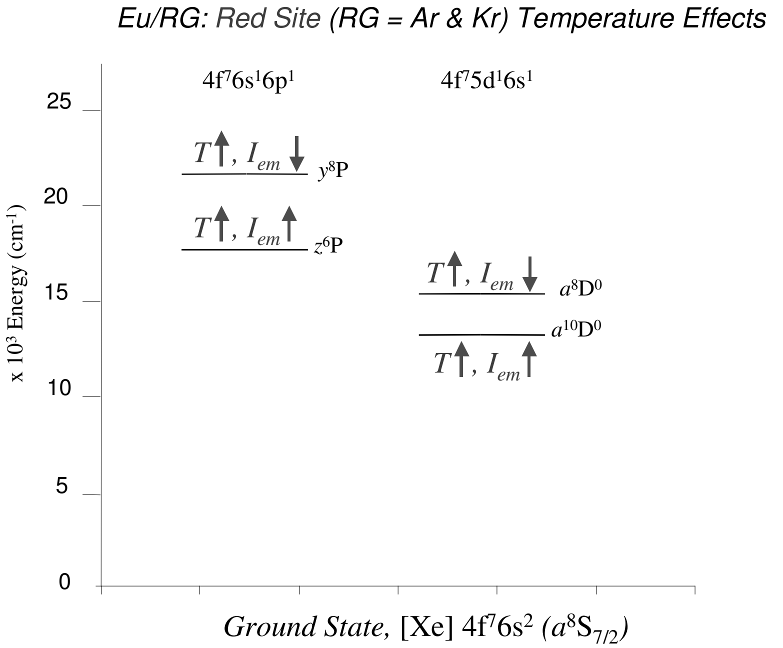

Figure IV.64 Summary plot of the effects of increased temperature on the intensity of each of the Eu/RG emission bands in the red site of isolation. The energy level schematic is simplified to show only the excited states observed in emission in the RG solids.

Coupled with this, a decrease of the a^8D → a^8S emission is observed in solid Ar at higher temperatures, implying competing relaxation to the metastable a^{10}D state is enhanced.

In contrast, emission from the a^{10}D state is promoted at elevated temperatures. The metastable a^{10}D state is the lowest energy excited state, there are no interlying states between it and the ground a^8S state so a^{10}D acts as a ‘population trap’ where any remaining population, which has not been radiatively emitted following y^8P excitation, is forced to relax to before finally being released from the sample as energy at approximately 800 nm corresponding to the a^{10}D → a^8S electronic transition. Thus by increasing the sample temperature one increases the rate of internal conversion/intersystem crossing to the a^{10}D state thereby increasing its population and hence its intensity.

IV.5.II.II <u>*Blue Site*</u>

An overview of the effects of increased temperature on steady-state emission spectra of europium atoms isolated in the blue site of isolation is presented in Figure IV.65. A weakening in emission strength of the y^8P state fluorescence is detected at raised sample temperatures but unlike in the red site, an unusual trend is identified for the z^6P state. A slight increase of intensity is first observed at elevated temperatures of 14 K and 19 K in Ar and Kr respectively caused by enhancement of non-radiative feeding from the upper y^8P state. However, at temperatures greater than this, there is a gradual decrease in emission intensity as other relaxation pathways competing with z^6P → a^8S electronic transition become more efficient. In contrast to this, a decrease in emission intensity of the y^8P state in Xe coincides with a concurrent decrease in z^6P state strength at elevated temperatures suggesting non-radiative relaxation pathways in solid Xe become more effective than the z^6P → a^8S electronic transition at all temperatures.

Emission from the a^8D state in blue sites of isolation follows no trend allowing few general conclusions to be drawn. In the case of Ar, a^8D state emission shows a progressive increase in strength at higher temperatures which can be rationalised as an increase in non-radiative relaxation of the upper P states. Kr however, exhibits completely opposite behaviour, showing a decrease in emission intensity, which indicates the non-radiative relaxation to the lower a^{10}D state is more efficient. While in the Xe lattice a^8D emission is not observed suggesting feeding to the lower a^{10}D state is even more efficient. Finally, the emission intensity of the metastable a^{10}D state increases at elevated temperatures in all RG's. This is caused by enhanced feeding from the higher energy levels which increases the population of this lowest energy excited state.

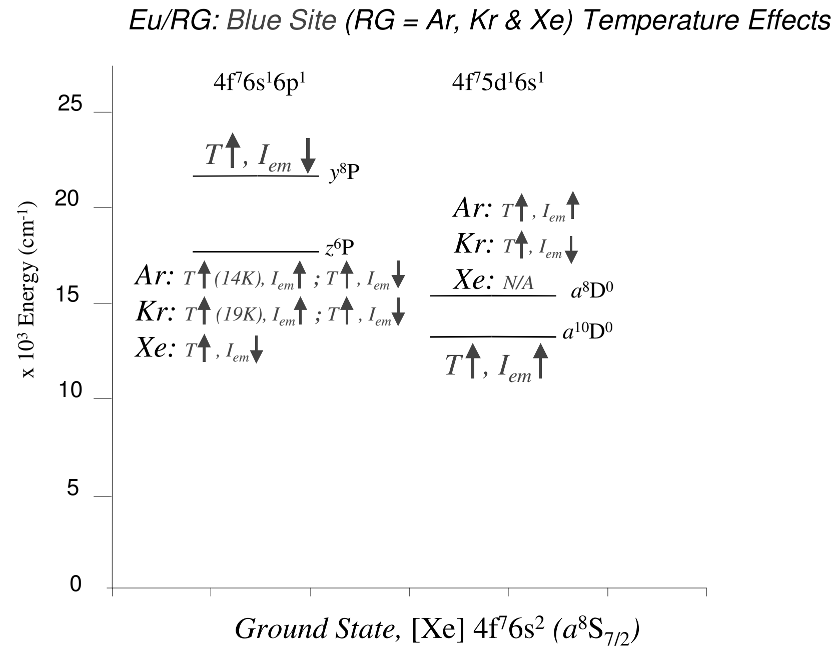

Figure IV.65 Summary plot of the effects of increased temperature on the intensity of each of the Eu/RG emission bands in the blue site of isolation. The energy level schematic is simplified to show only the excited states observed in emission in the RG solids.

IV.5.II.III Temperature Effects Discussion

In summary, atomic Eu isolated in both sites within the *fcc* RG lattices shows a progressive decrease in emission intensity of the y^8P state at elevated temperatures due to enhanced relaxation to the lower energy excited states. This is coupled with an increase in strength of the a^{10}D emission profiles, as this metastable state acts as a 'population trap'. The interlying z^6P and a^8D states show site-specific temperature effects as detailed in the preceding sections.

IV.6 Eu(z^6P)/RG Resonance Fluorescence

The preceding sections analysed the emission features produced with y^8P state excitation. Four features were observed and assigned as emission from the y^8P, z^6P, a^8D and a^{10}D states based on their spectral location and lifetimes. However, the lifetimes recorded for the z^6P state emission in the 560 nm region were not in complete agreement with the gas phase. The following sections aim to further probe the z^6P state emission through the simplest excitation pathway, i.e. direct $z^6\mathrm{P} \leftarrow a^8\mathrm{S}$ resonance excitation. Blue site excitation features identified in this region allow z^6P emission and decay profiles produced with direct excitation to be investigated. The corresponding red site emission features in Ar and Kr were much weaker in intensity and did not allow z^6P state luminescence to be recorded from this site.

IV.6.I Eu(z^6P)/Ar

Atomic Eu is observed to emit from the z^6P state at 556.9 nm in the Ar lattice produced with y^8P state blue site excitation. Excitation spectra recorded in this region, presented in Figure IV.66, show two structureless features centred at 541 and 552.7 nm. The gas phase position of the $z^6\mathrm{P}_J$ levels are displayed as dashed vertical lines. Emission produced with excitation of each of these excitation components yields an identical emission profile centred at 557 nm.

The temporal profile of this emission feature produced directly with excitation at 552.7 nm exhibits a double exponential decay with lifetime components of 30 and 96 ns at 10 K as shown in Figure IV.67. The lifetime of this emission produced indirectly with y^8P state excitation was 33 and 240 ns. The shorter lifetime components recorded using direct (z^6P) and in-direct (y^8P) excitation compare quite well.

Due to weak emission intensity in solid Ar the temporal profiles produced at elevated temperatures, presented in Figure IV.68, are quite noisy. However, it is obvious there is little temperature dependence in the 10 to 16 K range indicating the radiative lifetime of this electronic transition is identified in the Ar lattice. Matrix corrected lifetimes of 62 and 197 ns are calculated.

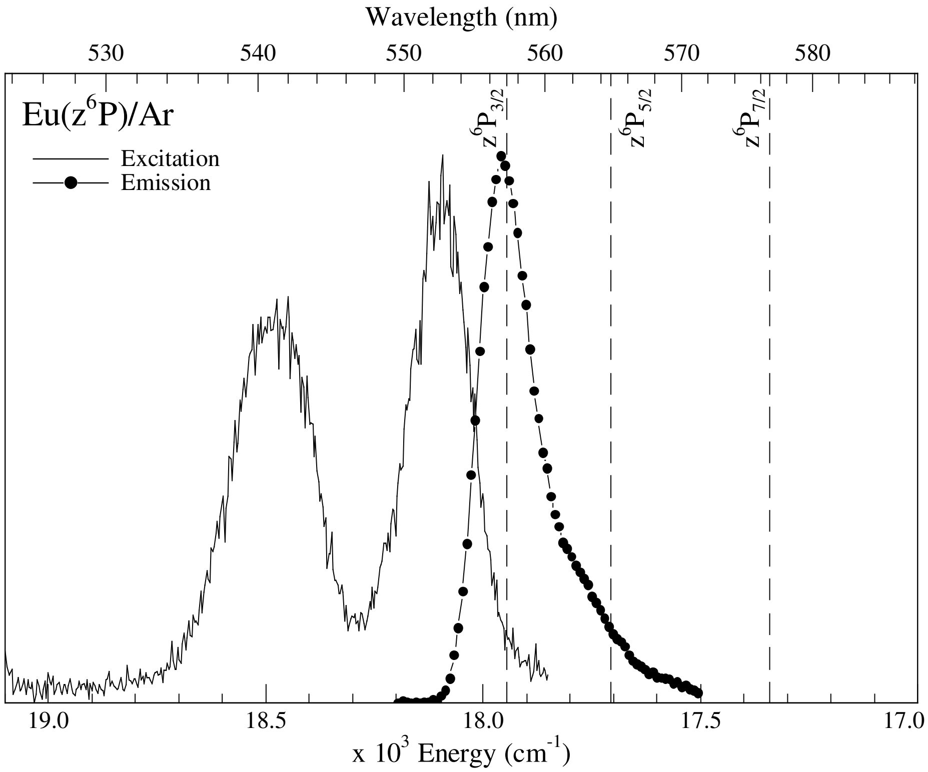

Figure IV.66 Eu/Ar blue site excitation spectra recorded in the region of the z^6P state of atomic Eu. The spectral position of each of the three z^6P spin-orbit levels in the gas phase are shown by the dashed vertical lines.

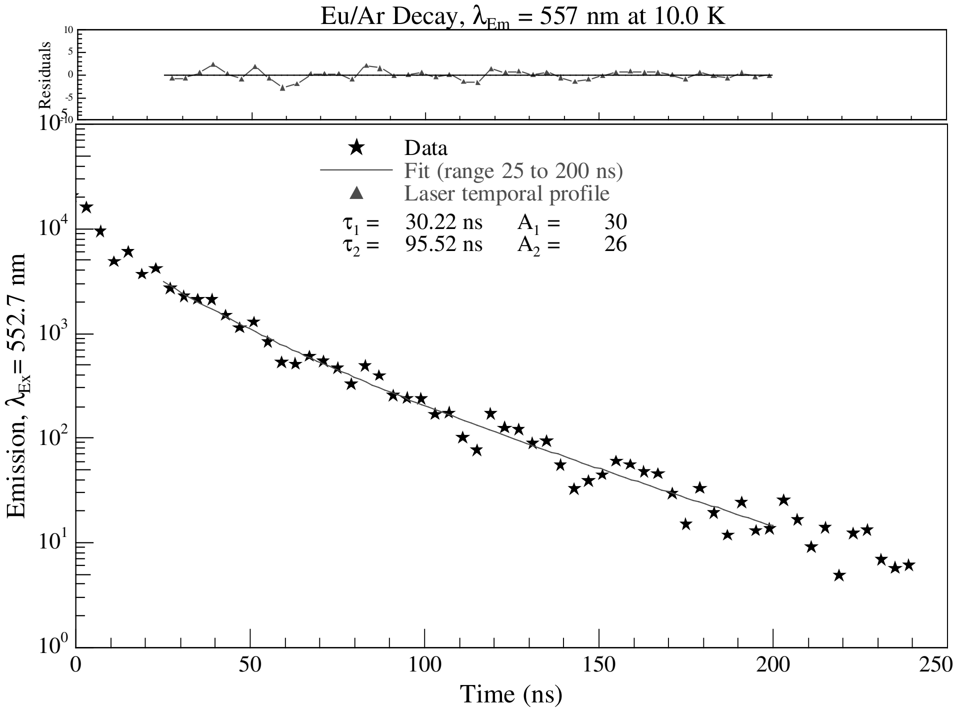

Figure IV.67 Decay profile of the Eu/Ar blue site emission at 557 nm produced with direct z^6P resonant excitation at 552.7 nm. The decay profile is satisfactorily fitted with a double exponential function.

Temperature dependence - $\lambda_{Em.}$= 557 nm decay curves

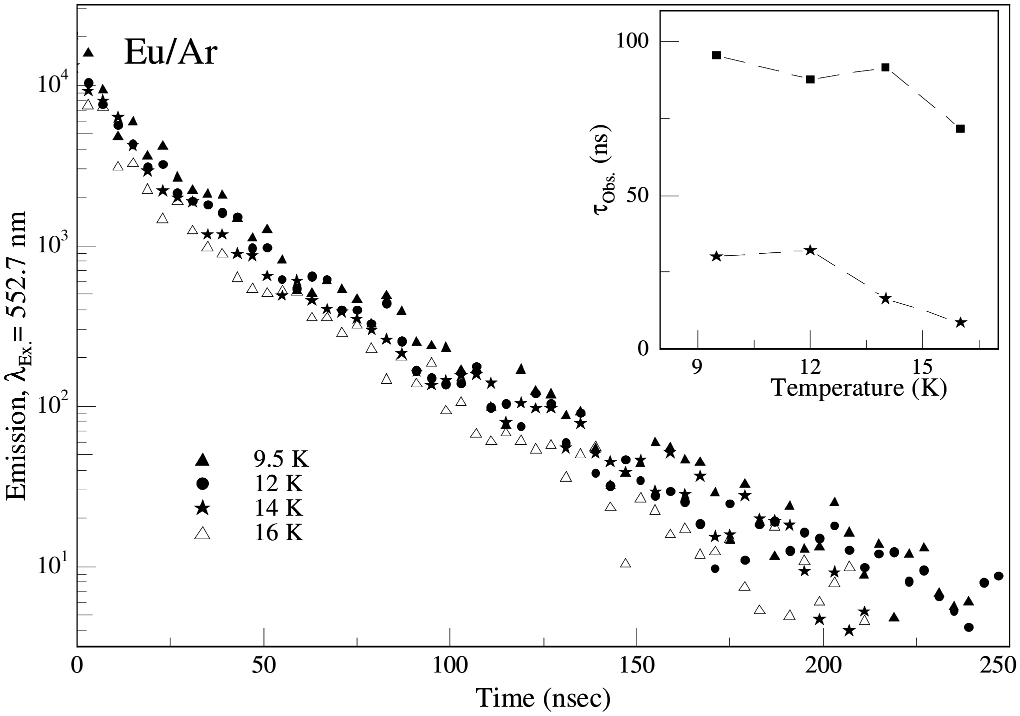

Figure IV.68 Decay profiles of the Eu/Ar emission at 557 nm produced with direct z^6P state excitation recorded at elevated temperatures in an annealed sample. Inset plots the lifetimes of these decay profiles versus temperature.

In summary, two excitation components are observed in solid Ar at 541 and 552.7 nm occurring as featureless bands with no evidence of any underlying structure. A double exponential decay profile is observed with direct z^6P state excitation yielding a radiative lifetime of 30 and 95 ns at 10 K which when corrected for the effective field of the matrix become 62 and 197 ns.

IV.6.II Eu(z^6P)/Kr

In the blue site of solid Kr, the z^6P state emits at 570.9 nm. Excitation spectra in this region show two features centred at 554.2 and 567 nm. The lower energy excitation component is structureless whilst the higher energy feature exhibits structure with resolvable features as displayed in Figure IV.69. This 554.2 nm band is fully accounted for by two gaussian curves of widths 126 and 89 cm^{-1} centred at 551.1 and 554.2 nm respectively.

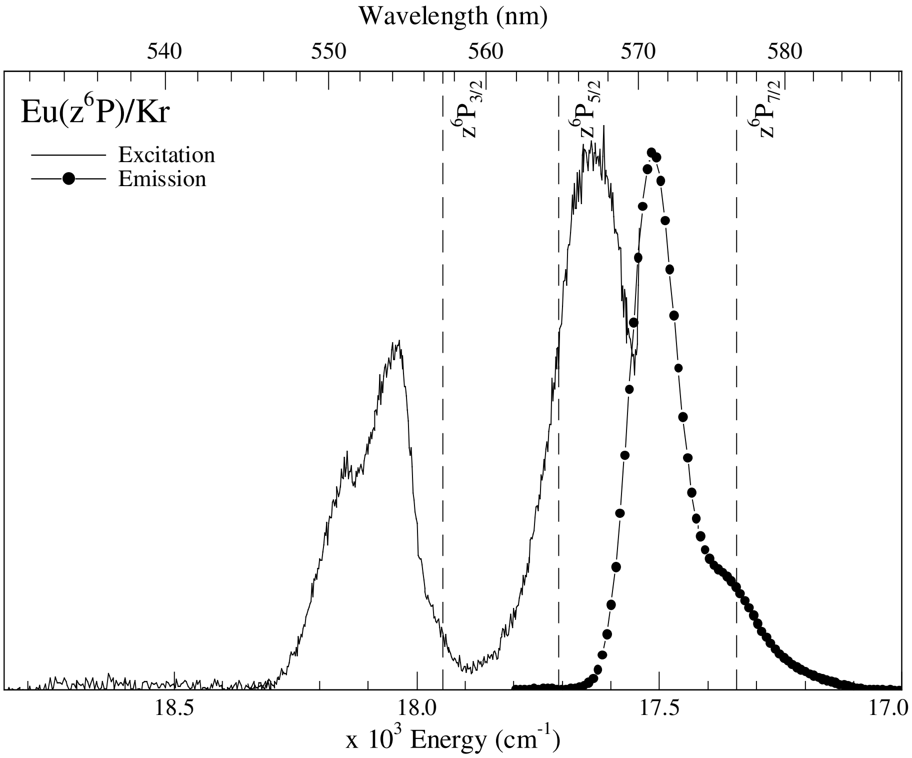

Figure IV.69 Eu/Kr high-resolution excitation spectra recorded in the region of the z^6P state of atomic Eu monitoring the 571 nm blue site emission feature. The spectral position of each of the three z^6P spin-orbit levels in the gas phase are shown by the dashed vertical lines.

Excitation of both spectral components at 554.2 and 567 nm produces an identical emission profile, only emission at 571 nm occurs. The temporal profile of this feature was recorded with direct 566 nm excitation in solid Kr at 13 K. Its characteristic decay curve is presented in Figure IV.70 and exhibits a double exponential decay yielding lifetimes of 38 and 107 ns.

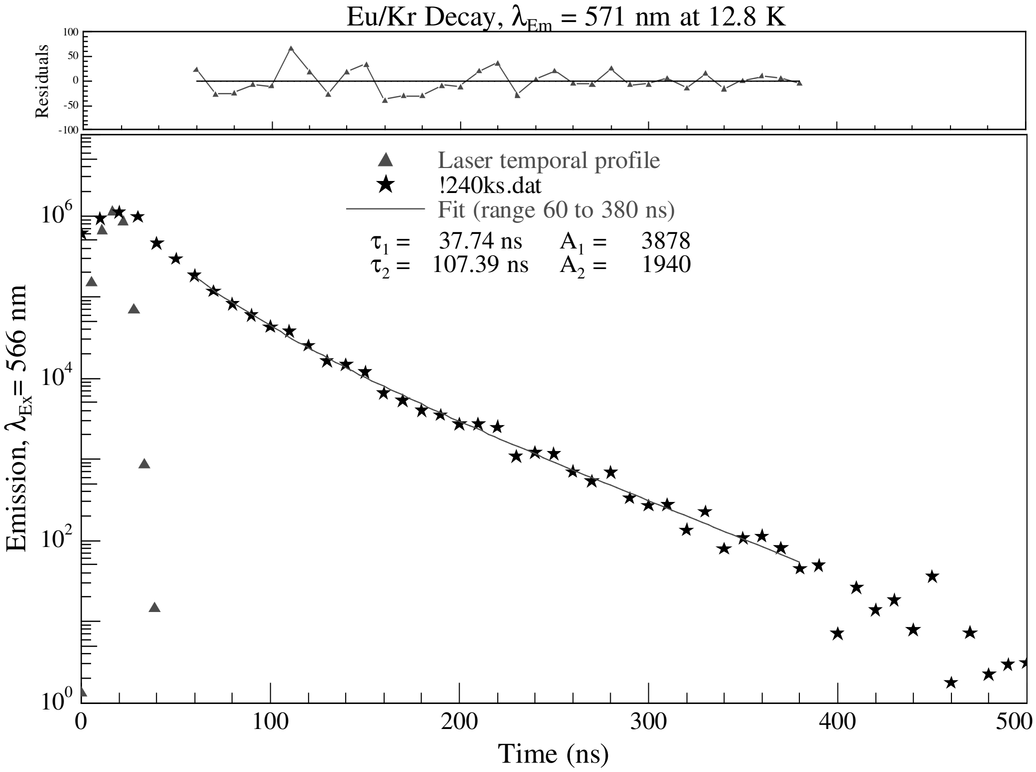

Figure IV.70 Decay profile of the Eu/Kr blue site emission at 571 nm produced with direct z^6P resonant excitation at 566 nm. The decay profile is satisfactorily fitted with a double exponential function.

These lifetimes are of the same order of magnitude as the lifetime recorded for this emission feature produced indirectly with y^8P state excitation (36 and 125 ns). A plot of the decay profiles produced by both methods are almost exactly the same and show no risetime implying the non-radiative $y^8\text{P} \rightarrow z^6\text{P}$ step is very fast and can not be identified on this nanosecond timescale as displayed in Figure IV.71

Further temporal profiles recorded with direct z^6P state excitation at elevated temperatures are displayed in Figure IV.72 and show little temperature dependence in the 13 to 23 K range. The radiative lifetime of this transition is identified, yielding matrix corrected lifetime components of 98 and 277 ns in solid Kr.

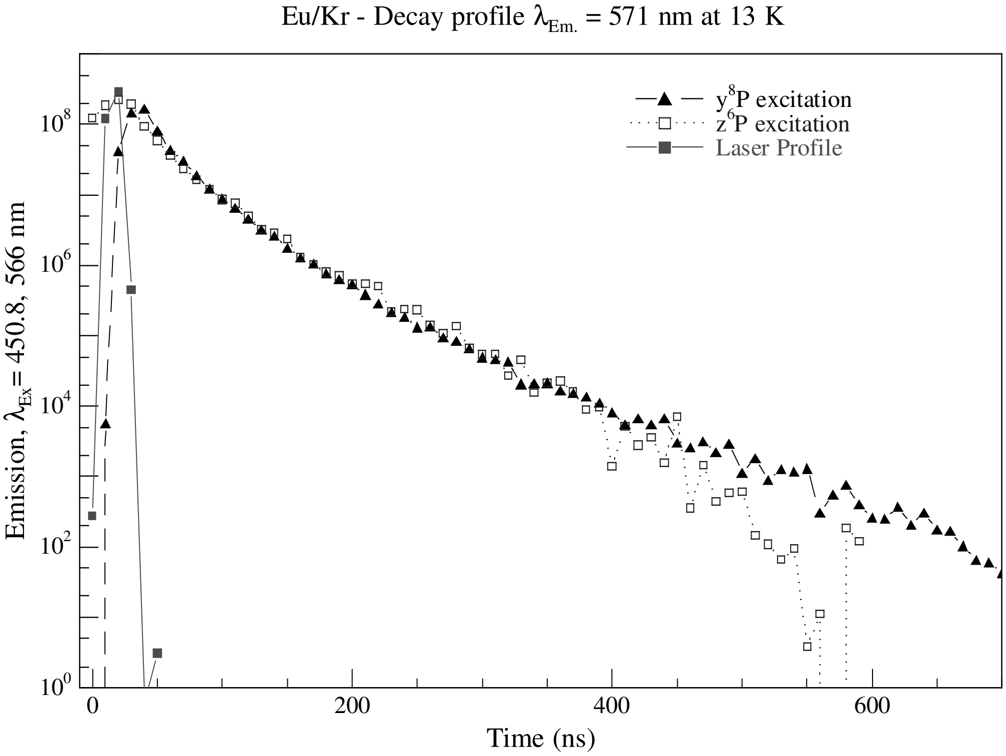

Figure IV.71 Decay profiles of the Eu/Kr blue site emission at 571 nm produced with direct *z*^{6}P resonant excitation at 566 nm (squares) and with indirect *y*^{8}P excitation at 450.8 nm (filled triangles).

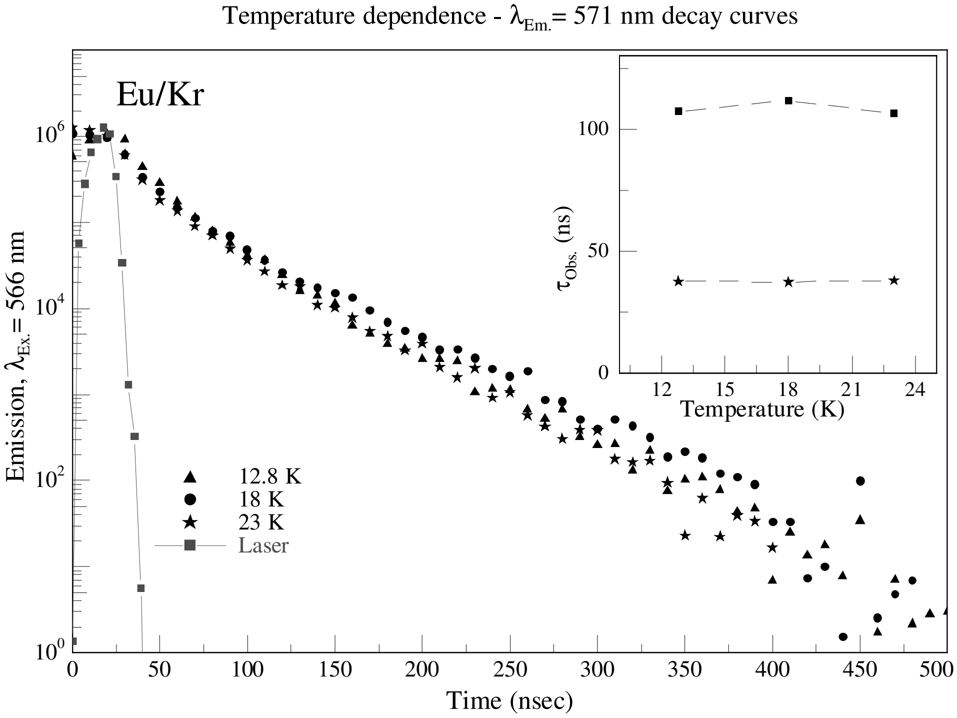

Figure IV.72 Decay profiles of the Eu/Kr emission at 571 nm produced with direct *z*^{6}P state excitation recorded at elevated temperatures in an annealed sample. Inset plots the lifetimes of these decay profiles versus temperature.

In summary, z^6P state emission is observed at 570.9 nm from atomic Eu in the blue site of the Kr lattice. Excitation spectra in this region exhibit a structureless band at 567 nm and a doublet with features at 554.2 and 551.1 nm. Emission produced with direct excitation in this region yields a double exponential decay profile with matrix corrected lifetime components of 98 and 277 ns.

IV.6.III Eu(z^6P)/Xe

Emission from the z^6P state is observed in solid Xe at 589 nm. Excitation spectra recorded in this region present two intense features at 568.7 and 584.4 nm as shown in Figure IV.73. The feature centred at 584.4 nm is structureless while the component at 568.7 nm suggests some further structure to higher energy. A high-resolution laser excitation scan in this region identifies resolved threefold splitting as presented in Figure IV.73. The gas phase position of the z^6P_J levels in this region are displayed as dashed vertical lines.

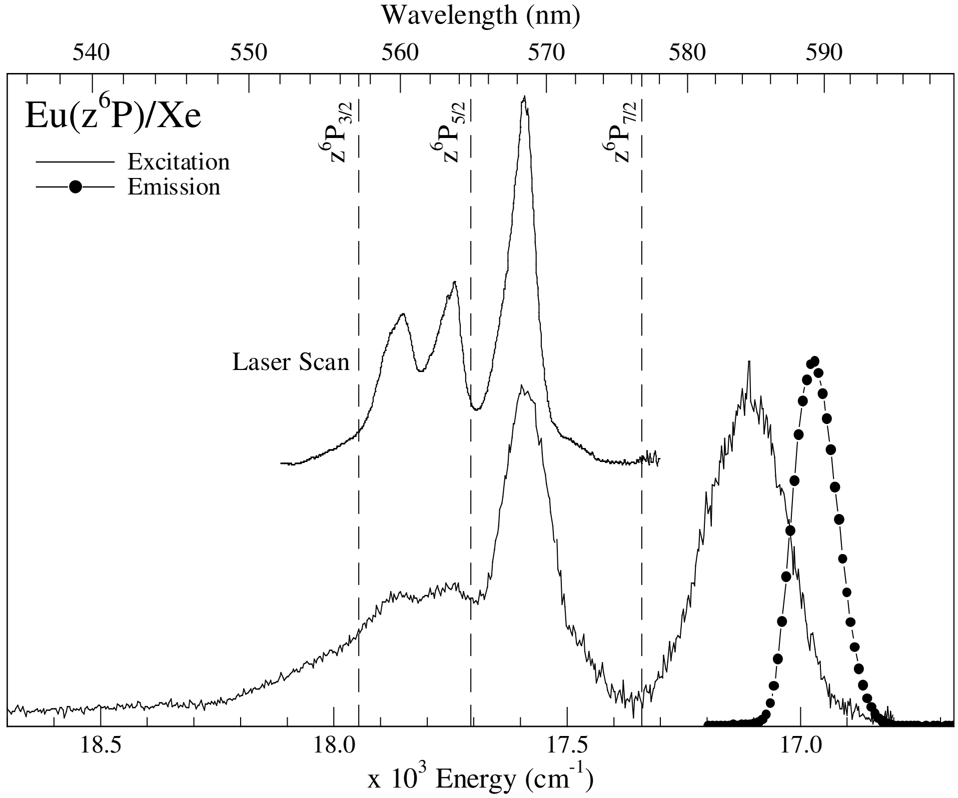

Figure IV.73 Eu/Xe excitation spectra recorded in the region of the z^6P state of atomic Eu monitoring the 589 nm emission feature. Inset of this plot is a high-resolution laser excitation scan recorded in the 550 to 575 nm spectral region. The spectral position of each of the three z^6P spin-orbit levels in the gas phase are shown by the dashed vertical lines.

Photoexcitation of all the structured bands in the excitation spectrum produced identical emission centred at 589 nm. The temporal profile of this 589 nm emission feature recorded with direct excitation at 568.3 nm exhibits a double exponential decay profile and is presented with resulting fit in Figure IV.74. Lifetime components of 37 and 88 ns are extracted at 12.8 K.

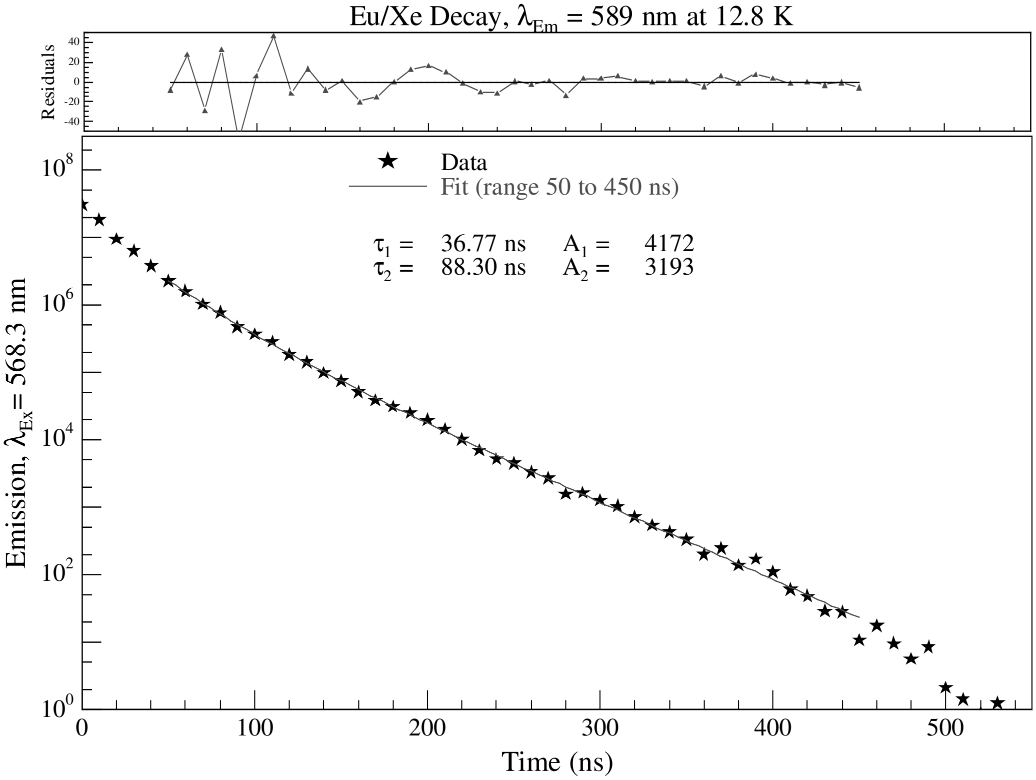

Figure IV.74 Decay profile of the Eu/Xe emission at 589 nm produced with direct z^6P resonant excitation at 568 nm. The decay profile is satisfactorily fitted with a double exponential function.

The same emission feature produced with indirect y^8P state excitation yielded a lifetime of the same order of magnitude (30 and 95 ns), and showed no risetime component. Thus the non-radiative feeding step from the y^8P state to the z^6P state is very fast and not identifiable on this nanosecond timescale. A plot of the temporal profiles of this emission feature produced with both direct (z^6P) and in-direct (y^8P) excitation is presented in Figure IV.75.

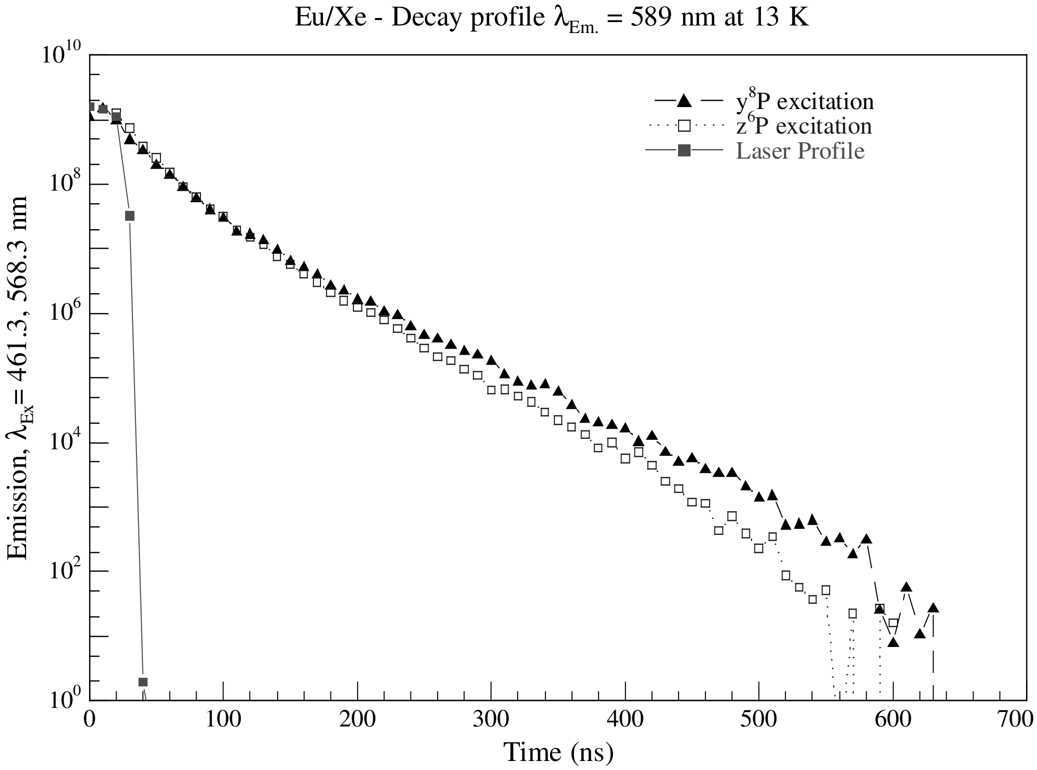

Figure IV.75 Decay profiles of the Eu/Xe emission at 589 nm produced with direct z^6P resonant excitation at 568 nm (squares) and with indirect y^8P excitation at 461 nm (filled triangles).

To further probe the temporal characteristics of the z^6P emission feature in solid Xe its decay profile, produced with direct excitation, was recorded at increased temperatures and is presented in Figure IV.76. Inset of Figure IV.76 is a plot of the lifetime components versus temperature in which the decay profile exhibits no temperature dependence in the range 12.8 to 15 K. This indicates the radiative lifetime of these components are identified in the matrix as 37 and 88 ns and when corrected for the effective field of the host become 109 and 260 ns.

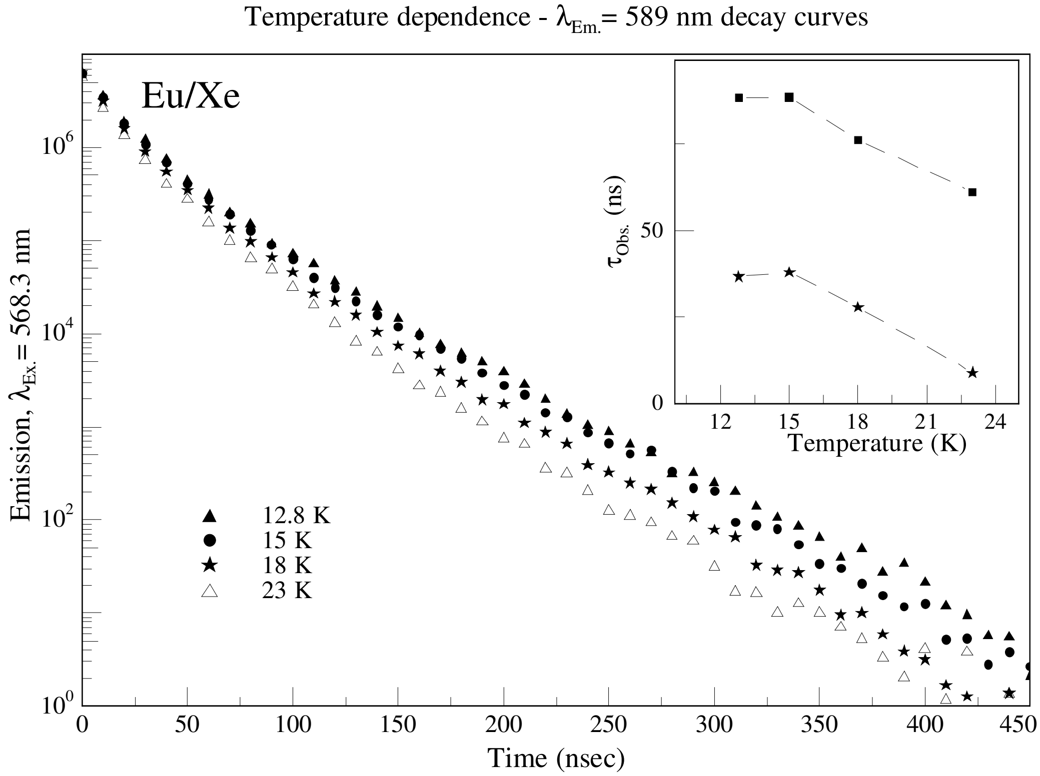

Figure IV.76 Decay profiles of the Eu/Xe emission at 589 nm produced with direct z^6P state excitation recorded at elevated temperatures in an annealed sample. Inset plots the lifetimes of these decay profiles versus temperature.

In summary, excitation spectra in the region of the z^6P state in solid Xe exhibit several features. The higher energy band displays threefold splitting whilst the lower energy feature is structureless. Lifetimes recorded with direct excitation in this region are the same as those produced with indirect y^8P excitation implying the feeding step between the y^8P and z^6P levels is very fast. Decay profiles at elevated temperatures allowed identification of the radiative lifetime of the z^6P state yielding matrix corrected values of 109 and 260 ns.

IV.6.IV Eu(z^6P)/RG

IV.6.IV.I *Eu(z^6P)/RG Excitation Spectra*

The preceding sections presented excitation spectra of the z^6P state of atomic Eu isolated in the blue site of the solid RG'S. Figure IV.77 presents a summary plot of the luminescence in this region in all three hosts for comparison purposes.

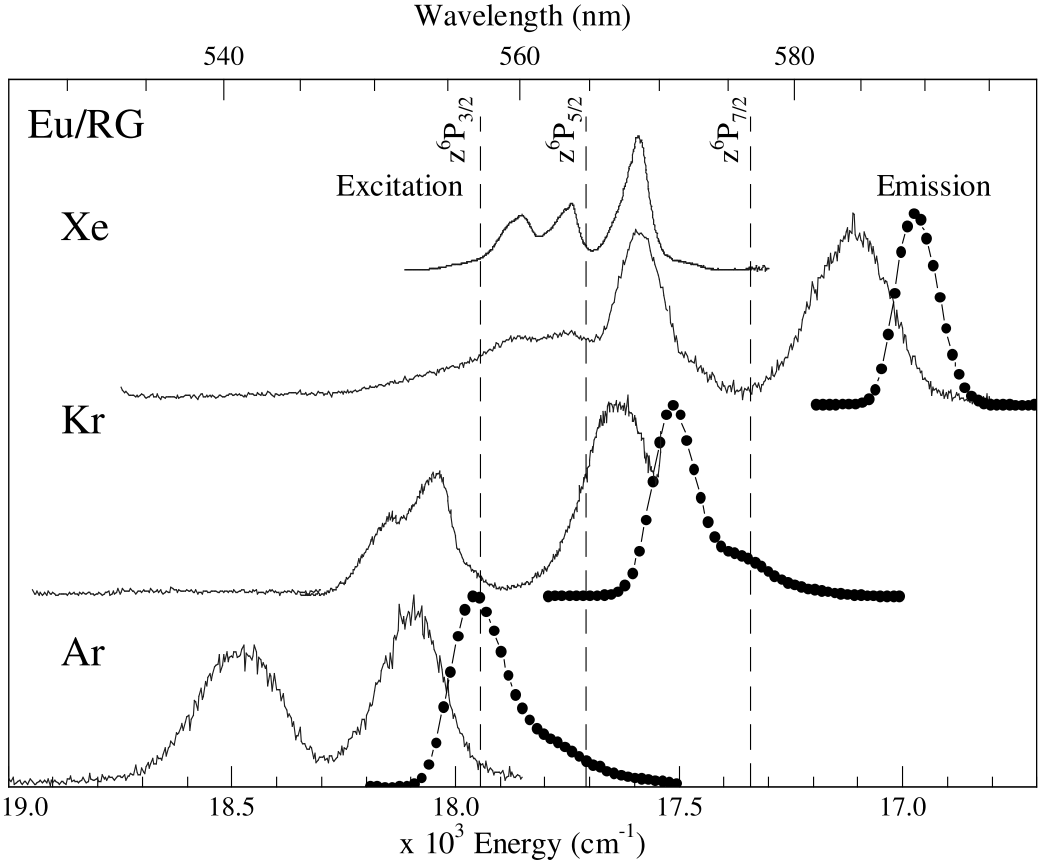

Figure IV.77 Eu/RG blue site z^6P excitation (solid trace) and emission (dotted trace) spectra recorded in the region of the gas phase z^6P state of atomic Eu. The spectral position of each of the three z^6P spin-orbit levels in the gas phase are shown by the dashed vertical lines.

Figure IV.78 presents the excitation spectra shifted to match the gas phase positions of the z^6P_J states. In the Ar matrix there is almost perfect agreement between the spectral location of the experimental data and the gas phase values of the z^6P_J (J=5/2,7/2) levels when a matrix shift of –750 cm^{-1} is accounted for. There is no evidence of a $z^6P_{3/2}$ excitation feature. However, this can be understood by considering the J selection rules for electronic transitions.

For a transition to be electric-dipole allowed[6]:
$\Delta J = 0, \pm 1$ ($0 \leftrightarrow 0$, not allowed).

Atomic Eu exists in a $a^8S_{7/2}$ ground state meaning excitation to the z^6P_J (J = 5/2, 7/2) levels are allowed, exhibiting $\Delta J = -1$ and 0 respectively. Excitation into the 3/2 spin-orbit level would break this selection rule as $\Delta J = -2$ so it is not observed in the RG matrices. As displayed in Figure IV.78, there is also quite good agreement between the experimental excitation spectra of Eu/Kr and Eu/Xe and the gas phase when matrix shifts of – 293 and + 230 cm^{-1} are accounted for.

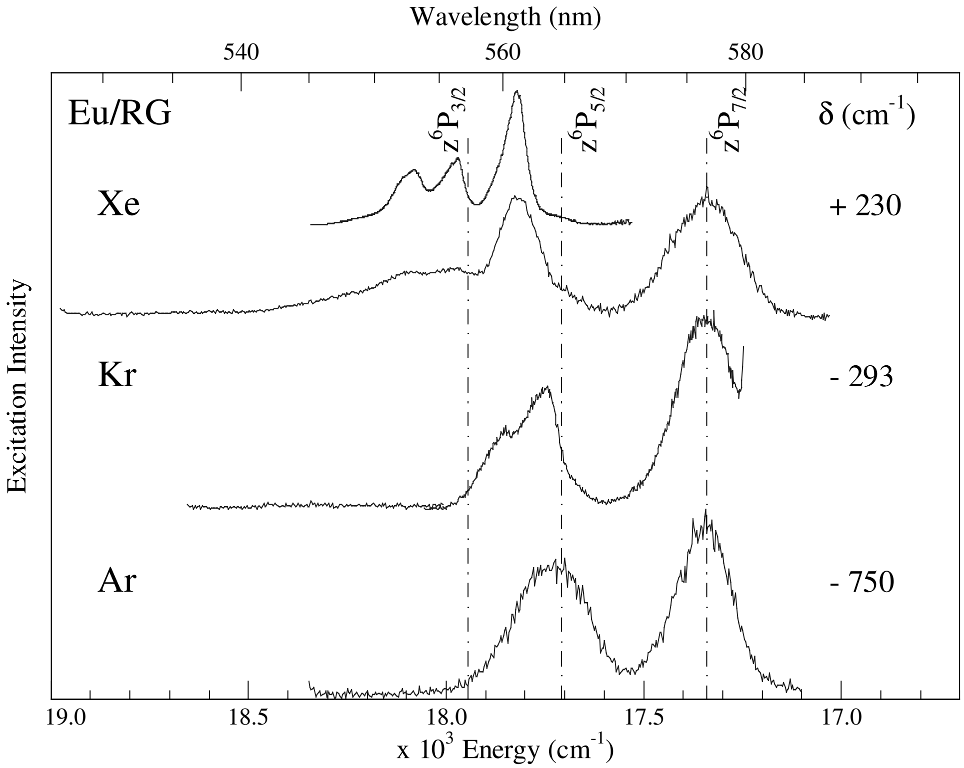

Figure IV.78 Eu/RG blue site excitation spectra recorded in the region of the z^6P state of atomic Eu, the recorded spectra are shifted by δ (cm^{-1}) to align with the gas phase $z^6P_{7/2}$ level. The spectral position of each of the three z^6P spin-orbit levels in the gas phase are shown by the dashed vertical lines.

It is proposed that the two excitation features observed in each RG correspond to the z^6P_J (J=5/2,7/2) states. This is based on the magnitude of their splitting in the RG hosts, which agrees with the size of the splitting between these levels in the gas phase. Further support that these excitation features relate to the z^6P_J (J=5/2,7/2) levels is established when a plot of their shift from the gas phase versus RG polarisability is made. The shift of the lower energy excitation feature from the J = 7/2 gas phase position is presented as filled circles in Figure IV.79. A corresponding plot of the shift of the higher energy excitation feature from the J = 5/2 level is displayed as filled squares. These features' shift from the gas phase position of the individual spin-orbit levels is almost exactly the same implying they originate from the z^6P_J (J=5/2,7/2) spin-orbit states.

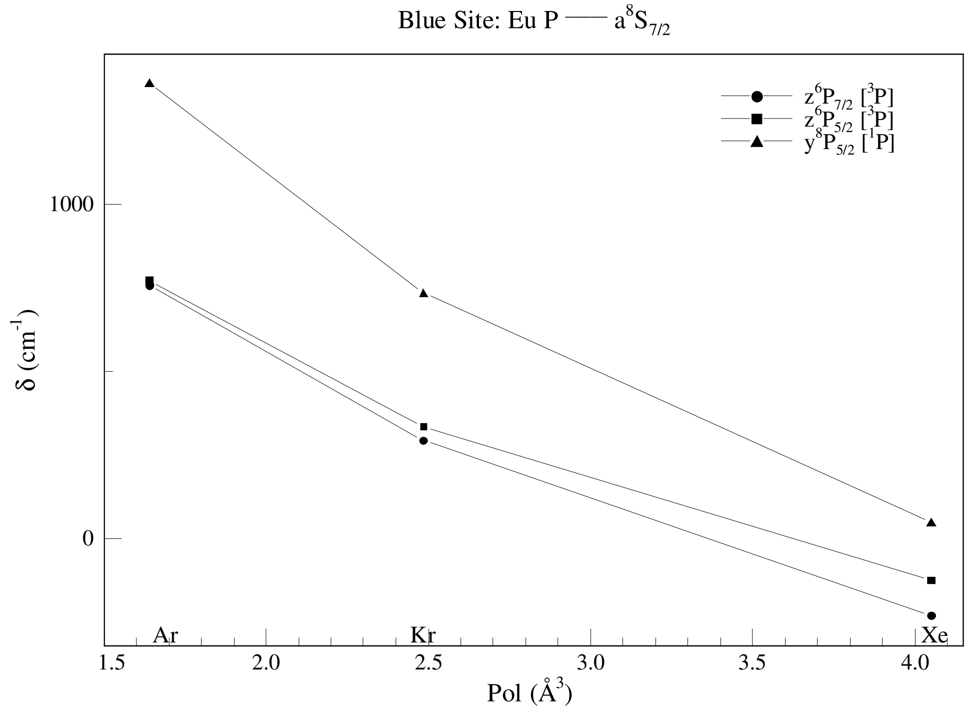

Figure IV.79 A plot of the gas phase to matrix frequency shifts (δ cm^{-1}) observed for the two most intense excitation components of the $z^6P_{7/2}$, $z^6P_{5/2} \leftarrow a^8S_{7/2}$ transitions of atomic Eu versus the RG host polarisabilities (filled circles and filled squares respectively). Also displayed is the gas phase to matrix frequency shift of the $y^8P \leftarrow a^8S_{7/2}$ transition (filled triangles). These plots highlight the linear correlation between the frequency shifts and rare gas polarisabilities.

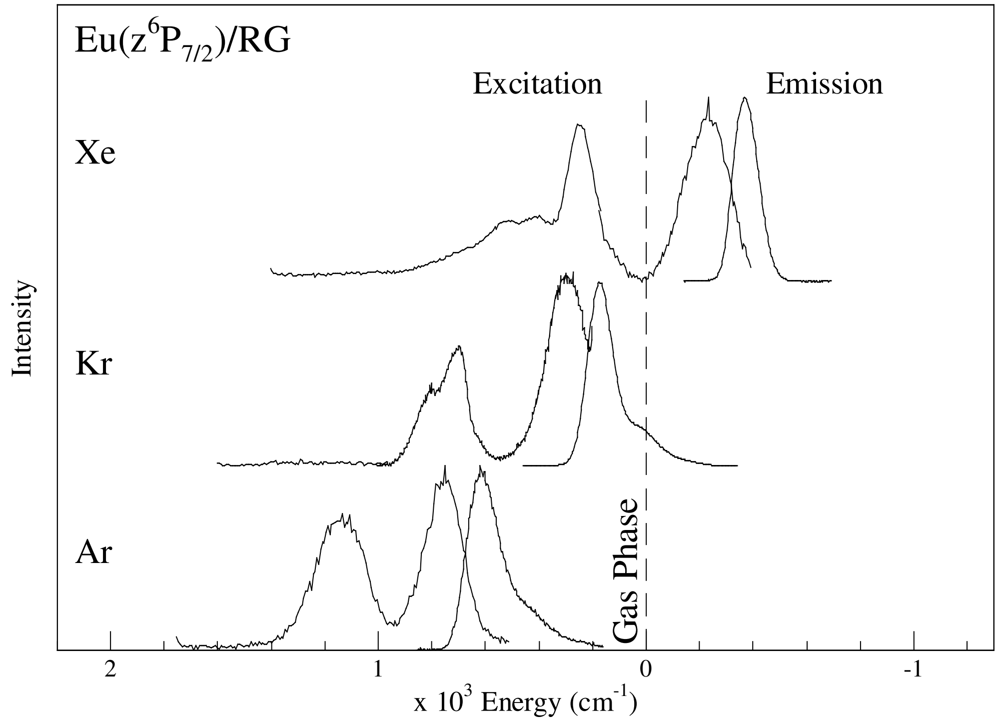

Figure IV.80 Excitation and emission spectra of the z^6P state recorded in the blue site of the Eu/RG's. The spectra are shown relative to the gas phase transition where the zero position represents the gas phase $z^6P_{7/2} \rightarrow a^8S_{7/2}$ transition.

Also of note in the polarisability plot of Figure IV.79 is the slightly steeper slope observed for the ‘singlet-like’ y^8P state when compared to the ‘triplet-like’ z^6P state. For matrix-isolated transition metal systems such as Mn[7], Zn, Cd and Hg[8] the slope of singlet P states are steeper when compared to triplet states. This is also the case here for atomic europium, however in this situation the difference in slopes is not as extreme as for the transition metal systems. This indicates the interactions occurring in the Franck-Condon region of both the y^8P and z^6P excited states are similar and not greatly effected by the spin ‘triplet’ or spin ‘singlet’ arrangement of the two electrons in the 6s and 6p orbitals.

Similar to the y^8P state presented in Figure IV.62, it is evident a matrix shift of the z^6P state occurs as the RG host is changed. Figure IV.80 displays the magnitude of the shifts of the emission and excitation spectra relative to the gas phase position of the $z^6P_{7/2}$ state. A shift to lower energy is observed in larger, more polarisable hosts.

Leading on from this, a comparison of the magnitude of the matrix shifts from the gas phase for both of these P states (y^8P, z^6P) in the three RG’s is compared in Figure IV.81. In Ar and Kr hosts, the magnitude of the matrix shift of the emission features relative to the gas phase is approximately the same. In solid Xe the y^8P state emission exhibits a noticeably greater red shift than the z^6P state.

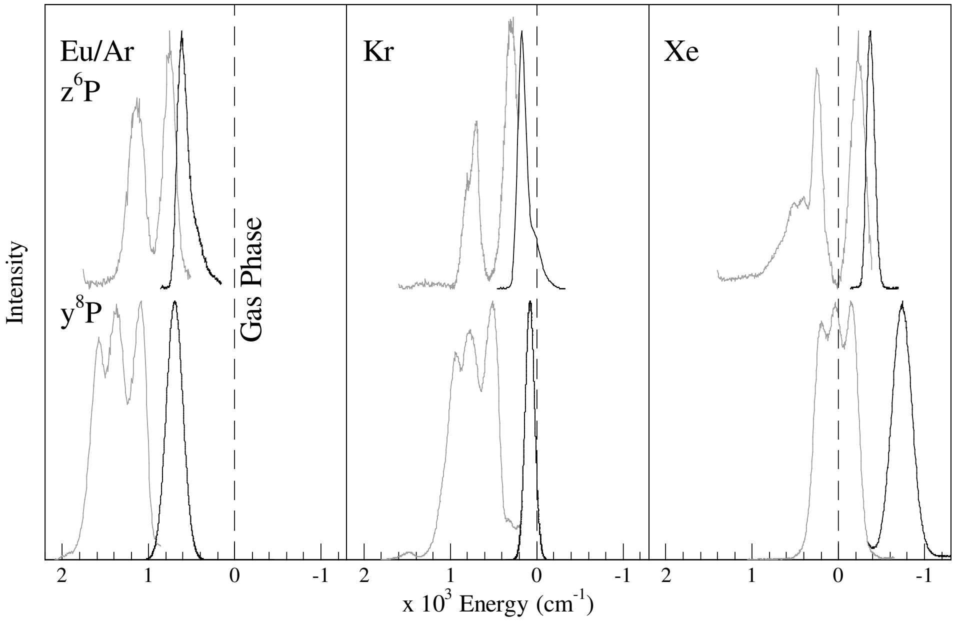

Figure IV.81 Excitation and emission spectra of the z^6P (upper traces) and y^8P (lower traces) states recorded in the blue site of the Eu/RG’s. The spectra are shown relative to the appropriate gas phase transition where the zero position represents the gas phase transitions involved.

Another point of discussion concerns the observation of structure on the higher energy $z^6P_{5/2}$ excitation feature in larger host lattices. As seen in Figure IV.78 it progresses from a structureless band in Ar, to a resolved doublet in Kr, and finally a triplet in solid Xe suggesting Jahn-Teller distortion. By definition the Jahn-Teller effect occurs for an electronically degenerate state in a site of high symmetry. Distortion occurs to lower the symmetry, remove the degeneracy, and thus lower the overall energy. In this case the excited state is a degenerate P state (p_X, p_Y, p_Z). The guest europium metal atom has more freedom of movement when isolated in the larger Xe host as it contains the largest guest lattice sites. This greater degree of freedom in solid Xe suggests there is more possibility of distortion leading to a greater likelihood of JT effects in solid Xe.

If this is the case, Eu/Xe is a uniquely interesting situation, where the same excited state of atomic Eu exhibits both the discreet $z^6P_{7/2}$ spin-orbit state and JT distortion of the accompanying $z^6P_{5/2}$ level. This may be rationalised in terms of the magnitude of the spin-orbit splittings of the z^6P state, the structureless 7/2 level is separated by 367 cm^{-1} from the next spin-orbit level, a large enough value to allow spin-orbit coupling to completely dominate. As the magnitude of the spin-orbit splitting decreases between the higher J-levels (J = 3/2 and 5/2) to two thirds this value it allows the JT effect to begin to dominate. Only becoming obvious in hosts with greater capabilities for distortion such as xenon.

IV.6.IV.II *Eu(z^6P)/RG Temporal Analysis*

With the excitation components of the z^6P state identified it allowed investigation of this feature's emission decay profile through the simplest relaxation pathway. Temporal profiles recorded with direct resonance excitation are displayed in Figure IV.74, Figure IV.70 and Figure IV.67. Although the lifetimes of these emission features are shorter than the z^6P state gas phase value quoted in Table IV.1, they are of the same order of magnitude and in closer agreement than any other P state in the gas phase. All other P states in this region exhibit longer microsecond lifetimes as listed in Table IV.8. The NIST Atomic Spectra Database[1] does not quote the accuracy of its lifetime values and references a source from 1975. There are now more recent gas phase lifetime measurements of this and other P states of atomic Eu available. The most recent study identified a lifetime of 870 +/- 44 ns for the $z^6P_{7/2} \leftrightarrow a^8S_{7/2}$

transition[9] using laser induced fluorescence. A plot of the matrix corrected lifetimes produced with direct z^6P state excitation versus a lambda cubed extrapolation of this most recent gas phase lifetime measurement is presented in Figure IV.82.

Table IV.8 Temporal and spectral characteristics of the P ($4f^7 6s^1 6p^1$) ↔ a^8S ($4f^7 6s^2$) type electronic transitions of atomic europium occurring at $\lambda > 500$ nm in the gas phase. The lifetimes quoted are from various sources, their year of publication is displayed in brackets. The most recent available is from 2002.

Gas Phase P → S type transitions >500 nm

Transition	λ (nm)	τ (2002)[9]	τ (1984)[10]	τ (1975)[1]
$z^6P_{5/2} \leftrightarrow a^8S_{7/2}$	564.5	1.38 μs	1.28 μs	1.85 μs
$z^6P_{7/2} \leftrightarrow a^8S_{7/2}$	**576.5**	**870 ns**	**858 ns**	**909 ns**
$z^8P_{9/2} \leftrightarrow a^8S_{7/2}$	601.8	1.05 μs	1.06 μs	1.18 μs
$z^8P_{7/2} \leftrightarrow a^8S_{7/2}$	626.7	-	14.9 μs	-
$z^8P_{5/2} \leftrightarrow a^8S_{7/2}$	629.1	-	4.92 μs	5.56 μs
$z^{10}P_{9/2} \leftrightarrow a^8S_{7/2}$	686.5	-	1.25 μs	1.72 μs
$z^{10}P_{7/2} \leftrightarrow a^8S_{7/2}$	710.6	-	3.44 μs	3.85 μs

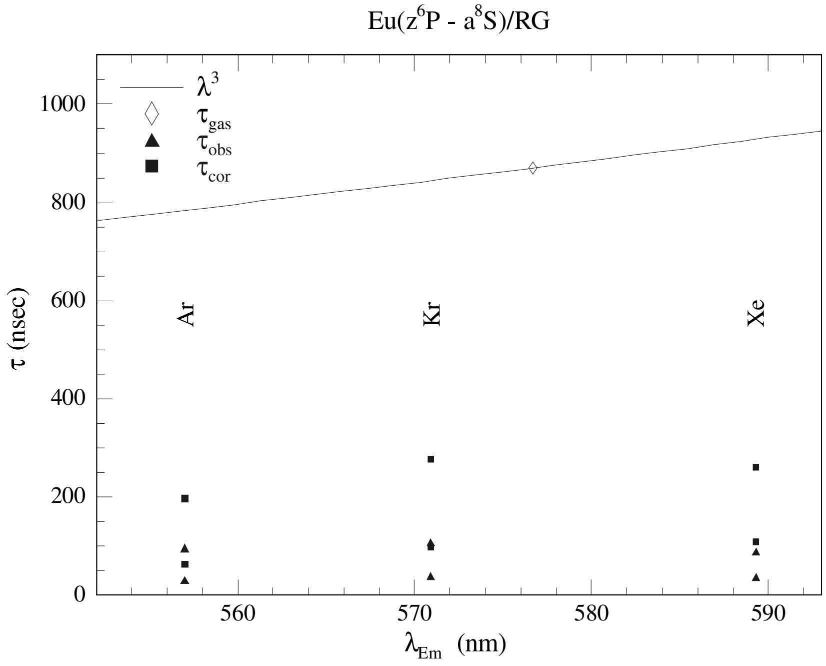

Figure IV.82 Comparison of the lifetimes recorded at 10 K for the Eu(z^6P → a^8S) emission features produced with direct excitation in the blue sites of the RG's and a λ^3 extrapolation of the gas phase lifetime[9] of the $z^6P_{7/2}$ state of atomic Eu. The uncorrected and the data corrected for the effective fields are shown by filled triangles and closed squares respectively.

Figure IV.82 shows there is clearly still a discrepancy between the solid state and the gas phase lifetimes recorded to date. Based on their spectral locations and the much longer microsecond lifetimes of the other P states in this region, these emission features observed in the RG's are confidently assigned to the $z^6P_{7/2} \rightarrow a^8S$ transition. The discrepancy between the solid state and the gas phase may be due to inaccuracies of the gas phase lifetimes recorded to date, the values of which are becoming closer in agreement with the matrix in recent times.

Another point of interest are the temporal profiles of the z^6P state emission feature produced with direct z^6P excitation and indirect y^8P excitation. As was seen in Figure IV.75 and Figure IV.71 the temporal profiles produced with both methods yielded approximately the same lifetimes of the z^6P state emission. This implies the non-radiative feeding step from the upper y^8P state, caused by a crossing of the y^8P and z^6P potential wells, is rapid and can not be detected on the nanosecond timescale used here. There is very efficient inter-system crossing of the electric-dipole spin forbidden $y^8P \rightarrow z^6P$ relaxation which may be due to the large Eu atom exhibiting an internal heavy-atom effect which by definition is enhancement of the rate of a spin-forbidden process by the presence of an atom of high atomic number, which is either part of, or external to, the excited molecular entity[11].

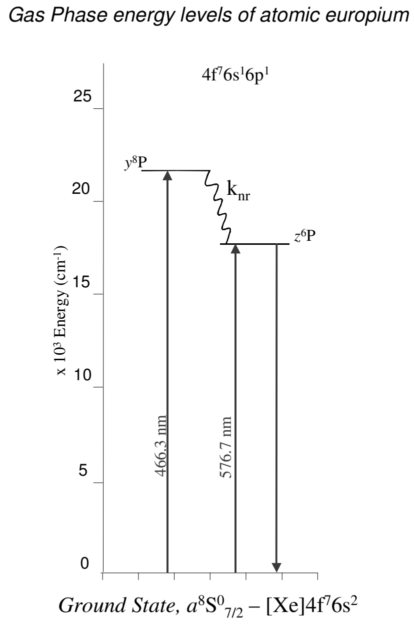

Figure IV.83 Simplified energy level diagram of the $4f^76s^16p^1$ excited states of atomic Eu producing z^6P state emission in the matrix. The non-radiative $y^8P \rightarrow z^6P$ relaxation is labelled k_{nr}.

IV.6.V Eu(z^6P)/RG Summary

In summary, excitation spectra in the region of the z^6P state of atomic Eu isolated in the solid RG's (RG = Ar, Kr and Xe) in the blue site of isolation allow identification of the z^6P_J (J=5/2,7/2) excitation features in the inert hosts. The remaining $z^6P_{3/2}$ level is not observed in accordance with electric-dipole selection rules. Although two spin-orbit levels are identified in excitation spectra, emission in this region is only observed from the lowest energy spin-obit state. Their spectral characteristics are listed in Table IV.9.

Lifetime components are much shorter than the gas phase values of the $z^6P \rightarrow a^8S_{7/2}$ electronic transition recorded to date but definitive assignment of observed emission to the z^6P state is possible due to its spectral location and lifetime of similar magnitude compared to the gas phase. Interestingly the J = 7/2 excitation feature is structureless in all hosts while the J = 5/2 level exhibits Jahn-Teller splitting, the extent of which increases in larger, more distortable hosts. Of particular interest, the z^6P state in solid Xe allows unique observation of both JT distortion and spin-orbit splitting on the same electronic state.

Table IV.9 Spectral and temporal characteristics of the z^6P state excitation and emission features of atomic Eu occupying the blue site of isolation in the solid RG's. Their spectral position in nanometres (nm) is labelled λ, while ν indicates their position in wavenumbers (cm^{-1}). Gas phase to matrix frequency shifts are presented as δ in wavenumber units. Matrix corrected lifetimes of the emission bands recorded in the matrices at 10 K are identified by τ_{Cor}.

	Excitation Features						Emission Features			
	ν (cm^{-1})	λ (nm)	δ (cm^{-1})	ν (cm^{-1})	λ (nm)	δ (cm^{-1})	ν (cm^{-1})	λ (nm)	δ (cm^{-1})	τ_{Cor} (ns)
		$z^6P_{5/2}$			$z^6P_{7/2}$			$z^6P_{7/2}$		
GasPhase[9]	17707	564.7	-	17341	576.7	-	17341	576.7	-	870
Eu/RG										
Xe	17584	568.7	– 124	17112	584.4	– 229	16969	589.3	– 372	**109** 260
Kr	18044	554.2	+ 337	17637	567	+ 296	17515	570.9	+ 174	**98** 277
Ar	18481	541.1	+ 774	18099	552.5	+ 759	17954	556.9	+ 614	**62** 197

IV.7 Conclusion

The luminescence produced with y^8P state excitation of atomic Eu in RG matrices is complicated by multiple sites of isolation in the lattices and numerous emission features. The current study has simplified this using site-specific spectroscopy allowing identification of just two thermally stable sites of isolation in solid Ar and Kr and only one site in the Xe host. Each site exhibits four excited states involved in emission. The expected y^8P fluorescence is identified but also present is emission from three other lower energy excited states. The excited states involved were confidently assigned as y^8P, z^6P, a^8D and a^{10}D based on their spectral positions and recorded lifetime values. It should be mentioned that in almost all cases, excluding the y^8P state fluorescence, the lifetimes recorded were multi-exponential. The origin of these multiple decay components may be due to overlap in the temporal profile of some emission from a residual amount of atoms remaining in the thermally unstable site of isolation after annealing. The decay profiles of the z^6P, a^8D and a^{10}D state were recorded with y^8P excitation but as can be seen in Figure IV.7, y^8P fluorescence in this region is re-absorbed by any atoms remaining in a thermally unstable site due to spectral overlap. Thus, in most cases due to y^8P state re-absorption, there is some thermally unstable site emission observed which is in the same spectral region as emission from the z^6P, a^8D and a^{10}D state emissions from the blue and red sites. The overlap of these emission features may be the source of multiple decay components.

Analysis of the Stokes shifts values observed for the y^8P state in each site re-enforced site attributions made in Chapter III, the smaller blue tv site having a greater repulsive interaction with the guest which is manifested as a larger Stokes shift.

z^6P state emission is identified in the 570 nm region. Lifetimes produced with indirect y^8P state excitation and direct z^6P state excitation yielded little difference suggesting the intervening $y^8\text{P} \rightarrow z^6\text{P}$ feeding step is very fast. Lifetimes recorded in the matrix do not agree with gas phase decay data published on this state. However, in recent times the values cited in the literature for the gas phase are becoming closer to the solid state value. Excitation spectra in the region of the z^6P state showed features corresponding to the $z^6P_{5/2}$, and $z^6P_{7/2}$ levels but no evidence of the $z^6P_{3/2}$ level due to the $\Delta J = 0, \pm 1$ electric-dipole selection rule. JT splitting is observed on the $z^6P_{5/2}$ excitation band in larger, more distortable hosts. It progresses from a structureless band in solid Ar, to a doublet in Kr and a JT threefold split feature in Xe.

a^8D state emission occurs in the 680 nm region. Based on its long-lived nature and spectral location it is assigned with confidence to the forbidden a^8D → a^8S electronic transition with a solid state lifetime of hundreds of microseconds. The lowest energy Eu/RG emission is observed in the 800 nm region. It is also long-lived and is assigned to the metastable a^{10}D state with a lifetime in the matrix of several milliseconds. Its assignment is supported by a temperature effects study which shows an increase in population for this state at elevated temperatures implying it is the lowest energy excited state acting as a 'population trap'. These are the first recorded lifetime values for these electric-dipole forbidden transitions which have not been measured in the gas phase. D → S type emission of atomic europium show little host change effects on their spectral location. However, unlike 'classical' D → S transitions they are broad and shifted from the gas phase position. This is an example of the effect of site size on D states of metal atom systems. Atomic europium causes significant site distortion in occupying the tetra-vacancies and hexa-vacancies of the RG solids causing broad and shifted D state emission.

References

[1] *NIST Atomic Spectra Database (version 3.1.5), available: http://physics.nist.gov/asd3 [2010, August].* (National Institute of Standards and Technology, Gaithersburg, MD).

[2] M. Jakob, H. Micklitz and K. Luchner, Berichte Der Bunsen-Gesellschaft-Physical Chemistry Chemical Physics **82** (1), 32 (1978).

[3] M. Jakob, H. Micklitz and K. Luchner, Physics Letters A **61** (4), 265 (1977).

[4] M. Jakob, H. Micklitz and K. Luchner, Physics Letters A **57** (1), 67 (1976).

[5] M. A. Collier, O. Byrne, C. Murray and J. G. McCaffrey, The Journal of Chemical Physics **132** (16), 164512 (2010).

[6] A. Corney, *Atomic and Laser Spectroscopy*. (Clarendon Press and Oxford University Press, 1977).

[7] M. A. Collier and J. G. McCaffrey, Journal of Chemical Physics **122** (5) (2005).

[8] S. L. Laursen and H. E. Cartland, Journal of Chemical Physics **95** (7), 4751 (1991).

[9] E. A. Den Hartog, M. E. Wickliffe and J. E. Lawler, Astrophysical Journal Supplement Series **141** (1), 255 (2002).

[10] N. P. Penkin, V. N. Gorshkov and V. A. Komarovsky, Optika I Spektroskopiya **57** (5), 803 (1984).

[11] *IUPAC Compendium of Chemical Terminology, available: http://old.iupac.org/publications/compendium/index.html [2010, April].* (International Union of Pure and Applied Chemistry).

Chapter V

Identification of matrix-isolated Europium ions.

Absorption and Luminescence Spectroscopy

V.1 Introduction

Laser irradiation of the y^8P state of Eu/RG samples was found quite unexpectedly to completely remove all atomic absorption features and replace them with new absorptions to higher energy. At first it was thought the origin of this effect was related to a recent study of atomic sodium isolated in the solid rare gases[1]. ^{2}P state laser irradiation very effectively induces site interconversion for the Na/RG system producing a new higher energy site not observed upon deposition. This was assigned to the smallest volume trapping site i.e. the single vacancy (sv).

The similarities between Na and Eu isolated in solid RG's were mentioned in Chapter III. As in the Na/RG systems, europium exists in two sites of isolation on deposition, postulated to be tetra-vacancies (tv) and hexa-vacancies (hv). The laser irradiated site interconversion utilised in Na/RG to form a sv site led to considering whether a similar effect was the cause of the new higher energy absorptions in Eu/RG. The following sections present this study, however the outcome led to strikingly different results.

Samples discussed in this section were deposited at elevated temperatures of 16, 21, 26 K in Ar, Kr and Xe respectively followed by slow sample cooling to 10 K. The sample was then annealed slowly at a rate of 1 K/minute to temperatures of 31, 38, 60 K respectively. This procedure of warm sample deposition followed by matrix annealing was pursued to ensure the formation of highly crystalline lattices with minimum possibilities for imperfect trapping sites of atomic Eu. Following this, samples underwent 10 Hz unfocussed laser irradiation of the y^8P state for periods of 15 to 30 minutes at laser powers in the region of 250 to 300 μJ/mm^2.

The results are presented in the following manner. Firstly, the Eu/Xe system is discussed as Xe contains one thermally stable site of isolation and is thus the simplest case. Following this, the effects of y^8P state laser irradiation of Eu/Kr and Eu/Ar are presented before finally a comparison of results observed in all three RG's is made.

V.2 Eu/Xe

The bottom trace of Figure V.1 presents the absorption spectrum of matrix-isolated atomic Eu in a Xe lattice deposited at 26 K following sample annealing to 60 K. Clearly evident is the strong absorption of the y^8P state in the blue site of isolation centred at 465 nm. A brief luminescence study was performed on this sample affirming it as a standard sample with typical Eu/Xe emission and excitation features such as those presented and discussed in Chapter IV. Following confirmation of sample reliability, y^8P state laser irradiation at 465.5 nm was performed. The resulting spectrum is presented in the top trace of Figure V.1. As revealed by the comparison in Figure V.1 the blue site y^8P state absorption features (461.2, 465.2 and 469.7 nm) are completely removed and replaced by five higher energy bands occurring at 445.7, 436.2 and 408.3, 398, 393.5 nm.

Annealing of an irradiated sample returns some blue site occupancy and it is also returned via lamp irradiation of the new absorption features as shown in Figure V.2. In each case the increase in blue site absorption is accompanied by a concurrent decrease in the new absorption features.

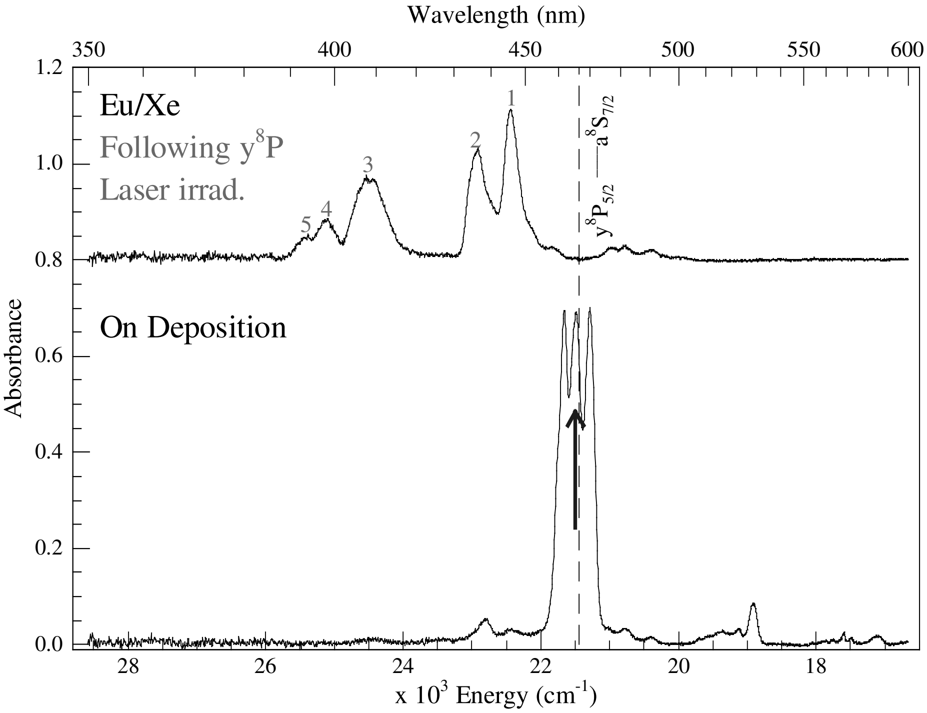

Figure V.1 Eu/Xe visible absorption spectra recorded at 10 K. Bottom trace is following deposition at 26 K and matrix annealing to 60 K. Top trace shows the absorption spectrum recorded after y^8P state laser irradiation. The arrow depicts the wavelength at 465.5 nm selected for irradiation of the y^8P state.

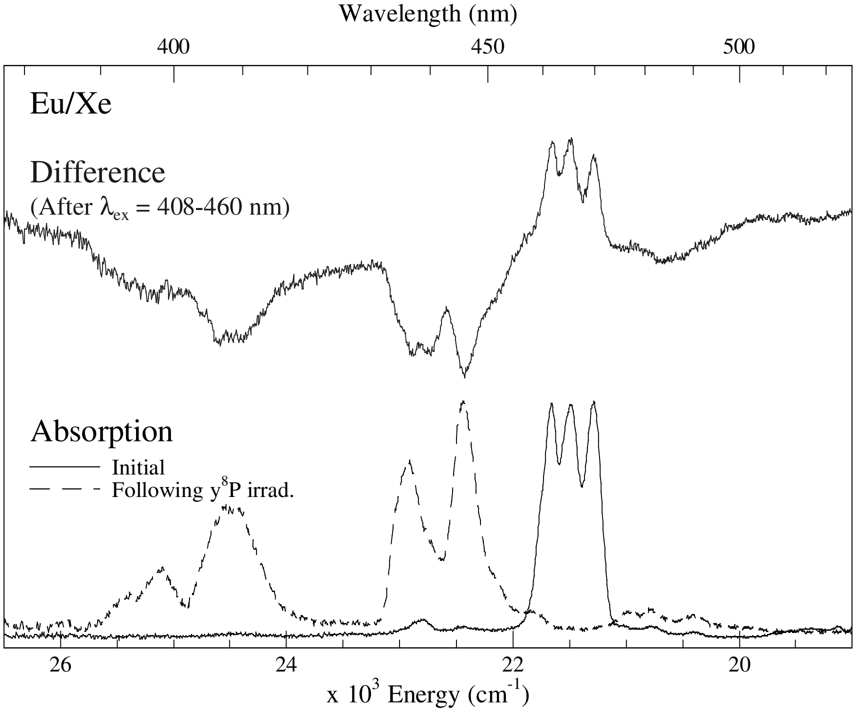

Figure V.2 Eu/Xe visible absorption spectra recorded at 10 K. Bottom traces compare the effects of y^8P state laser irradiation at 465.5 nm. Top trace presents the difference spectrum produced following lamp irradiation of the new absorption features.

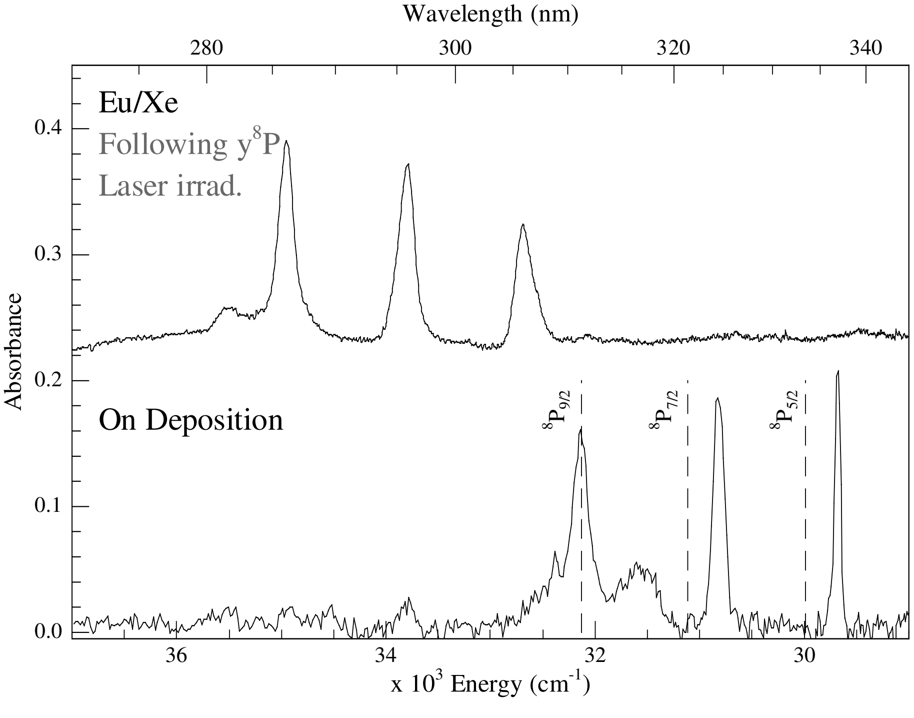

Figure V.3 Eu/Xe UV absorption spectra recorded at 10 K. Bottom trace is following deposition at 26 K and matrix annealing to 60 K. Top trace shows the absorption spectrum recorded after y^8P state laser irradiation at 465.5 nm. A larger linewidth and better signal to noise ratio is observed due to the lower resolution scan conditions employed in order to compensate for decreased sample throughput following laser irradiation.

Also monitored were ^{8}P state absorptions of atomic Eu isolated in the Xe host in the UV spectral region. Figure V.3 presents the absorption spectrum recorded in this range before and after *y*^{8}P state laser irradiation in a solid Xe sample. Clearly, blue site atomic absorption features centred at 311.1, 324.3 and 336.8 nm are removed and replaced by higher energy absorptions at 286.1, 295.9 and 305.9 nm. The bandwidths of the upper trace in Figure V.3 are not fully resolved and are broader than the original spectrum due to the lower spectral resolution employed in order to compensate for decreased sample throughput following laser irradiation.

In summary, absorption spectroscopy demonstrates that atoms isolated in the blue site of solid Xe are entirely eliminated by strong *y*^{8}P state resonant laser irradiation, producing new higher energy absorptions. Emission produced by these absorption features is presented in Figure V.4 and Figure V.8. The luminescence from the 430 to 450 nm absorption bands is quite different to that of the 390 to 410 nm absorptions so these features are first presented separately.

The luminescence produced with excitation of the new absorption features in the 430 to 450 nm region is displayed in Figure V.4. Excitation at 446.5 nm (Band A) yields an emission feature centred at 452.4 nm of width (fwhm) 161 cm^{-1} representing a Stokes shift (SS) of 292 cm^{-1}. In an effort to assign the origin of this feature its temporal profile was recorded at 10 K and is presented in Figure V.5. A lifetime of 2.1 ns is extracted.

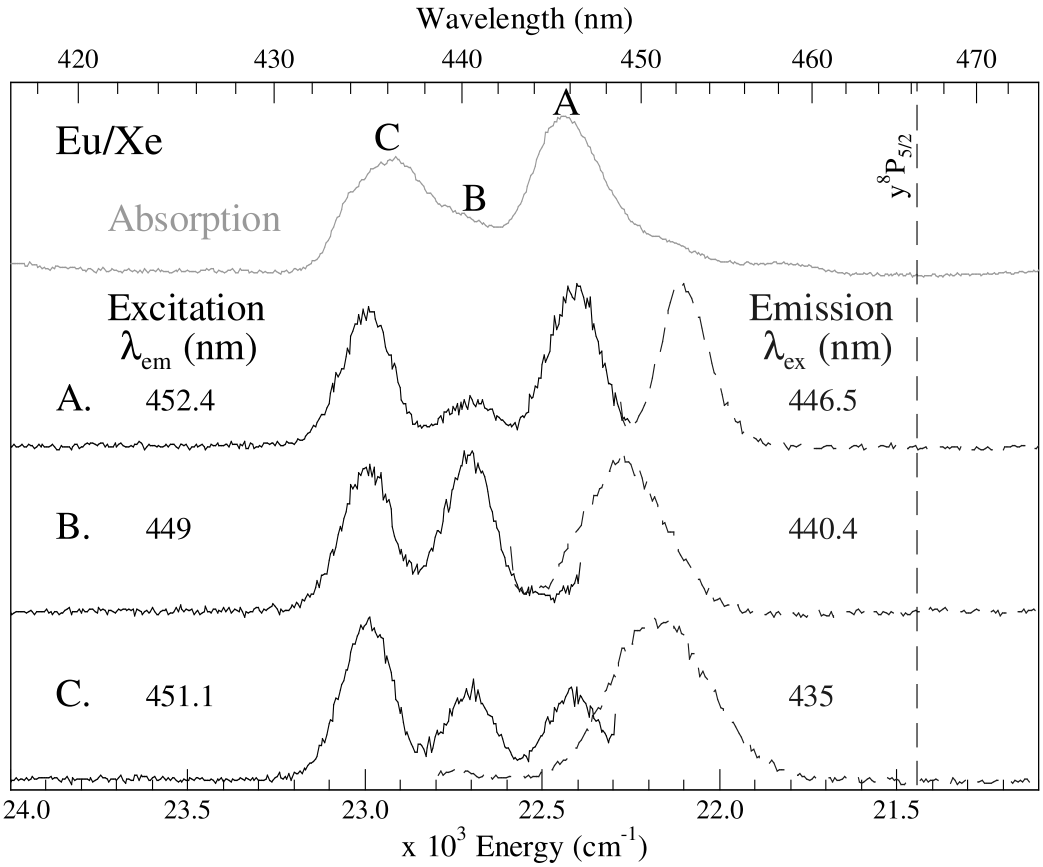

Figure V.4 Emission (dashed traces) recorded at 10 K for the Eu/Xe system in the 430 to 450 nm region with excitation at 435, 440.4 and 446.5 nm. The excitation spectra were recorded by monitoring emission at 451.1, 449 and 452.4 nm respectively and are shown by the solid traces. The absorption spectrum in this region is displayed in top trace. Spectra were recorded following Eu/Xe sample deposition at 26 K and matrix annealing to 60 K followed by y^8P state laser irradiation. The spectral position of the gas phase y^8P transition of atomic Eu is shown by the dashed vertical line[2].

Excitation of the next highest energy absorption feature, band B, at 440.4 nm produces a much broader emission feature located at 449 nm of width 277 cm^{-1}. A time-resolved emission spectrum in this region was recorded with excitation at 440 nm (B). The temporal profile monitoring emission at 449 nm at 10 K is presented in Figure V.6. A lifetime of 2.2 ns yields a satisfactory fit with the experimental data.

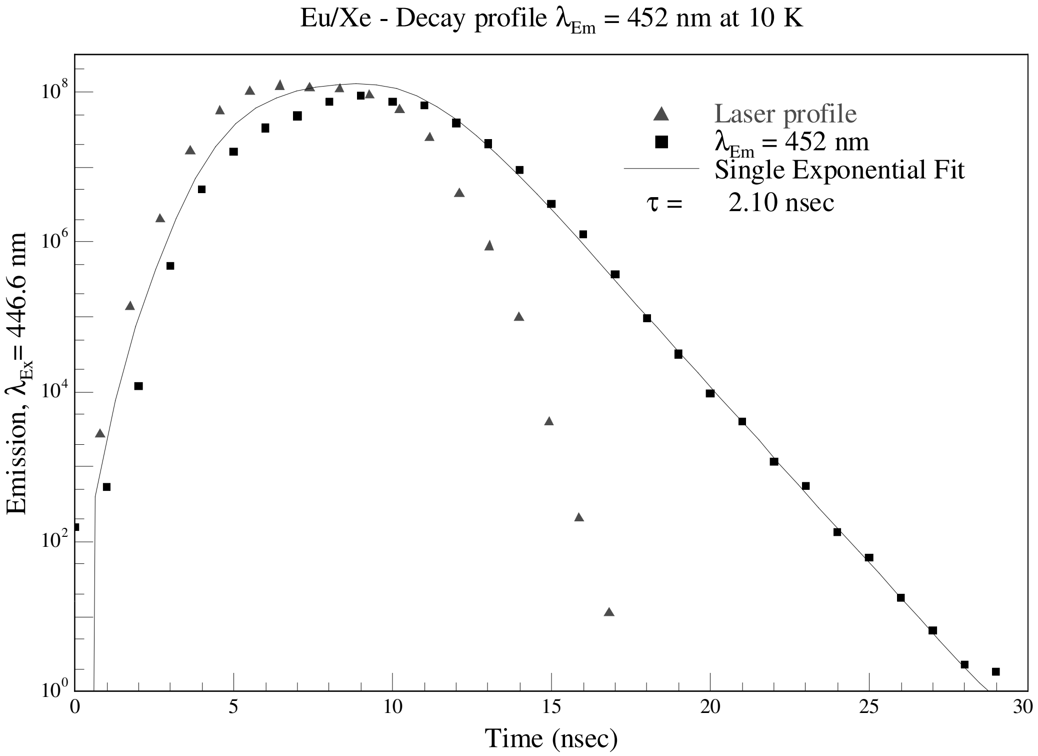

Figure V.5 Decay profile of the Eu/Xe emission at 452 nm recorded at 10 K. The decay profile is convoluted with the temporal profile of the laser excitation source at 446.6 nm.

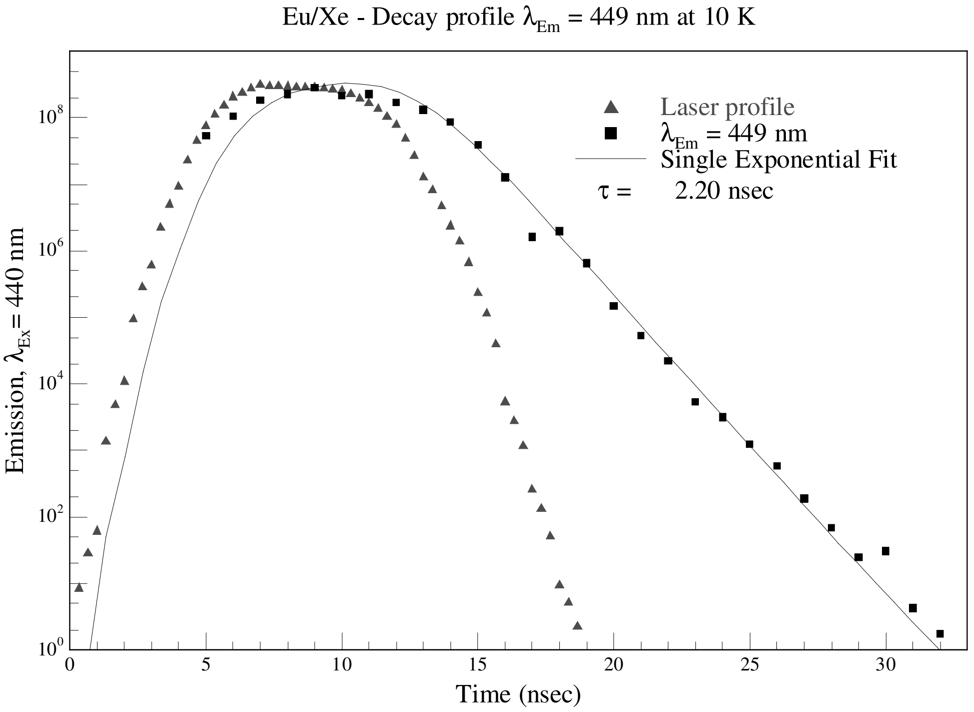

Figure V.6 Decay profile of the Eu/Xe emission at 449 nm recorded at 10 K. The decay profile is convoluted with the temporal profile of the laser excitation source at 440 nm.

Excitation of the final band, C, in this spectral region involves excitation at 435 nm generating an emission centred at 451.1 nm exhibiting a broader width of 325 cm^{-1}. The decay characteristics of this 451.1 nm emission feature were recorded and are presented in Figure V.7 allowing identification of a lifetime of 1.8 ns.

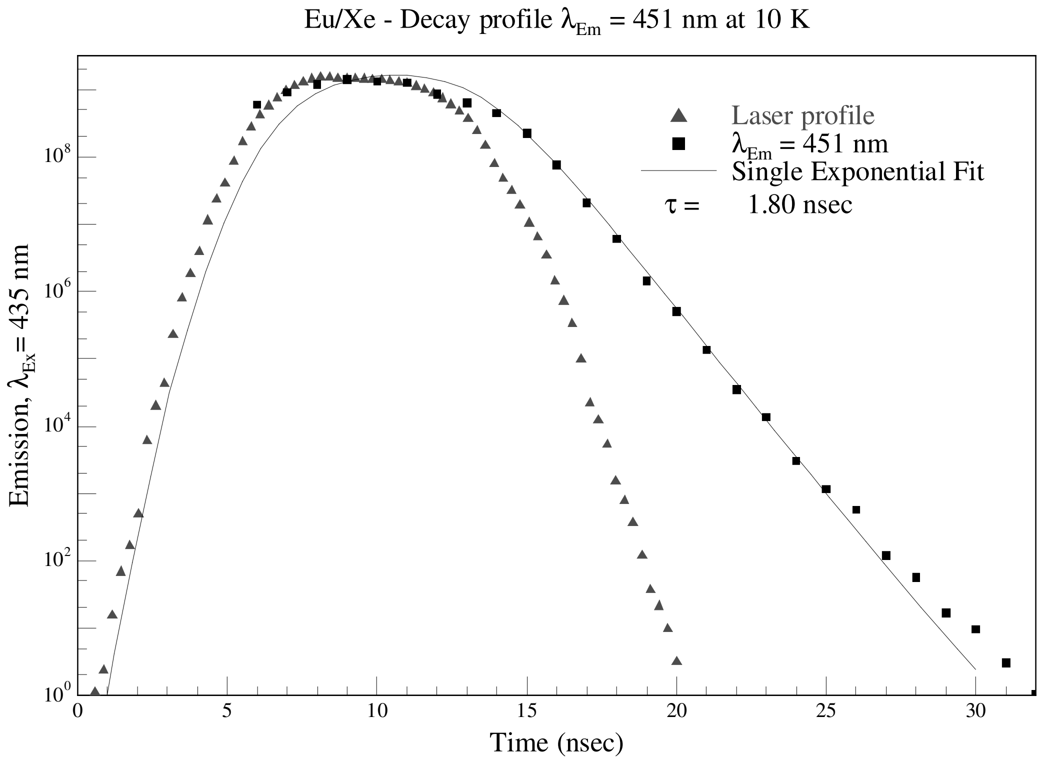

Figure V.7 Decay profile of the Eu/Xe emission at 451 nm recorded at 10 K. The decay profile is convoluted with the temporal profile of the laser excitation source at 435 nm.

Excitation spectra monitoring these 452.4, 449 and 451.1 nm emission features yielded three distinct excitation features centred at 446.5, 440.4 and 435 nm respectively. The excitation features exhibit bandwidths of 160 cm^{-1} which coincide with and completely account for the 445.7 and 436.2 nm absorption bands. The spectral characteristics and extracted lifetimes (τ_{10K}) of the luminescence features of these 430 to 450 nm absorptions in solid Xe are listed in Table V.1. Temporal profiles at elevated temperatures to identify if these are the radiative lifetimes of the transitions were not recorded as increasing sample temperature caused a loss of the new higher energy absorption features. Notwithstanding this, Table V.1 also presents the 10 K lifetimes (τ_{10K}) corrected for the effective field of the surrounding lattice (τ_{Cor}).

Table V.1 Photophysical characteristics of the new 430 to 450 nm features in solid Xe formed by sample y^8P state laser irradiation. Their spectral position in nm is labelled λ, while the bandwidths, Δ, of the observed features are shown in cm^{-1}. Their lifetimes recorded in the matrix at 10 K (τ_{10K}) and lifetimes corrected for the effective field of the surrounding lattice (τ_{Cor}) are also displayed.

Excitation Features		Emission Features			
λ (nm)	Δ (cm^{-1})	λ (nm)	Δ (cm^{-1})	τ_{10K} (ns)	τ_{Cor} (ns)
446.5	153	452.4	161	2.1	6.2
440.4	160	450.9	277	2.2	6.5
435	169	448.9	342	1.8	5.3

Luminescence produced from the higher-energy 390 to 410 nm absorption features is now presented in Figure V.8. Two distinct emission features are identifiable, a strong band centred at 467.3 nm and a weaker feature at 488.4 nm.

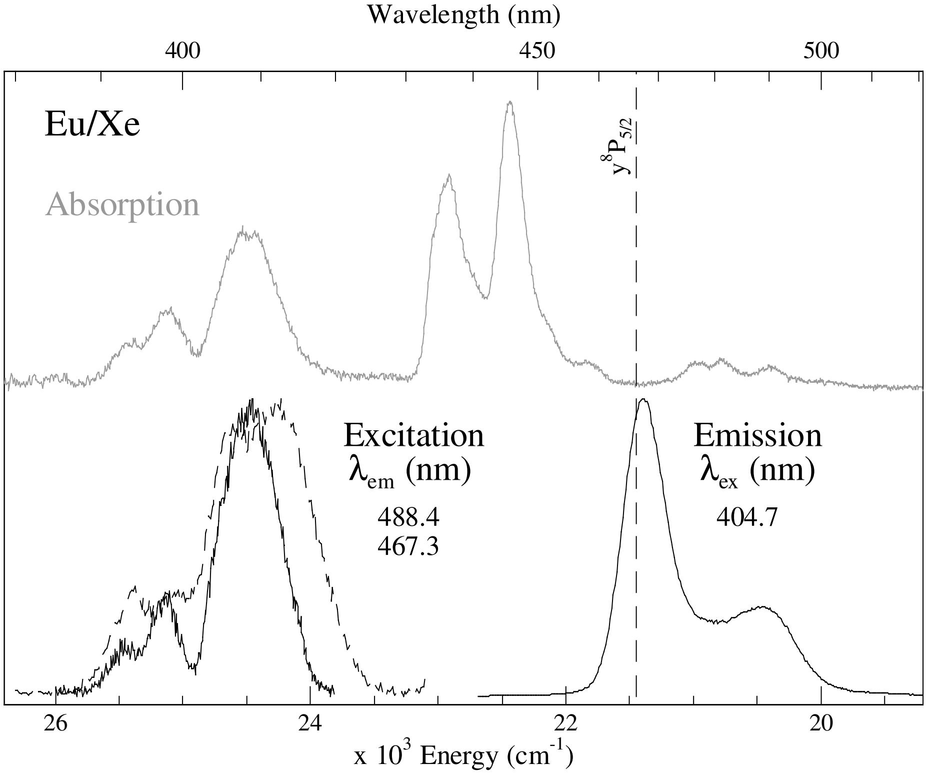

Figure V.8 Emission (solid trace, right) recorded at 10 K for the Eu/Xe system with excitation at 404.7 nm. The excitation spectra were recorded by monitoring emission at 467.3 nm (solid trace) and 488.4 nm (dashed trace) and are shown on the left. The absorption spectrum in this region is displayed in top trace. Spectra were recorded following Eu/Xe sample deposition at 26 K, matrix annealing to 60 K followed by y^8P state laser irradiation. The spectral position of the gas phase y^8P transition of atomic Eu is shown by the dashed vertical line[2].

Excitation spectra recorded monitoring the 467.3 nm feature shows intensity in the 390 to 410 nm region. The excitation feature of greatest strength is located at 408.7 nm, representing a Stokes shift of 3068 cm^{-1}. It is displayed to the left in the bottom trace of Figure V.8 as a solid line. The excitation spectrum monitoring the weaker 488.4 nm emission is represented by a dashed trace and shows greatest intensity at 412.1 nm yielding a Stokes shift of 3791 cm^{-1}.

To probe the source of these emissions and identify the electronic transition involved, their temporal profiles were recorded at 10 K. Monitoring the more intense feature at 467 nm yielded the decay profile presented in Figure V.9. A lifetime of 4.5 ns was extracted.

The decay profile produced monitoring the weaker emission centred at 488.4 nm is presented in Figure V.10 and yielded a slightly shorter lifetime of 4.0 ns. This is of the same order of magnitude as the 467 nm feature. It should be noted that excitation of the other absorption features in this region at 398 and 393.5 nm produced the same emission features and lifetimes of equal values.

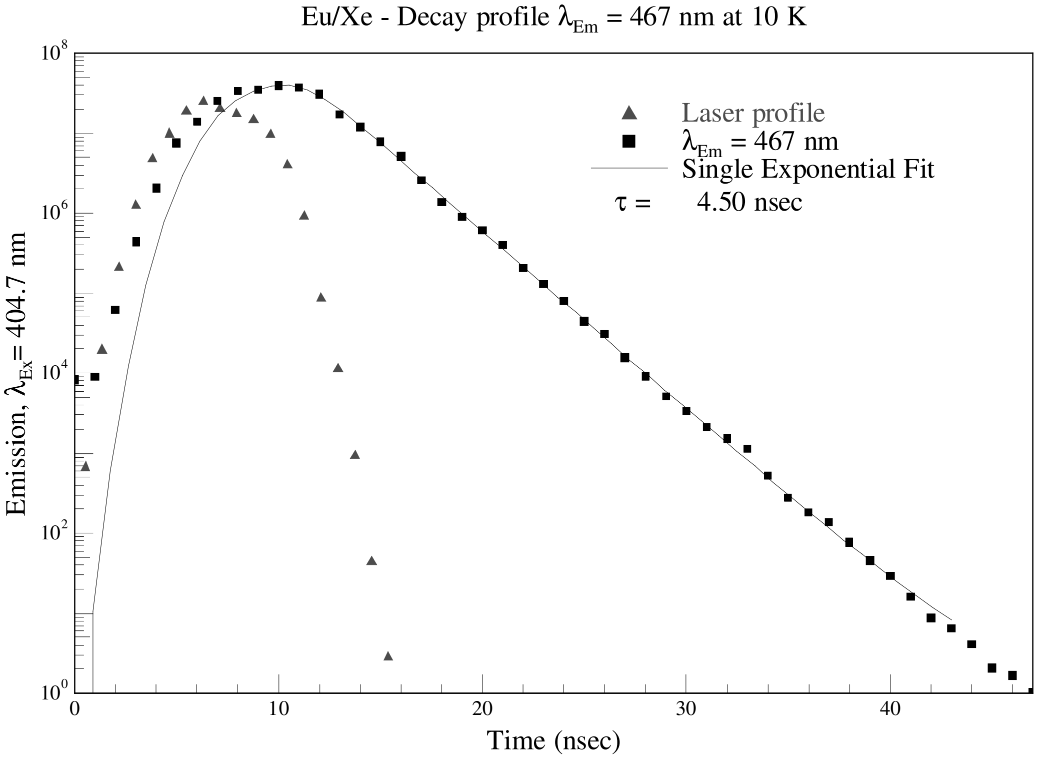

Figure V.9 Decay profile of the more intense emission feature of Eu/Xe at 467 nm recorded at 10 K. The decay profile is convoluted with the temporal profile of the laser excitation source at 404.7 nm.

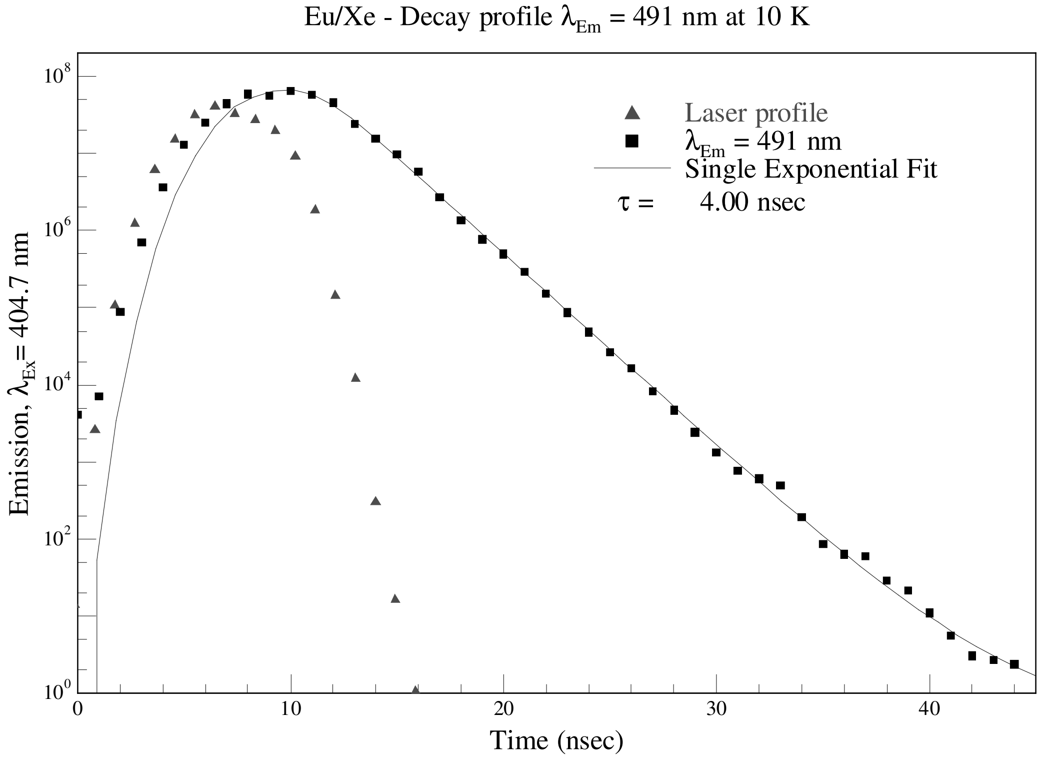

Figure V.10 Decay profile of Eu/Xe monitoring emission at 491 nm recorded at 10 K. The decay profile is convoluted with the temporal profile of the laser excitation source at 404.7 nm.

A summary plot of the luminescence produced by the new absorption features in Eu/Xe is presented in Figure V.11. The luminescence of the 390 to 410 nm absorption bands, displayed in the bottom trace, is noticeably different from that of the 430 to 450 nm absorption features having a Stokes shift in the region ten times larger in magnitude and lifetimes twice as long. To study these new spectral features further, the following section investigates the effects of y^8P state laser irradiation in Eu/Kr samples.

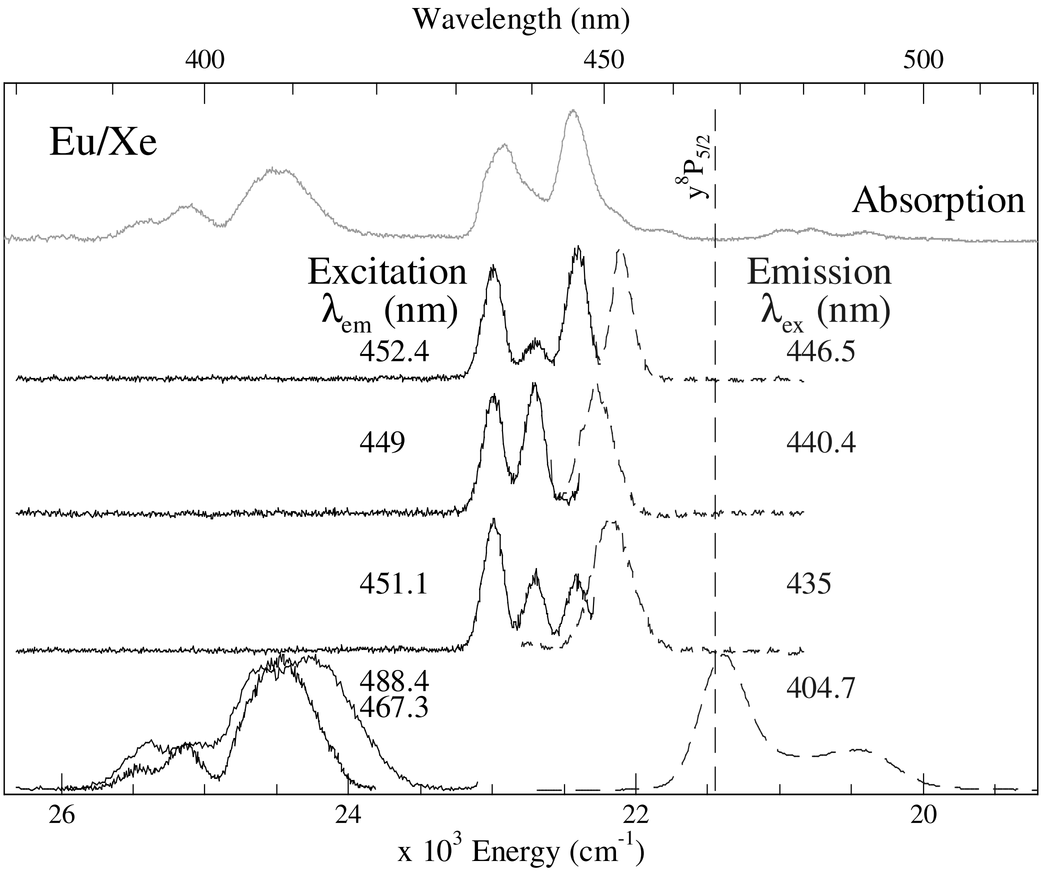

Figure V.11 Summary plot of the luminescence of the new absorption features formed following y^8P state laser irradiation in solid Xe. Spectra were recorded following sample deposition at 26 K, matrix annealing to 60 K followed by y^8P state laser irradiation. Top trace presents the absorption spectrum in this region. The spectral position of the gas phase y^8P transition of atomic Eu is shown by the dashed vertical line.

V.3 Eu/Kr

Absorption spectra of a Eu/Kr sample are presented in Figure V.12. The bottom trace displays the absorption spectrum of a sample deposited at 21 K, followed by annealing to 38 K. The top trace shows the effects of blue site y^8P state laser irradiation. It is clear all blue site atomic absorption features are completely removed and seven new absorptions, occurring to higher energy, are observed centred at 372.1, 376.3 and 385.7 nm and 416.3, 426.3, 435.7 and 442.6 nm.

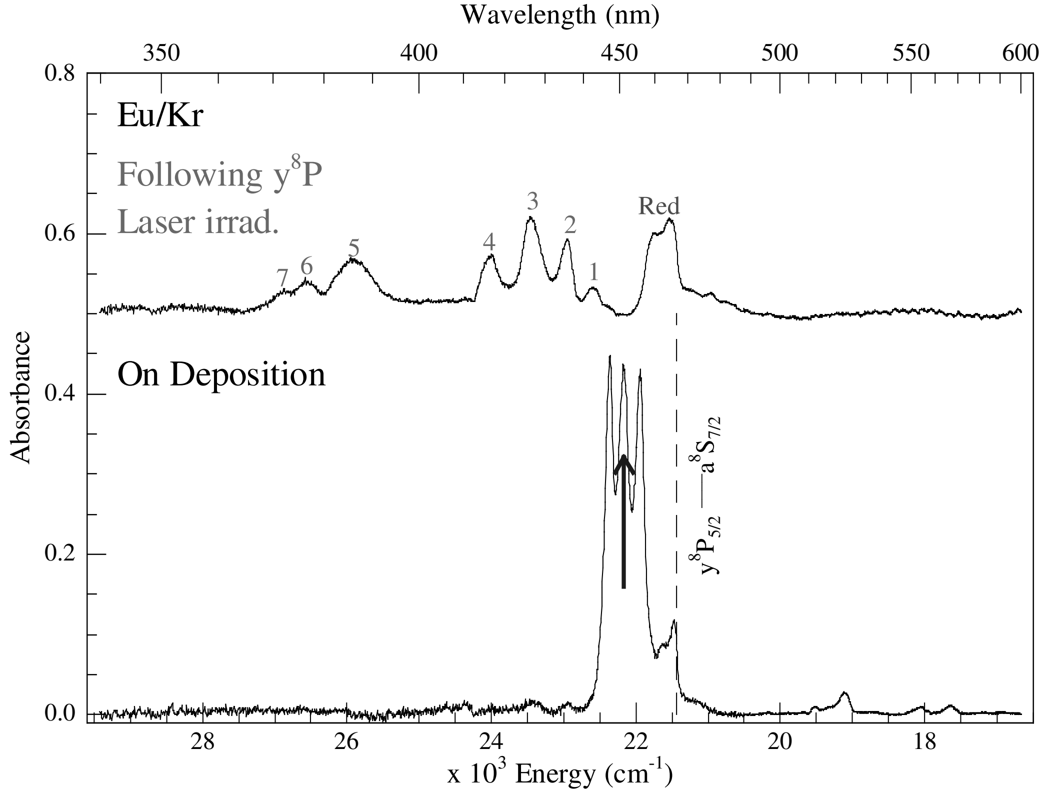

Figure V.12 Eu/Kr visible absorption spectra recorded at 10 K. Bottom trace is following deposition at 21 K and matrix annealing to 38 K. Top trace shows the absorption spectrum recorded after blue site *y*^{8}P state laser irradiation at 451 nm depicted by the vertical arrow. Seven new absorptions are observed centred at 372.1, 376.3 and 385.7 nm and 416.3, 426.3, 435.7 and 442.6 nm.

Red site absorption features can also be removed by *y*^{8}P state laser irradiation however the growth in intensity of the new features is negligible due to the low concentrations of Eu occupying red sites in Kr lattices. As was the case for Eu/Xe, the new higher energy absorption features can be partially removed by sample annealing, an effect coupled with a return of the blue site.

Furthermore, higher energy transitions of atomic Eu occurring in the UV spectral region are removed by *y*^{8}P state laser irradiation. The bottom trace of Figure V.13 presents the UV absorptions of the ^{8}P state of europium atoms isolated in solid Kr in a freshly deposited sample. Blue site *y*^{8}P state laser irradiation produces the absorption spectrum shown in the upper trace of Figure V.13. The blue site atomic absorptions are completely removed (some atoms in red site remain). Three new absorptions to higher energy are identified at 283.5, 293.0 and 302.8 nm.

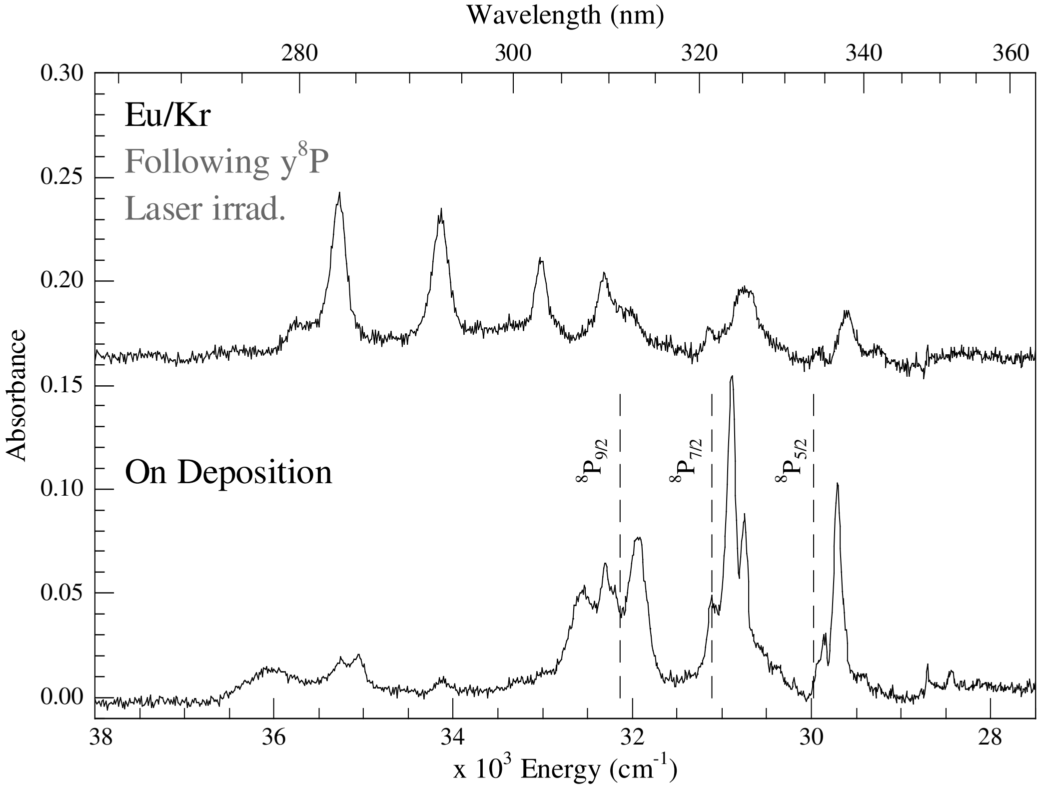

Figure V.13 Eu/Kr UV absorption spectra recorded at 10 K. Bottom trace is following deposition at 21 K and matrix annealing to 38 K. Top trace shows the absorption spectrum recorded after blue site *y*^{8}P state laser irradiation at 451 nm.

Absorption spectroscopy demonstrates that atoms isolated in the blue site within the Kr lattice are completely removed by site-specific *y*^{8}P state laser irradiation. New features to higher energy are formed. A summary of the luminescence produced with excitation of the new absorption features in the visible 370 to 445 nm region in solid Kr is presented in Figure V.14.

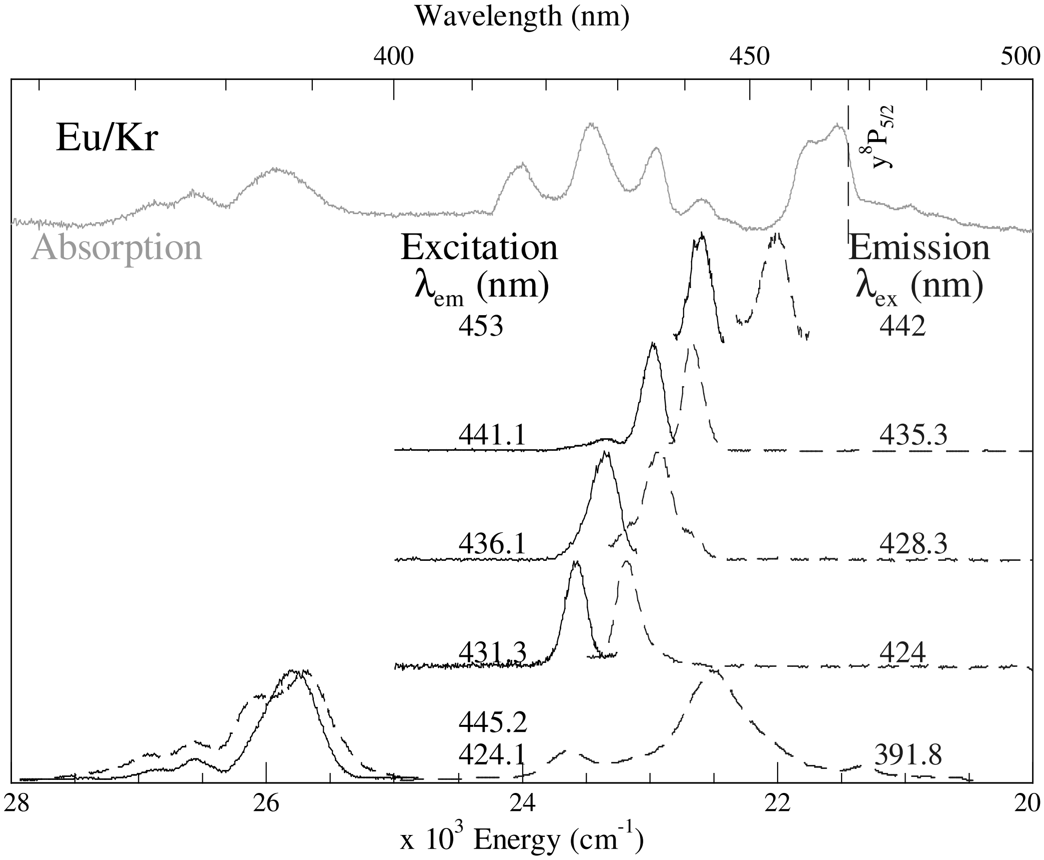

Figure V.14 Summary plot of the luminescence produced in Eu/Kr following sample deposition at 21 K, matrix annealing to 38 K followed by blue site y^8P state laser irradiation. Top trace presents the absorption spectrum in this region. The spectral position of the gas phase y^8P transition of atomic Eu is shown by the dashed vertical line[2].

There are four absorption bands in the 415 to 445 nm region located at 416.3, 426.3, 435.7 and 442.6 nm. Excitation of the 416 nm band yields no observable emission. Excitation of the 426 nm band produces two unique emission features located at 431.3 and 436.1 nm. Excitation spectra monitoring both these emission wavelengths show the 426 nm absorption comprises of two distinct excitation features centred at 424 and 428.3 nm. Bandwidths of approximately 195 cm^{-1} are observed and Stokes shifts of 410 cm^{-1} are identified.

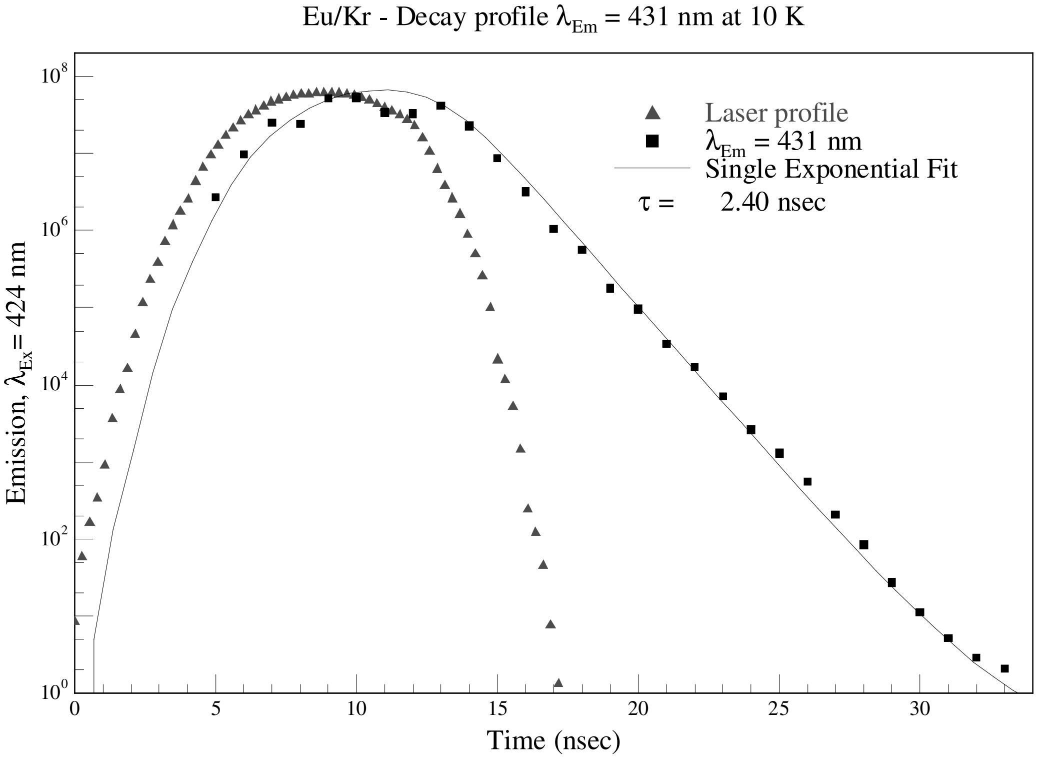

Figure V.15 Decay profile of the Eu/Kr emission at 431 nm recorded at 10 K. The decay profile is convoluted with the temporal profile of the laser excitation source at 424 nm.

The origin of these features was probed by recording temporal profiles. The decay characteristics of the 431 nm emission produced with 424 nm excitation is displayed in Figure V.15. A lifetime of 2.4 ns is extracted for this feature at 10 K. The decay profile monitoring the 436 nm emission produced with 428 nm excitation yielded a lifetime of the same order of magnitude, 1.9 ns.

Emission from the 435.7 nm absorption feature is observed at 441.1 nm. It displays a width of 179 cm^{-1} and a lifetime of 2.4 ns, the fitted decay profile is presented in Figure V.16.

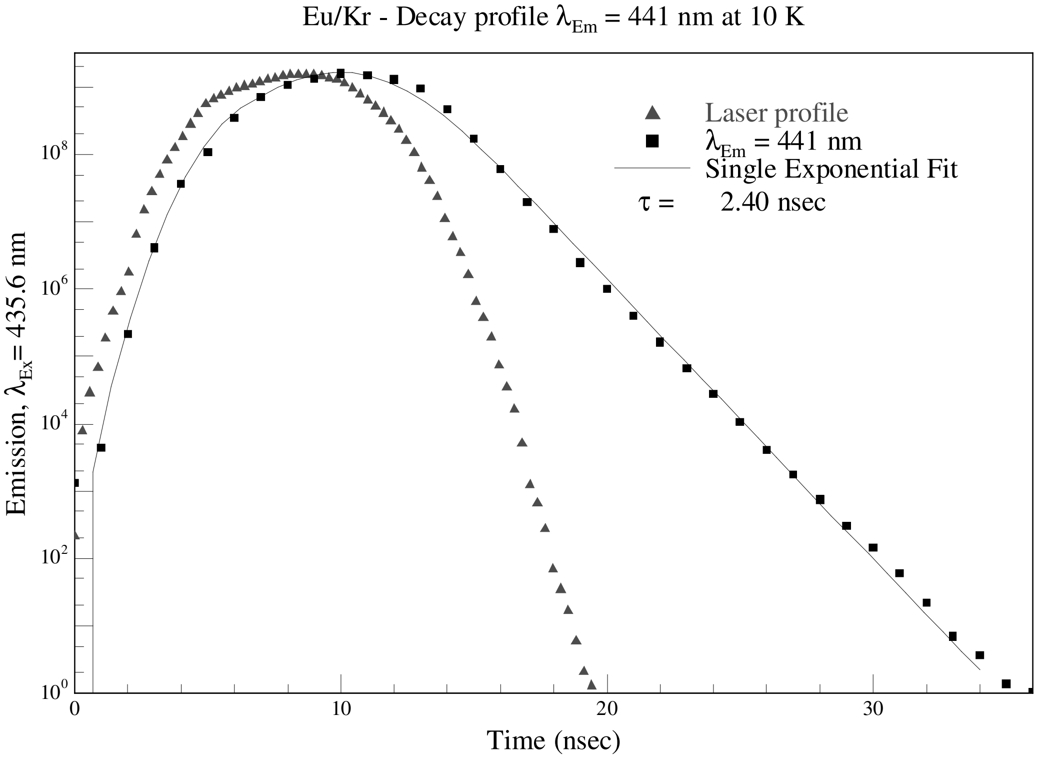

Figure V.16 Decay profile of the Eu/Kr emission at 441 nm recorded at 10 K. The decay profile is convoluted with the temporal profile of the laser excitation source at 435.6 nm.

The final, least intense absorption feature located at 442 nm yields a weak emission centred at 453 nm exhibiting a bandwidth of 235 cm^{-1}. Decay profile analysis revealed a lifetime of 1.3 ns for this feature. Table V.2 collates the spectral and temporal characteristics of the above discussed 415 to 445 nm luminescence of Eu/Kr along with their matrix corrected lifetimes (τ_{Cor}).

Table V.2 Photophysical characteristics of the 415 to 445 nm luminescence features in solid Kr. Their spectral position in nm is labelled λ, while the bandwidths , Δ, of the observed features are shown in cm^{-1}. Their lifetimes recorded in the matrix at 10 K (τ_{10K}) and lifetimes corrected for the effective field of the surrounding lattice (τ_{Cor}) are also displayed.

Excitation Features		Emission features			
λ (nm)	Δ (cm^{-1})	λ (nm)	Δ (cm^{-1})	τ_{10K} (ns)	τ_{Cor} (ns)
442	174	453	235	1.3	3.4
435.3	192	441.1	179	2.4	6.2
428.3	198	436.1	245	1.9	4.9
424	190	431.3	176	2.4	6.2

The bottom trace of Figure V.14 displays the luminescence produced with excitation into the higher energy 370 to 400 nm absorption features. A broad emission feature is observed in the 420 to 460 nm range with two clear emission maxima identifiable at 424.1 and 445.2 nm. The excitation spectrum recorded monitoring the more intense emission feature at 445.2 nm is presented in bottom left of Figure V.14 as a dashed trace. It exhibits an intensity maximum at 389.1 nm, yielding a Stokes shift of 3239 cm^{-1}. To identify the excited state producing this emission, its temporal characteristics were recorded. The decay profile produced monitoring emission at 445 nm is displayed in Figure V.17. A lifetime of 4.6 ns is extracted at 10 K.

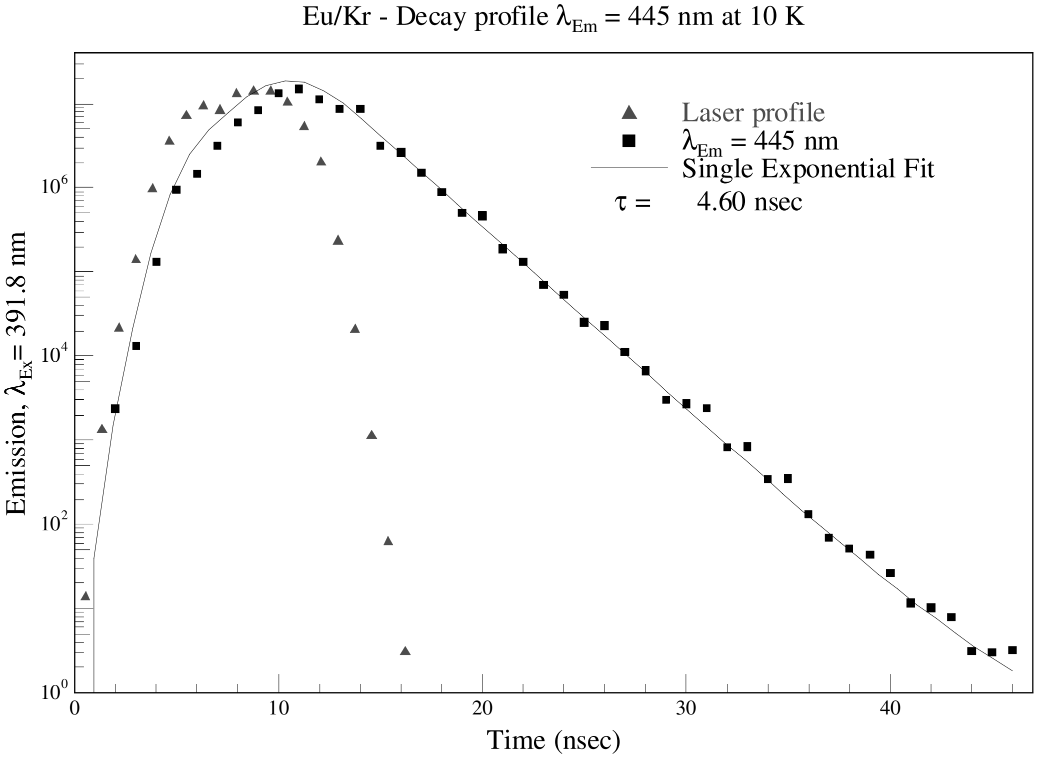

Figure V.17 Decay profile of the emission at 445 nm recorded at 10 K in Eu/Kr. The decay profile is convoluted with the temporal profile of the laser excitation source at 391.8 nm.

The excitation spectrum monitoring the less intense 424.1 nm emission feature displays an intensity maximum at 387.5 nm, yielding a Stokes shift of 2227 cm^{-1}. The decay profile of this feature was recorded and a lifetime of 3.6 ns was calculated with a single exponential fit of the data as displayed in Figure V.18.

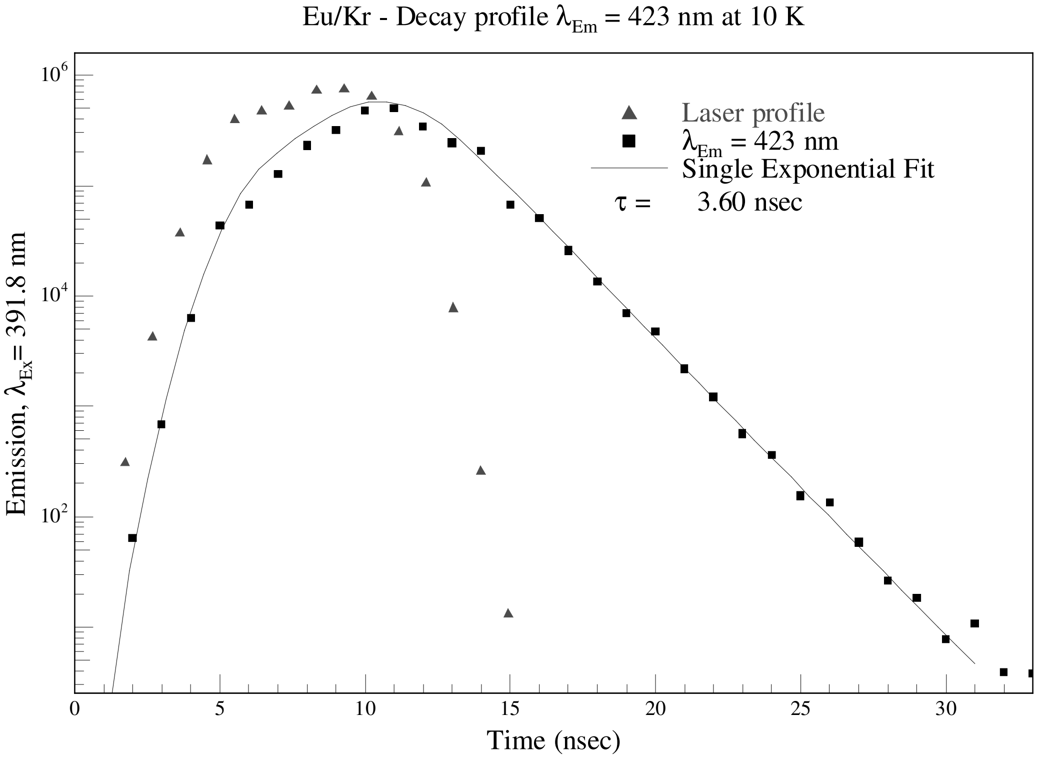

Figure V.18 Decay profile produced monitoring emission at 423 nm recorded at 10 K in Eu/Kr. The decay profile is convoluted with the temporal profile of the laser excitation source at 391.8 nm.

As was the case in solid Xe, the emission produced from the highest energy absorption features, centred at 386 nm, was broad and largely shifted. The lower energy absorptions in the 415 to 435 nm region are narrower and exhibit much smaller Stokes shifts. To complete the y^8P state laser irradiation study, the Eu/Ar system is presented in the following section.

V.4 Eu/Ar

The bottom trace of Figure V.19 presents the Eu/Ar absorption spectrum recorded for a sample deposited at 16 K and annealed to 21 K. In contrast to Kr and Xe, Eu atoms occupy both the red and blue sites of isolation to quite a significant degree in solid Ar. The middle trace of Figure V.19 shows the effects of red site y^8P state laser irradiation of a freshly deposited Eu/Ar sample. Red site absorption features centred at 450.1 nm are removed by this process. A very minor but noticeable growth in higher energy absorptions in the 395 to 440 nm region is observed. The blue site absorption features remain unchanged.

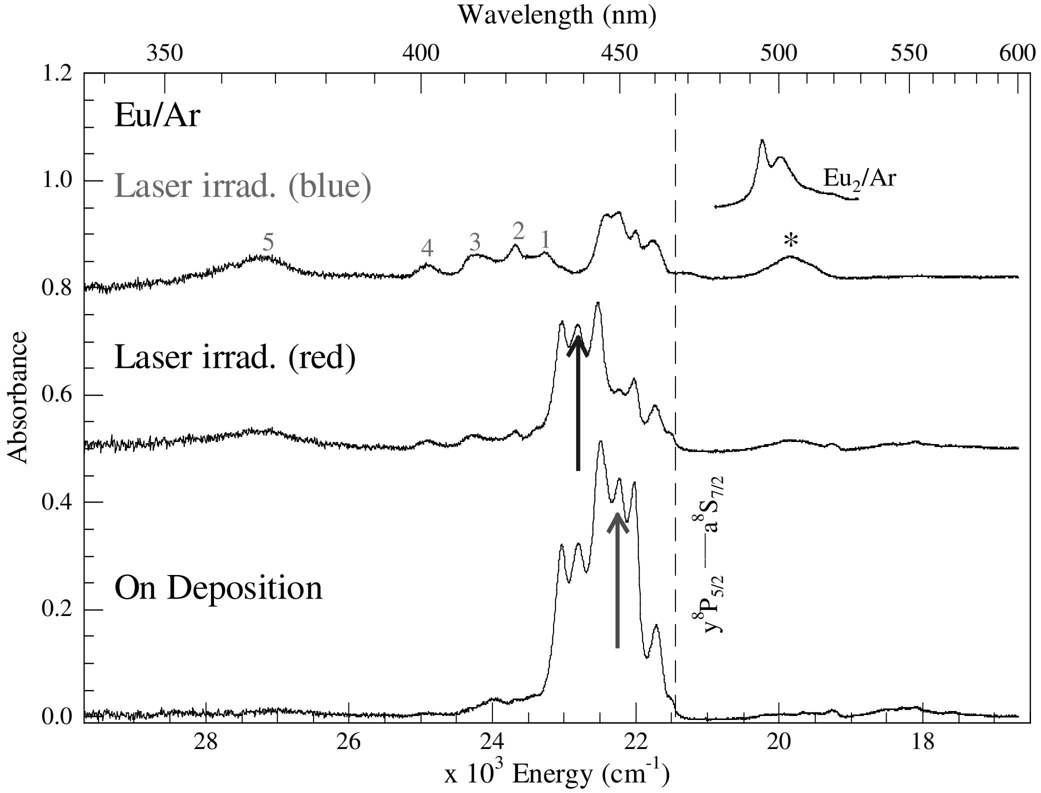

Figure V.19 Eu/Ar visible absorption spectra recorded at 10 K. Lowest trace is following deposition at 16 K and matrix annealing to 21 K. Middle trace shows the absorption spectrum recorded after red site *y*^{8}P state laser irradiation at 450.1 nm. Top trace shows the resulting spectrum following blue site *y*^{8}P state laser irradiation at 438.4 nm. Eu dimer absorption observed at 503 nm is identified in top trace by an asterisk and is overlaid with the Eu_2 dimer absorption spectrum for comparison.

Subsequent blue site *y*^{8}P state laser irradiation completely removed the absorption features centred at 438.4 nm as seen in top trace of Figure V.19. A further increase in the new 395 to 440 nm region absorptions is observed and a weak feature to higher energy centred at 367.2 nm is identified. Also evident is growth of a band at 503 nm (indicated by the asterisk) due to formation of the europium dimer identified in Chapter III.

Monitoring f → d type atomic transitions of Eu/Ar in the UV spectral region also showed a gradual removal of red and blue site features following site-specific *y*^{8}P state laser irradiation as displayed in Figure V.20. The top trace presents the absorption spectrum following removal of almost all red and blue site absorption features by laser irradiation, three new features located at higher energy are identifiable centred at 280.2, 289.7 and 300.1 nm.

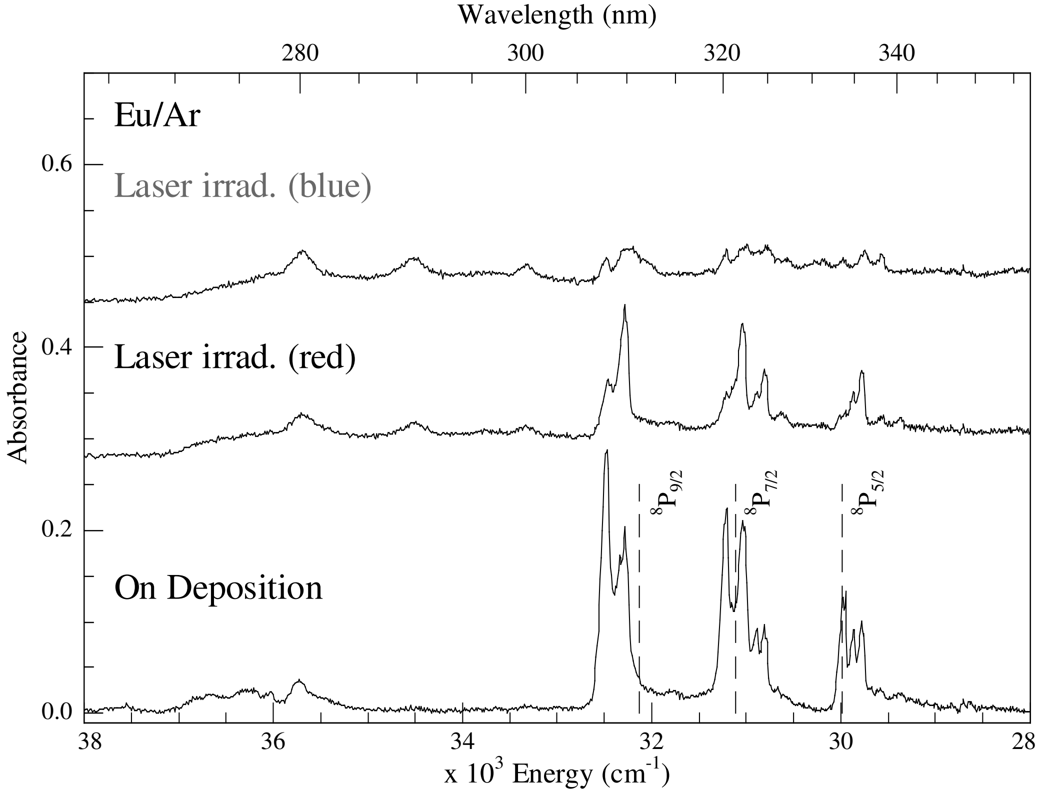

Figure V.20 Eu/Ar UV absorption spectra recorded at 10 K. Lowest trace is following deposition at 16 K and matrix annealing to 21 K. Middle trace shows the absorption spectrum recorded after red site y^8P state laser irradiation at 450.1 nm. Top trace shows the resulting spectrum following blue site y^8P state laser irradiation at 438.4 nm.

Absorption spectroscopy allowed identification of new, low intensity, higher energy absorption features in Eu/Ar. A complete summary of the new visible region features' luminescence is displayed in Figure V.21. Similar to the Kr and Xe cases, the emission from the higher energy visible absorptions is broad and exhibits a large Stokes shift as shown in bottom trace of Figure V.21. The luminescence in the 395 to 440 nm region is narrower and yields Stokes shifts lesser in magnitude.

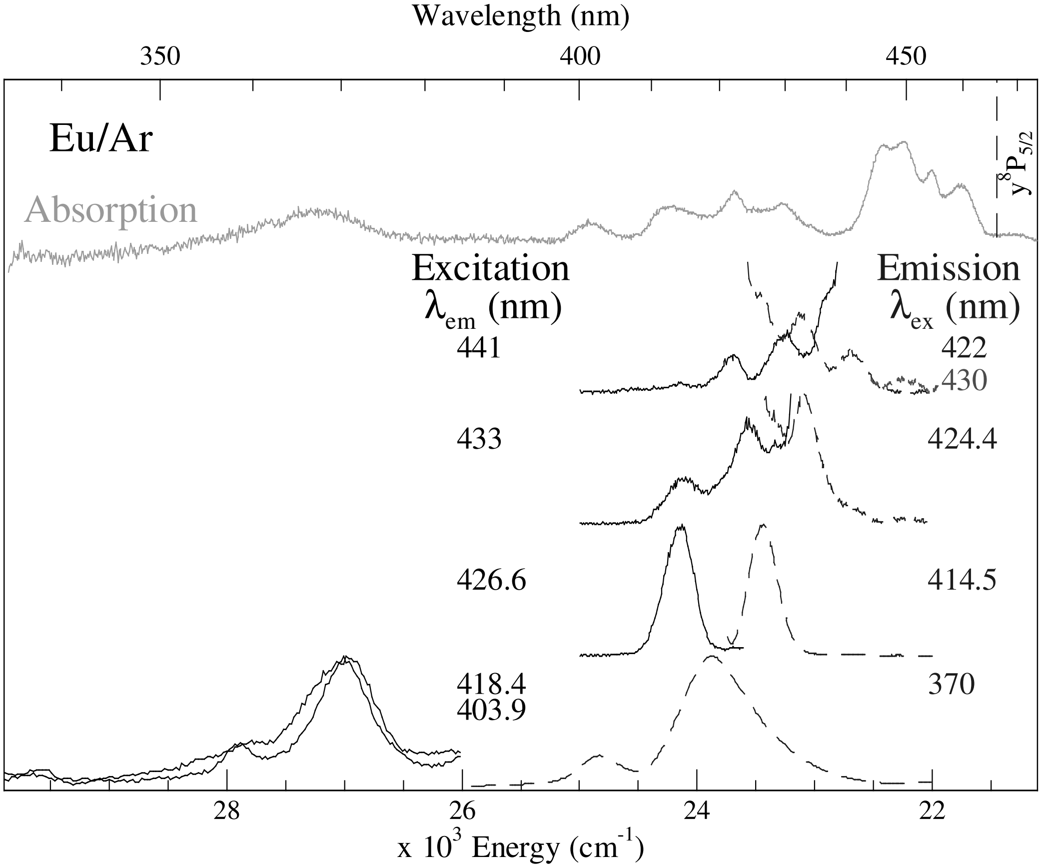

Figure V.21 Summary plot of the luminescence produced in Eu/Ar following y^8P state laser irradiation. Spectra were recorded following sample deposition at 16 K, matrix annealing to 21 K followed by y^8P state laser irradiation. Top trace presents the absorption spectrum in this region, lowest trace displays the 370 nm luminescence, and the 395 to 440 nm spectroscopy is presented in the interlying traces. The spectral position of the gas phase y^8P transition of atomic Eu is shown by the dashed vertical line[2].

Four absorption features are identified in the 395 to 440 nm region, occurring at 401.3, 412.5, 422.2 and 429.7 nm. Excitation of the highest energy feature at 401 nm yields no observable emission in the Ar matrix. Excitation of the feature at 413 nm exhibits quite strong emission centred at 426.6 nm with a bandwidth of 280 cm^{-1}. In an effort to identify the source of this emission, excitation spectra were recorded monitoring this feature and yielded one intense band centred at 414.5 nm with a width 289 cm^{-1}. To aid in the assignment of the source of this feature its temporal profile was recorded and is displayed in Figure V.22. A single exponential fit of the decay data allowed a lifetime of 2.1 ns to be extracted.

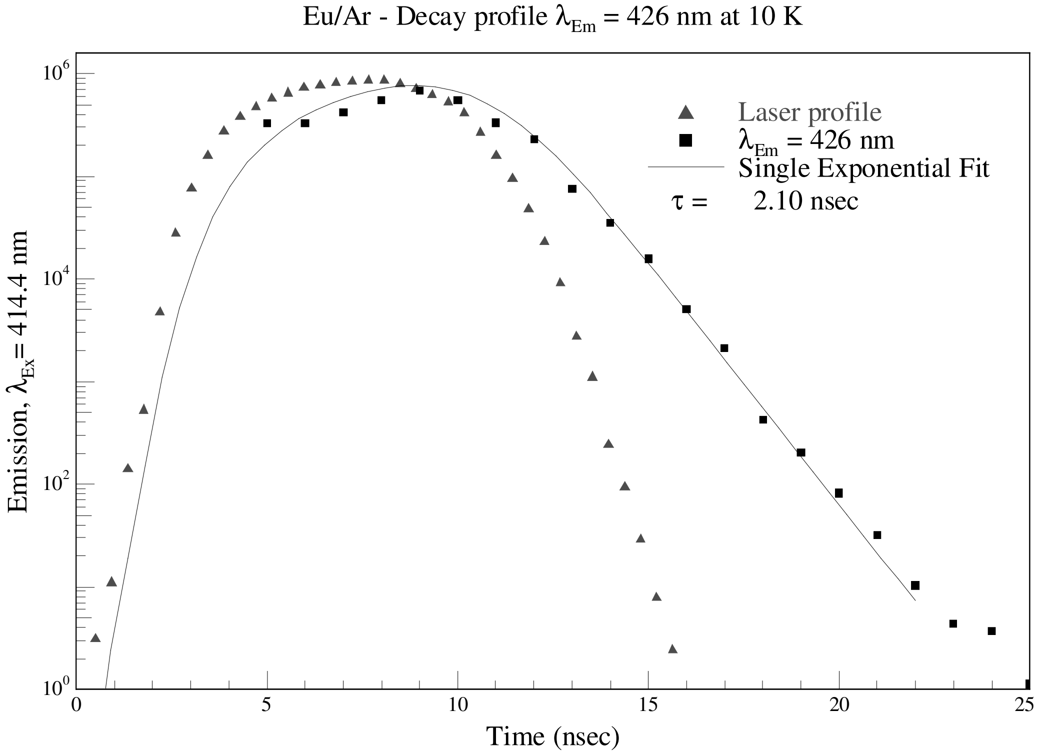

Figure V.22 Decay profile of the emission at 426 nm recorded at 10 K in Eu/Ar. The decay profile is convoluted with the temporal profile of the laser excitation source at 414.4 nm.

Excitation of the 422.2 nm absorption band produced two emission bands centred at 433 and 441 nm with bandwidths of 280 cm^{-1}. Excitation spectra recorded monitoring these features revealed the 422 nm absorption band is in fact composed of two distinct excitation features centred at 422 and 424.4 nm each with a bandwidth of approximately 280 cm^{-1}. Lifetimes of 1.8 and 1.1 ns were recorded for the 433 and 441 nm emission features respectively.

Table V.3 Photophysical characteristics of the 395 to 440 nm spectral features of Eu/Ar. Their spectral position in nm is labelled λ. The bandwidths, Δ, are shown in cm^{-1} (* implies the bandwidth was not fully resolved). Their lifetimes recorded in the matrix at 10 K (τ_{10K}) and lifetimes corrected for the effective field of the surrounding lattice (τ_{Cor}) are also displayed.

Excitation Features		Emission Features			
λ (nm)	Δ (cm^{-1})	λ (nm)	Δ (cm^{-1})	τ_{10K} (ns)	τ_{Cor} (ns)
414.5	290	426.6	286	2.1	4.3
424.4	279	433	281	1.8	3.7
422	277	441	281	1.1	2.3
430	280	449.5	399*	~ 1.1	2.3

The final absorption feature at 430 nm produces a very weak emission band centred at 449.5 nm. Its lifetime was identified as being short, in the region of 1 ns. Table V.3 presents the spectral and temporal characteristics of these 395 to 440 nm features for comparison. All exhibit short nanosecond lifetimes.

The remaining higher energy absorption feature, located at 367 nm, produces a broad and largely Stokes shifted emission with two discernable peaks at 403.9 and 418.4 nm as seen in bottom trace of Figure V.21. Excitation spectra monitoring these emission features confirm they originate from the 367 nm absorption feature exhibiting Stokes shifts of 2239 and 3097 cm^{-1} respectively. Temporal profiles monitoring both these emission wavelengths were recorded and are displayed overlaid with single exponential fits in Figure V.23 and Figure V.24. Emission at 418 nm is longer lived than its 404 nm counterpart, lifetimes of 4.2 and 2.0 ns are extracted.

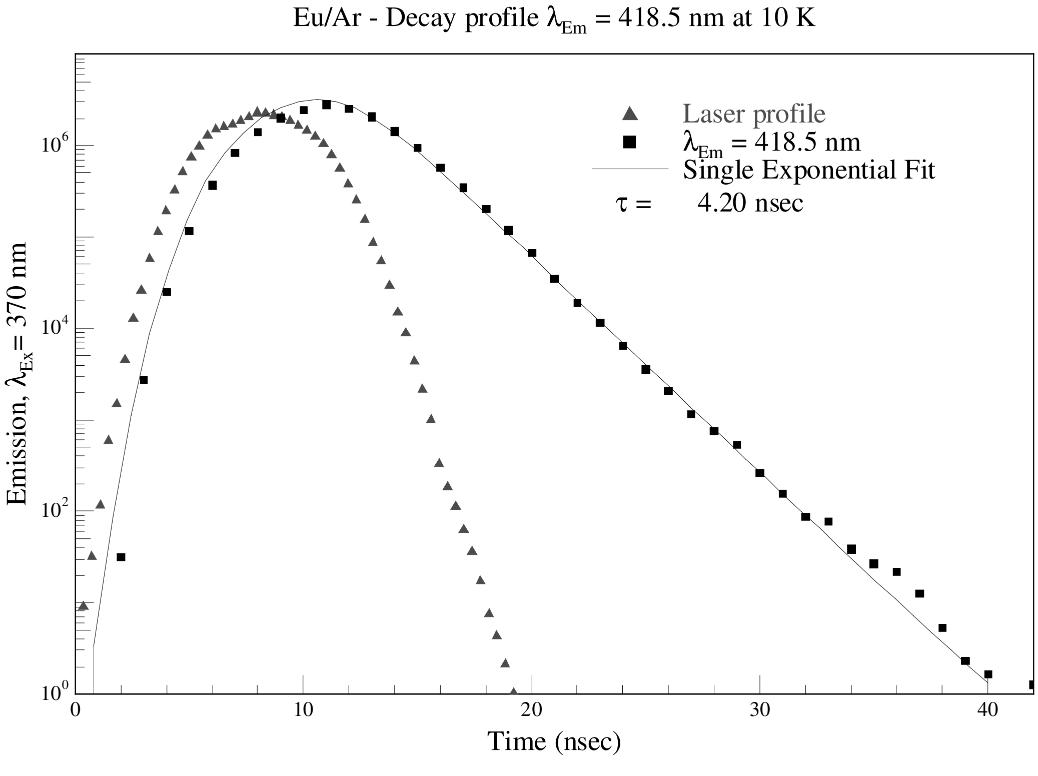

Figure V.23 Decay profile of the emission at 418.5 nm recorded at 10 K in Eu/Ar. The decay profile is convoluted with the temporal profile of the laser excitation source at 370 nm.

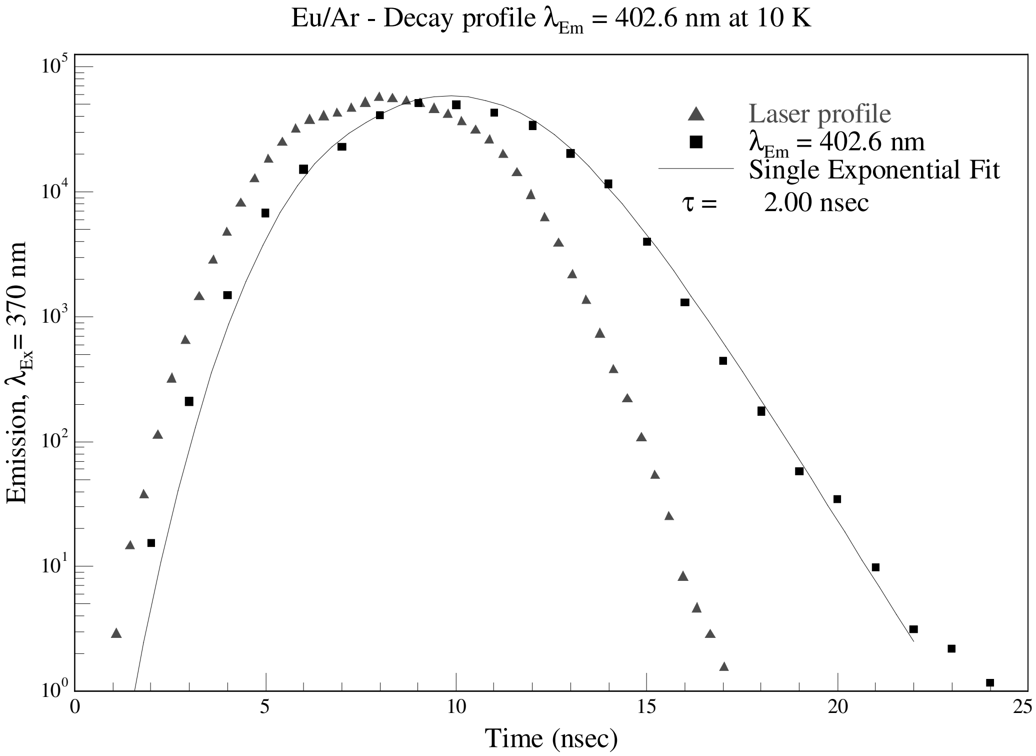

Figure V.24 Decay profile recorded monitoring emission at 402.6 nm recorded at 10 K in Eu/Ar. The decay profile is convoluted with the temporal profile of the laser excitation source at 370 nm.

In summary, new higher energy absorption features are identified in solid Ar following y^8P state laser irradiation. Although weaker than the corresponding features in Kr and Xe, these bands were identified and investigated. They exhibited two emission types. Emission from the higher energy visible absorption bands exhibit large Stokes shifts and much longer lifetimes than the less shifted and shorter lived 395 to 440 nm features.

V.5 Eu/RG Discussion

V.5.I Eu/RG Visible Absorption Spectroscopy

Previous sections presented evidence of new absorption features in each of the RG's (RG = Ar, Kr, Xe) formed by y^8P state laser irradiation of the blue and/or red sites. When these new absorption features are compared to the known gas phase transitions of the singly ionised europium cation (Eu^+) a clear correspondence is seen. Figure V.25 presents the visible absorption spectrum of a Eu/Xe sample following y^8P state irradiation overlaid with the positions of the Eu ion transitions in this region shifted by 1690 and 1330 cm^{-1} from the gas phase. A summary of the gas phase photophysical characteristics of the energy levels of Eu$^+$ are listed in Table V.4. Some are defined using the *jj*-coupling scheme notation as discussed in Chapter I. Three states arising from the $4f^7(^8S°_{7/2})6p_{3/2}$ configuration and two states of $4f^7(^8S°_{7/2})6p_{1/2}$ configuration exist in the visible region. When plotted with the relative intensities, remarkable agreement between Eu/Xe and the gas phase is obtained suggesting these new absorption features arise from matrix-isolated Eu$^+$. The intensity distribution of the higher energy $4f^7(^8S°_{7/2})6p_{3/2}$ configuration matches perfectly the intensities of the 390 to 410 nm absorptions in solid Xe as seen in Figure V.25. Furthermore, the absorption bands at 445.7 and 436.2 nm correspond very well with the $4f^7(^8S°_{7/2})6p_{1/2}$ configuration absorptions when a shift of –1330 cm^{-1} from the gas phase is considered.

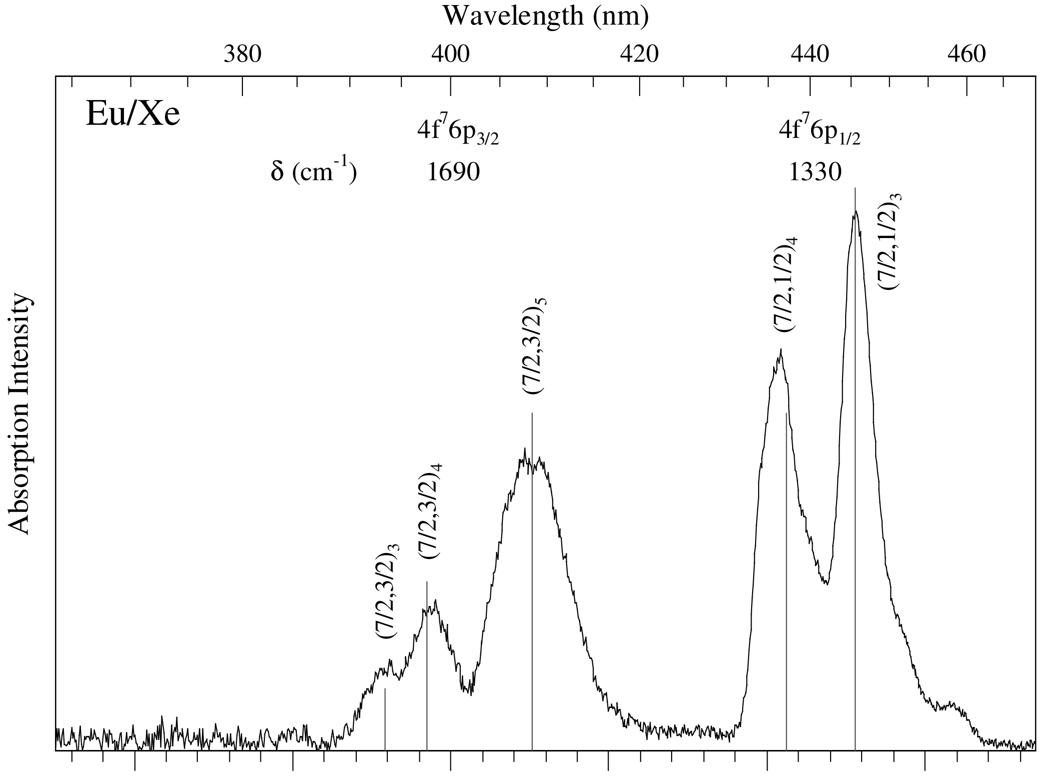

Figure V.25 A plot of the gas phase transition intensities of singly ionised europium shifted by δ = 1690 and 1330 cm^{-1} (solid vertical lines) versus the new absorption features formed in the visible spectral region of Eu/Xe following y^8P state laser irradiation.

The intensity distribution of the $4f^7(^8S°_{7/2})6p_{3/2}$ configuration is also evident in solid Ar and Kr and is displayed in Figure V.26 with matrix shifts of +1100 and –290 cm^{-1} respectively. The two higher energy absorptions in Ar and Kr in the $4f^7(^8S°_{7/2})6p_{1/2}$ region appear to correlate to the $(7/2, 1/2)_4$ and $(7/2, 1/2)_3$ states of Eu^+ shifted by +550 and –290 cm^{-1} respectively as seen in Figure V.26. The remaining two lower energy absorption features may be explained by the existence of a second site of isolation of the europium ion in these lattices. Evidence of a second site in the solid RG's was implied in the bottom traces of Figure V.11, Figure V.14 and Figure V.21. Two unique excitation spectra were recorded in the region of the $4f^7(^8S°_{7/2})6p_{3/2}$ absorption when independent emission features were monitored. A second site is now further suggested for the $4f^7(^8S°_{7/2})6p_{1/2}$ configuration by the occurrence of these two additional absorption bands in the 400 to 450 nm region of Ar and Kr.

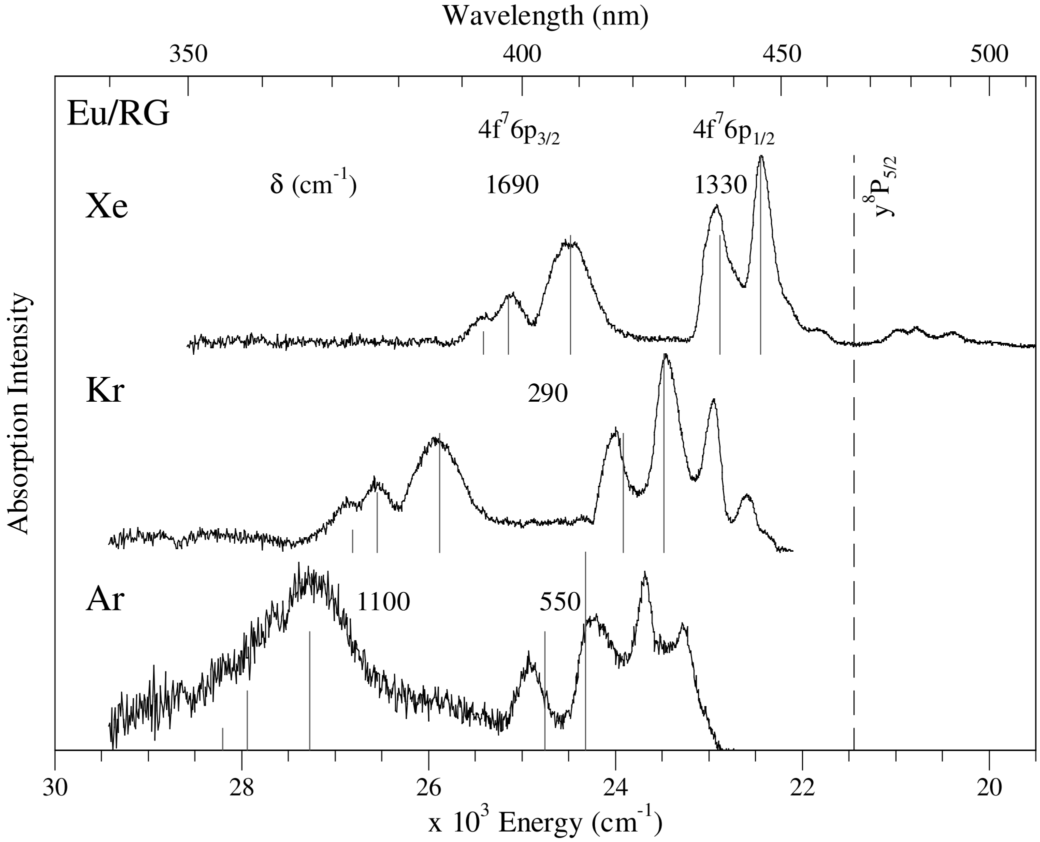

Figure V.26 Normalised absorption spectra of Eu/RG following y^8P state laser irradiation. The spectral position and relative intensities of the absorptions of Eu^+ in the gas phase shifted by δ cm^{-1} are displayed as solid vertical lines. The gas phase position of the y^8P state of atomic Eu is displayed as a dashed vertical line.

Table V.4 Spectral and temporal characteristics of the allowed transitions from the $a^9S°_4$ ground state of the europium cation in the gas phase.

Persistent Lines[2] of Singly Ionised Europium (Eu^+)

Configuration	Terms	λ (nm)	cm^{-1}	Intensity	τ (ns)[3]
$4f^7(^8S°)6s$	$a^9S°_4$	N/A	0	N/A	-
$4f^7(^8S°_{7/2})6p_{1/2}$	$(7/2, 1/2)_3$	420.51	23774.28	1000	8.6
	$(7/2, 1/2)_4$	412.97	24207.86	600	8.4
$4f^7(^8S°_{7/2})6p_{3/2}$	$(7/2, 3/2)_5$	381.97	26172.83	600	6.2
	$(7/2, 3/2)_4$	372.49	26838.5	300	6.9
	$(7/2, 3/2)_3$	368.84	27104.07	110	7.2
$4f^6(^7F)5d\ (^8P)6s$	y^9P_3	290.67	34393.57	50	19.2
	y^9P_4	281.39	35527.02	60	13.8
	y^9P_5	272.78	36648.95	70	13.9

Neutral europium atoms exist in two different lattice vacancies in solid Ar and Kr as discussed in Chapter III. Analogous to this, it seems two sites of isolation exist for the Eu^+ ion in these hosts, explaining the origin of the two lower energy absorption bands in the 400 to 450 nm region. A plot of these absorption features shifts from the $(7/2, 1/2)_4$, $(7/2, 1/2)_3 \leftrightarrow a^9S_4$ gas phase positions versus RG polarisability is displayed in Figure V.27. A linear correlation exists between the features in Xe and the higher energy doublets in Ar and Kr labelled in Figure V.28 as the blue site (B^+) of Eu^+. The linear correspondence of these features in the polarisability plot allows attribution of these bands to ionic Eu isolated in the same site types in the RG hosts. The remaining lower energy pair of absorptions in Ar and Kr are attributed to ions undergoing the $(7/2, 1/2)_4$, $(7/2, 1/2)_3 \leftrightarrow a^9S_4$ state transitions in a lower energy site type labelled the red site (R^+) in Figure V.28. This is in accord with the neutral Eu/RG systems where Ar and Kr hosts exhibit two metal atom trapping sites.

In an effort to attribute these site-specific features to particular vacancies the *ab initio* post-Hartree-Fock MP2 method was employed to calculate counterpoise-corrected equilibrium bond lengths of the Eu^+-RG (RG = Ar, Kr and Xe) diatomics. The augmented[4] segmented[5,6] basis set and 28 electron ECP[6,7] described in Chapter I was employed on the europium ion. Gaussian03 Software[8] pre-defined aug-cc-pVTZ basis sets were used for Ar and Kr. The aug-cc-pVTZ-PP[9,10,11,12] basis set and 28 electron ECP[10,11,12] of Xe were sourced from the basis set exchange website[10,11,12].

The resulting calculated diatomic bond lengths are listed in Table V.5 in Angstrom units.

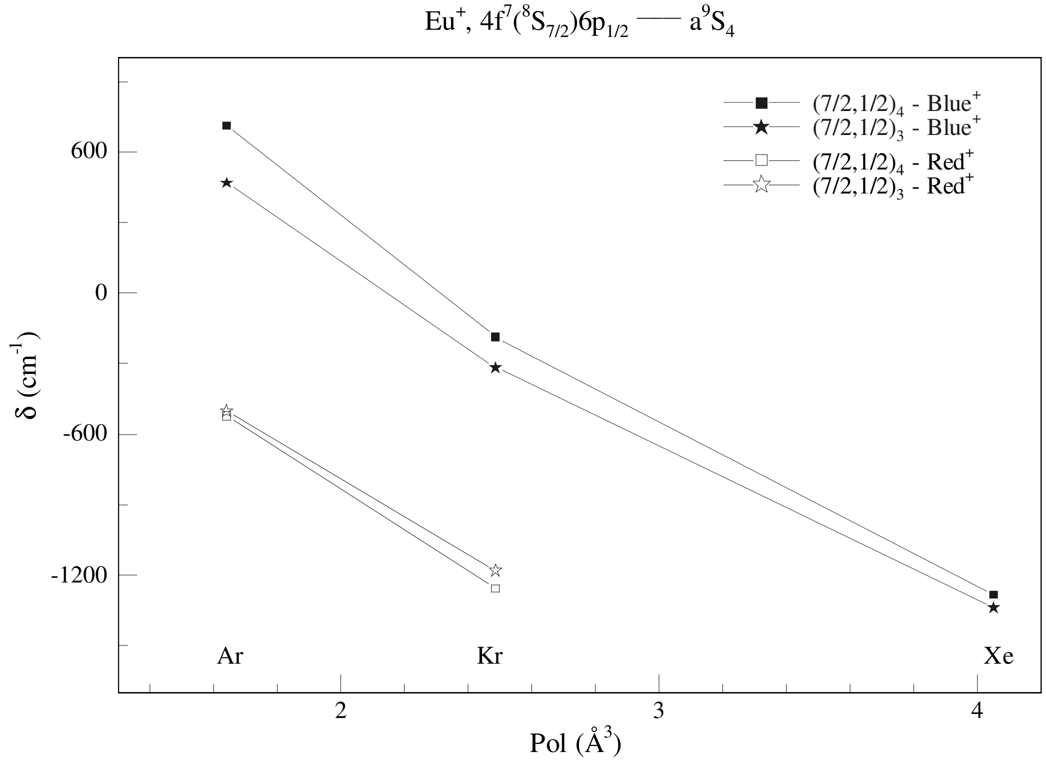

Figure V.27 A plot of the gas phase to Eu^+/RG matrix frequency shifts (δ cm^{-1}) observed for each of the $(7/2, 1/2)_4$, $(7/2, 1/2)_3 \leftrightarrow a^9S_4$ transitions of the blue and red sites of ionic europium versus the RG host polarisabilities. The filled squares and stars (connected by the solid line) highlights the linear correlation between the frequency shifts and rare gas polarisability observed for the Eu^+ $(7/2, 1/2)_4$, $(7/2, 1/2)_3 \leftrightarrow a^9S_4$ transitions occurring in the single site in Xe and the blue (B^+) sites of Ar and Kr.

Table V.5 Site sizes in angstrom units (Å) for specific spherically symmetric site types in the solid rare gases. Also shown is the lattice parameter, *a*, of each *fcc* solid. The details of these sites was presented in Chapter I. The MP2 calculated $Eu^+(a^9S_4)$-RG diatomic ground state bond lengths are presented in Angstrom units. Attempts to calculate the neutral diatomic bond lengths with the MP2 method failed. This functional is unsuitable for predicting such weak neutral-neutral van der Waals interactions. Therefore, the Luiti-Pirani (LP) calculated $Eu(^8S_{7/2})$-RG equilibrium distances from Chapter III are displayed for comparison.

RG	***a* (Å)**	**I_{oh} (Å)**	**sv (Å)**	**tv (Å)**	**hv (Å)**	Eu-RG (Å)	**Eu^+-RG (Å)**
Ar	5.31	2.655	3.755	4.403	4.598	5.17	**3.32**
Kr	5.64	2.82	3.988	4.676	4.884	5.18	**3.37**
Xe	6.13	3.065	4.330	5.083	5.308	5.21	**3.51**

The Xe lattice is the simplest case where the ion exists in only one site. The predicted Eu^+-Xe bond length of 3.51 Å lies between the size of the I_{oh} and sv sites and therefore the guest may occupy either. It is known from Chapter III that the neutral metal occupies only the tv site of size 5.08 Å in annealed Xe solids. The sv site of 4.33 Å is 85.2 % of this size while the 3.065 Å I_{oh} site is 60.3 % the size of the original tv site. Inspection of Table V.5 and Table V.6 shows the metal-Xe bond length decreases from 5.21 Å to 3.51 Å upon removal of an electron, a decrease to 67.3 %. It is suggested the ion will occupy a site with a similar decrease in volume i.e. the I_{oh} site which is 60 % the size of the initial tetra-vacancy. The europium ion is therefore proposed to occupy an octahedral interstitial site (I_{oh}) in Xe. The polarisability plot of Figure V.27 allowed a correlation to be made between this site and the blue (B^+) sites in Ar and Kr. These sites are accordingly also attributed to I_{oh} lattice trapping vacancies in these hosts.

Table V.6 The size of the Eu-RG diatomic bond lengths upon removal of a metal electron are presented in terms of percentage of initial size. The remaining columns identify the decrease in size of the initial hv and tv vacancies occupied by neutral Eu compared to the I_{oh} and sv sites.

RG	$\frac{Eu^+ \bullet RG}{Eu \bullet RG}$	$\frac{I_{oh}}{tv}$	$\frac{I_{oh}}{hv}$	$\frac{sv}{tv}$	$\frac{sv}{hv}$
Ar	64.2 %	60.3 %	57.7 %	85.2 %	81.7 %
Kr	65.1 %				
Xe	67.3 %	60.3 %		85.2 %	

The remaining red sites (R^+) in Ar and Kr are unaccounted for. The Eu^+-RG diatomic distances lie between the size of the I_{oh} and the sv vacancies implying either of these sites may be populated by the ion. The B^+ site features are attributed to I_{oh} occupancy. The R^+ features occur to lower energy than B^+ site absorptions, implying they are larger trapping sites which must therefore be single vacancies.

The neutral metal initially occupies a tv or hv while the singly ionised species is proposed to reside in the I_{oh} and the sv. Considerable re-arrangement of the host lattice must occur during this change in occupied vacancies. Transposition to a I_{oh} site is reasonably straightforward involving minimal lattice distortion as these vacancies are inherent to the *fcc* RG host solids. However, site transformation from a hv or tv to a sv would require significant lattice re-arrangement during Eu^+ migration. Recent Molecular Dynamic simulations[1] of the excited state of atomic Na found a significant rearrangement of the rare gas atoms around the excited sodium was observed due to the strongly attractive interactions occurring when in the $^2\pi$ state. For example, in Na/Kr, two Kr atoms migrate in sequence after the Na atom in the excited state has moved. The trajectory is not direct, the excited sodium explores different geometries with close Kr atoms. It begins its stabilisation by moving very close to two Kr (~ 40 ps) atoms, one more Kr atom is attracted near Na (~ 65 ps) followed by a second one (~ 75 ps), leading to a more compact site, involving four very close neighbours. Such movements of rare gas atoms toward the guest Na atom create sv sites from larger vacancies such as tv or hv sites.

Table V.7 Well-depths of the ground state Eu^+-RG and neutral Eu-RG diatomics in wavenumber units calculated with the MP2 and Luiti-Pirani methods respectively. The corresponding dissociation energies, De's, of the attractive A states of atomic sodium in its ^2P excited state are also displayed.

Well Depths, De (cm^{-1})

RG	Eu^+-RG	Eu-RG	$Na(^2P)$-RG[13,14,15] $A^2\pi_{1/2}$	$Na(^2P)$-RG[13,14,15] $A^2\pi_{3/2}$
Ar	677	86	581	576
Kr	1079	126	795	760
Xe	1162	188	1215	1120

The binding energies of the Eu^+-RG species were calculated with the MP2 method and are listed in Table V.7. These values are larger than the excited state $Na(^2P)$-RG interaction strengths. The much stronger attractive forces of Eu^+-RG imply it is possible for the ion to 'pull' RG atoms into position after it has migrated from a large hv or tv into a smaller I_{oh} or sv site much like the Na/RG system.

Further evidence supporting the assignment of these features to europium ions is collected by monitoring the relative intensities of the absorptions as one progresses through the RG hosts. As shown in Figure V.28 solid Xe displays the greatest ion absorption strengths while the ion absorptions are least intense in solid Ar. A factor which contributes to this may be the relative polarisability of the RG host and consequently its ability to stabilise a positively charged species. Ar being the least polarisable host has a lesser ability to delocalise the ionic charge and thus has the smallest Eu^+ population. This is exhibited by its weaker ionic absorption intensities. The relative intensities in Ar and Kr may also be effected by the fact the absorption intensity in these hosts is distributed over two sites occupied by Eu^+ in these lattices causing them to seem weaker compared to Xe. Other factors relating to the relative intensities in each host are discussed in Section V.5.IV.

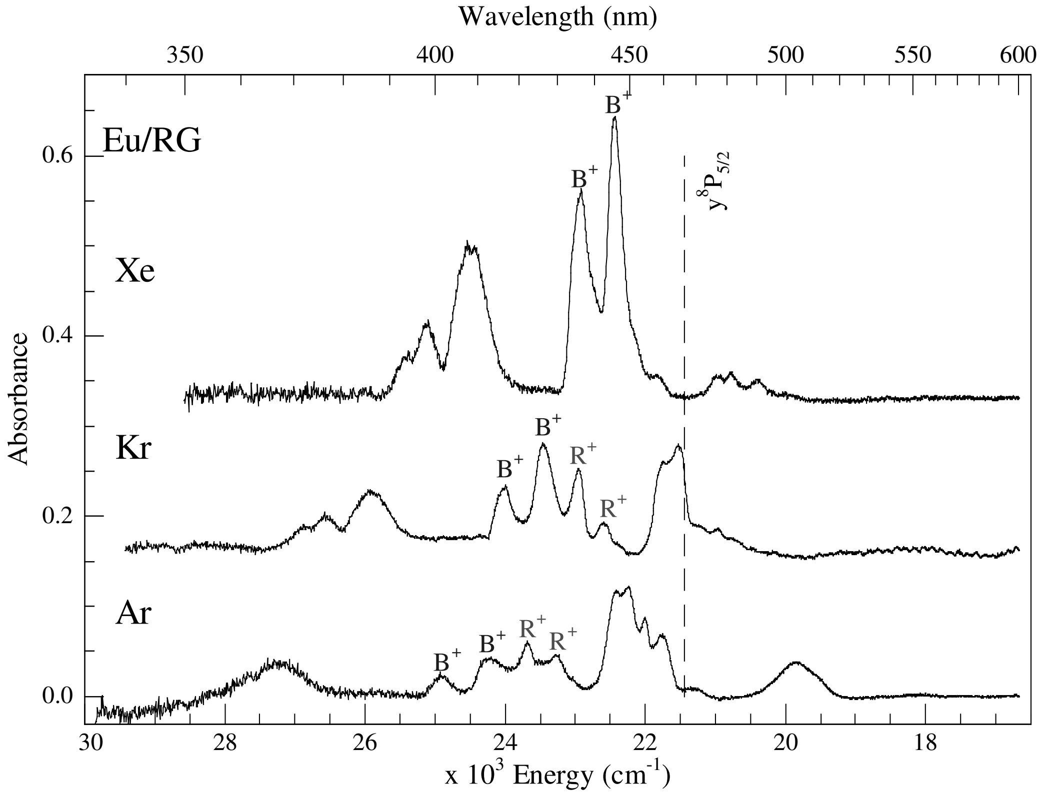

Figure V.28 Plot of the absolute absorption intensities of the new Eu/RG absorption features formed following y^8P state laser irradiation. The spectral position of the gas phase y^8P transition of atomic Eu is shown by the dashed vertical line. Site-specific features of the $4f^7(^8S°_{7/2})6p_{1/2}$ states are labelled blue (B^+) and red (R^+).

V.5.II Eu/RG UV Absorption Spectroscopy

Absorption spectra in the UV region, presented in Figure V.29 before and after y^8P state irradiation, also show the new absorptions formed in this region are in agreement with attribution to the Eu ion. As is evident in Figure V.29, the splitting of the new absorptions match perfectly the splitting of the y^9P spin-orbit states of Eu^+ in the gas phase. The right panel of Figure V.29 displays the new spectral features overlaid with the gas phase positions of the y^9P state shifted by –1350 cm^{-1}.

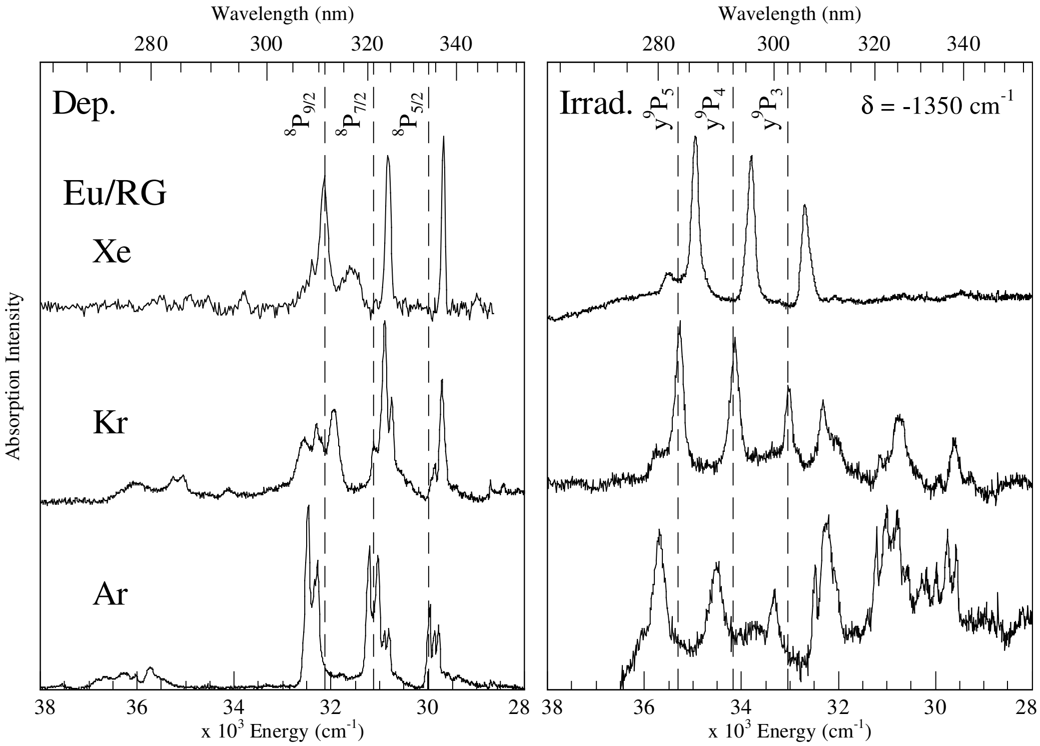

Figure V.29 Summary plot of the UV absorption spectra of Eu/RG. Left panel displays the absorption spectra recorded in this region on deposition with the dashed vertical lines representing the gas phase positions of the ^{8}P states of atomic Eu. Right panel presents the absorption spectra in this region following y^8P state laser irradiation, the dashed vertical lines represent the gas phase positions of the y^9P states of the europium cation shifted to lower energy by 1350 cm^{-1}.

Features pertaining to the two, B$^+$ and R$^+$, sites of isolation of the ion identified in the visible region are not obvious for the UV transitions of Figure V.29. The $y^9P_3 \leftrightarrow a^9S°_4$ ionic transition is a f → d type absorption involving core electrons and thus expected to be narrow. The UV spectral features observed in this work are not fully resolved due to the very small linewidth of these core transitions. There exists underlying site structure which could not be identified with the maximum resolution available in this study.

V.5.III Eu$^+$/RG Luminescence

Further evidence that the new Eu/RG absorption features are Eu$^+$ ions is also gained by analysis of their emission features. The band locations and their lifetimes are discussed in the following sections.

V.5.III.1 Eu^+ ($4f^7(^8S°_{7/2})6p_{3/2}$)/RG Luminescence

The highest energy visible region absorption features are proposed to be $(7/2, 3/2)_3$, $(7/2, 3/2)_4$ and $(7/2, 3/2)_5$ state transitions of matrix-isolated europium cations in a $4f^7(^8S°_{7/2})6p_{3/2}$ configuration as presented in Figure V.26. Two discernable peaks are identifiable in the emission profile in each RG yielding two similar but slightly different excitation bands. This suggests two sites of isolation within the matrices. Figure V.30 displays a summary of these luminescence features in all of the solid RG's. Excitation of each of the three $4f^7(^8S°_{7/2})6p_{3/2}$ features produces the same emission profile suggesting all emission is observed from the lowest energy $4f^7(^8S°_{7/2})6p_{3/2}$ state, the $(7/2, 3/2)_5$ state. Decay characteristics recorded of all the emission bands observed in these regions are on the nanosecond timescale and their complete spectral and temporal characteristics are listed in Table V.8.

Table V.8 Spectral and temporal characteristics of the $4f^7(^8S°_{7/2})6p_{3/2}$ configuration luminescence of singly ionised Eu in the solid RG's at 10 K. Their spectral position in nm is labelled λ, while *ν* indicates their position in cm^{-1}. Gas phase to matrix frequency shifts are presented as δ in wavenumber units. Lifetimes recorded in the matrices at 10 K are identified by τ_{10K} and when corrected for the effective field of the surrounding lattice as τ_{Cor} in nanosecond units. The dominant/primary (1^o), secondary (2^o) features are labelled to reflect their relative luminescence strengths.

	Excitation Features			Emission Features				
	ν (cm^{-1})	λ (nm)	δ (cm^{-1})	ν (cm^{-1})	λ (nm)	δ (cm^{-1})	τ_{10K} (ns)	τ_{Cor} (ns)
	$(7/2, 3/2)_5 \leftrightarrow a^9S°_4$			$(7/2, 3/2)_5 \leftrightarrow a^9S°_4$				
Gas phase	26172.83	381.97	-	26172.83	381.97	-	6.2	6.2
Eu/RG								
Xe (2^0)	24266	412.1	– 1907	20475	488.4	– 5698	4.0	11.8
Xe (1^0)	24468	408.7	– 1705	21399	467.3	– 4773	4.5	13.3
Kr (1^0)	25700	389.1	– 473	22462	445.2	– 3711	4.6	11.9
Kr (2^0)	25807	387.5	– 366	23579	424.1	–2593	3.6	9.3
Ar (1^0)	26998	370.4	+ 825	23901	418.4	– 2272	4.2	8.6
Ar (2^0)				24759	403.9	– 1414	2.0	4.1

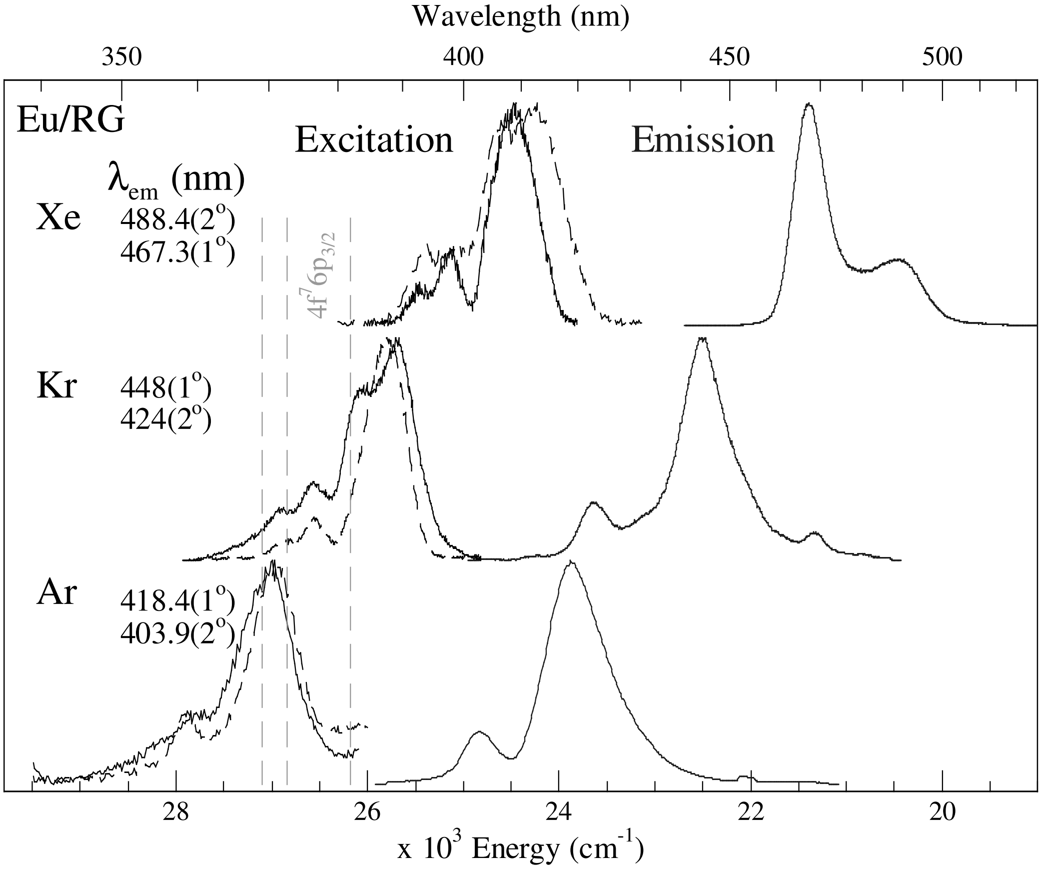

Figure V.30 Summary plot of the Eu^+/RG $4f^7(^8S°_{7/2})6p_{3/2}$ luminescence. Excitation spectra are shown to the left, emission spectra are displayed as solid traces to the right. The spectral positions of the gas phase $4f^7(^8S°_{7/2})6p_{3/2}$ states are identified by the dashed vertical lines.

The lifetime values of the emission produced with $4f^7(^8S°_{7/2})6p_{3/2}$ excitation in the matrix compare quite well to the lifetime of the lowest energy $4f^7(^8S°_{7/2})6p_{3/2} \leftrightarrow a^9S°_4$ transition of Eu^+ occurring at 381.97 nm with a lifetime of 6.2 ns in the gas phase[2,3]. This, and its spectral location, suggest the $(7/2, 3/2)_5 \leftrightarrow a^9S°_4$ transition of the europium ion is the source of the observed emission. This assignment is further supported when the lifetimes of these emission features are corrected for the effective field of the surrounding RG matrix and are plotted against a lambda cubed extrapolation of the gas phase $(7/2, 3/2)_5 \leftrightarrow a^9S°_4$ transition as presented in Figure V.31. There is very good agreement between the observed matrix features and the gas phase transition. The matrix corrected values lie in close proximity to the λ^3 line. This allows confident assignment of these features as $(7/2, 3/2)_5 \leftrightarrow a^9S°_4$ fluorescence of matrix-isolated Eu^+.

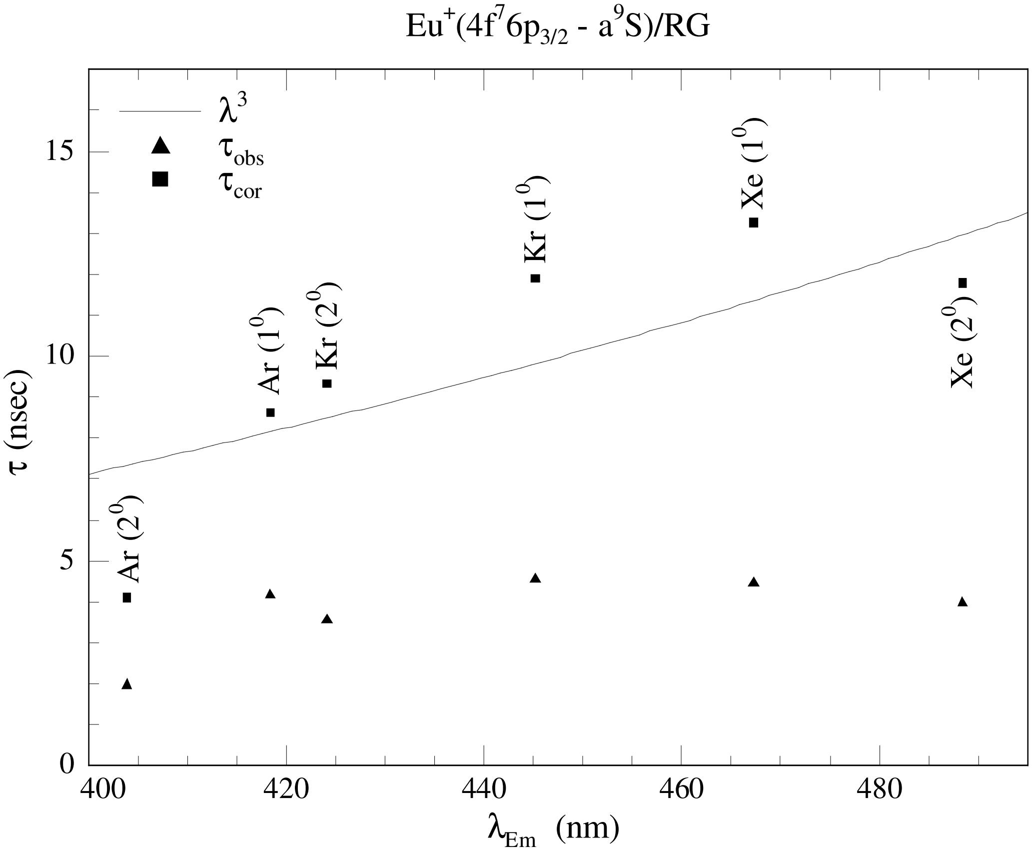

Figure V.31 A comparison of the lifetimes recorded at 10 K for the $Eu^+(4f^7(^8S°_{7/2})6p_{3/2} \rightarrow a^9S)$ emission features in Ar, Kr and Xe and a λ^3 extrapolation of the gas phase lifetime of the $(7/2, 3/2)_5$ state of the Eu cation. The uncorrected data and the data corrected for the effective fields are shown by closed triangles and closed squares respectively.

V.5.III.2 Eu^+ $(4f^7(^8S°_{7/2})6p_{1/2})$/RG Luminescence

The remaining luminescence features in the visible region appear to correspond to excitation of the $4f^7(^8S°_{7/2})6p_{1/2}$ configuration of europium ions which exhibits two electronic states labelled $(7/2, 1/2)_3$ and $(7/2, 1/2)_4$. Unlike the $4f^7(^8S°_{7/2})6p_{3/2}$ luminescence, distinct emission occurs from individual absorption features which can be seen in Figure V.11, Figure V.14 and Figure V.21. Again lifetimes on the nanosecond scale compare favourably to the gas phase[3] values of the $4f^7(^8S°_{7/2})6p_{1/2} \leftrightarrow a^9S°_4$ transitions which are 8.6 and 8.4 ns. This allows assignment of these features as emission of the $4f^7(^8S°_{7/2})6p_{1/2}$ states of matrix-isolated ionic europium. The temporal and spectral characteristics of these $(7/2, 1/2)_3$ and $(7/2, 1/2)_4$ states can be found summarised in Table V.9.

Table V.9 Spectral and temporal characteristics of the $4f^7(^8S°_{7/2})6p_{1/2}$ states emission of Eu^+ isolated in the solid RG's at 10 K. Their spectral position in nanometre is labelled λ_{em}, while v indicates their position in cm^{-1}. Nanosecond lifetimes recorded in the matrices at 10 K are identified by τ_{10K} and the lifetime corrected for the effective field of the surrounding RG matrix are displayed as τ_{Cor}.

	λ_{em} (nm)	v (cm^{-1})	τ_{10K} (ns)	τ_{Cor} (ns)
Gas phase				
$(7/2, 1/2)_3 \leftrightarrow a^9S°_4$	420.51	23774.28	8.6	8.6
$(7/2, 1/2)_4 \leftrightarrow a^9S°_4$	412.97	24207.86	8.4	8.4
Eu/RG				
Xe	452.4	22104	2.1	6.2
	450.9	22178	2.2	6.5
	448.9	22277	1.8	5.3
Kr	453	22075	1.3	3.4
	441.1	22671	2.4	6.2
	436.1	22931	1.9	4.9
	431.3	23186	2.4	6.2
Ar	449.5	22247	~ 1.1	2.3
	441	22676	1.1	2.3
	433	23095	1.8	3.7
	426.6	23441	2.1	4.3

V.5.IV Matrix-isolated ion formation *in situ*

Formation of a metal cation in a RG matrix with laser irradiation is surprising and was completely unexpected. The only other known occurrence of a metal cation formed *in situ* in a matrix is for the Ca/Ar system[16]. However, very large laser powers and short wavelengths were employed. Exposure of the Ca/Ar matrix to the ionising radiation of a hydrogen discharge lamp at the 121.6 nm (10.2 eV) Lyman-alpha line or 10 pulses of an ArF excimer laser at 187.0 nm (6.63 eV) produced a new high intensity emission band at 25100 cm^{-1} assigned as Ca^+ ions. The ionisation potential[2] of free atomic Ca is 6.11 eV (203.1 nm) so clearly the excitation wavelengths employed may form the Ca^+ ion via a one photon process.

In contrast to this, atomic Eu appears to have been ionised in the matrix with lower energy irradiation. Laser energies in the region of 2.7 eV (450 nm) and powers of 250 μJ/mm^2 were employed to produce the new Eu$^+$ ion features. The ionisation potential[2] of Eu in the gas phase is 5.67 eV (218.7 nm) suggesting that either the ionisation energy of the metal atom is strongly reduced in the rare gas matrices or a multi-photon ionisation process is occurring.

Considering the first possibility, ionisation energies of alkali atoms are known to be strongly reduced in RG matrices by 1 eV (Ar) up to 1.9 eV (Xe) due to the polarisation energies of the core and due to the electron affinities[17]. A similar reduction of the ionisation energy of Eu in the matrix would lower it to 3.77 eV in the most extreme case of Xe which is still 1 eV larger in value than the wavelength of irradiating light (2.7 eV) suggesting ionisation does not occur via a one photon matrix reduced ionisation energy process.

An indication of the involvement of a multi-photon event is identified when the effect of increased irradiation power is considered. The bottom traces of Figure V.32 shows the Eu/Xe absorption spectra of two different samples on deposition.

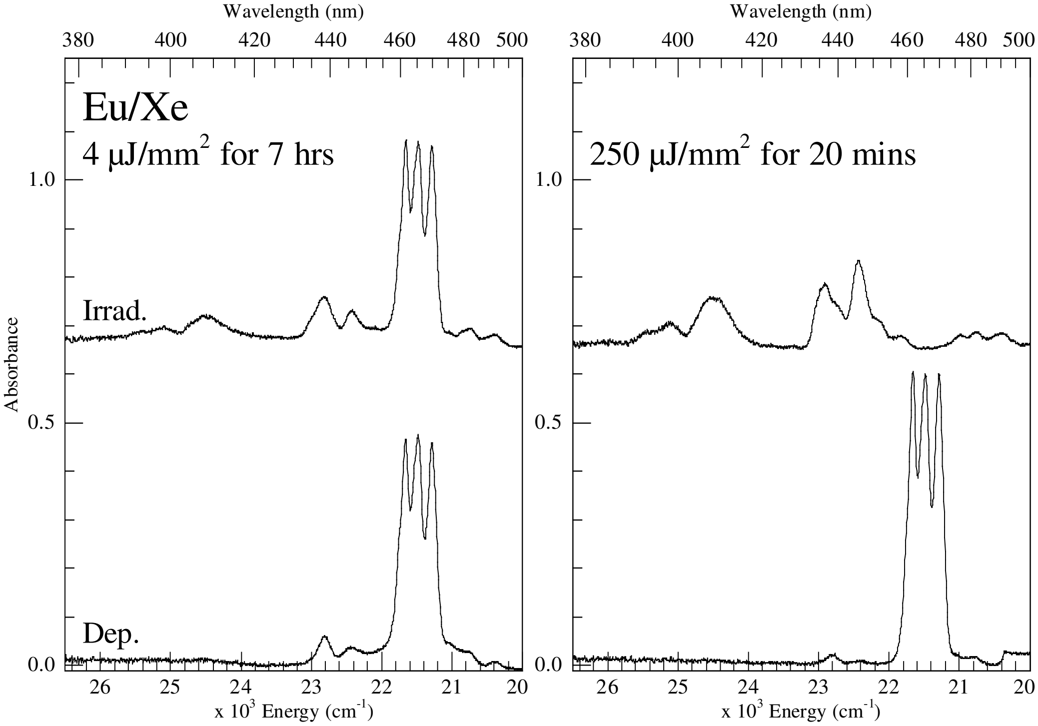

Figure V.32 Absorption spectra of two different Eu/Xe samples. Bottom traces were recorded at 10 K following deposition at 26 K and sample annealing to 60 K. Top traces present the absorption spectra following laser y^8P state irradiation which exhibit a clear power dependence. Laser energies of 4 μJ/mm^2 for 7 hours were employed in left trace. Right trace was following exposure to powers of 250 μJ/mm^2 for 20 minutes.

A minimum amount of Eu^+ ions formed during deposition by the electron bombardment vaporisation process are present to the blue of the intense y^8P state atomic feature in Figure V.32. The top traces of Figure V.32 display the resulting absorption spectra following laser irradiation of Eu/Xe at 465 nm at different powers. Irradiation at a power of 4 μJ/mm^2 for 7 hours caused some but very little formation of the ion as seen in the top trace of Figure V.32. However, irradiation at a power of 250 μJ/mm^2 for 20 minutes completely removed all neutral atomic Eu resulting in formation of europium ions. There is a strong power dependence, indicating this is a multi-photon ionisation process. It is likely both factors play a role in the ionisation. The ionisation energies are reduced by the RG matrix but ultimately the ion can only be formed by a multi-photon process.

The next issue of matrix ionisation of metals *in situ* concerns the removed electron. Previous work on Ca/Ar[16] stated the highest electron is loosely bound and will have, particularly in the excited state, to some extent a Rydberg character. This loosely bound electron will be relatively strongly delocalised into the lattice. Proof of this was seen by the fact that sample annealing to 30 K almost completely destroyed the new Ca^+ emission band which could then be regenerated by further photolysis. This is also the case for Eu/RG. Annealing decreases the ionic features but they can be returned by further irradiation. It is possible the Eu^+ ion exists in the matrix with its ionised electron delocalised into the lattice which becomes available again for recombination to reform neutral Eu atoms during annealing.

Free, localised electrons in low temperature solids have been identified before[18]. Polar matrices of alkanes, ethers, alcohols and aqueous glasses at temperatures of 1.6, 4.2 and 77 K showed evidence of pre-solvated electrons which did not readily react becoming stabilised in the solid matrix. It was found that as the thermal energy of the host was lowered a greater and greater fraction of electrons were localised in non-equilibrium solvation shells. The solid RG matrices in this study are at 10 K, leading to the possibility that the free ionised electron may be stabilised in these low temperature lattices.

Further proof of matrix stabilised electrons is evidenced in the fact that the Eu_2 dimer is formed during the irradiation/ionisation process in solid Ar. The ionised electron can be stabilised to a lesser degree in the less polarisable Ar host. Thus the unstable electron is attracted to and recombines with the positively charged Eu^+ ion. This produces a release of energy into the lattice causing thermal heating of the surrounding matrix environment and localised annealing. This allows some freedom of movement of the regenerated neutral europium atoms which may combine with another Eu atom to form Eu_2 observed absorbing at 503 nm. The poor stabilisation of the free electron in solid argon partly explains why the weakest Eu^+ intensities are observed in Ar samples in Figure V.28. Dimer formation is not observed in solid Kr or Xe because of these hosts' greater stabilisation of the free electron, reducing the probability of electron recombination with a europium cation. This decreases the probability of dimer formation, therefore yielding a larger amount of matrix-isolated ions.

In contrast to the proposed delocalisation of the free electron in the solid lattice there is also the possibility that perhaps the ionised electron is stabilised on another Eu atom in the matrix forming the Eu^- anion. Recent calculations predict stable negative lanthanide ions by the attachment of a 6p electron are possible[19]. As atomic number becomes large for lanthanides there may be sufficient potential to bind an extra electron to a neutral system. Europium anions have been produced in the gas phase[19] with a measured electron affinity of 1.05 eV so it is possible neutral Eu could stabilise the ionised electron as Eu^-. However, this seems unlikely when annealing effects are considered. If both the cation and anion were present in the matrix, annealing would be expected to produce europium dimer as the two oppositely charged metal species recombine. This is not the case, there is no evidence of dimer formation upon annealing. In fact, regeneration of the neutral atom occurs which suggests a matrix stabilised ionised electron becomes available for recombination reforming the neutral metal.

A final consideration is that the electron resides as an appropriate anion in a trap such as an impurity molecule (O_2, N_2, H_2O, CO_2). However, this seems unlikely as the level of impurities in the system should not be sufficient to allow such an effect. High-vacuum in the region of 10^{-8} mbar is maintained in the matrix sample chamber and in the gas handling system. The host gases employed are of high purity (> 99.995 %). Thus there are minimal impurities present in the system, making this possibility unlikely.

V.5.V Eu/RG - UV Site-Specific Features

A previous study of the UV transitions of atomic Eu from the 1970's was re-analysed in Chapter III using excitation spectroscopy. Vacancy occupancies can now be further supported using the site-specific laser irradiation process. As seen in Figure V.20, red site y^8P state irradiation of Eu/Ar removed all red site features in the visible and UV spectral regions leaving only the blue site isolated atoms.

The bottom trace of Figure V.33 presents the UV absorption spectrum of Eu/Ar on deposition. The middle trace of this figure displays the absorption spectrum in this region following red site laser irradiation, all red site features are removed thus only blue site features remain. The top trace of Figure V.33 shows the site-specific excitation spectrum recorded in this region monitoring blue site emission features as presented in Chapter III. Clearly there is excellent agreement between the middle and top traces further supporting these features' site attributions made in Chapter III.

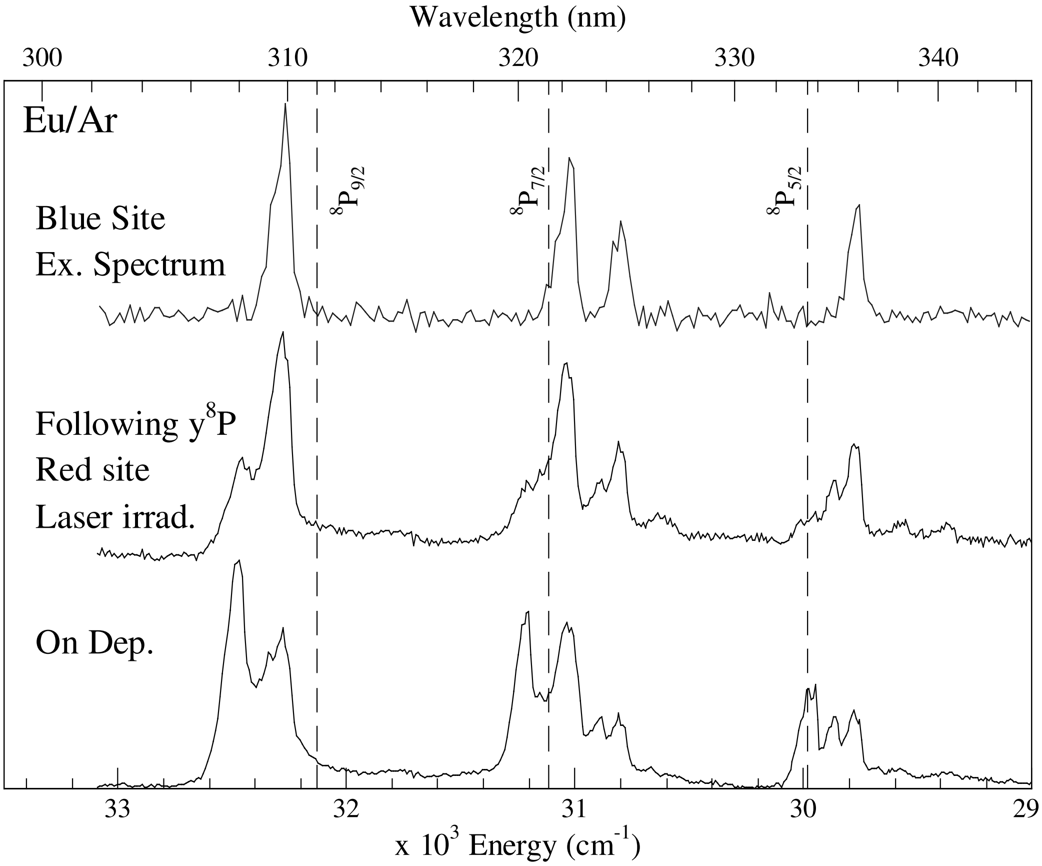

Figure V.33 Eu/Ar atomic UV absorption spectra recorded at 10 K. Bottom trace is following deposition at 16 K and matrix annealing to 31 K. Middle trace shows the absorption spectrum recorded after red site y^8P state laser irradiation at 450.1 nm. The top trace displays the site-specific excitation spectrum recorded in this region monitoring blue site emission features.

V.6 Conclusion

New absorptions to higher energy formed with blue and/or red site y^8P state laser irradiation are identified in Eu/RG samples and appear to correspond to matrix-isolated Eu ions formed in the lattice by a multi-photon ionisation process with laser irradiation.

Initially it was considered these new higher energy absorptions of Eu/RG might be the result of site interconversion to a sv upon laser irradiation similar to the Na/RG system. However, if a sv was formed one would expect to observe a single Jahn-Teller threefold split y^8P state absorption band to higher energy of the blue site. Instead, multiple complex absorption/excitation features, not exhibiting clear-cut threefold Jahn-Teller splitting are observed. Coupled with the fact the absorption features produce characteristically different emission and excitation spectra, demonstrates that these new features do not correspond to Eu atoms isolated in a sv.

Based on its intensity distribution, spectral location and temporal characteristics, the visible absorption to highest energy is proposed to be the $4f^7(^8S°_{7/2})6p_{3/2} \leftrightarrow a^9S°_4$ type transitions of Eu^+ cations trapped in the RG matrices. It is suggested the lowest energy absorption features correspond to the $4f^7(^8S°_{7/2})6p_{1/2} \leftrightarrow a^9S°_4$ transitions of ionic Eu and the final absorptions identified in the UV are postulated as originating from the y^9P state of positively charged Eu^+ isolated in the RG solids. It seems the two different electronic configurations observed in the visible region behave very differently. Both undergo different strength matrix shifts as seen in Figure V.26. The higher energy $4f^7(^8S°_{7/2})6p_{3/2}$ configuration emits from the lowest energy state but it appears emission from the $4f^7(^8S°_{7/2})6p_{1/2}$ configuration states occurs from individual energy levels.

The newly formed UV absorptions also support identification of the ion and refute attribution of these bands to neutral europium isolated in a sv. The f → d type transitions of neutral Eu in the UV region are identified in Chapter III to follow a trend where blue site absorptions occur to lower energy than red site. If a sv site was being formed by the irradiation process, the new absorptions would be expected to follow this trend and occur to lower energy. This is not the case, the new UV absorptions occur to higher energy, in close agreement with the location of the Eu ion transitions in the gas phase further dispelling the origin of these bands as neutral atomic Eu in sv sites.

Multiple absorption features in the region of the $4f^7(^8S°_{7/2})6p_{1/2} \leftrightarrow a^9S°_4$ transitions of ionic Eu established evidence of two sites of isolation of the Eu^+ ion. A lower energy red (R^+) site observed in Ar and Kr and a higher energy blue (B^+) site identified in all three hosts. A polarisability plot allowed identification of the B^+ features as corresponding to the ion trapped in the same lattice environment in each RG. Occupancy of two sites in Ar and Kr is analogous to the neutral system where atomic Eu occupies both hv's (R) and tv's (B). A comparison with the predicted RG equilibrium distances involving neutral europium shows the ionic species to be much smaller indicating it will occupy smaller lattice trapping vacancies. The Eu^+-RG diatomic bond lengths lie between the size of the I_{oh} and sv and it is proposed both of these sites are populated by the ion in Ar and Kr while only the I_{oh} site is occupied in solid Xe.

In summary, based on the excellent agreement between the absorption intensities and their spectral positions the new absorption features observed in the solid RG's following y^8P state laser irradiation are proposed to correspond to matrix-isolated europium ions. The higher energy visible absorptions in Ar, Kr and Xe show excellent agreement with the states of $4f^7(^8S°_{7/2})6p_{3/2}$ configuration of Eu^+ in the gas phase when matrix shifts of +1100, –290 and –1690 cm^{-1} are accounted for. The lower energy doublet at 452.4 and 448.9 nm in solid Xe is explained by absorption of the $4f^7(^8S°_{7/2})6p_{1/2}$ configuration with a matrix shift of –1330 cm^{-1}. The corresponding absorptions in Kr and Ar are more complicated showing four instead of two features in this region due to two sites of isolation in these matrices. These sites are labelled blue (B^+) and red (R^+) and are proposed to correspond to octahedral interstitial and single vacancy sites respectively. They are formed from the initially occupied tv's and hv's during ionisation. Strong Eu^+-RG attractive forces allows lattice re-arrangement during the formation of these sites.

References

[1] M. Ryan, M. Collier, P. de Pujo, C. Crepin and J. G. McCaffrey, Journal of Physical Chemistry A **114** (9), 3011 (2009).

[2] *NIST Atomic Spectra Database (version 3.1.5), available: http://physics.nist.gov/asd3 [2010, March 22].* (National Institute of Standards and Technology, Gaithersburg, MD.).

[3] E. A. Den Hartog, M. E. Wickliffe and J. E. Lawler, Astrophysical Journal Supplement Series **141** (1), 255 (2002).

[4] A. Buchachenko, G. Chałasiński and M. Szcześniak, Structural Chemistry **18** (6), 769 (2007).

[5] X. Cao and M. Dolg, Journal of Molecular Structure: THEOCHEM **581** (1-3), 139 (2002).

[6] X. Y. Cao and M. Dolg, Theoretical Chemistry Accounts **108** (3), 143 (2002).

[7] M. Dolg, H. Stoll and H. Preuss, The Journal of Chemical Physics **90** (3), 1730 (1989).

[8] M. J. Frisch, G. W. Trucks, H. B. Schlegel, G. E. Scuseria, M. A. Robb, J. R. Cheeseman, J. A. Montgomery, T. Vreven, K. N. Kudin, J. C. Burant, J. M. Millam, S. S. Iyengar, J. Tomasi, V. Barone, B. Mennucci, M. Cossi, G. Scalmani, N. Rega, G. A. Petersson, H. Nakatsuji, M. Hada, M. Ehara, K. Toyota, R. Fukuda, J. Hasegawa, M. Ishida, T. Nakajima, Y. Honda, O. Kitao, H. Nakai, M. Klene, X. Li, J. E. Knox, H. P. Hratchian, J. B. Cross, V. Bakken, C. Adamo, J. Jaramillo, R. Gomperts, R. E. Stratmann, O. Yazyev, A. J. Austin, R. Cammi, C. Pomelli, J. W. Ochterski, P. Y. Ayala, K. Morokuma, G. A. Voth, P. Salvador, J. J. Dannenberg, V. G. Zakrzewski, S. Dapprich, A. D. Daniels, M. C. Strain, O. Farkas, D. K. Malick, A. D. Rabuck, K. Raghavachari, J. B. Foresman, J. V. Ortiz, Q. Cui, A. G. Baboul, S. Clifford, J. Cioslowski, B. B. Stefanov, G. Liu, A. Liashenko, P. Piskorz, I. Komaromi, R. L. Martin, D. J. Fox, T. Keith, A. Laham, C. Y. Peng, A. Nanayakkara, M. Challacombe, P. M. W. Gill, B. Johnson, W. Chen, M. W. Wong, C. Gonzalez and J. A. Pople, *Gaussian 03, Revision E.01.* (Gaussian Inc., Wallingford CT, 2004).

[9] K. A. Peterson, D. Figgen, E. Goll, H. Stoll and M. Dolg, The Journal of Chemical Physics **119** (21), 11113 (2003).

[10] D. Feller, Journal of Computational Chemistry **17** (13), 1571 (1996).

[11] K. L. Schuchardt, B. T. Didier, T. Elsethagen, L. Sun, V. Gurumoorthi, J. Chase, J. Li and T. L. Windus, Journal of Chemical Information and Modeling **47** (3), 1045 (2007).

[12] *EMSL Basis Set Exchange v1.2.2, available: https://bse.pnl.gov/bse/portal [2010, August].*

[13] R. Bruhl, J. Kapetanakis and D. Zimmermann, Journal of Chemical Physics **94** (9), 5865 (1991).

[14] D. Schwarzhans and D. Zimmermann, European Physical Journal D -- Atoms, Molecules, Clusters & Optical Physics **22** (2), 193 (2003).

[15] E. Zanger, V. Schmatloch and D. Zimmermann, Journal of Chemical Physics **88** (9), 5396 (1988).

[16] V. E. Bondybey and J. H. English, The Journal of Chemical Physics **75** (1), 492 (1981).

[17] N. Schwentner and M. Chergui, The Journal of Chemical Physics **85** (6), 3458 (1986).

[18] G. Dolivo and L. Kevan, Journal of Chemical Physics **70** (6), 2599 (1979).

[19] V. T. Davis and J. S. Thompson, Journal of Physics B: Atomic, Molecular and Optical Physics **37**, 1961 (2004).

Chapter VI

UV/Vis, Infrared and DFT study of the reactivity of matrix-isolated europium atoms with dinitrogen and carbon monoxide

VI.1 Eu/N_2

VI.1.I UV/Vis Absorption Spectroscopy

Atomic europium was successfully isolated in solid nitrogen (N_2). The bottom trace of Figure VI.1 presents the UV/Vis absorption spectrum of Eu/N_2 upon deposition. The strong y^8P state absorption of atomic Eu is evident in the 450 nm spectral region. Also present to the blue of this are the three UV absorptions arising from the spin-orbit states of the ^8P state. No emission was seen with y^8P state excitation at 450 nm. In fact, following 10 minutes of lamp irradiation all atomic features were completely removed and the absorption spectrum presented in top trace of Figure VI.1 resulted.

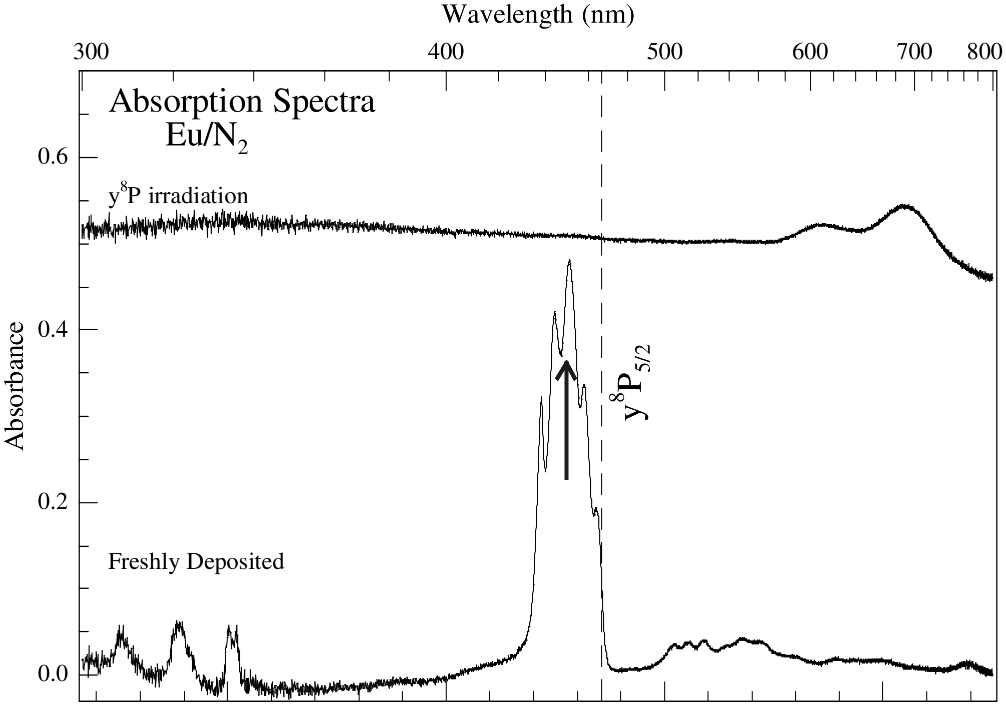

Figure VI.1 UV/Vis absorption spectra of Eu/N_2 deposited at 10 K. Bottom trace shows the absorption spectrum on deposition. The y^8P and ^8P state features of atomic Eu are evident. Top trace displays the effect of y^8P state irradiation at the wavelength indicated by the vertical arrow, all atomic features are removed and new absorptions at 609 and 690 nm are observed.

Evident in this spectrum following y^8P state irradiation, is the appearance of a new broad absorption band appearing as a doublet with features at 609 and 690 nm. Excitation of these new features yielded no observable emission.

Europium atoms appear to react with the surrounding dinitrogen matrix during irradiation. A higher temperature deposition at 13.5 K showed this reactivity to be temperature dependent. Fewer atoms are isolated, and some product absorption features are observed at 690 nm upon deposition as displayed in top trace of Figure VI.2. This indicates the europium-dinitrogen species can react thermally.

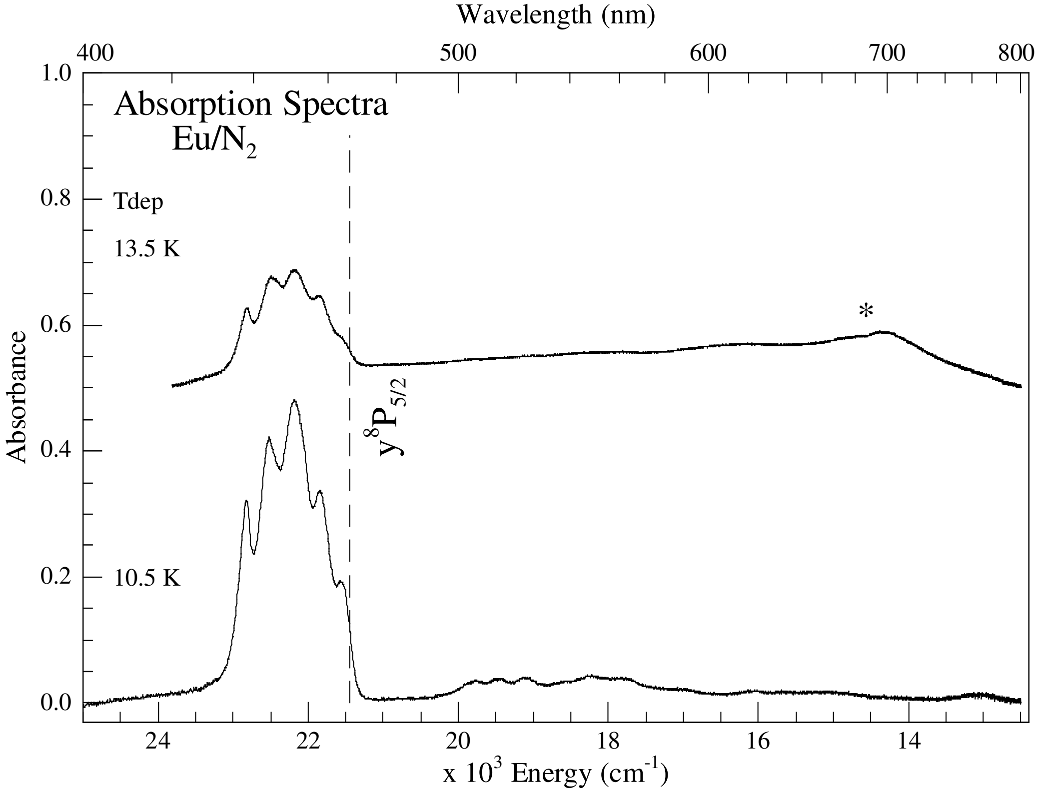

Figure VI.2 Visible absorption spectra of europium isolated in neat N_2 matrices deposited at 10.5 K (bottom trace) and 13.5 K (top trace). Some weak absorption features relating to the product are observed in the 690 nm region in the top trace and are highlighted by an asterisks.

To probe the reasons for europium atom removal during irradiation, a UV/Vis guest N_2 concentration study in Ar matrices was performed and is presented in Figure VI.3. The top trace displays the absorption spectrum of a Eu/Ar sample. The bottom trace presents the absorption spectra before and after irradiation of a neat N_2 matrix as seen in Figure VI.1 earlier. The interlying traces show the absorption spectra in samples with 1.0 and 0.1 % host nitrogen concentrations. Clearly at 100 % N_2 all Eu is removed by irradiation suggesting the guest is reacting photochemically with the surrounding matrix. At lower N_2 concentrations Eu atoms are only partially removed upon y^8P state irradiation. Fewer guest atoms neighbour a N_2 molecule thus not all Eu can react such that some atomic features remain. In order to investigate this further, infrared absorption spectra of Eu/N_2 were recorded monitoring of the N-N stretching mode of dinitrogen.

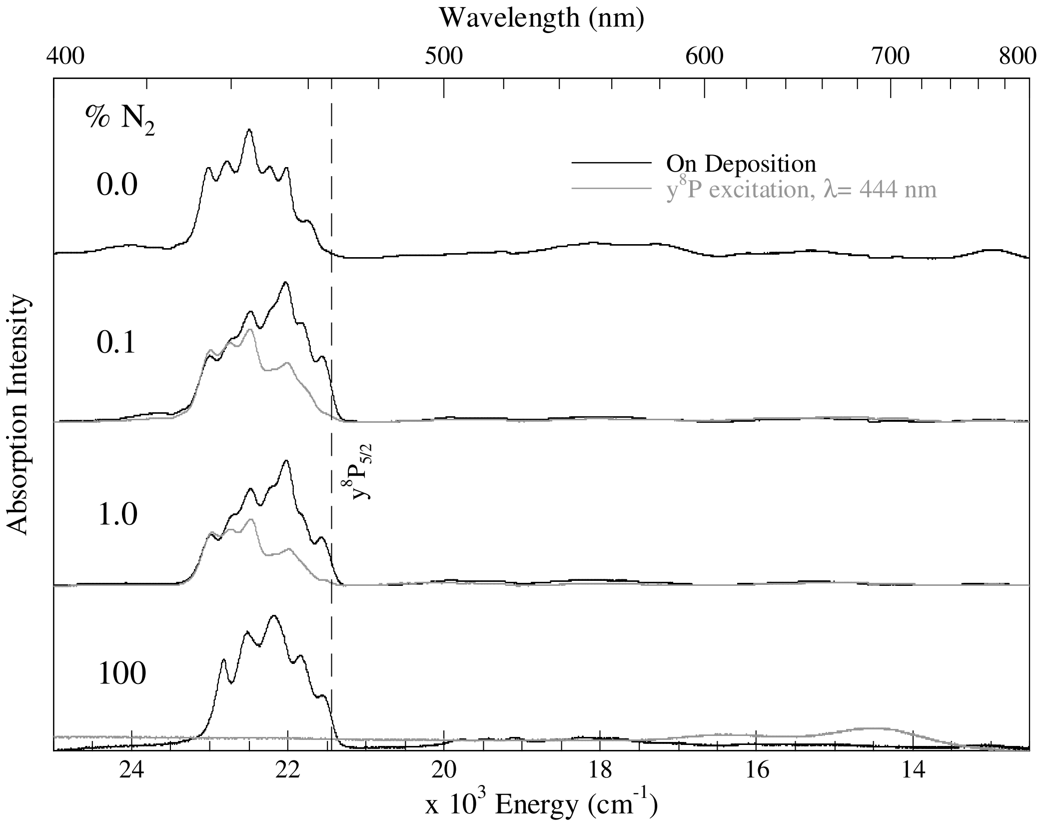

Figure VI.3 UV/Vis absorption spectra of atomic Eu co-deposited with various concentrations of N_2 in Ar. Spectra are displayed on deposition and following y^8P state irradiation.

VI.1.II Infrared Absorption Spectroscopy

The infrared absorption spectrum of a freshly deposited europium in pure N_2 sample in the region of the N-N stretch is presented in Figure VI.4. Numerous complicated absorption features are observed. A weak feature is seen at 1347 cm^{-1}, a range of features occur in the 1550 to 1850 cm^{-1} region as well as a band centred at 1892 cm^{-1}. Also evident are multiple broad absorptions centred around 2200 cm^{-1}.

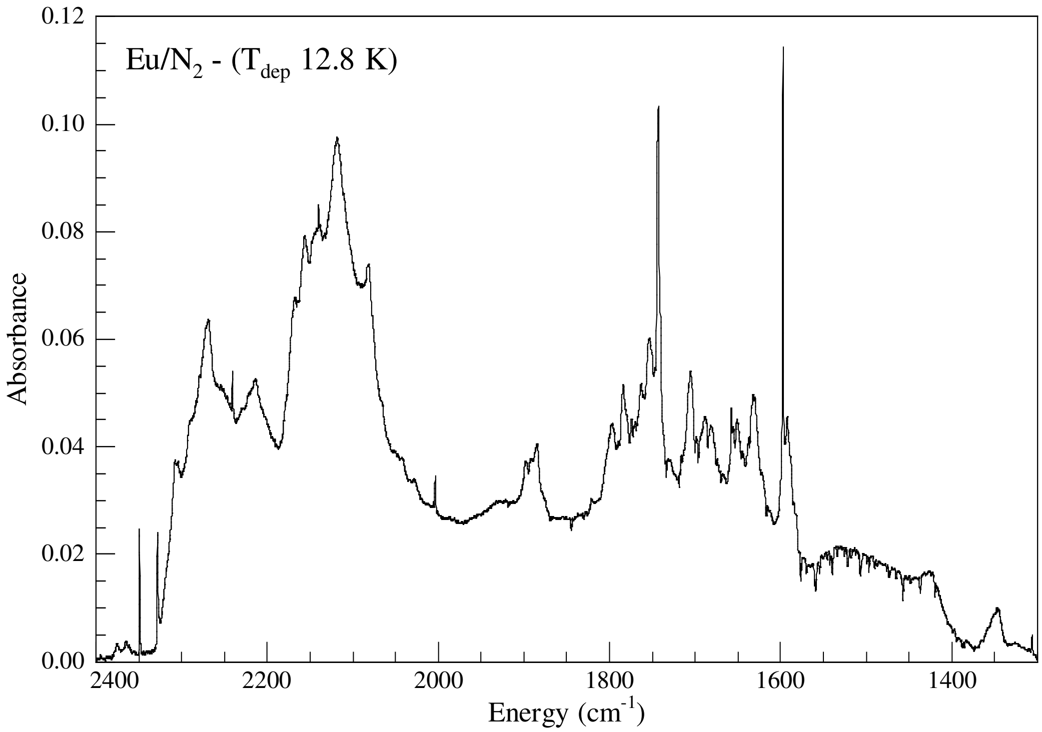

Figure VI.4 Infrared absorption spectrum of Eu in a 100 % N_2 host lattice on deposition.

The bottom and middle traces of Figure VI.5 display the IR absorption spectra recorded before and after y^8P state irradiation. Little change is evident but the normalised difference spectrum displayed in the top trace of Figure VI.5 allowed accurate identification of features undergoing growth during irradiation. The band at 1347 cm^{-1} is seen to increase slightly. In the 1550 to 1850 cm^{-1} region six features at 1592, 1631, 1742, 1755, 1784 and 1798 cm^{-1} show growth. The greatest increase is observed for the absorption centred at 2117 cm^{-1} while further to the blue of this a triplet absorption centred at 2291 cm^{-1} also becomes enhanced. These spectra are complex, containing multiple features. In order to simplify this study, samples were deposited at lower concentrations of N_2.

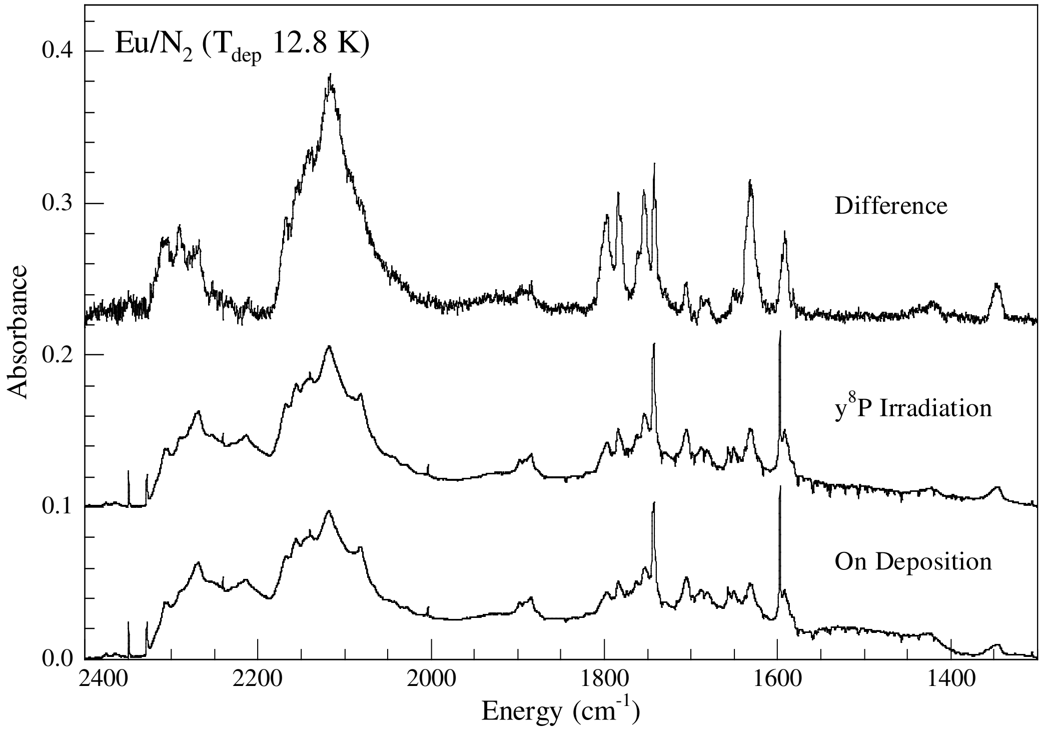

Figure VI.5 Bottom trace displays the IR absorption spectrum of Eu in a 100 % N_2 host lattice on deposition. Middle trace displays the absorption spectrum following y^8P state irradiation. Top trace presents a normalised difference spectrum highlighting the features which increase during irradiation.

Figure VI.6 shows the absorption spectra of europium in a host of 10% N_2 in Ar recorded at hourly intervals during deposition. Two intense features centred at 2102 and 1739 cm^{-1} are identified increasing over time. Also identifiable in the top trace after a four hour deposition is a weak feature at 1601 cm^{-1} which pertains to matrix-isolated water in the sample. There is also evidence of a broad band centred at 1785 cm^{-1} which is seen more clearly in Figure VI.7. The bottom trace of Figure VI.7 presents the absorption spectrum of a fresh sample after a four hour deposition. The absorption spectrum following y^8P state irradiation is shown in the top trace. The 2102 cm^{-1} feature increases significantly during irradiation.

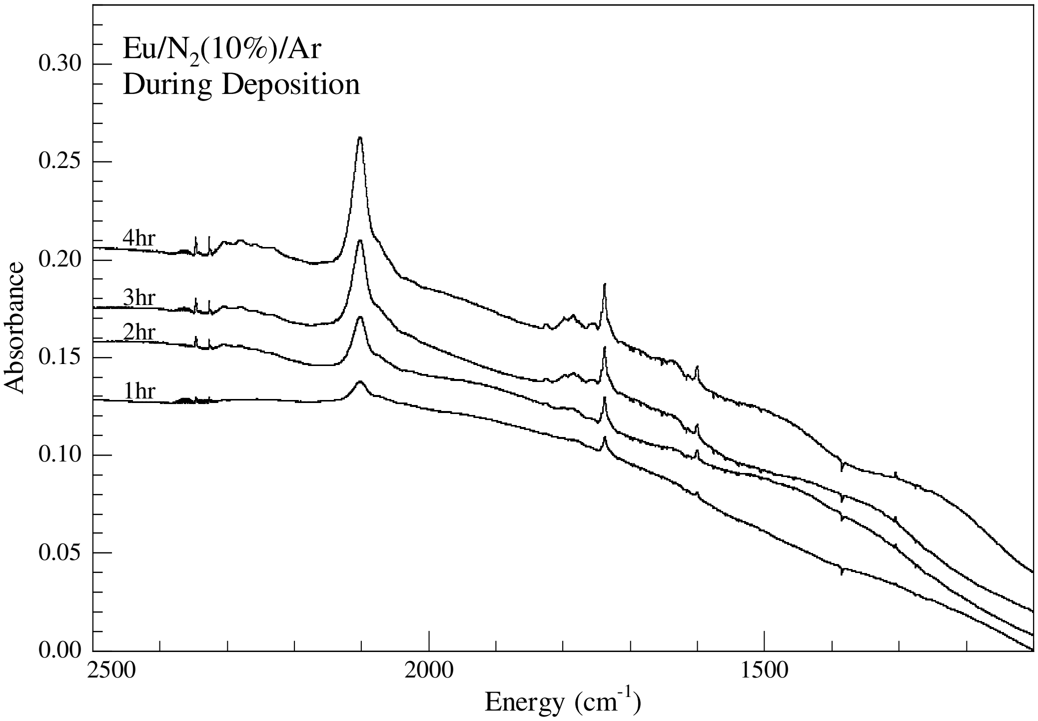

Figure VI.6 IR absorption spectra of Eu in a 10 % N_2 in Ar host recorded at hourly intervals during a four hour deposition.

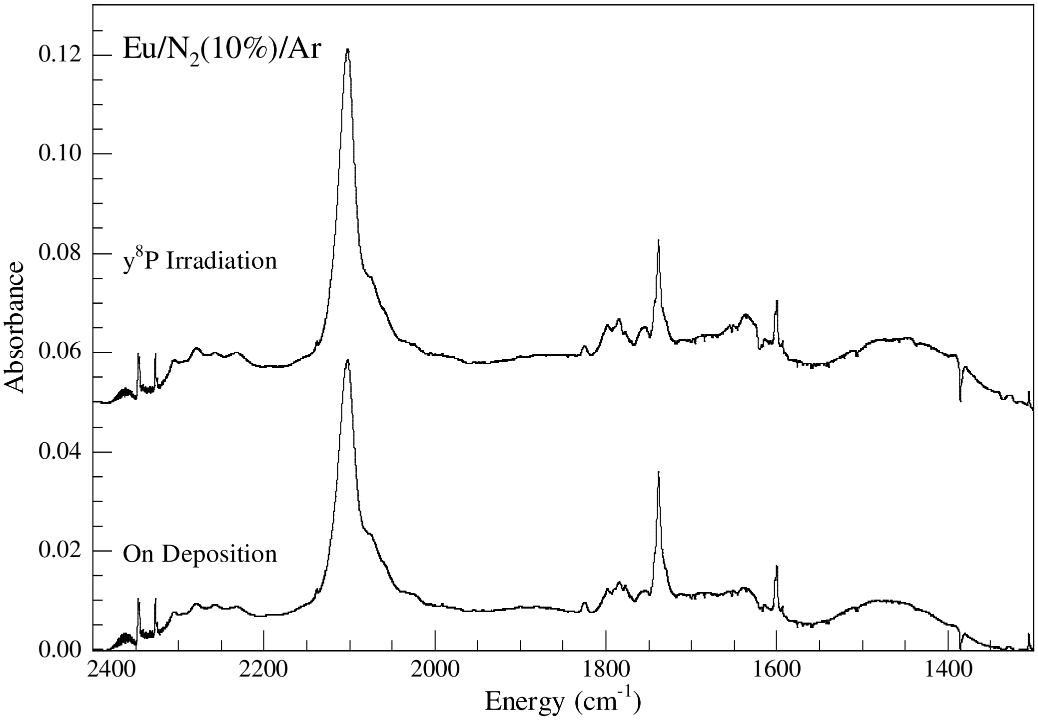

Figure VI.7 Bottom trace displays the IR absorption spectrum of Eu in a 10 % N_2 in Ar host lattice on deposition. Top trace displays the absorption spectrum following y^8P state irradiation. The feature at 2102 cm^{-1} increases during irradiation.

The absorption spectra were greatly simplified by decreasing the concentration of N_2 in the host from 100 % to 10 %. Figure VI.8 now presents absorption spectra at the lower concentration of 5 % N_2 in Ar. On deposition four features are observed at 2103, 1824.3, 1786 and 1739 cm^{-1} and a 1601 cm^{-1} water band. Irradiation greatly increased the feature at 2103 cm^{-1} as seen in top trace of Figure VI.8. The bands at 1824.3 and 1739 cm^{-1} are both decreased during irradiation coupled with a slight increase of the feature at 1786 cm^{-1}.

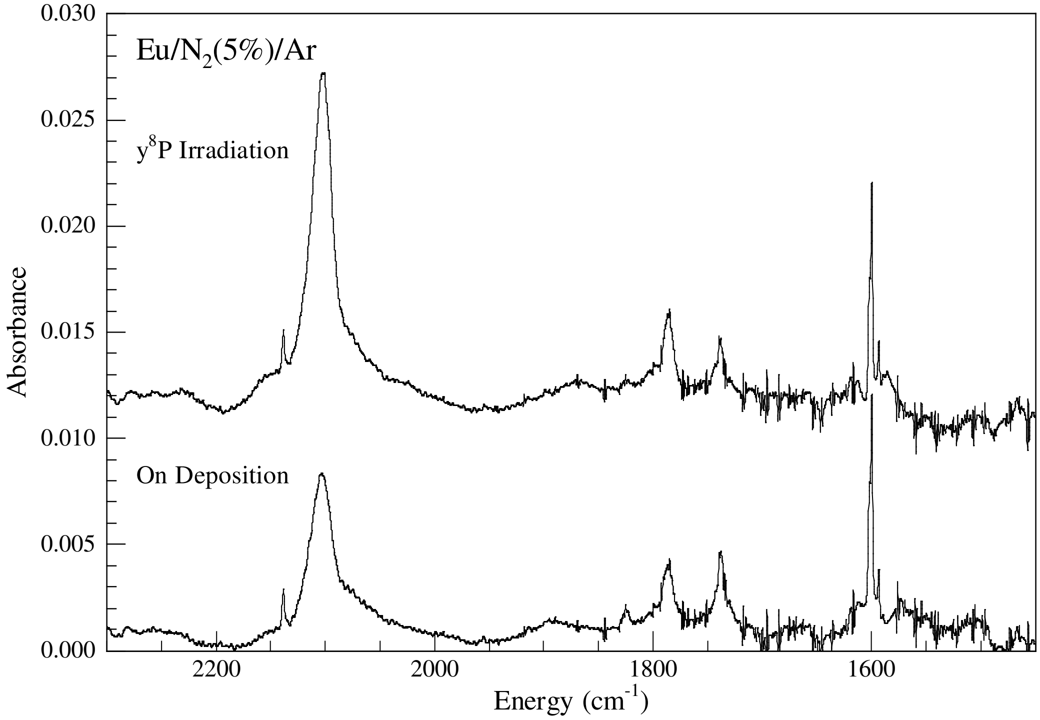

Figure VI.8 Bottom trace displays the IR absorption spectrum of Eu in a 5 % N_2 in Ar host lattice on deposition. Top trace displays the absorption spectrum following y^8P state irradiation.

An even lower concentration sample of 2.5 % N_2 in Ar was then investigated. The same spectral features are observed. However, in this case the relative intensities change considerably. The bottom trace of Figure VI.9 presents the absorption spectrum recorded on deposition. The bands identified at 2103, 1824.3, 1787.5 and 1739 cm^{-1} are observed as before, however the 1787.5 cm^{-1} band is now the most intense. The absorption spectrum produced following y^8P state excitation is present in the middle trace of Figure VI.9. An increase of the 2103 and 1787.5 cm^{-1} bands occurs but notably the 1787.5 cm^{-1} feature remains the most intense.

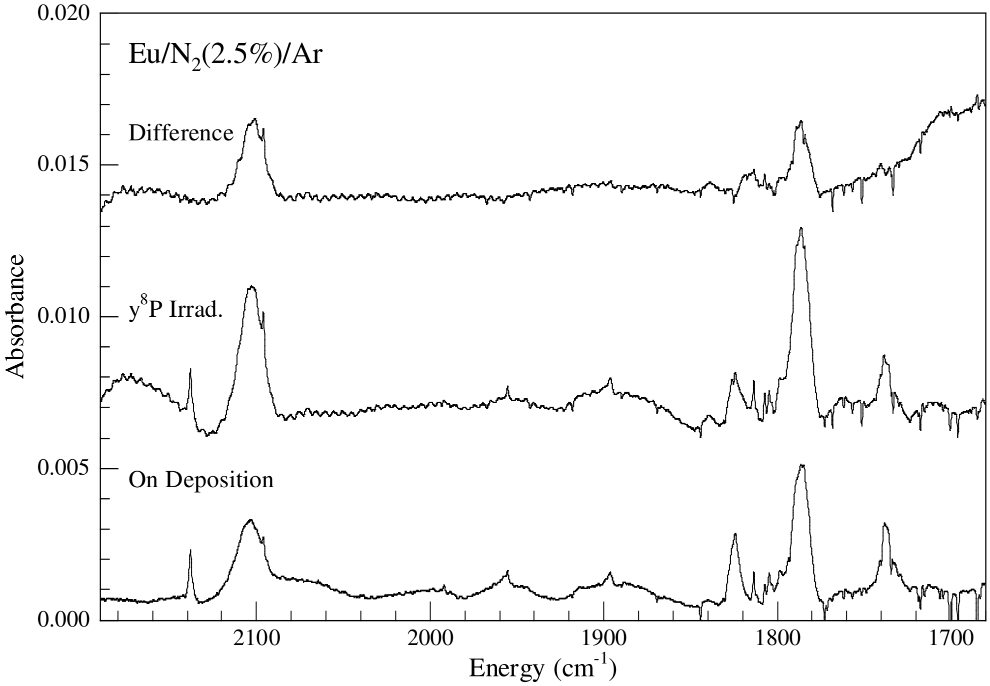

Figure VI.9 Bottom trace displays the IR absorption spectrum of Eu in a 2.5 % N_2 in Ar host lattice on deposition. Middle trace displays the absorption spectrum following y^8P state irradiation. Top trace presents the difference spectrum highlighting the features at 2102 and 1787.5 cm^{-1} which increase during irradiation.

The final concentration studied was a host of 1 % N_2 in Ar. The absorption spectrum recorded of this sample upon deposition is shown in top trace of Figure VI.10. The features at 1824.3 and 1787.5 cm^{-1} are again identifiable, and as in the 2.5 % sample the 1787.5 cm^{-1} band is most intense and increases during irradiation. The 2103 and 1739 cm^{-1} bands are almost completely absent at these low concentrations. The bottom traces of Figure VI.10 overlaps the absorption spectra in samples of 10 %, 5 % and 2.5 % host nitrogen concentrations, scaled to the 2103 cm^{-1} feature. Clearly as nitrogen host concentration is decreased the 1787.5 and 1824.3 cm^{-1} bands become much more prominent relative to the 2103 cm^{-1} band. Also of note is that the relative intensity of the 2103 and 1739 cm^{-1} bands remains constant at all concentrations implying there is a relationship between these features.

A plot of the absolute absorption intensities of these features in hosts of various concentrations is displayed in Figure VI.11. As the N_2 concentration is decreased, the absorption strengths become very weak. With higher amounts of N_2 the 2103/1739 cm^{-1} pair dominate the spectrum while at concentrations lower than 2.5 % the 1787.5 cm^{-1} band is most intense. Also present at all concentrations is the 1824.3 cm^{-1} feature.

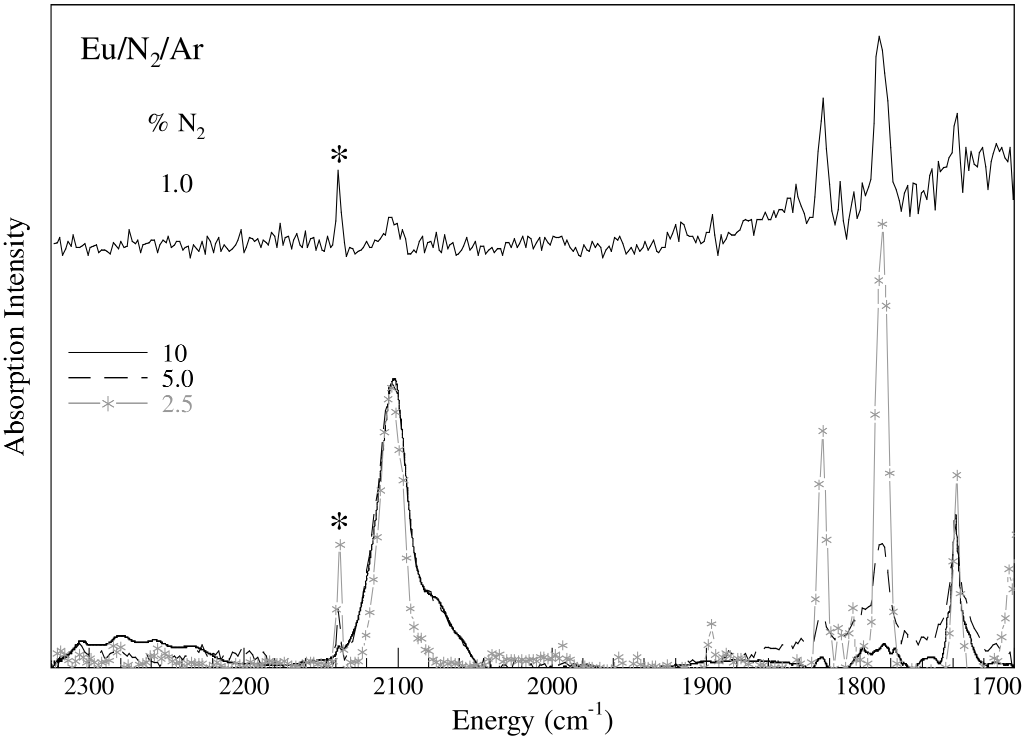

Figure VI.10 Top trace displays the IR absorption spectrum of Eu in a 1 % N$_2$/Ar host lattice on deposition. Bottom traces displays the absorption spectra in this region in samples of 10, 5 and 2.5 % N$_2$ in Ar scaled to the feature at 2103 cm^{-1}. The sharp absorption at 2138 cm^{-1} highlighted by the asterisks relates to a minimum amount of matrix-isolated CO contaminants in the sample[1].

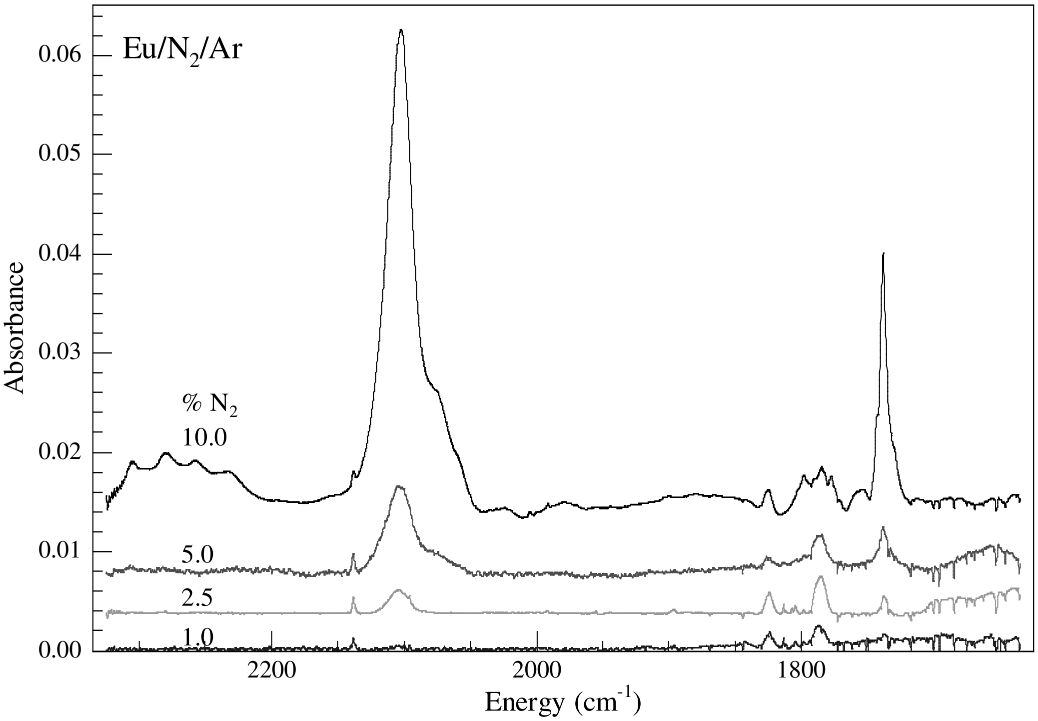

Figure VI.11 IR absorption spectra of Eu in matrices of various amounts of N$_2$ in Ar, displaying the absolute absorption strengths of each feature.

VI.1.III Eu/N_2 Absorption Summary

In summary, UV/Vis absorption spectra showed atomic Eu was successfully isolated in nitrogen matrices on deposition. Irradiation of these samples removed all UV/Vis atomic features and produced two broad absorptions at 609 and 690 nm. Infrared absorption spectra of Eu in pure N_2 host matrices yielded complex spectral features in the 1300 to 2400 cm^{-1} region. These features were simplified and resolved in hosts of decreasing amounts of N_2. Four absorptions remained, a pair at 2103 and 1739 cm^{-1}, a band at 1824.3 cm^{-1} and a final band at 1787.5 cm^{-1} which becomes the most prominent feature in lower concentration samples.

VI.2 Eu/CO

VI.2.I UV/Vis Absorption Spectroscopy

The UV/Vis and IR absorption spectra of matrix-isolated atomic europium in solid nitrogen were presented in the preceding sections. The following section concerns a study of Eu in carbon monoxide (CO) matrices. CO was chosen as it is iso-electronic to nitrogen and so allows a useful comparative study. Bottom trace of Figure VI.12 displays the UV/Vis absorption spectra of a Eu/CO sample deposited at 13 K. There is no evidence of any atomic features, only a broad absorption centred at 530 nm is observed. y^8P state irradiation at 450 nm causes little change in the absorption spectrum and excitation of the absorption band at 530 nm produces no observable emission.

It seems in the case of the more reactive CO molecule all guest Eu atoms have reacted with the host upon deposition. A study of the effects of concentration of CO in the host is presented in Figure VI.13. The top trace shows a Eu/Ar absorption spectrum, while the bottom trace displays Eu in a 100 % CO host. The interlying traces present samples deposited with 1.0 and 0.1 % CO in solid Ar. In both cases atomic Eu is isolated on deposition with the y^8P state absorption centred at 448 nm. In the case of 1.0 % CO in Ar, almost all guest atoms are removed by y^8P state irradiation. In contrast to this, isolation in a host of 0.1 % CO removed limited amounts of the atomic features due to there being less likelihood of the guest atom neighbouring a CO molecule at these low concentrations. In order to investigate the reactivity further, absorption spectra monitoring the C-O stretch in the infrared region were recorded and are presented hereafter.

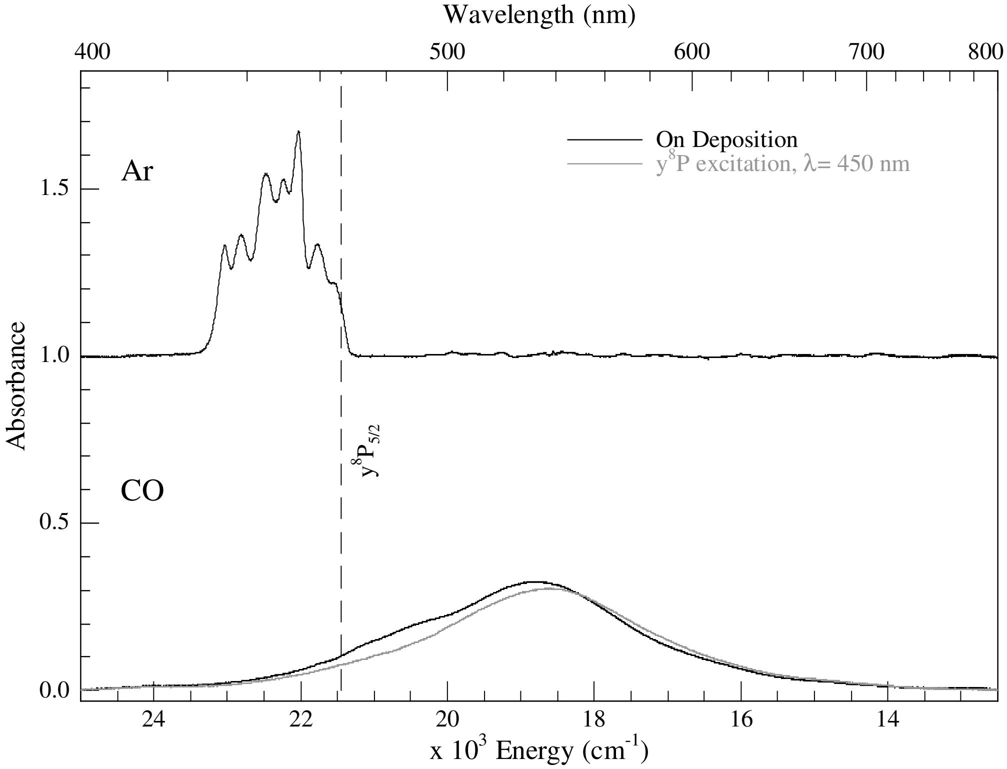

Figure VI.12 UV/Vis absorption spectra of Eu/CO and Eu/Ar. The gas phase position of the y^8P state is identified by the dashed vertical line.

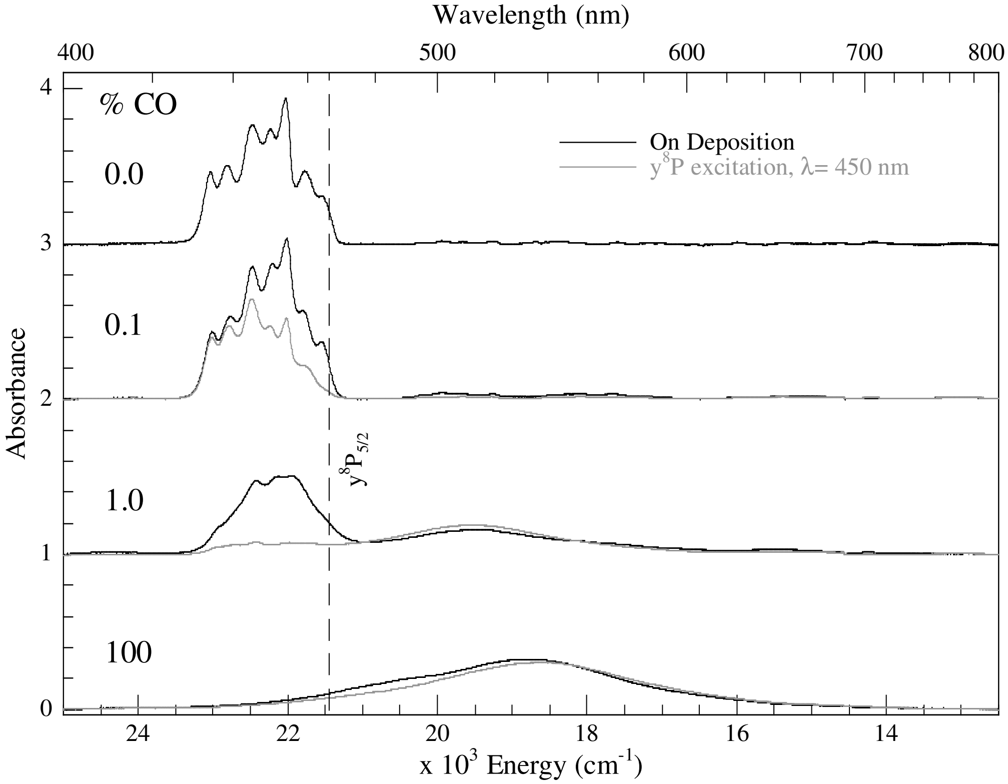

Figure VI.13 UV/Vis absorption spectra of atomic Eu co-deposited with various concentrations of CO in Ar. Spectra are displayed on deposition and following y^8P state irradiation.

VI.2.II Infrared Absorption Spectroscopy

The bottom trace of Figure VI.14 presents the IR absorption spectrum of atomic Eu isolated in a host consisting of 10% CO in Ar. The high energy side of this spectrum is cut to exclude the free CO vibration which saturates centred at 2138 cm^{-1}. The most intense band is at 1999 cm^{-1} with a shoulder evident to either side of it at 1969 and 2011 cm^{-1}. A weaker band to higher energy is observed at 2029 cm^{-1}. Also evident is a quite intense feature at 1895 cm^{-1} neighboured by a weak band at 1855 cm^{-1}. To lower energy of this there is a weak feature at 1601 cm^{-1} pertaining to matrix-isolated water. At even lower frequency there is band of very weak intensity centred at 1508.7 cm^{-1}. The middle trace of Figure VI.14 shows the effect of y^8P state irradiation in which the weak 1508.7 cm^{-1} feature increases slightly. The difference spectrum on the top trace of Figure VI.14 identifies the 1999 cm^{-1} band and its shoulder at 2011 cm^{-1} as the features which grow significantly during irradiation.

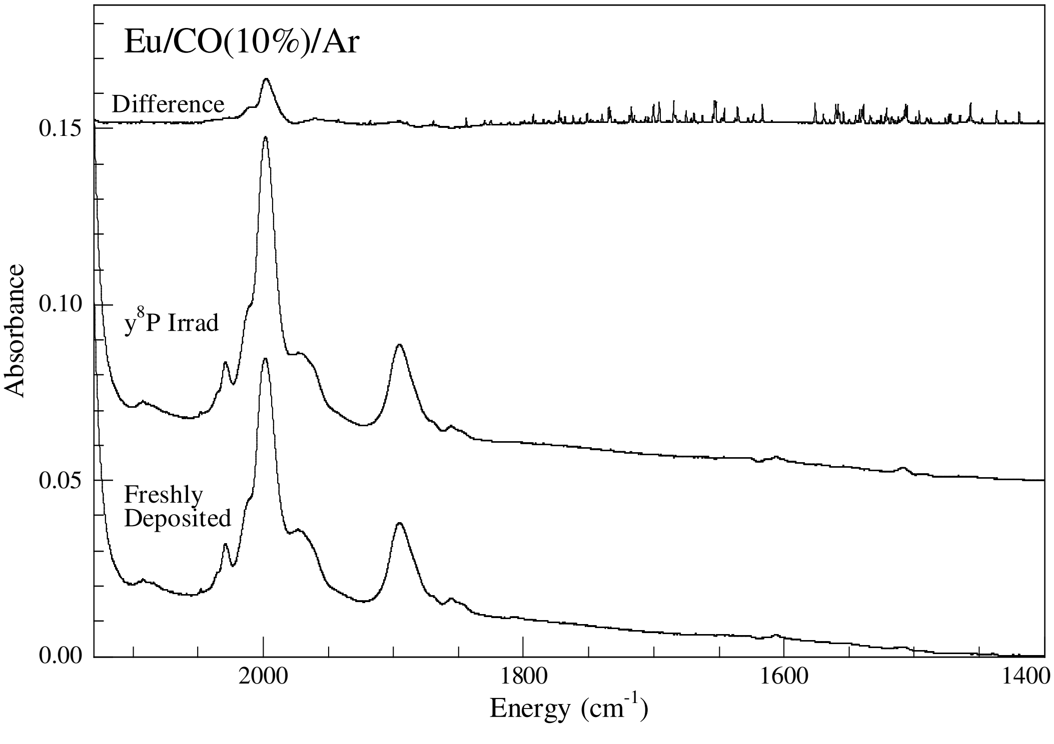

Figure VI.14 Bottom trace displays the IR absorption spectrum of Eu in a 10 % CO/Ar host lattice on deposition. Middle trace displays the absorption spectrum in this region following y^8P state irradiation. Top trace presents the difference spectrum highlighting the 1999 and 2011 cm^{-1} features which increase during irradiation. The high energy side of these spectra has been cut to remove the free CO vibration which saturates centred at 2138 cm^{-1}.

In an attempt to simplify the spectra, samples were deposited with lower host concentrations of CO. The bottom trace of Figure VI.15 presents the absorption spectrum recorded in a freshly deposited sample with a 5 % CO in Ar host. Spectral features are observed in the same location as for the 10 % sample with the only major differences being the shoulder at 1971 cm^{-1} is now more resolved and the band centred at 1895 appears broader and is centred in this case at 1890 cm^{-1}. Also of note is a new weak absorption at 1807 cm^{-1} which is not observed in the 10 % sample. The effects of irradiation are slightly different, again showing the 1999 cm^{-1} band and its shoulder at 2011 cm^{-1} increase during irradiation but so also does the 1971 cm^{-1} feature. This is coupled with a slight decrease of the 1890 cm^{-1} feature.

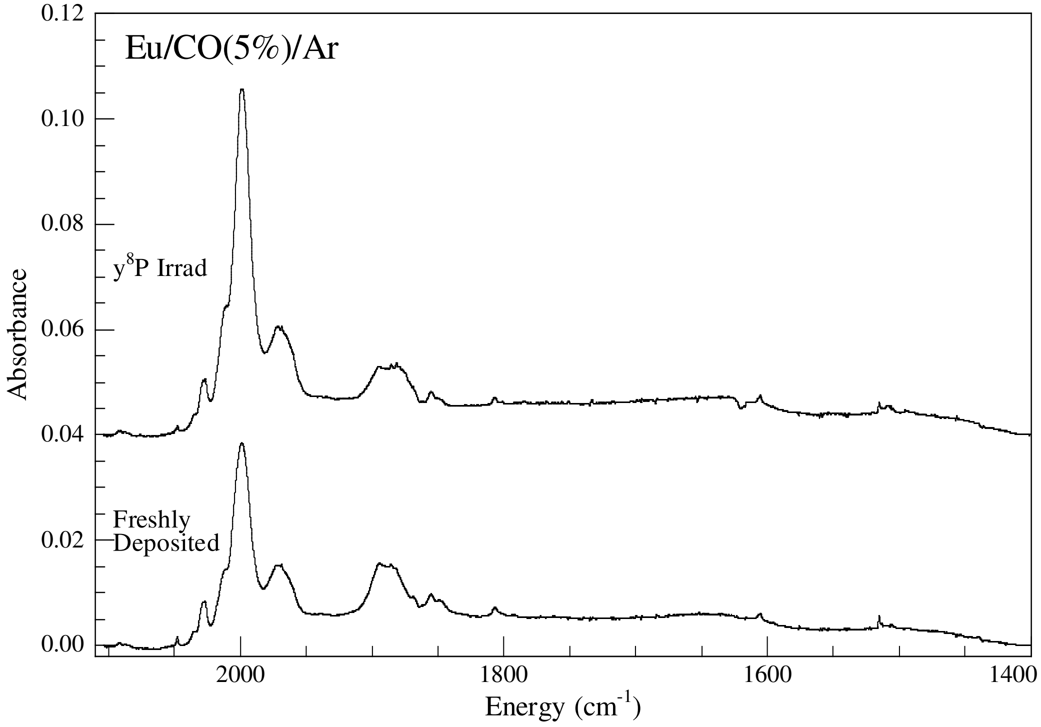

Figure VI.15 Bottom trace displays the IR absorption spectrum of Eu in a 5 % CO/Ar host lattice on deposition. Top trace shows the absorption spectrum in this region following y^8P state irradiation. The 1971, 1999 and 2011 cm^{-1} features increase during irradiation.

At the lower host concentration of 1 % CO in Ar, the infrared absorption spectrum becomes more complicated. The bottom trace of Figure VI.16 presents the spectrum of a freshly deposited sample. As for the 10 % and 5 % samples, features are identified at 2028, 2011, 1999, 1971, 1880 and 1855 cm^{-1}. However, a new feature is evident at 1864 cm^{-1} and the band at 1807 cm^{-1} is now more prominent. The middle trace of Figure VI.16 displays the absorption spectrum after y^8P state irradiation. The difference spectrum in the top trace of Figure VI.16 shows the features at 2013, 1999, 1971 and 1880 cm^{-1} are increased by the irradiation process.

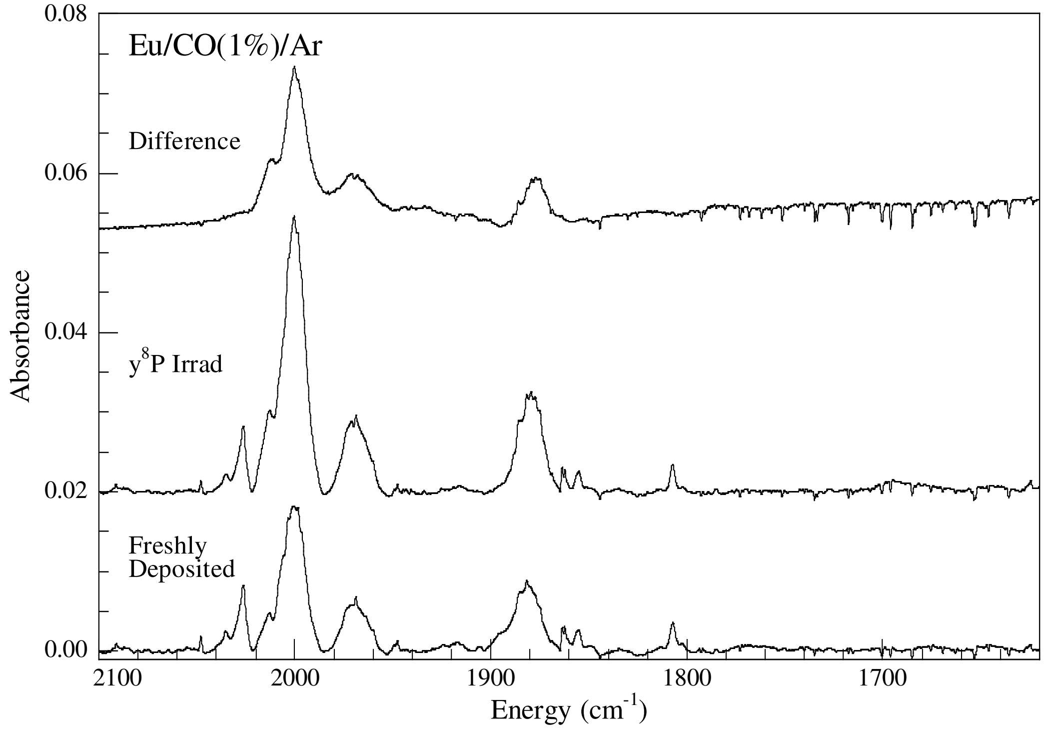

Figure VI.16 Bottom trace displays the IR absorption spectrum of Eu in a 1 % CO/Ar host lattice on deposition. The middle trace displays the absorption spectrum in this region following y^8P state irradiation. The top trace presents the difference spectrum highlighting the 1877, 1971, 1999 and 2011 cm^{-1} features which increase during irradiation.

In a final attempt to simplify the Eu/CO infrared absorption spectra, samples were formed with 0.1 % host CO concentrations. The absorption spectra before and after y^8P state irradiation are presented in Figure VI.17. Four weak absorptions are observed on deposition, located at 1854.5, 1863.6, 1896 and 1907 cm^{-1}. Irradiation simplifies the spectrum. The band at 1907 cm^{-1} is removed while there is a concurrent increase in the prominent band at 1863.6 cm^{-1} neighboured by the feature at 1854.5 cm^{-1}.

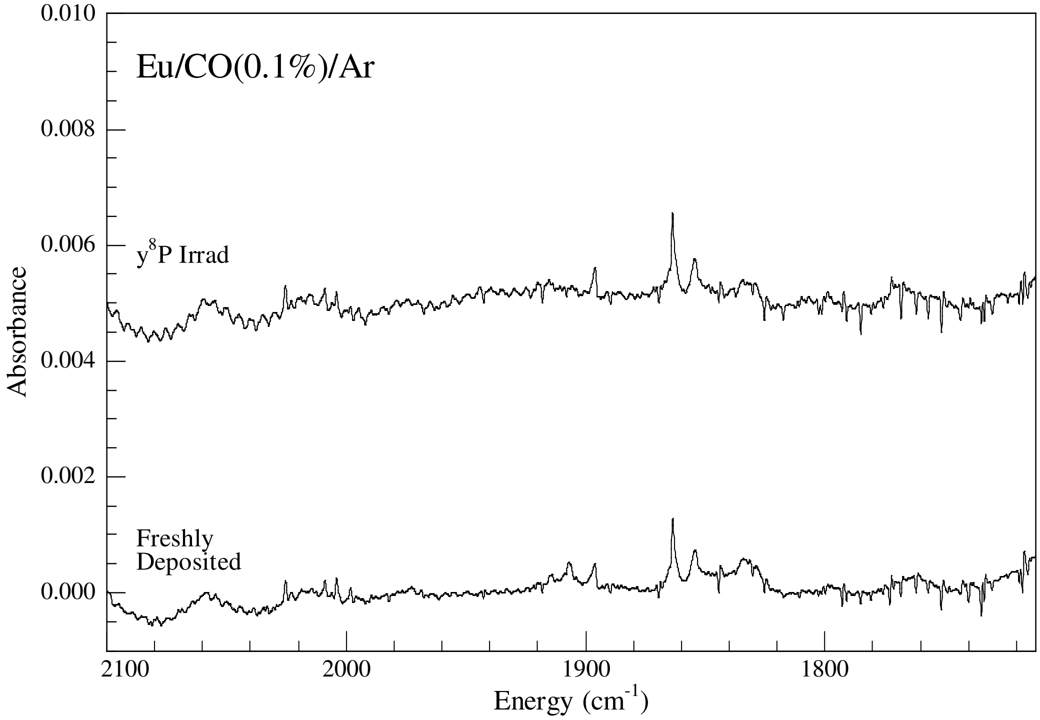

Figure VI.17 Bottom trace displays the IR absorption spectrum of Eu in a freshly deposited 0.1 % CO/Ar sample. Top trace displays the absorption spectrum in this region following y^8P state irradiation. The feature at 1863.6 cm^{-1} is most prominent following irradiation.

VI.2.III Eu/CO Absorption Summary

UV/Vis absorption spectra of Eu in 100 % CO hosts show no evidence of atomic isolation. Samples formed with lower matrix concentrations of CO in Ar allowed identification of the y^8P state absorption of Eu atoms. These atomic features could be removed by lamp irradiation of the y^8P state. A broad UV/Vis absorption band is formed centred in the 530 nm region. Infrared spectra monitoring the C-O stretching region allowed identification of bands at 2029, 2011, 1999, 1971 and 1880 cm^{-1} which increase upon irradiation. A comparison of the IR spectral features in samples of decreasing CO concentration is presented in Figure VI.18. Samples of 0.1 % CO in Ar showed the simplest spectra. Following y^8P state irradiation they yielded the formation of a dominant band at 1863.6 cm^{-1} and a weaker neighbouring absorption at 1854.5 cm^{-1}.

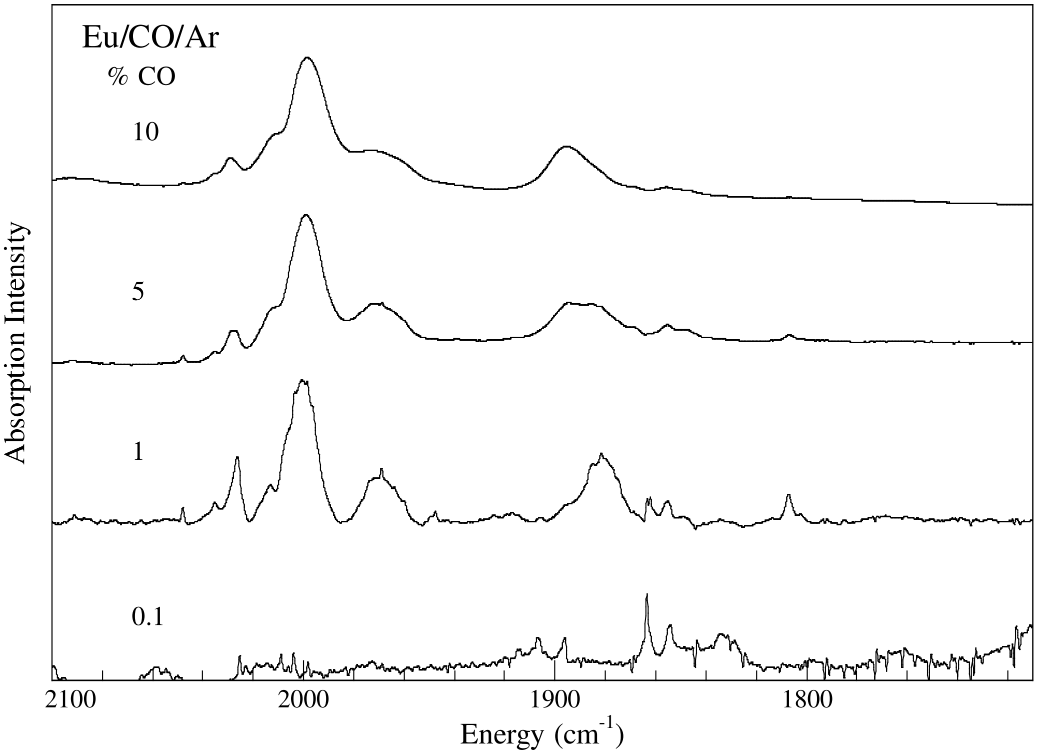

Figure VI.18 Normalised IR absorption spectra of Eu isolated in Ar matrices with various host concentrations of carbon monoxide.

VI.3 Geometry Optimisation and Vibrational Analysis

VI.3.I Introduction

In previous sections the photoreactivity of atomic Eu with both dinitrogen (N_2) and carbon monoxide (CO) was investigated. UV/Vis absorption spectra allowed identification of atomic isolation in solid N_2 which was completely removed by lamp irradiation of the y^8P state. In the case of the more reactive carbon monoxide host, all guest atoms react with CO molecules during deposition. Both these systems were investigated in the infrared spectral region monitoring the N-N and C-O stretches. IR spectra were complicated, exhibiting multiple features. However, at extremely low host concentrations simplified spectra were obtained. Two features are identified in solid nitrogen at 1787.5 and 1824.3 cm^{-1} and one major feature in CO at 1863.6 cm^{-1}. The 1:1 metal:ligand stoichiometry is expected to be most intense at these low concentrations. The following sections aim to identify and assign the geometry and vibrational frequencies of the Eu:X (X = N_2, CO) complexes by comparison of experimental spectra with counterpoise (CP) corrected DFT and MP2 calculations. In this case two fragments were considered for the CP correction, fragment one being the 'ligand' molecule (N_2 or CO) in a singlet spin state with no unpaired electrons and the second fragment is the europium atom in a high-spin dectet state leaving all valence electrons unpaired and fully available for bonding.

The basis sets used in these calculations were the Gaussian[2] pre-defined aug-cc-pVTZ basis set for the C, O and N atoms and the segmented basis set[3,4] augmented by 2pdfg diffuse functions[5] and a 28 electron core potential[4,6] (ECP28MWB) for the europium atom.

VI.3.II Eu:N_2

In order to attribute the experimentally observed IR bands at 1824.3 and 1787.5 cm^{-1}, geometry optimisation with vibrational frequency calculations were performed. There are two basic orientations of the N_2 molecule with respect to the complexed metal centre i.e., side-on bonded which is generally denoted Eu(N_2) and end-on bonded denoted as Eu(NN). The most stable geometries of both these orientations were found at the BP86, B3LYP and MP2 levels and their geometric details are presented in Figure VI.19.

A vibrational analysis of the optimised structures was performed, the results of which are presented in tabular form in Table VI.1. The BP86 method yields frequencies in closest agreement with experiment.

As a test of the three different methods used, the vibrational frequency of free nitrogen was calculated and compared to well known experimental values[1]. The results of this comparison are presented in Table VI.2. Again, the BP86 method gives results in best agreement, differing from experiment by only 0.6 %. The MP2 method underestimates the vibrational frequency by 6 % and the B3LYP method overestimates it by 5 %. The BP86 method is the technique of choice for assigning the vibrational frequencies of many transition-metal:dinitrogen systems (Fe[7], Ti[8], Zr[8], Hf[8], Sc[9], La[10], Y[10]) and also appears to be the most appropriate in this case, although overestimating vibrational frequencies by up to 100 cm^{-1} as shown in Table VI.1.

Europium dinitrogen complexes

Eu(NN)

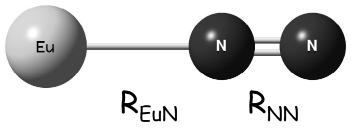

Method	R_{EuN} (Å)	R_{NN} (Å)
BP86	2.382	1.147
B3LYP	2.399	1.137
MP2	2.378	1.128

Eu(N_2)

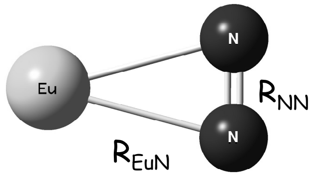

Method	R_{EuN} (Å)	R_{NN} (Å)
BP86	2.525	1.166
B3LYP	2.534	1.156
MP2	2.465	1.178

Figure VI.19 Left of figure shows the geometry optimised structures of the end-on (NN) and side-on (N_2) europium:dinitrogen complexes. Tables to the right of the structures display the calculated bond lengths of these molecules in Angstrom units performed at the BP86, B3LYP and MP2 levels with counterpoise correction.

Table VI.1 Vibrational frequencies and intensities of the vibrational modes of the end-on and side-on bound Eu:N_2 complexes calculated at the MP2, B3LYP and BP86 levels with counterpoise correction. The N-N stretch which is the focus of this study is highlighted in bold.

Eu-(N_2)	MP2		B3LYP		BP86		Experiment
	ν (cm^{-1})	Intensity	ν (cm^{-1})	Intensity	ν (cm^{-1})	Intensity	ν (cm^{-1})
End-on	**2051.6**	5371	**1955.5**	1177	**1930.6**	771.6	**1824.3**
Eu(NN)	262.9	27	260.6	0.3	252.7	0.16	
	241.2	10.4	208.6	10	206.6	3.2	
	167	1.3	160.2	0.002	151.1	0.05	
Side-on	**1733.8**	307.9	**1916.9**	435	**1861.9**	380.1	**1787.5**
Eu(N_2)	355.9	11.4	297.3	12	288.2	16.1	
	316.9	21.5	271.4	9	258.5	5	

Table VI.2 Vibrational frequencies and equilibrium bond lengths of free dinitrogen and carbon monoxide calculated at the BP86, B3LYP and MP2 levels with counterpoise correction.

	Experiment	BP86	B3LYP	MP2
N_2				
ν (cm^{-1})	**2330**[1]	**2344.4**	**2447.5**	**2186.8**
R_e (Å)	1.0977[11]	1.103	1.091	1.114
CO				
ν (cm^{-1})	**2140**[1]	**2116.8**	**2207.3**	**2109.7**
R_e (Å)	1.1283[11]	1.138	1.126	1.139

The vibrational frequencies listed in Table VI.1 are calculated using the simple harmonic oscillator method and have not been scaled to account for any anharmonic contributions. As discussed in Chapter I, molecules are described more realistically using the anharmonic oscillator model. When an anharmonic frequency analysis is performed using the BP86 method for both the side-on and end-on geometries, the vibrations become closer in agreement to experiment as shown in Table VI.3 and displayed graphically in the right panel of Figure VI.20. The energy spacing of 36.8 cm^{-1} between the two vibrations is now exactly the same as the spacing between the experimental bands. There is near perfect agreement with the experimental spectrum when a shift of 49 cm^{-1} and a linewidth of 3.3 cm^{-1} (fwhm) is considered. This can be seen clearly in Figure VI.21.

Table VI.3 Anharmonic vibrational frequencies of the N-N stretch of the end-on and side-on bound europium:dinitrogen complexes calculated at the BP86 level with counterpoise correction. δ represents the difference in energy between the vibrational bands of each orientation in wavenumber units.

	BP86 anharmonic frequency of N-N stretch		Experiment
	ν (cm^{-1})	Intensity	ν (cm^{-1})
End-on Eu(NN)	1874.6	771.6	1824.3
Side-on Eu(N_2)	1837.7	380.1	1787.5
δ (cm^{-1})	36.9	-	36.8

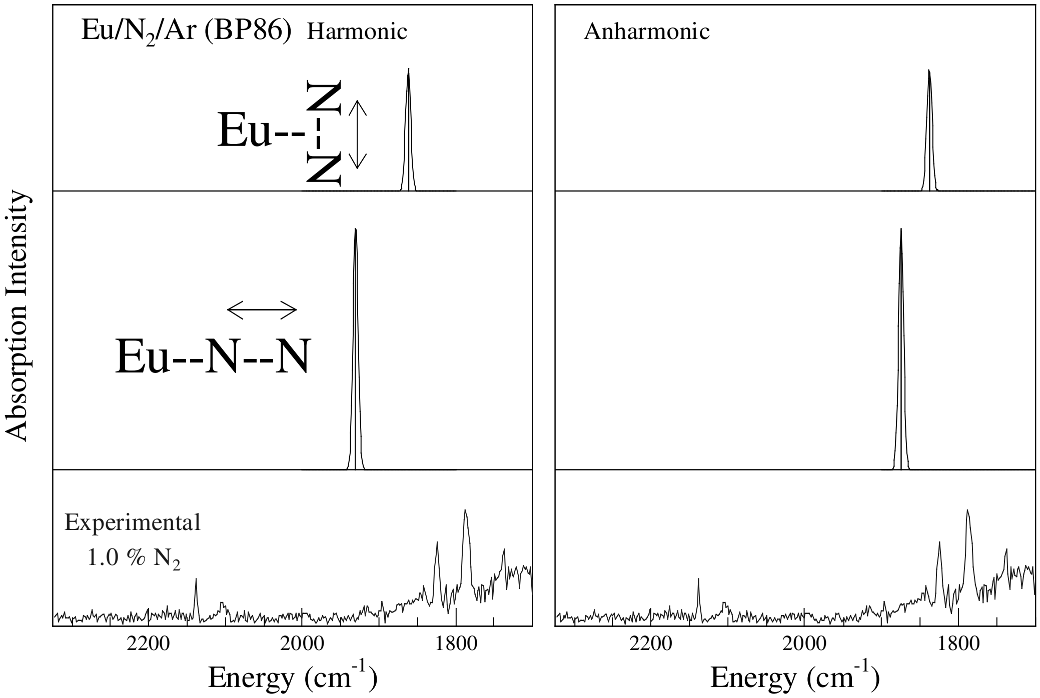

Figure VI.20 Calculated IR absorption spectra of the end-on (NN) and side-on (N_2) bound europium:dinitrogen complexes. Calculations were performed at the BP86 level with counterpoise correction. Left panel displays the calculated harmonic frequencies. Right panel presents the vibrational frequencies calculated using the anharmonic technique. The calculated spectra are plotted with their predicted relative intensities. The experimental IR absorption spectrum in this region in a 1% N_2 in Ar host is seen in the bottom traces.

A contributing factor for this overestimation of the vibrational frequency may be due to matrix shifts, which lower the energy of the absorptions in the solid state. For example, the binary transition metal carbonyls of manganese and iron show respective shifts of 21.4 and 24.5 cm^{-1} to lower energy in solid Ar compared to the gas phase[12]. An Ar matrix shift of this magnitude for the Eu:N_2 system would imply the BP86 calculations overestimate the solid state by only 25 cm^{-1}.

The disparity between the experimental and predicted vibrational frequencies could be investigated by studying the europium:dinitrogen species in other RG matrices. Monitoring the Eu:N_2 vibrational bands isolated in hosts such as Ne, Kr and Xe would allow identification of the effect of the surrounding lattice. The least polarisable Ne host would be expected to yield vibrational frequencies in closest agreement with the predicted gas phase values.

When the experimental spectrum of Eu:N_2 in Ar is overlaid with the end-on Eu(NN) and side-on (N_2) calculated anharmonic BP86 spectra shifted by 49 cm^{-1} there is excellent agreement, as displayed in Figure VI.21. The band observed at 1787.5 cm^{-1} in the most dilute host samples corresponds to the dinitrogen stretch of a side-on orientated complex and the N-N stretch of a end-on bound Eu(NN) complex occurs in the matrix at 1824.3 cm^{-1}.

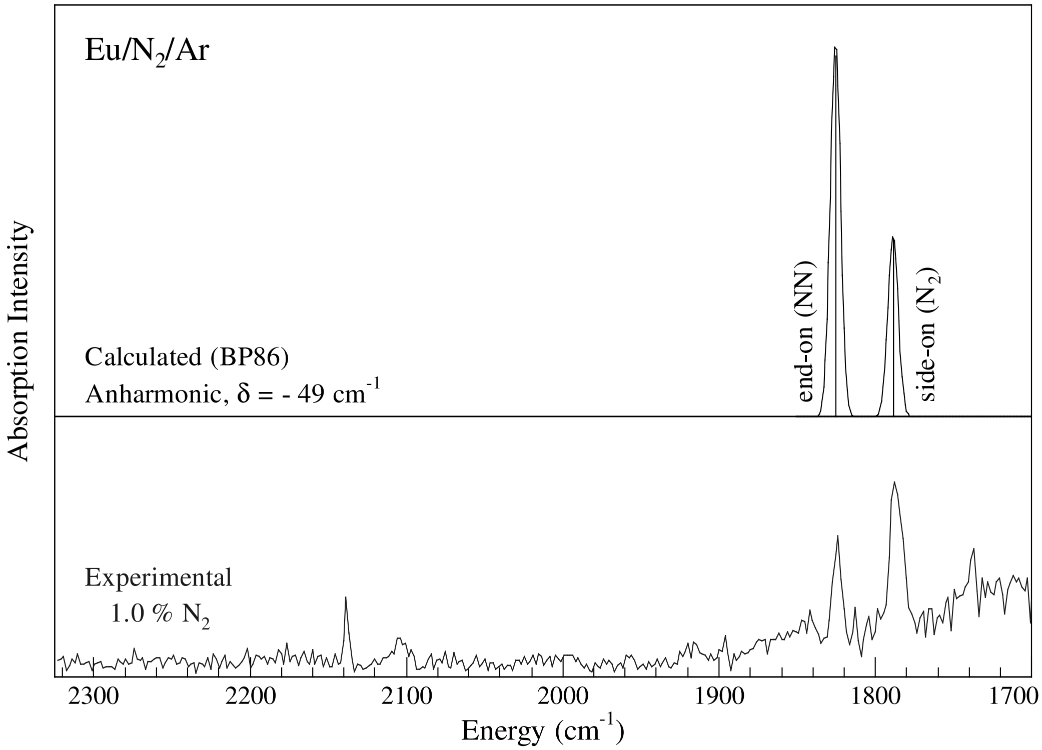

Figure VI.21 Bottom trace displays the experimental spectrum of Eu in a 1.0 % N_2/Ar sample in the region of the N-N stretch. Top trace exhibits the excellent agreement between the BP86 anharmonic calculated end-on, Eu(NN), and side-on, Eu(N_2) IR spectra and the experimental data when a shift of 49 cm^{-1} and linewidth of 3.3 cm^{-1} (fwhm) is employed. The BP86 spectral bands are plotted with their calculated relative intensities.

A previous matrix infrared study[13] of the reaction products of laser-ablated europium with dinitrogen was carried out in 1998. This investigation was complicated by the laser ablation method used to form the metal vapour, as not only M:N_2 complexes were created but so also were metal nitrides caused by the large number of metal ions produced during vaporisation. Thus the spectra were complex, with additional metal nitride features. The current study allowed simplification of this system as the electron bombardment technique forms little to no metal ions, yielding only metal atom:dinitrogen complexes. The possibility of large amounts of nitrides in samples can be ignored. It is difficult to make a direct comparison between the current work and the 1998 study as no experimental spectrum of the Eu:N_2 system was presented in the previous work, the spectral bands were simply listed in a table. The 1998 study did not perform any calculations to compare with experimental spectra. Isotopic substitution data was the only method employed in an attempt to make band assignments. The band identified in this study at 1787.5 cm^{-1} in 1 % N_2 in solid Ar was also observed in the previous study in a matrix of 2 - 4 % nitrogen in argon. In agreement with our BP86 calculations, it was assigned as corresponding to the side-on bonded dinitrogen complex.

With the experimental spectral features confidently assigned, the calculated relative intensities of the vibrational bands are used to postulate an estimate of the relative population of each geometry in the experimental matrix sample. It should be noted that the accuracy of the predicted intensities are known to be significantly sensitive to basis set and computational method and do not generally agree with observations better than ± 30 %. In order to ascertain some measure of their accuracy in this case, a detailed study of well-known metal bound dinitrogen systems would be needed to compare predicted intensities with known experimental observations. In any case, a rudimentary estimate of the relative population of each geometry in the experimental matrix sample is made here using the predicted intensities.

From Table VI.3 their <u>predicted relative intensities</u> are

Eu(NN), end : Eu(N_2), side
771 : 380
2 : 1

i.e. the N-N stretch of the end-on oriented complex is approximately twice as intense as the side-on species.

<u>Experimentally</u> they are observed in the following ratio
Eu(NN), end (1824.3 cm^{-1}) : Eu(N_2), side (1787.5 cm^{-1})
0.78 : 1

Considering the end-on species is in the region of two times more intense than the side-on complex, the population ratio in the matrix sample is estimated to be

(0.78/2) : 1
0.39 : 1
i.e. 1 : 2.6 ± 0.9 [assuming an error of ± 30 %]

That is to say, for each end-on bonded molecule in the sample there are 2.6 (± 0.9) side-on species. The side-on Eu(N_2) complex dominates.

This is supported by the energies of each of these different orientations, which are compared in Table VI.4. The equilibrium dissociation energy (De), defined as the minimum of the potential well, with respect to the free europium and free N_2 species, shows the side-on complex is 862 cm^{-1} lower in energy.

Table VI.4 The equilibrium dissociation energy (De) of the end-on and side-on bound europium:dinitrogen complexes, with respect to the free europium and free N_2 species, calculated at the BP86 level with counterpoise correction. δ displays the difference in energy between each orientation.

BP86	De (cm^{-1})
Eu(NN) end	7,983
Eu(N_2) side	8,845
δ (cm^{-1})	862

In summary, two absorption features in samples of Eu in 1 % N_2 in Ar are assigned as pertaining to the 1:1 europium:dinitrogen complexes in side-on and end-on orientations based on comparison to a BP86 DFT vibrational frequency analysis. The BP86 method yields excellent results for the vibrational analysis of the europium:dinitrogen complex. The assigned vibrations involve shifts in the region of 500 cm^{-1} to lower energy compared to free dinitrogen (2330 cm^{-1}). Shifts of this magnitude suggest significant N-N bond lengthening in the complex. The geometry optimised structures of Figure VI.19 calculate the N-N bond length to increase by 0.063 and 0.044 Angstrom in the side-on and end-on orientations respectively. One might expect the N-N bond to increase more than this, given the large red shift in vibrational frequency compared to free N_2. However this is not the case, suggesting the BP86 method may not fully account for all interactions in the europium:dinitrogen complex.

In any case, the BP86 vibrational frequency analysis, which has been used successfully for many transition metal:dinitrogen systems, allowed the two absorption features in samples of Eu in 1 % N_2 in Ar observed at 1787.5 and 1824.3 cm^{-1} to be assigned. They pertain to the N-N stretch of the 1:1 europium:dinitrogen complexes in side-on and end-on orientations respectively. The side-on species is calculated to be 862 cm^{-1} lower in energy and exhibits a dominance over the end-on species in matrix samples.

VI.3.III Eu:CO

A matrix infrared study of europium carbonyls was performed previously[14] in 1973. An absorption spectrum in a 2 % CO in Ar host showed qualitatively the same bands as seen in the 1 % sample formed in this study in Figure VI.16. The bands at 2000, 1974, 1968 and 1873 cm^{-1} were assigned as corresponding to $Eu(CO)_6$, $Eu(CO)_5$, $Eu(CO)_4$ and $Eu(CO)_2$ respectively. Weaker bands at 1863.6 and 1854.5 cm^{-1}, which were not identified in the past, are observed in the current work. The $Eu(CO)_1$ complex was not identified previously due to the weak strength of this feature in low concentration samples. In the previous study no other absorptions could be observed for europium in matrices of lower (< 2 %) carbon monoxide concentration. The higher sensitivity of the current spectrometer allowed new, previously unobserved absorption features to be identified in low, 0.1 %, concentration samples. The following section aims to assign the dominant absorption band observed in 0.1 % samples at 1863.6 cm^{-1} by comparison to DFT and MP2 geometry optimisations and vibrational frequency calculations.

In the case of CO complexed to a metal centre, three possible orientations need to be considered, two end-on options bound through either the carbon atom or the oxygen atom or a side-on bound CO complex. The results of structural geometry optimisation calculations at the BP86, B3LYP and MP2 levels are displayed with their bond lengths in Angstrom units in Figure VI.22.

In an effort to attribute the experimentally observed absorption at 1863.6 cm^{-1} to one of these orientations a frequency analysis was performed using each method. First a comparison of the abilities of the BP86, B3LYP and MP2 methods to calculate the C-O stretch of free carbon monoxide was performed, the results are listed in Table VI.2. B3LYP yields the worst result, overestimating the frequency by 3.1 %. Both BP86 and MP2 reproduce the free CO vibration very well, overestimating the CO vibrational energy by only 1.1 and 1.4 % respectively. As was the case for the Eu:N_2 system, BP86 is the best method although only marginally in this case.

The increased ability of BP86 to predict the vibrational frequency of CO is not surprising. In a study of a large range of transition metal carbonyls it was found the BP86 approach is superior to MP2 providing more reliable results[15] (M = Cr, Mo, W, Fe, Ru, Os, Ni, Pd Pt). In matrix-isolation studies of first row transition metal carbonyls the BP86 method is found to yield calculated harmonic stretching frequencies within 1 % of the experimental fundamentals[12].

The results of the frequency analysis with all methods is presented in Table VI.5. The carbon bound end-on species shows remarkable agreement with the experimental band at 1863.6 cm^{-1}. BP86 is in excellent agreement, overestimating the frequency by only 3.2 cm^{-1} without any scaling factors. This is also the case for many transition metal carbonyl systems where BP86 results were found to be in good agreement without any scaling[16].

Europium carbon monoxide complexes

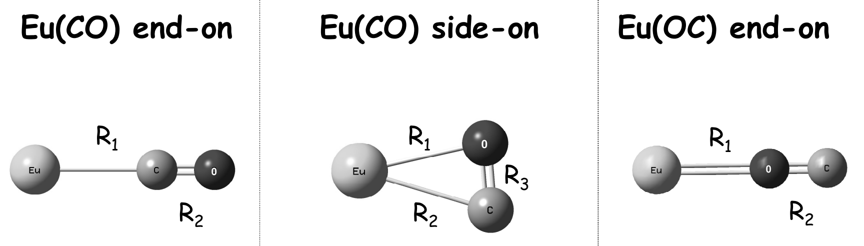

Method	Dist. (Å)	
	R_1	R_2
BP86	2.47	1.17
B3LYP	2.50	1.16
MP2	2.47	1.17

Method	Distance (Å)		
	R_1	R_2	R_3
BP86	2.50	2.58	1.21
B3LYP	2.49	2.60	1.20
MP2			

Method	Dist. (Å)	
	R_1	R_2
BP86	2.34	1.20
B3LYP	2.32	1.20
MP2		

Figure VI.22 Top of figure shows the geometry optimised structures of both end-on (C bonded and O bonded) and the side-on bound europium:carbon monoxide complexes. Tables to the bottom of these structures display the calculated interatomic distances of these molecules in Angstrom units performed at the BP86, B3LYP and MP2 levels with counterpoise correction.

Table VI.5 Vibrational frequencies and IR intensities of the vibrational modes of all three possible orientations of europium carbonyl complexes calculated at the BP86, B3LYP and MP2 levels with counterpoise correction. The C-O stretch which is the focus of this study is highlighted in bold.

Eu(CO)	B3LYP		MP2		BP86		Experiment
	v (cm^{-1})	Intensity	v (cm^{-1})	Intensity	v (cm^{-1})	Intensity	v (cm^{-1})
End-on Eu(CO)	**1923.5**	929	**1879.4**	704	**1866.8**	710	**1863.6**
	257.8	4	269.8	3	251.8	2.1	
	227.1	12	262.3	20	223.5	0.96	
	177.8	0.02	187.8	0.6	158.8	6.2	
End-on Eu(OC)	**1508.7**	1902			**1564.5**	929.5	**1508.7**
	252.9	13			236.8	3.3	
	130.7	3			140.9	3.5	
	123.7	3			119.4	3.2	
Side-on Eu(CO)	**1685.2**	252			**1643.7**	232.9	
	306.7	18			297.5	17	
	248.6	7			232.9	5.4	

The 0.1 % CO in Ar experimental spectrum in the C-O stretching region is overlaid in Figure VI.23 with the BP86 carbon bound end-on species vibrational frequency results to allow comparison. Remarkably good agreement between the experimental 1863.6 cm^{-1} band and the calculated end-on carbon bonded CO complex is observed when a linewidth of 1 cm^{-1} (fwhm) is employed. This allows definitive assignment of this spectral feature to carbon bound Eu(CO)$_1$.

Also identifiable in the experimental spectrum is a weaker absorption feature to lower energy at 1854.5 cm^{-1}. This may be due to the Eu(CO)$_1$ complex occupying a second site of isolation in the predominately argon matrix. From Chapter III, europium is known to exist in two sites in solid Ar. Evidence of Eu atoms occupying a second lattice vacancy in the 0.1 % CO in Ar host following y^8P state irradiation is present in the UV/Vis absorption spectrum in Figure VI.13. This observation suggests this feature relates to a second trapping environment. A study of the transition metal scandium, isolated in a solid CO in Ar host, attributed bands at 1834.2 and 1842.4 cm^{-1} to the binary Sc(CO)$_1$ species occupying two different lattice sites[17]. This represents a site splitting of 8.2 cm^{-1} for these IR absorption features which is of the same magnitude as the splitting observed for the 1863.6 and 1854.5 cm^{-1} bands in this study thus further supporting attribution of this feature to Eu(CO)$_1$ occupying a second site.

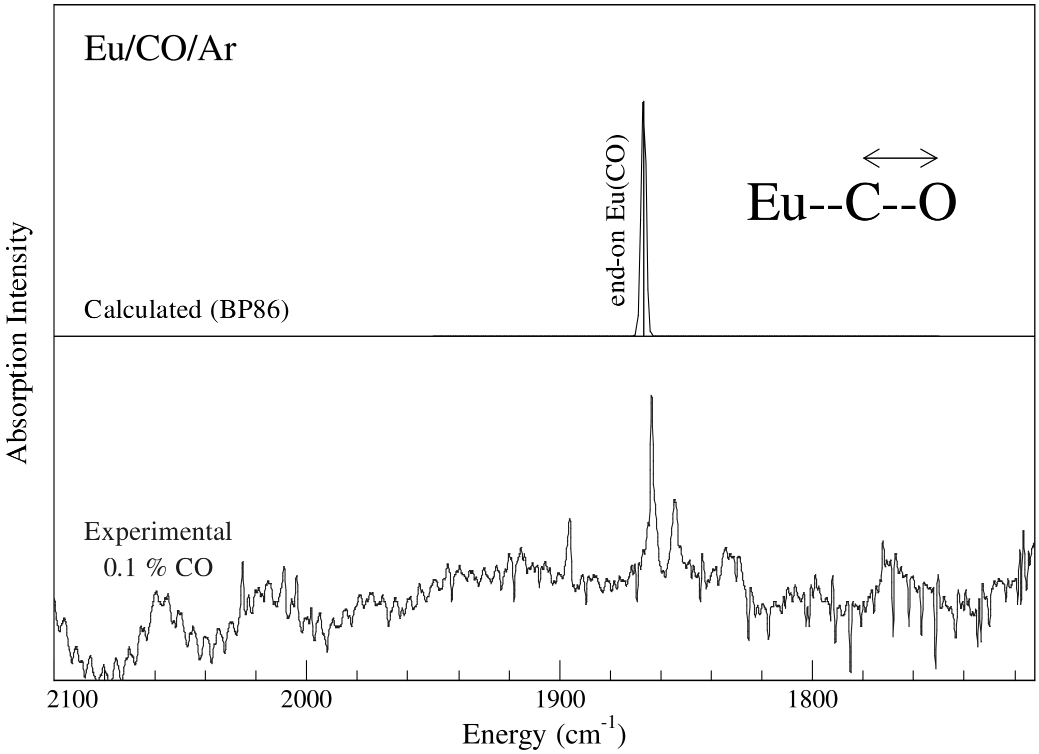

Figure VI.23 Bottom trace displays the experimental spectrum of a 0.1 % CO/Ar sample in the region of the C-O stretch. Top trace exhibits the excellent agreement between the BP86 calculated carbon bound end-on, Eu(CO), species and the IR spectrum in the solid state when linewidth of 1.0 cm^{-1} (fwhm) is employed.

Finally, a weak feature at 1508.7 cm^{-1} identified in high concentration 10 % CO/Ar samples (Figure VI.14) which increased slightly during *y*^{8}P state irradiation is presented in more detail in Figure VI.24. Based on comparison to the calculated frequencies in Table VI.5, this feature may be evidence of a end-on oxygen bound Eu(OC) complex which is predicted to have a C-O vibrational frequency in this region at 1564.5 cm^{-1}. It may be possible a minimum amount of europium atoms exist with an end-on oxygen bound CO molecule at high concentrations of 10 % of CO. Bonding through the oxygen of the carbonyl moiety would be quite unusual and to the best of our knowledge would be the first reported oxygen bound metal carbonyl species. It is approximately 5500 cm^{-1} less stable than the carbon bound analogue as can be seen by the comparison of their binding energies in Table VI.6 and Figure VI.25. There is no evidence in experimental spectra of the side-on bound species with a predicted C-O vibrational frequency at 1643.7 cm^{-1} which is calculated to be more stable than the Eu(OC) complex. This may be due to the dipole on the carbonyl molecule which causes it to be orientated in an end-on fashion towards the metal centre causing no side-on species to be observed.

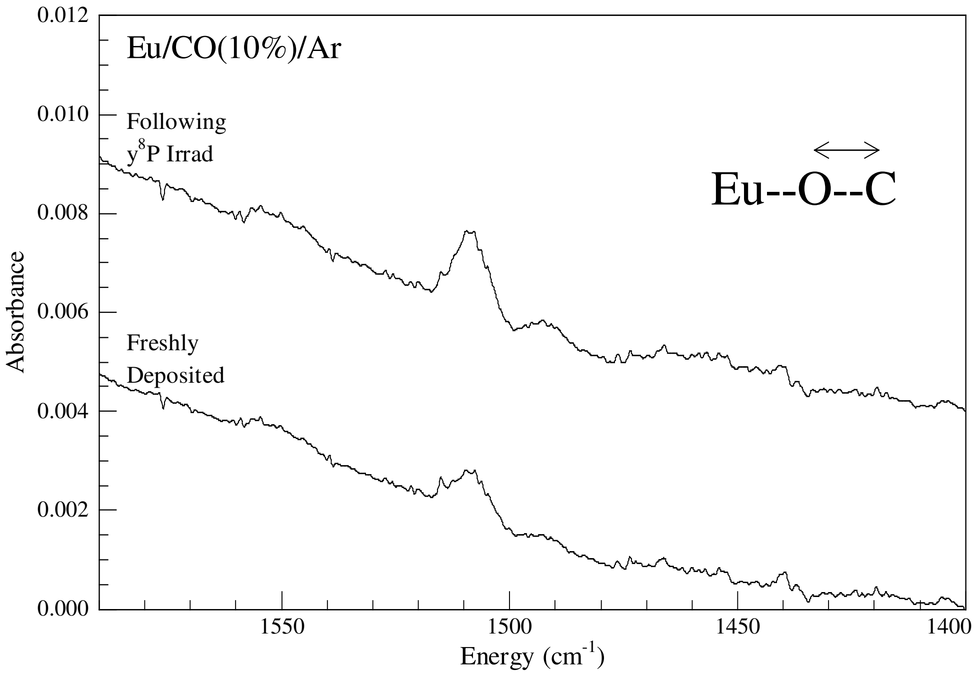

Figure VI.24 An expanded view of the end-on oxygen bound Eu(OC) vibrational energy region for a 10 % CO in Ar sample. Bottom trace displays the IR absorption spectrum on deposition. Top trace presents the absorption spectrum in this region following *y*^{8}P state irradiation.

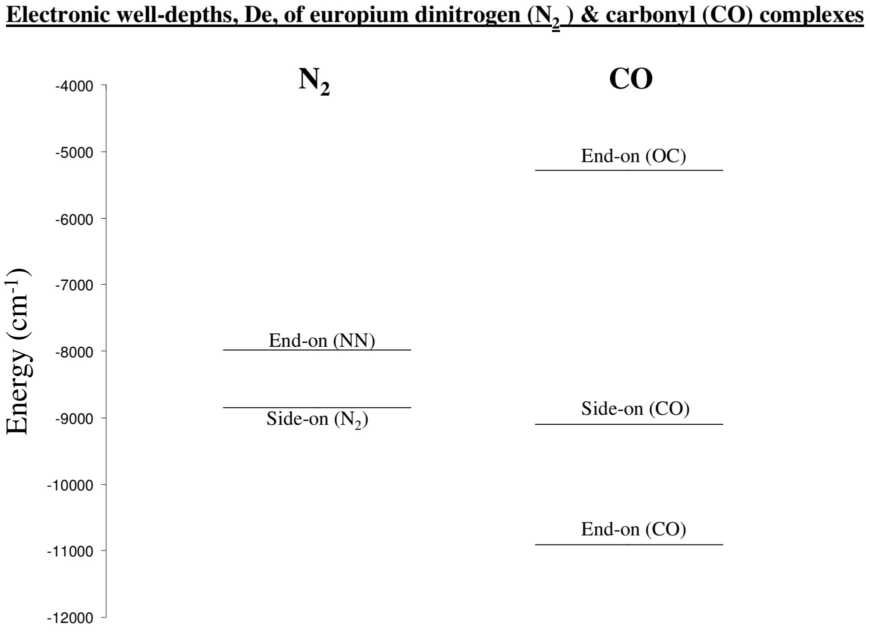

Figure VI.25 Comparison of the electronic well depths, De, in wavenumber units for the various possible configurations of the binary europium dinitrogen and carbonyl complexes calculated at the BP86 level with counterpoise correction.

Table VI.6 The equilibrium well depths (De) of the end-on carbon bound, Eu(CO), side-on bound and end-on oxygen bound, Eu(OC) europium carbonyl complexes, with respect to the free europium and free CO species, calculated at the BP86 level with counterpoise correction.

BP86	De (cm^{-1})
Eu(CO)	10,909
Eu(CO) side-on	9,105
Eu(OC)	5,290

In summary, based on a comparison between the experimental spectra and the calculated vibrational energies, the feature observed in the matrix at 1863.6 cm^{-1} is assigned as corresponding to the C-O vibrational stretch of end-on carbon bound $Eu(CO)_1$ complex. A neighbouring absorption at 1854.5 cm^{-1} is attributed to a second trapping site in the matrix. The absorption band identified at 1508.7 cm^{-1} in samples with high CO concentrations may be evidence of the unusual oxygen bound end-on $Eu(OC)_1$ analogue. Figure VI.25 compares the dissociation energies of each of the calculated binary europium dinitrogen and carbonyl complexes. Clearly the end-on carbon bound $Eu(CO)_1$ complex is the most stable of all. It is 2064 cm^{-1} lower in energy than the side-on dinitrogen species.

VI.4 Molecular Bonding and MO Diagrams of Eu:X (X = N_2, CO)

VI.4.I Introduction

The UV/Vis and IR absorption spectra in the preceding sections coupled with a vibrational analysis of the Eu:X (X = N_2, CO) systems allowed confident assignment of the observed spectral features as binary europium dinitrogen and carbonyl compounds.

The bonding of carbon monoxide to transition metal centres is well known. The metal-CO bond consists of two synergistic components. The first component is electron donation of the lone pair on carbon into a vacant metal orbital (s, p, d_{x2-y2}, d_{z2}) through a σ bond. This electron donation makes the metal more electron rich. To compensate for the increased electron density, a filled metal d-orbital (d_{xy}, d_{yz}) interacts with the empty π^* anti-bonding orbital on the carbonyl ligand to relieve itself of the added electron density through a π bond. This second component is called π back-bonding. Occupation of the π^* on CO leads to a decreased bond order in the carbon monoxide molecule thus a decrease in the carbonyl stretching frequency compared to the free ligand is observed[18,19].

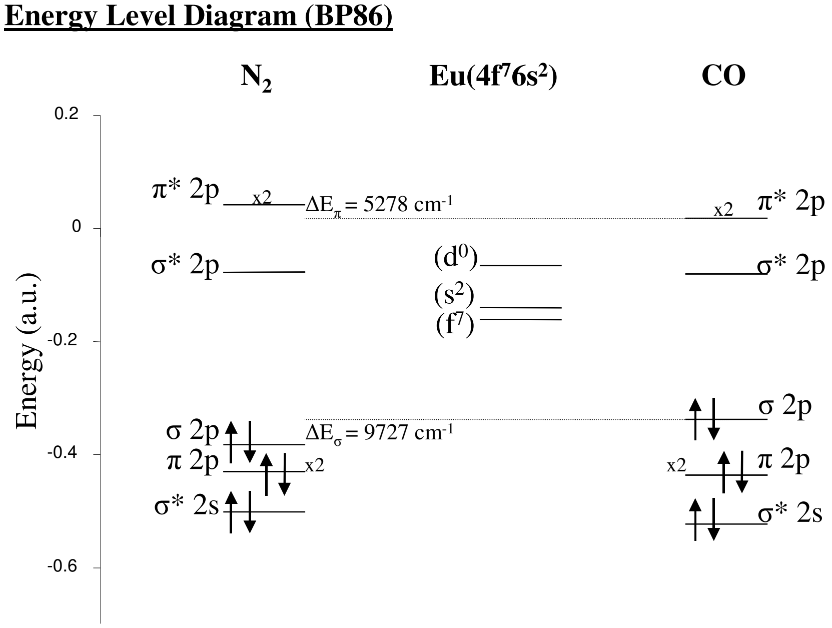

Figure VI.26 Energy levels of the atomic and molecular orbitals involved in the bonding process forming Eu:N_2 and Eu:CO complexes. The energy match of the σ donating σ2p orbital of the ligand and the s-orbital of the metal is best for CO. Also there is better energy agreement between the π accepting π*2p orbital of the carbonyl ligand and the d-orbital of the metal. Both bonding contributions are best for the carbonyl molecule making it more suited to act as a ligand.

The dinitrogen molecule is iso-electronic to CO but it is much less suited to act as a ligand. It is both a poorer σ-donor and a weaker π-acceptor and lacks a dipole moment. This can be seen in Figure VI.26. The energies of the atomic and molecular orbitals of un-complexed Eu and the free ligands are displayed. Clearly there is a better energy match between the d-orbital of Eu and the π* anti-bonding orbital of the CO ligand leading to more efficient π back-bonding. Furthermore, the metal s-orbital involved in σ donation from the ligand shows the best energy agreement for the CO molecule, making CO a better σ donor than N_2.

Nevertheless, dinitrogen zero valence metal complexes have been prepared for many transition metals[20]. Although there are two possible co-ordination geometries of N_2, end-on and side-on, it is found that generally the end-on coordination mode is preferred. In analogy to the interpretation for CO complexes the metal-dinitrogen interaction includes σ and π bond contributions. The σ bond is formed from vacant s, p, d_{x2-y2}, d_{z2} orbitals on the metal and a p-orbital on N_2. The π back-bond involves an occupied d_{xy} or d_{yz} orbital on the metal and one of the π* orbitals[20] on N_2.

The bonding involved in the binary europium carbonyl and dinitrogen compounds are discussed in the following sections with the aid of molecular orbital (MO) diagrams.

VI.4.II Europium dinitrogen complexes - MO diagrams

Experimental and theoretical investigations proposed nitrogen binding to the europium metal centre in both a side-on and end-on fashion in solid Ar. The molecular orbital (MO) diagram of the more stable side-on co-ordinated Eu(N_2) in the region of the valence electrons of Eu is presented in Figure VI.27. Europium exists in a high-spin $[Xe]4f^7 6s^1 5d^1$ configuration in the complex. The highest occupied molecular orbital (HOMO) involves a 5d-orbital (d_{yz}) of atomic Eu interacting with the p-orbitals of N. The second highest occupied molecular orbital (HOMO-1) is a σ type bond resulting from contributions of the Eu 6s and N p-orbitals. These interactions make up a classic synergistic π back-bonding scheme. Electron donation from N_2 into the semi-vacant metal s orbital makes the metal more electron rich. To dissipate some of the increased electron density, a filled metal d-orbital interacts with the empty π* anti-bonding orbital on the ligand, releasing some electron density from the metal centre. The f-orbitals of atomic europium which occur to lower energy than the 6s and 5d orbitals can not be ignored. An enlarged MO diagram in the f-orbital region is presented in Figure VI.28. Most have no interaction with the N_2 ligand. However, f_{xyz} (1) and f_{z3} (3) interact with the p-orbitals of N in a π bonding fashion.

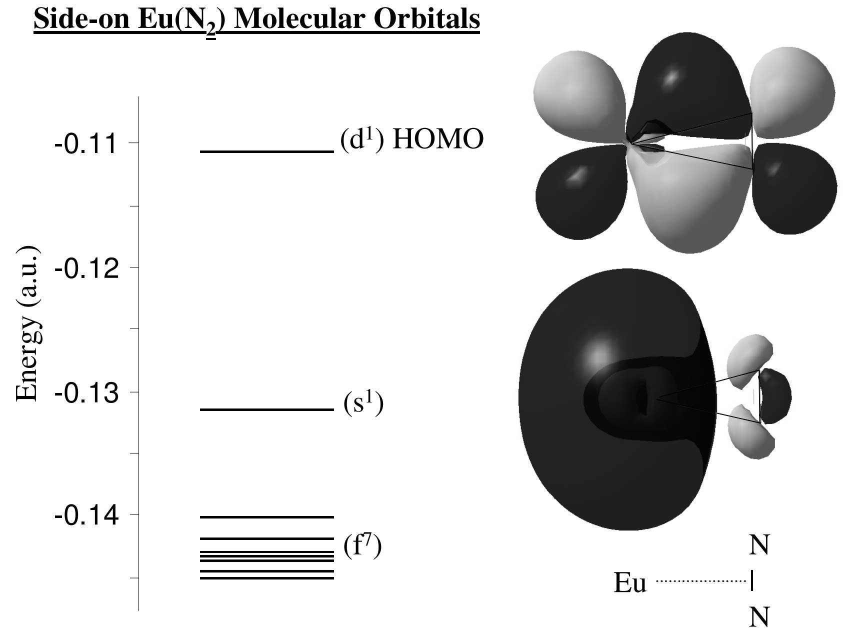

Figure VI.27 Molecular orbital depictions of the highest occupied molecular orbital (HOMO) and HOMO-1 of the Eu(N_2) complex calculated at the BP86 level with counterpoise correction. The energies of the MO's involving f-orbitals of atomic Eu are also displayed.

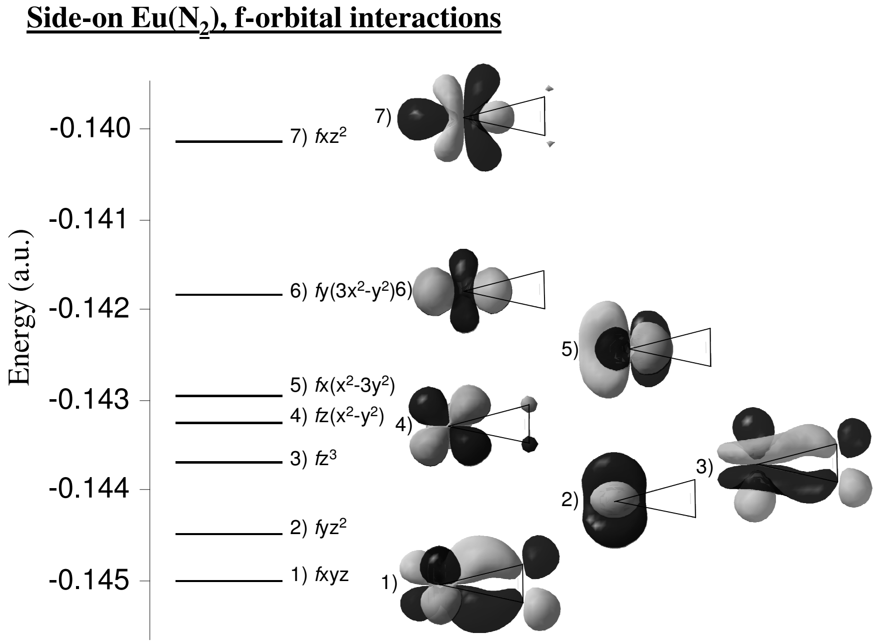

Figure VI.28 Expanded scale view of the MO's of the Eu(N_2) complex involving f-orbitals of atomic Eu calculated at the BP86 level with counterpoise correction.

The other possible bonding orientation of the dinitrogen ligand is in an end-on mode. The MO diagram of the end-on bound species in the region of the valence orbitals of atomic Eu is presented in Figure VI.29. The HOMO seems to involve metal dπ to N_2 π^* donation via the $5d_{xz}$ orbital of Eu. The HOMO-1 is a σ type interaction involving N_2 σ donation to the half filled 6s orbital of atomic europium. Again europium in a $[Xe]4f^7 6s^1 5d^1$ configuration appears to be involved in the bonding with the nitrogen ligand. The MO diagram in the region of the f-orbitals is presented in Figure VI.30. The half-filled $f_{y(3x2\text{-}y2)}$ (6) orbital interacts in a π bonding fashion with the ligand.

A comparison of the molecular orbital energies of both orientations of N_2 is displayed in Figure VI.31. The HOMO of the side-on species is much lower in energy than that of the end-on bound complex. This is in agreement with Table VI.4 which predicted that the side-on species is more stable.

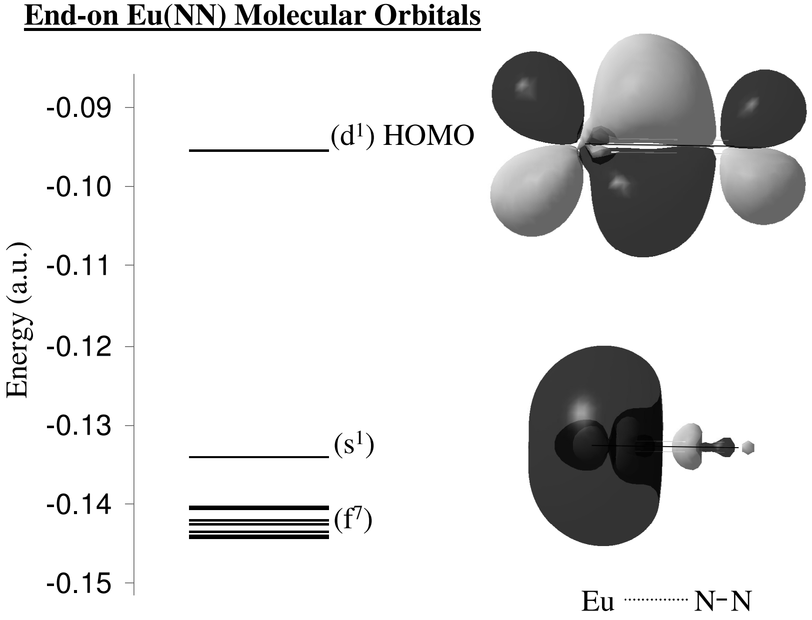

Figure VI.29 Molecular orbital depictions of the highest occupied molecular orbital (HOMO) and HOMO-1 of the Eu(NN) complex calculated at the BP86 level with counterpoise correction. The energies of the MO's involving f-orbitals of atomic Eu are also displayed.

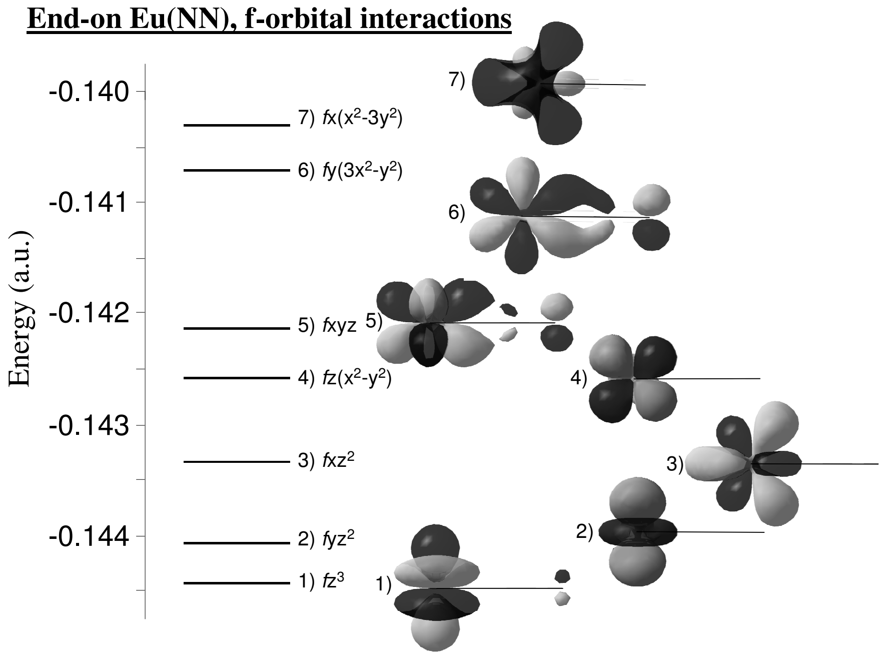

Figure VI.30 Expanded scale view of the MO's of the Eu(NN) complex involving f-orbitals of atomic Eu calculated at the BP86 level with counterpoise correction.

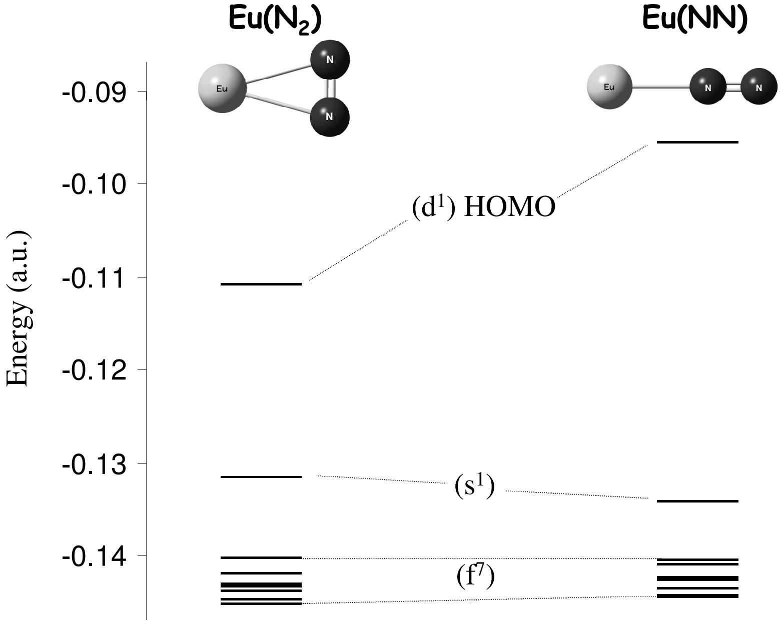

Figure VI.31 Comparison of the MO diagrams of the side-on, Eu(N_2), and end-on Eu(NN) complexes calculated at the BP86 level with counterpoise correction.

In summary, europium existing in a [Xe]$4f^7 6s^1 5d^1$ configuration is involved in the bonding with the nitrogen molecule. The 6s atomic orbital of Eu accepts σ donation from the N_2 molecule in both cases. In the side-on species, the $5d_{yz}$, f_{xyz} and f_{z3} atomic orbitals of Eu undergo π bonding with N_2. In the end-on co-ordinated species the $5d_{xz}$ and $f_{y(3x2-y2)}$ orbitals of europium are involved in π interactions with the ligand.

VI.4.III Europium carbonyl complexes - MO diagrams

Infrared spectra of 0.1 % CO in Ar matrices yielded one dominant absorption feature pertaining to the end-on carbon bound $Eu(CO)_1$ complex. Its molecular orbital diagram is presented in Figure VI.32. The 6s orbital of atomic Eu is involved in a σ bond with the CO molecule and the $5d_{xz}$ HOMO undergoes π interaction with the ligand π* orbitals. Two of the f-orbitals also undergo π interaction with the ligand thorough the f_{xyz} (5) and $f_{y(3x2-y2)}$ (6) orbitals as displayed in Figure VI.33.

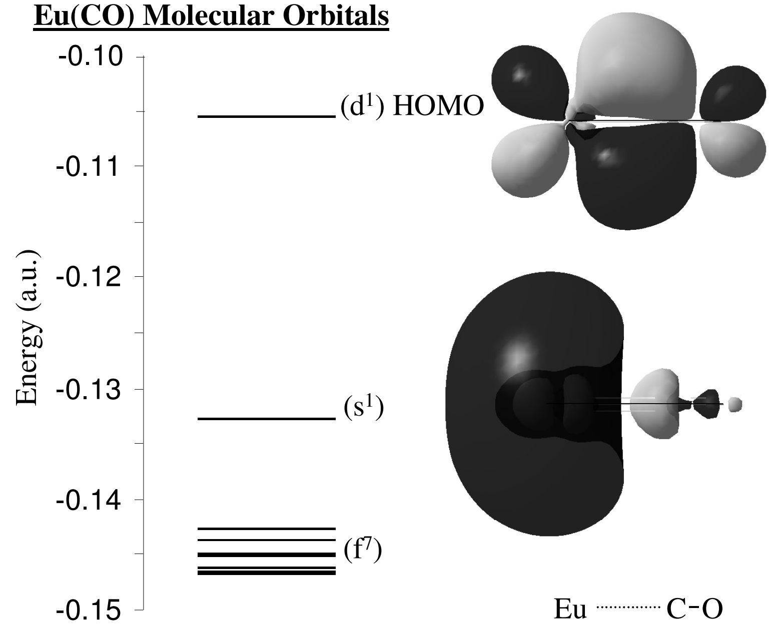

Figure VI.32 Molecular orbital depictions of the highest occupied molecular orbital (HOMO) and HOMO-1 of the Eu(CO) complex calculated at the BP86 level with counterpoise correction. The energies of the MO's involving f-orbitals of atomic Eu are also displayed.

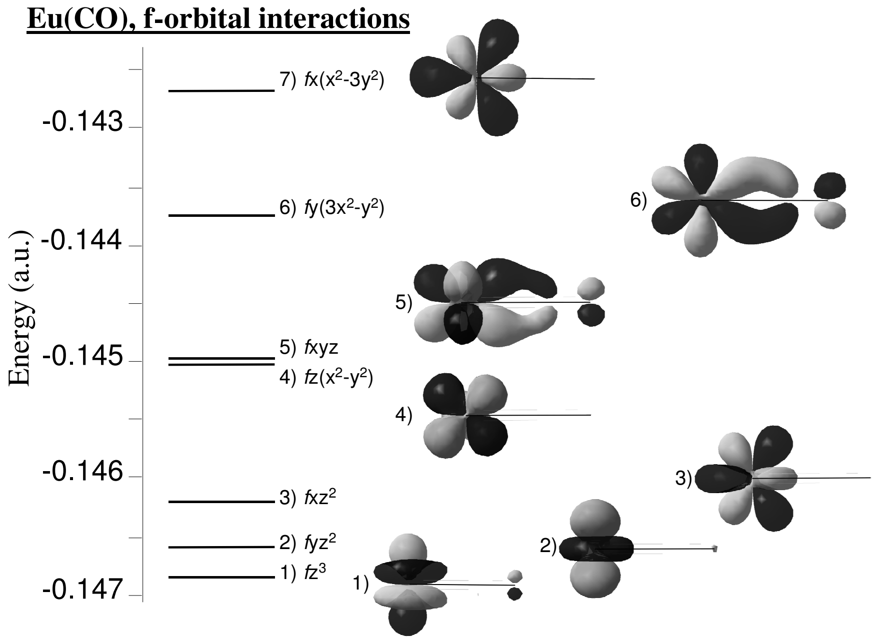

Figure VI.33 Expanded scale view of the MO's of the Eu(CO) complex involving f-orbitals of atomic Eu calculated at the BP86 level with counterpoise correction.

VI.4.IV Molecular Bonding of Eu:X (X = N_2, CO) Summary

From the MO diagrams presented, europium existing in a [Xe]$4f^7 6s^1 5d^1$ configuration is identified as being involved in the bonding with the both the dinitrogen and carbonyl molecules. Although a [Xe]$4f^7 6s^1 6p^1$ state is excited during sample irradiation, an inter-electronic cascade would allow the 'forbidden' [Xe]$4f^7 5d^1 6s^1$ state to be populated by non-radiative relaxation processes from the higher y^8P state under excitation[21]. Occupancy of a high-spin metal state in the bonding process may be expected based on numerous transition metal systems studied to date[12,20]. All transition metal:X (X = N_2, CO) complexes investigated thus far involved high-spin metal centres in which an electron was promoted from the s-orbital to the d-orbital. This reduced the σ repulsion between the metal and the ligand and maximised the number of dπ electrons hence maximising the π donation to the ligand[12,20].

Even though the transition metal:X (X = N_2, CO) systems have been subject to widespread study, there are very few theoretically supported lanthanide:X (X = N_2, CO) assignments available in the literature to date. Possibly this is due to the large computational resources needed to calculate the bonding vibrational frequency of such many electron systems. However, recent theoretical and experimental studies of two lanthanide carbonyls [Ln(CO), Ln = Gd[22] and Ce[23]] found that similar to the transition metal carbonyls[12], the Ln(CO) complexes involved high-spin states of the metal atoms formed by promotion of an s electron to a d-orbital. In the case of Gd it has a ground state configuration[24] of $[\mathrm{Xe}]4f^7 5d^1 6s^2$ but the metal occupancy in the carbonyl complex is $[\mathrm{Xe}]4f^7 5d^2 6s^1$, an s-electron is promoted to the d-orbital. Similarly, Ce which exists in a ground state configuration[24] of $[\mathrm{Xe}]4f^1 5d^1 6s^2$ involves bonding through a high-spin state metal centre in a $[\mathrm{Xe}]4f^1 5d^2 6s^1$ configuration. In both cases an s electron is transferred to a d-orbital causing a reduction of the Ln-CO σ repulsion and an increase of the CO σ donation coupled with an increase of the amount of d electron density on the metal available for π back-donation. This is also precisely as is the case for the europium carbonyl.

Theoretical studies of the dinitrogen ligand with lanthanide metal centres are not present in the literature to date. Although N_2 is a weaker ligand, it is found that changing the electronic state of the metal has a substantial effect on ligand activation for the transition metal dinitrogen systems[20]. The metals often have electrons in the valence s-orbital causing a significant degree of σ repulsion and a reduced possibility for π back-bonding. Photoactivation to a high-spin state can enhance the reactivity as it reduces the σ repulsion and increases the number of electrons in valence d-orbitals. For example[20], Ti atoms in their electronic ground ($3d^2 4s^2$) state do not react with N_2 because of significant σ repulsion. It has been shown in the case of the CO complex of Ti that the $3d^3 4s^1$ configuration is more reactive as there is less σ repulsion and a greater possibility for π back-donation. Only after photolytic activation do Ti atoms form a weakly bound N_2 complex. This is because the metal atom must effectively populate the π* MOs of the ligand. After irradiation the increased number of electrons in the valence d-orbitals lead to π back-bonding.

A similar effect is evidenced in the current study. With the less reactive N_2 ligand there is little to no reaction of atomic Eu in its ground state, just as in the Ti example. Photoactivation is necessary for Eu:N_2 bonding to occur. During sample y^8P state irradiation, the Eu atom is promoted to the $[\mathrm{Xe}]4f^7 6s^1 6p^1$ configuration excited state. From here relaxation to the metastable ^{10}D state of $[\mathrm{Xe}]4f^7 5d^1 6s^1$ configuration is possible. This configuration has one s electron removed so less σ repulsive interaction and the d-orbital is now populated making electrons available for π back-bonding. From this electronic configuration complexation of Eu with a neighbouring N_2 molecule occurs.

VI.5 Conclusion

The photoreactivity of atomic Eu with both dinitrogen (N_2) and carbon monoxide (CO) was investigated. UV/Vis absorption spectra provided evidence of isolation of atomic Eu in solid N_2. These atoms could be removed by lamp irradiation of the y^8P state. In the iso-electronic, but more reactive carbon monoxide host, UV/Vis absorption spectra exhibit no guest atom isolation. Reaction with CO molecules occurs during deposition.

Both the Eu:N_2 and Eu:CO systems were investigated diluted in solid Ar in the infrared spectral region monitoring the N-N and C-O stretches. With high concentrations of N_2 or CO in the host, the resulting IR spectra were complicated exhibiting multiple features. However, at low host concentrations the spectra were simplified and could be analysed. In hosts of 1 % N_2 in Ar two features are observed at 1787.5 and 1824.3 cm^{-1}. Samples of 0.1 % CO in argon exhibited a prominent feature at 1863.6 cm^{-1}. At these low metal-ligand ratios, the binary metal-ligand species are expected to dominate.

Geometry optimisation and vibrational frequency analysis were carried out on the possible binary structures using the DFT BP86, the B3LYP hybrid functional which includes a mixture of Hartree-Fock (HF) exchange with DFT exchange-correlation and the post-Hartree-Fock MP2 methods. Transition metal chemistry is known to be notoriously problematic for HF based theories[25]. Orbitals tend to be too localised on the metal atom or the ligands due to the small spatial extent of the d-orbitals. It is known that MP2 does not fully capture the effects of correlation in transition metal-ligand bonds. In particular, for transition metal carbonyls MP2 overestimates the bond energies[25]. The B3LYP hybrid functional which, to some degree, is also a HF based theory is observed to describe transition metal carbonyl bonding poorly also. It suffers from underbinding and overestimation of M-CO distances[26]. However, the DFT BP86 method is found to yield excellent results for transition metal systems to date[12,15]. This also appears to be the case in this study of lanthanide dinitrogen and carbonyl complexes. The DFT BP86 method yielded vibrational frequencies and results in closest agreement with experiment, much better than the HF based MP2 and B3LYP predictions.

An anharmonic frequency analysis using the BP86 method allowed assignment of the experimental bands at 1787.5 and 1824.3 cm^{-1} in dinitrogen/argon matrices as being due to the binary side-on and end-on species respectively. The side-on species is calculated to be 862 cm^{-1} lower in energy and exhibits a 2.6(± 0.9)-fold dominance over the end-on orientated complex in matrix samples.

Vibrational frequency analysis of the europium carbonyl system at the BP86 level allowed the feature observed in the carbon monoxide/argon matrix at 1863.6 cm^{-1} to be assigned as corresponding to the C-O stretch of the end-on carbon bound $Eu(CO)_1$ complex. A weak absorption feature identified in samples of 10 % CO in Ar at 1508.7 cm^{-1} may be evidence of the unusual oxygen bound end-on $Eu(OC)_1$ analogue. A list of these assignments with their experimental and calculated vibrational frequencies are presented in Table VI.7.

Table VI.7 A summary of the spectral features identified in matrix samples of europium co-deposited with low concentrations of N_2 or CO in Ar. The experimentally observed values are listed in wavenumber units. Also shown are the results of vibrational analysis using the counterpoise corrected BP86 method and their spectral assignments.

Eu/Ar/X Host	Vibrational Frequency		
X	Experimental (cm^{-1})	BP86 (cm^{-1})	Assignment
N_2	1824.3	1874.6	End-on, $Eu(N\text{-}N)_1$
	1787.5	1837.7	Side-on, $Eu(N_2)_1$
CO	1863.6	1866.8	End-on, $Eu(CO)_1$
	1854.5		*End-on, $Eu(CO)_1$ [Site]*

Molecular orbital theory allowed investigation of the orbitals involved in bonding in the europium:dinitrogen and europium:carbonyl species. In all cases europium is bound in a high-spin $[Xe]4f^75d^16s^1$ electronic configuration. For the weaker N_2 ligand, europium atoms can be isolated on deposition as evidenced by the atomic absorptions in the bottom trace of Figure VI.1. The dinitrogen complexed products are formed via irradiation to a $[Xe]4f^75d^16s^1$ state which has increased metal $d\pi$ to N_2 π^* donation capabilities and decreased metal-N_2 σ repulsion thus promoting metal-ligand bonding. With the more reactive CO, bonding occurs without any activation. The results of previous lanthanide carbonyl [Ln(CO), Ln = Gd[22] and Ce[23]] studies are listed in Table VI.8 with the Eu(CO) data from the present work to allow comparison. Experimentally the C-O vibrational frequency is observed to decrease upon progressing from Eu to Gd to Ce. Lower C-O frequencies imply a weaker carbon-oxygen bond caused by a greater degree of π back-bonding into the π^* orbitals of CO.

The electronic configuration of each metal when bound to a carbonyl molecule is shown. In all cases a high-spin state involving promotion of an s-electron to a d-orbital is observed. Both Gd and Ce have two electrons in their d-orbitals. This is twice as many as atomic Eu, leaving a greater amount of d electron density available for π back-bonding which leads to lower C-O vibrational frequencies.

Table VI.8 Comparison of theoretically studied lanthanide carbonyl systems to date. The electronic configuration of the metal centre in its free ground state, G.S., and when complexed to carbon monoxide, M(CO), are listed. Calculated metal-carbon, M-C, and carbon-oxygen, C-O, bond lengths are displayed in Angstrom units along with calculated (Calc.) and experimentally (Exp.) observed C-O vibrational frequencies in wavenumber units. Calculation methods were BP86 (Eu), PW91 (Gd), B3LYP (Ce).

M(CO)	Electronic Config.		Calculated Re		ν (C-O)	
M	G.S.	M(CO)	M-C (Å)	C-O (Å)	Calc. (cm^{-1})	Exp. (cm^{-1})
Eu	$4f^7 6s^2$	**$4f^7 5d^1 6s^1$**	2.468	1.173	1866.8	**1863.6**
Gd	$4f^7 5d^1 6s^2$	**$4f^7 5d^2 6s^1$**	2.224	1.179	1817.4	**1809.7**
Ce	$4f^1 5d^1 6s^2$	**$4f^1 5d^2 6s^1$**	2.289	1.172	1849.8	**1771.8**

In conclusion, a vibrational frequency analysis of the binary Eu:N_2 and Eu:CO complexes was performed. Their experimentally observed spectral features were attributed based on comparison to predicted vibrational frequencies. These appear to be the first theoretically supported lanthanide:dinitrogen assignments. A comparison of various theoretical methods, BP86, B3LYP and MP2, found that the BP86 method is the most appropriate for describing lanthanide metal bonding.

References

[1] S. Cradock and A. J. Hinchcliffe, *Matrix Isolation, A technique for the study of reactive inorganic species, page 24*. (Cambridge University Press, 1975).

[2] M. J. Frisch, G. W. Trucks, H. B. Schlegel, G. E. Scuseria, M. A. Robb, J. R. Cheeseman, J. A. Montgomery, T. Vreven, K. N. Kudin, J. C. Burant, J. M. Millam, S. S. Iyengar, J. Tomasi, V. Barone, B. Mennucci, M. Cossi, G. Scalmani, N. Rega, G. A. Petersson, H. Nakatsuji, M. Hada, M. Ehara, K. Toyota, R. Fukuda, J. Hasegawa, M. Ishida, T. Nakajima, Y. Honda, O. Kitao, H. Nakai, M. Klene, X. Li, J. E. Knox, H. P. Hratchian, J. B. Cross, V. Bakken, C. Adamo, J. Jaramillo, R. Gomperts, R. E. Stratmann, O. Yazyev, A. J. Austin, R. Cammi, C. Pomelli, J. W. Ochterski, P. Y. Ayala, K. Morokuma, G. A. Voth, P. Salvador, J. J. Dannenberg, V. G. Zakrzewski, S. Dapprich, A. D. Daniels, M. C. Strain, O. Farkas, D. K. Malick, A. D. Rabuck, K. Raghavachari, J. B. Foresman, J. V. Ortiz, Q. Cui, A. G. Baboul, S. Clifford, J. Cioslowski, B. B. Stefanov, G. Liu, A. Liashenko, P. Piskorz, I. Komaromi, R. L. Martin, D. J. Fox, T. Keith, A. Laham, C. Y. Peng, A. Nanayakkara, M. Challacombe, P. M. W. Gill, B. Johnson, W. Chen, M. W.

Wong, C. Gonzalez and J. A. Pople, *Gaussian 03, Revision E.01.* (Gaussian Inc., Wallingford CT, 2004).

[3] X. Cao and M. Dolg, Journal of Molecular Structure: THEOCHEM **581** (1-3), 139 (2002).

[4] X. Y. Cao and M. Dolg, Theoretical Chemistry Accounts **108** (3), 143 (2002).

[5] A. Buchachenko, G. Chałasiński, and M. Szcześniak, Structural Chemistry **18** (6), 769 (2007).

[6] M. Dolg, H. Stoll and H. Preuss, The Journal of Chemical Physics **90** (3), 1730 (1989).

[7] Z. H. Lu, L. Jiang and Q. Xu, The Journal of Physical Chemistry A **114** (5), 2157 (2010).

[8] G. P. Kushto, P. F. Souter, G. V. Chertihin and L. Andrews, The Journal of Chemical Physics **110** (18), 9020 (1999).

[9] G. V. Chertihin, L. Andrews and C. W. Bauschlicher, Journal of the American Chemical Society **120** (13), 3205 (1998).

[10] Y. L. Teng and Q. Xu, The Journal of Physical Chemistry A **112** (16), 3607 (2008).

[11] *CRC Handbook of Chemistry and Physics*, 76th ed. (CRC Press, 1995).

[12] M. Zhou, L. Andrews and C. W. Bauschlicher, Chemical Reviews **101** (7), 1931 (2001).

[13] S. P. Willson and L. Andrews, The Journal of Physical Chemistry A **102** (50), 10238 (1998).

[14] J. L. Slater, T. C. DeVore and V. Calder, Inorganic Chemistry **13** (8), 1808 (1974).

[15] V. Jonas and W. Thiel, The Journal of Chemical Physics **102** (21), 8474 (1995).

[16] W. Koch and M. C. Holthausen, *A Chemist's Guide to Density Functional Theory*, 2nd ed. (Wiley-VCH, 2000).

[17] M. Zhou and L. Andrews, The Journal of Physical Chemistry A **103** (16), 2964 (1999).

[18] K. F. Purcell and J. C. Kotz, *Inorganic Chemistry, Chapter 16: Organometallic Chemistry: Synthesis, Structure and Bonding.* (W.B. Saunders Company, 1977).

[19] *OrganometallicHyperTextBook.* *http://www.ilpi.com/organomet/carbonyl.html [Last accessed August 2010].*

[20] H. J. Himmel and M. Reiher, Angewandte Chemie International Edition **45** (38), 6264 (2006).

[21] V. E. Bondybey and J. H. English, The Journal of Chemical Physics **75** (1), 492 (1981).

[22] X. Jin, L. Jiang, Q. Xu and M. Zhou, The Journal of Physical Chemistry A **110** (46), 12585 (2006).

[23] M. Zhou, X. Jin and J. Li, The Journal of Physical Chemistry A **110** (34), 10206 (2006).

[24] *NIST Atomic Spectra Database (version 3.1.5), available: http://physics.nist.gov/asd3 [2010, March 22].* (National Institute of Standards and Technology, Gaithersburg, MD).

[25] E. R. Johnson and A. D. Becke, Canadian Journal of Chemistry **87**, 1369 (2009).

[26] F. Furche and J. P. Perdew, The Journal of Chemical Physics **124** (4), 044103 (2006).

Chapter VII

Conclusion

Previous studies by the Maynooth group focused on the luminescence and reactivity of spherical ground state main group metal atom systems isolated in low temperature solids. To advance this research to the lanthanide series a detailed spectroscopic study of matrix-isolated europium was performed. UV/Vis absorption spectra of Eu/RG (RG = Ar, Kr, Xe) samples deposited at 10 K showed two regions of absorption. The intense visible y^8P ↔ a^8S transition which was the focus of this study and a weaker ^{8}P ↔ a^8S transition occurring in the UV spectral region. Concentration studies of samples deposited at 10 K exhibited no evidence of metal aggregates indicating only atomic absorption bands are observed with these low temperature deposition conditions. Matrices formed at higher temperatures, to promote metal clusters, exhibited new non-atomic absorption features in the 495 to 520 nm and 540 to 580 nm regions, bands attributed to europium dimer and higher aggregates respectively. Previous matrix-isolation studies by the Maynooth Group generally formed considerable amounts of dimer even during cold depositions. In contrast, in the case of europium, specific preparation conditions must be employed to observe aggregates. This is partly due to the weak van der Waals bond involved in Eu_2 which does not encourage self aggregation but more importantly is the much larger mass of Eu which is three times heavier than any metal previously studied by the Maynooth Group. The increased weight decreases the guest's freedom of movement upon arrival on the growing sample thus limiting the probability of dimer formation during deposition.

Interestingly, absorption of the individual J-levels of the ^{8}P state in the UV is observed due its large spin-orbit splitting, whereas the y^8P state absorption shows Jahn-Teller threefold structure. Europium is a unique case where Jahn-Teller and spin-orbit splitting can be identified in the same metal-RG system and shows that JT effects can be completely 'washed out' by large enough magnitude SO splitting.

Structure evident on the y^8P state absorption features of annealed samples was resolved as Jahn-Teller splitting in solid Ar and Kr using site-specific excitation spectroscopy. Its origin pertained to atoms trapped in two different lattice sites within the matrices. Only one site of isolation is observed in solid Xe. Excitation spectra for each site displayed resolved JT threefold splitting. Absorption spectra in Ar and Kr were completely accounted for by these two sites implying no other vacancy is occupied in annealed samples. A plot of gas phase-matrix shift versus RG polarisability displayed a linear correlation between the single thermally stable site in Xe and the blue sites in Ar and Kr suggesting these are vacancies of the same site type within the lattices. Luiti-Pirani calculations of Eu-RG diatomic bond lengths compared to the available lattice vacancy sizes and site occupancy of the Na/RG system allowed the blue site to be attributed to metal occupancy of a tetra-vacancy (tv). The red site observed in Ar and Kr is a slightly larger hexa-vacancy (hv).

The Eu/RG luminescence produced with y^8P state excitation was complex. Multiple emission features were observed in each host. However, with site-specific excitation the emission profiles could be simplified, each site yielding only four emission bands. There are seven lower energy excited states below the y^8P state from which emission could occur. Based on spectral location and lifetime measurements the four features are assigned to y^8P, z^6P, a^8D and a^{10}D state emission to the ground a^8S state.

The y^8P state resonance fluorescence is the most intense emission feature in the solid state. The radiative lifetime of this y^8P ↔ a^8S transition was identified for atoms isolated in the red site but could not be observed for the blue site due to much greater involvement of competing non-radiative relaxation pathways. Atoms in this vacancy exhibited Stokes shifts of almost twice the value of the red site y^8P fluorescence implying a greater interaction with the surrounding matrix supporting attribution of the blue site to smaller tetra-vacancies.

z^6P state emission was observed in the 570 nm region. Lifetimes produced with indirect y^8P state excitation and direct z^6P state excitation yielded little difference suggesting the intervening y^8P → z^6P feeding step is very fast. Lifetimes recorded in the matrix do not agree with gas phase decay data published on this state. Recording accurate lifetimes of this state in the gas phase is hindered by its hundreds of nanoseconds lifetime, making it difficult to generate and maintain in appreciable abundance. In recent times the values cited in the literature for the gas phase are becoming closer to the solid state. Interestingly, blue site excitation spectra in the region of the z^6P state showed features corresponding to the $z^6P_{5/2}$, and $z^6P_{7/2}$ levels but no evidence of the $z^6P_{3/2}$ level. This is due to europium obeying the $\Delta J = 0, \pm 1$

electric-dipole selection rule where transition from the $a^8S_{7/2}$ state to the J = 5/2 and 7/2 levels are allowed. This J selection rule is also obeyed in the UV region ^{8}P state absorptions. Transitions from the fully relaxed $a^8S_{7/2}$ state to the ^8P_J (J = 5/2, 7/2, 9/2) levels are identified. Also of note in z^6P excitation spectra is the observation of JT splitting on the $z^6P_{5/2}$ band in increasingly distortable hosts. It progresses from a structureless band in solid Ar, to a doublet in Kr and a threefold split feature in Xe. As one moves to hosts with greater ability for distortion the Jahn-Teller effect becomes more evident.

Emission in the 680 nm region is quite weak but based on its long-lived nature and spectral location it can be assigned to the forbidden $a^8D \rightarrow a^8S$ electronic transition with a solid state lifetime of hundreds of microseconds. Currently no experimental gas phase lifetime data is available for this transition which is electric-dipole forbidden.

The final emission at ~800 nm is also long-lived and is assigned to the metastable a^{10}D state with a lifetime in the matrix of several milliseconds. This is the first recorded decay data for this electric-dipole forbidden transition which has not been measured in the gas phase. Its assignment is supported by a temperature effects study which shows an increase in population for this state at elevated temperatures implying it is the lowest energy excited state acting as a ‘population trap’.

D → S type emission of atomic europium obey traditional expectations in one regard, showing little host change effects on their spectral location. However, unlike ‘classical’ D → S transitions they are broad and shifted from the gas phase position. This is an example of the effect of site size on D states of metal atom systems. Atomic europium occupies tv’s and hv’s both of which are quite cramped in accommodating the large lanthanide metal causing broad and shifted D state emission. This was observed previously by the Maynooth Group for D → S transitions of atomic Mn isolated in small single-vacancy (sv) sites.

Following a complete analysis of the solid state luminescence of atomic Eu isolated in the RG’s, a laser irradiation study was performed. Irradiation of Eu/RG samples removed all atomic features and formed new higher energy absorptions. Based on their spectral locations, intensity distributions and emission features the new absorptions are attributed with confidence to matrix-isolated singly ionised europium.

Analogous to neutral europium, the ion was identified to occupy two matrix trapping sites in solid Ar and Kr and one vacancy type in the Xe lattice. A polarisability plot allowed attribution of the two higher energy absorptions (B^+) in the region of the $4f^7(^8S°_{7/2})6p_{1/2}$ configuration to the same site type in each host. Eu^+-RG diatomic bond lengths calculated with the MP2 method attributed this site to an octahedral interstitial (I_{oh}) vacancy while the remaining lower energy R^+ site features in Ar and Kr correspond to ions occupying single vacancy sites. These sites are formed from atoms initially occupying tv's and hv's. The site transformation process involves significant lattice re-arrangement which is possible due to the strong binding energy of the Eu^+-RG diatomics.

The existence of europium ion absorptions with significant oscillator strength occurring in close proximity to the y^8P state transition of atomic Eu may explain why the visible luminescence of Eu/RG has not been studied before. Samples formed by the laser vaporisation technique would create both europium atoms and ions which would be observed upon deposition as a continuum of complex multi-component absorption bands in the 300 to 480 nm region. Only the use of electron bombardment used in this study or thermal vaporisation allows the formation of purely neutral atomic samples unhindered by the complex 350 to 450 nm ion absorption features.

The final section of this thesis studied the photochemical reactivity of europium isolated in argon matrices with small ligand molecules. UV/Vis absorption spectra confirmed atomic isolation is achieved on deposition in pure molecular dinitrogen matrices. The metal atoms are completely removed during gentle lamp irradiation of the y^8P state. In matrices of the iso-electronic but more reactive carbon monoxide, europium atoms fully reacted with the ligand molecule during deposition. Atomic isolation was achieved in argon solids with low CO concentrations and removed by y^8P state irradiation. In order to investigate this photoreactivity an infrared absorption study monitoring the N-N and C-O stretching regions was performed. Spectra were complex, involving multiple features. However, samples of low concentrations of N_2 and CO in Ar simplified the spectra and allowed resolution of the complex features. In samples of 1 % dinitrogen in argon, two bands were observed at 1787.5 and 1824.3 cm^{-1}. Various theoretical methods (B3LYP, BP86 and MP2) were employed in an effort to attribute these spectral features. As for transition metal chemistry the post-Hartree-Fock MP2 and hybrid B3LYP functionals were found to be poor at describing lanthanide metal bonding. A vibrational frequency analysis using the DFT BP86 method attributed the 1787.5 and 1824.3 cm^{-1} bands to binary europium dinitrogen complexes in both the side-on and end-on bound geometries. The side-on species is found to be most stable. It is 862 cm^{-1} lower in energy and is estimated to be 2.6 (± 0.9) times more dominant than the end-on orientated species in matrix samples.

Samples of 0.1 % CO in Ar yielded one dominant spectral feature at 1863.6 cm^{-1}. Vibrational frequencies of the three possible carbonyl bonding geometries, side-on and oxygen or carbon bound end-on, were considered using the B3LYP, BP86 and MP2 methods. The BP86 method appears to be the most appropriate for describing lanthanide metal carbonyl bonding. The carbon bound end-on species is predicted to be most stable and its BP86 calculated vibrational frequency shows remarkable agreement with experiment. There is no evidence of the other binary carbonyl species in low CO concentration samples.

A study of the molecular orbitals involved in the bonding of these complexes showed that europium exists in a high-spin $[Xe]4f^7 5d^1 6s^1$ state in the product species. This high-spin state enhances bonding as it reduces the σ repulsion by removal of an s electron and increases the metals ability for π back-bonding by promotion of an electron to the d-orbital. Occupancy of this high-spin state is achieved during irradiation of the $[Xe]4f^7 6s^1 6p^1$ y^8P state via an inter-electronic cascade.

In conclusion, atomic europium was a worthwhile advancement of matrix-isolated metal atom spectroscopy from s and d block elements to the relatively unchartered lanthanide series. The spectroscopy was complex but simplified in this study with the possibility of site-specific excitation. Europium proved to dimerise very inefficiently allowing ready atomic isolation. Lifetimes of the forbidden ^8D, $^{10}D \rightarrow {}^8S$ relaxation are the first reported values for these transitions. Recorded lifetimes of the z^6P state do not agree with gas phase data published to date but may be more accurate due to difficulty in monitoring the gas phase lifetime of this relatively long-lived transition. The formation of europium metal ions during laser irradiation was unexpected and may open a whole new branch of matrix-isolated metal atom spectroscopy. The lanthanides may be a unique case where they can be ionised *in situ* in the RG lattices with relative ease. The stability of the positive ion due to the large nuclear charge of the lanthanide atom allowing this. Studies of other lanthanide metals to investigate this effect would be very enlightening and may even open up new avenues to investigating the reactivity of ions in solid state surroundings. The study of europium dinitrogen and carbonyl complexes using various theoretical methods (B3LYP, BP86 and MP2) compared the appropriateness of different theoretical functionals for lanthanide chemistry. Like transition metal systems it seems the pure DFT BP86 method is most appropriate for describing lanthanide bonding. This thesis proposes that future theoretical studies of lanthanide complexes should employ the BP86 functional.